Flow analysis within the well dock of an LPD

Konstantinos C. Fotis

Flow analysis within the well dock of an LPD

by

Konstantinos C. Fotis

Student Name	Konstantinos C. Fotis
Student Number	5380588

University Supervisor:	Dr.ir. M.J.B.M. Pourquie
University Supervisor:	Dr.ir. PR Wellens
Faculty:	Mechanical Engineering (3mE), TU Delft
Company Supervisor:	Filippos Kalofotias
Company:	Damen Naval
Project Duration:	November, 2022 - September, 2023

Preface

This thesis is the final product of a research study that is conducted in the graduation phase at the Delft University of Technology's Faculty of Mechanical, Maritime, and Materials Engineering, within the section of Energy, Flow, and Process Technology. This research was conducted in collaboration with Damen Schelde Naval Shipbuilding and was guided by the Research and Technology Support section. The subject of this report is the flow analysis within the well dock of an LPD and related design improvements. In this report, readers will find a detailed numerical model, its validation, and the concluding findings. This document is tailored for individuals involved in or curious about ship hydromechanics, with a particular emphasis on numerical modeling.

My thanks go out to everyone who supported me throughout this journey. First and foremost, I would like to express my gratitude to my supervising committee for their invaluable advice and guidance. I have special appreciation for Filippos, not only for his expertise in the ComFLOW program but also for his insightful advice and the enriching conversations we shared. I would also like to thank Dr.ir. MJBM Pourquie and Dr.ir. PR Wellens for guiding me through this research. Further appreciation goes to my colleagues at Damen for their support. Finally, profound thanks to my family and close friends who have been my pillar of support throughout my studies.

Konstantinos C. Fotis
Delft, December 2023

Abstract

The Landing Platform Dock vessel is mainly designed to support amphibious operations in which landing operations play an important role. For operating landing craft the vessel has a well dock at the stern, designed to station several landing craft. Landing operations are restricted by the motions of the Landing Platform Dock vessel and by the motions of the water in the flooded well dock. Due to turbulent flow in the dock entrance and nonlinear wave motions inside the dock, the (dis)embarking procedure can be very hazardous for landing craft. Therefore it is necessary to execute this operation as safe as possible, meaning that the water motions in the well dock should be investigated thoroughly.

The primary objective of this thesis is to investigate how various physical mechanisms, when combined with wave characteristics, influence the flow within the well dock. The wave profile within the dock arises from the interaction of two physical mechanisms: radiation, caused by ship motions, and diffraction, which is observed when the ship remains stationary, causing incoming waves to diffract around its hull. Specifically, this study wants to determine which of the two physical mechanisms radiation or diffraction has a more pronounced influence. Also, it investigates how different wavelengths impact these mechanisms and the results combination of independently analysed mechanisms with a model that integrates both mechanisms from the start of the simulation.

The second objective centers on the development of an accurate and efficient model to capture the physical mechanisms of the flow within the well dock of an LPD. The validation for this model derives from model tests conducted at TU Delft[20].

The third objective focuses on simplifying the model in order to facilitate the design process. Upon validating the model from the second research question, wave kinematics are captured using a wave probe located at the dock entrance. These kinematics are then used as inputs for a 2D model. Notably, this model specifically represents the well dock and the ramp region, excluding the complete ship structure. For validation, the same procedure employed in the second objective is followed, referencing experiments conducted at TU Delft[20].

All Computational Fluid Dynamics (CFD) calculations were executed using the ComFLOW program.

Contents

List of Figures

List of Tables

Nomenclature

Abbreviations

Abbreviation	Definition
ATS	Amphibious Transport Ship
CEO	Chief Executive Officer
CFD	Computational Fluid Dynamics
CJTF	Combined Joint Task Force
FVM	Finite Volume Method
GABC	Generating and Absorbing Boundary Condition
HNLMS	His/Her Netherland Majesty's Ship
LHD	Landing Helicopter Dock
LPD	Landing Platform Dock
MARIN	Maritime Research Institute Netherlands
NATO	North Atlantic Treaty Organization
NWT	Numerical Wave Tank
PDE	Partial Differential Equation
RAO	Response Amplitude Operator
RLNL	Royal Netherlands Navy
RN	Royal Navy
RNG	Re-Normalization Group
SPH	Smoothed Particle Hydrodynamics
UDF	User Defined Functions
UK/NL AF	United Kingdom/Netherlands Amphibious Force
VOF	Volume of Fluid

1

Introduction

1.1. Problem description

The development of the Landing Platform Dock (LPD) ship is a direct response to the growing need for enhanced capability in transporting and supporting amphibious operations. Its primary function is to facilitate these operations, with a particular focus on landing activities. To fulfill this purpose, the LPD incorporates a specialized well dock located at the stern of the vessel, which is specifically designed to accommodate multiple landing craft (see Appendix A.1).

As part of the vessel's design process, a significant consideration was ensuring the ability to embark and disembark under various sea conditions, specifically up to Sea State 4 [8]. To meet this requirement, the wave motions in the flooded well dock of the LPD should be investigated.

Once the vessel is in position, the well dock is flooded by trimming the stern until the desired water level is reached, then the stern gate is lowered. This procedure can be hazardous due to the wave motions within the well dock [8].In particular, swell plays a significant role in this scenario, as the downward movement of the stern displaces water and creates a vortex. This vortex causes water particles to move around the bottom of the ship. Consequently, water accumulates directly behind the ship and flows into the dock, resulting in the formation of shallow water sloshing waves as the water depth decreases rapidly [2].

To improve the safety of embarking and disembarking procedures, it is crucial to evaluate the wave conditions within the flooded well dock of an LPD in advance and afterward to propose potential design improvements for the well dock. This can be accomplished by precisely modeling the flow analysis within the flooded well dock by use of Computational Fluid Dynamics (CFD) and utilizing specialized software such as ComFLOW.

1.2. State of the art

Over the past years, there have been different research studies on the modeling of the wave climate in a well dock of an LPD vessel. The research study primarily focuses on the computational domain and the design of the well dock, both of which will significantly impact the future work of this thesis. In terms of the computational domain, most researchers have made various simplifications due to limited computational capacity. They have employed the linear diffraction theory method to calculate the amplitude of incoming waves, neglecting viscous forces and non-linearities in the flow. Additionally, they have only modeled the well dock using a CFD code. However, this modeling approach is not accurate since the linear diffraction theory assumes small wave amplitudes, in contrast to CFD codes that can consider nonlinear effects around the structure, resulting in more precise results.Furthermore, in most cases, it has been assumed that sloshing forces within the well dock do not significantly affect the ships motion, without providing any evidence to support this assumption. Moreover, these studies have relied on 2D simulations, overlooking physical mechanisms in the y-direction, such as reflection and diffraction. Most of these CFD studies are carried out by foreign navies, like the Canadian and the Australian navy.

A second CFD investigation was the research study of the well dock design. most researchers have investigated four key factors:

1. The slope or flatness of the well dock's bottom floor
2. The configuration of well dock door
3. The depth and length of the well dock
4. Different beach designs at the end of the well dock

These four factors will be thoroughly examined in the final stage of this thesis to propose potential design improvements during the construction of the new LPD.

The overview above, and more specifically in the second chapter of this thesis, shows that currently, neither the studies nor the models have attempted to sufficiently predict the flow analysis within the well dock of an LPD vessel. The challenge in this thesis is to provide a complete determination of the wave profile in the well dock of an LPD vessel using a numerical model, validated with experimental data.

1.3. Research questions

The research questions of this Thesis are:

1. What is the influence of the various physical mechanisms in combination with wave characteristics on the flow within the well dock?
2. What would be an efficient and relatively accurate model setup for capturing the physical mechanisms of the flow within the well deck of an LPD?
3. What kind of model simplifications can be justified to facilitate the design process?

1.4. Research Approach

This research study consists of three main parts, which are divided in sub-parts going deeper into the subject. The three main phases are: literature study, model set-up phase and validation phase. On the start of the research a time schedule has been made to distribute the parts over the time that is specified for the whole research study. The first months are mainly meant for literature study on the computational domain and the design of the well dock, earlier studies that have been done on this subject using CFD. On the outcome of this literature study was chosen to simulate the whole ship in order to be included all the physical mechanisms. Firstly, the creation of a validated model for analyzing the complex flow phenomena taking place inside the well dock of the LPD. The flow inside the well dock, before even the landing craft enters the dock, is influenced by the wave environment, the diffraction of waves due to the presence of the ship hull, the motions of the ship, the associated sloshing of water and the reflection of waves generated inside the well dock. Capturing the physical mechanisms of this complex, interactive system is the start for deriving the hydrodynamic behavior of the LPD-landing craft system under various environmental conditions. Moreover, the developed model should be efficient enough to be usable during design phase. The development of an efficient model would require good insight in the physical mechanisms of the system. For the validation of the developed model, there is model test data available referring to the HNLMS Rotterdam LPD. The advantage of the available model test data is that experiments were conducted for both regular and irregular waves and in different wave heights, so the frequency characteristics of the flow and non-linearities associated with wave height can be studied in more detail

After validation, the viability of the model from a 3D domain in a 2D domain is investigated in order to facilitate the design process. Following this methodology will help in answering the research questions. This is a general approach for this project. More details about the approach which use for each numerical model is described in chapter 3.

1.5. Thesis Outline

This thesis is built up of nine chapters, of which this introductory chapter is the first. Chapter 2 presents an overview of the literature reviewed, followed by Chapter 3, which offers a concise description of the methodology employed to address each research question. Chapter 4 elucidates the model tests conducted for an earlier research study on this subject. Chapter 5 provides an overview of the foundational studies that underpin the investigations conducted in Chapters 6, 7 and 8. The subsequent three chapters delve into each numerical model used to address the research questions. Chapter 9 serves to summarize the research and offers conclusions and recommendations for future work.

2

Literature Study

This chapter provides a literature review of articles examining wave behavior within the well dock using Computational Fluid Dynamics (CFD). The theoretical background of computational fluid dynamics can be found in Appendix B.1. Additionally, this appendix details the methods used to track the free surface in each of the articles discussed below.

2.1. Simulating wave action in the well deck of Landing Platform Dock ships using computational fluid dynamics

In 2004 in Canada, they researched the LPD ship when its well dock is partially flooded and is impacted by waves. The motion of the ship induces sloshing of the contained fluid, which subsequently creates forces that affect the motion of the ship. In this paper they try to simplify the model in order to save the computational time but simultaneously to setup a model which will be accurate in order to study various modifications in the well dock design.

The most complex case is referred to as "fully coupled" which involved the full coupling of the CFD code with the ship motions code. The CFD code includes the diffracted waves by the ship's hull and the code of ship motions includes the ship motions and the fluid forces. The second case was "partly coupled", which involved a simplification in that the forces caused by the sloshing of the fluid did not affect the ship motions. Furthermore, there is the third case called "head sea static" which assumes that the waves are small and do not cause any movement of the ship. For this case, they explored the amount of reduction of the waves close to the hull and their dependence on the amplitude and frequency of the far field waves. They realised that waves with small amplitude and high frequency are affected by the presence of the ship that means the wave height is considerably reduced. On the other hand, the waves with low frequency and high amplitude were unaffected by the ship. Finally, The last case called "static" was that the waves were only generated at the entrance of the well deck, and only internal flow was taken into account.

As far as the model setup is concerned, two domains were established: the external domain which contained the waves outside of the ship, and the internal domain which contained the waves within the well dock. The two domains were merged at the boundary of the well dock to examine the level of diffraction of the wave field at the stern of the ship. This was important because it affected the wave elevation at the entrance of the well dock. The resulting relative motion and velocity distribution can then be used as input for the static model of just the internal structure of the well deck. The same boundary conditions at the entrance to the dock can be used for different internal well dock structures.

The next step was the simulation of the waves within the well dock. In order to save some computational time, they separated the well dock from the rest of the ship. Therefore, they used as input the results of the external domain in order to prescribe the velocity at the entrance of the well dock. In this way, they captured only the internal flow in the well dock in order to use the smallest computational domain within Flow-3D. In addition, they studied the most common scenario in which the LPD impacts the head waves (where the relative angle between the ship's bow and the wave direction is 0 degrees), and the ship is either stopped or moving slowly ahead. In this study, most comparisons were based on the mathematical parameter of RAO (Response Amplitude Operator) which is used to describe a ship's motion in response to waves. Specifically, the RAO measures the amplitude of a ship's motion in response to a unit amplitude wave input at a given frequency. According to figures 2.1 and 2.2, they realised that the forward speed reduces the wave elevation within the well dock, so they were focused on the case of zero speed which is the most challenging. Especially, this observation is clear in figure 2.2 where the RAO for low frequencies has small value and it increases at higher frequencies, and especially at 0.7 rad/s, reaching the value of 1.35 which means that the waves at the well dock entrance could be 35 percent higher than the external waves.

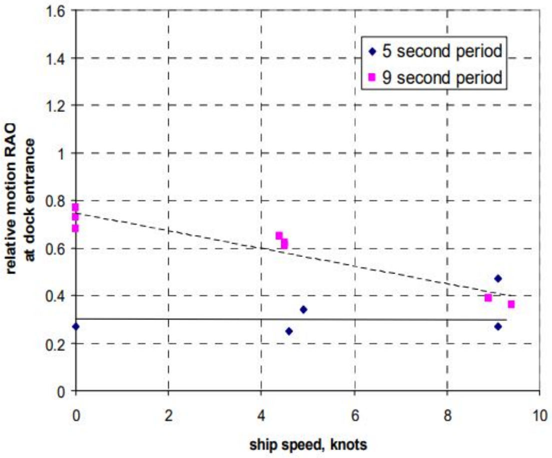

Figure 2.1: RAO for relative motion at well dock entrance, for head waves and forward speed

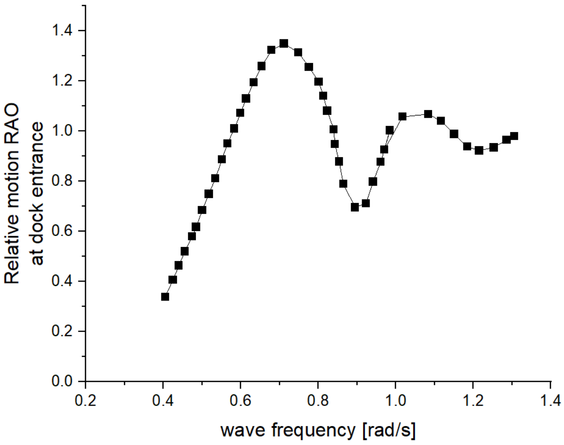

Figure 2.2: RAO for relative motion at well dock entrance, for head waves and zero speed

Also, they compared all the cases of simulations for the purpose of testing if it is possible to save some computational capacity for the study of the well dock design. For instance, they measured the wave height at various locations along the length of the well dock. From figures 2.3 and 2.4 it is clear that there was little difference between the fully coupled case and the static case. So the use of a simplified model was reasonable.

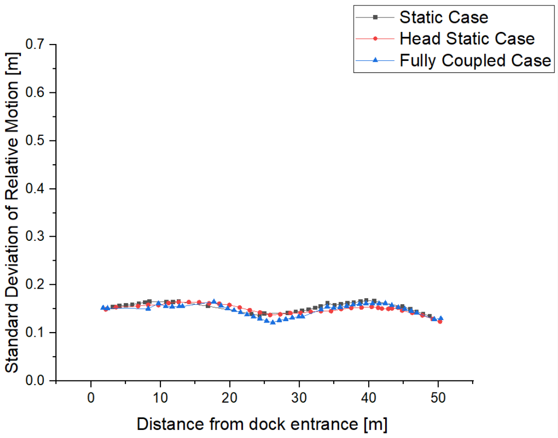

Figure 2.3: Standard deviation of relative motion in well dock with period of 5 second

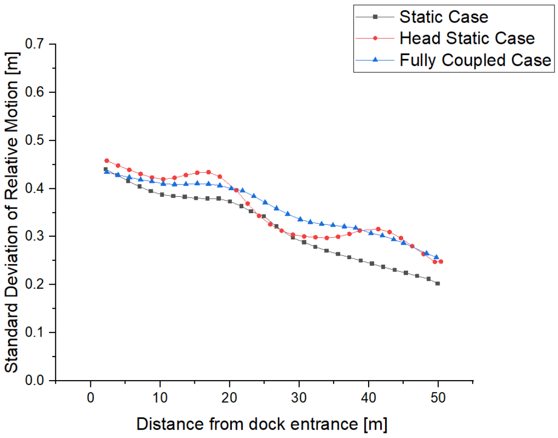

Figure 2.4: Standard deviation of relative motion in well dock with period of 9 second

Reviewing the previous results, they concluded that the most efficient way of predicting the wave heights within the well dock was to run the CFD code for the head sea static in order to obtain the diffraction effects close to the hull. Taking into account the resulting relative motion of amplitude and the velocity distribution of the ship as input in the static case. So, they just modelled the internal structure of the well dock. The first trials were carried out using three dimensional simulations but it was not effective for design evaluation due to the limited computational time. The three-dimensional simulations, in combination with the experimental models, indicate that the major wave action was along two dimensions (X, Z), and the width of the well dock (Y) did not significantly affect it. This conclusion led to the simplification of the CFD simulations in two dimensions for the evaluation of the preliminary stages of design alternatives.

The examined factors were the effect of a sloping floor on the bottom of the well dock (fig. 2.5), the effectiveness of different beach designs (fig. 2.6) and the effect of dock size on the wave amplitude within the well dock.

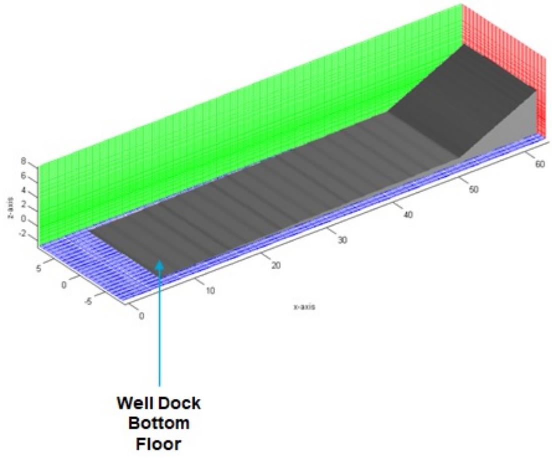

Figure 2.5: Position specification of the sloping floor within the well dock

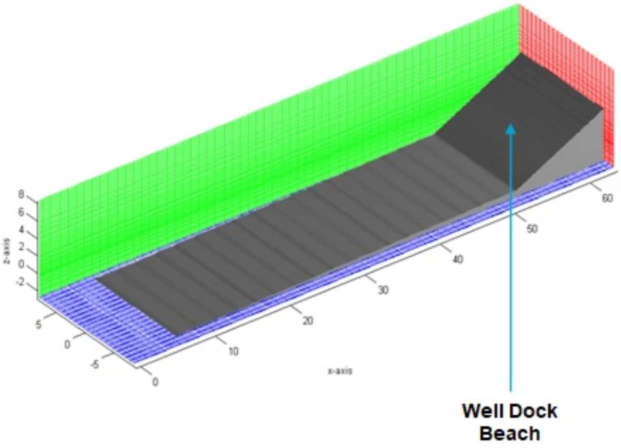

Figure 2.6: Position specification of the beach within the well dock

Regarding the factor of the sloping floor (figure 2.5), they investigated two cases when the dock was flat and when it had a 15-degree solid floor. Based on the results of the simulations (figure 2.7) the flat dock floor was preferred both in high and low wave amplitudes which correspond to 0.39m and 0.19m.

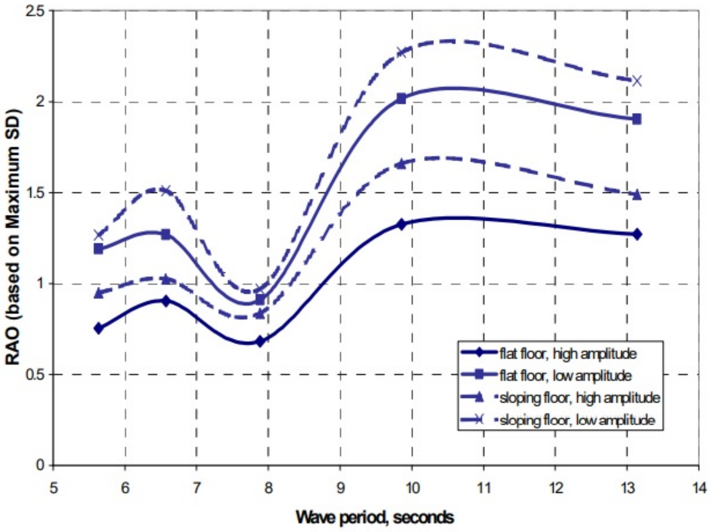

Figure 2.7: The influence of sloping dock floor for wave amplitudes of 0.19m (low amplitude) and 0.39m (high amplitude)

About the second design factor of the well dock beach (figure 2.6), they examined 4 cases with two different inclinations of the beach sloping ramps (15 and 90 degrees) and two levels of porosity (0% and 20%). These simulations were realised in a well dock 60 metres long, with a flat dock floor. The use of porosity is for reducing the wave elevation within the well dock. According to the results (figures 2.8, 2.9) the most effective design was the beach sloping ramp of 90° (vertical wall) with 20% porosity.

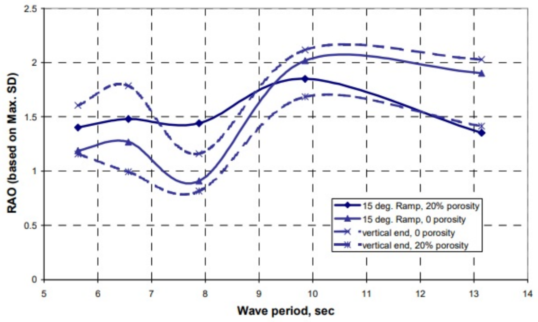

Figure 2.8: Standard deviation of relative motion in well dock, at zero speed in head waves, 5 second period

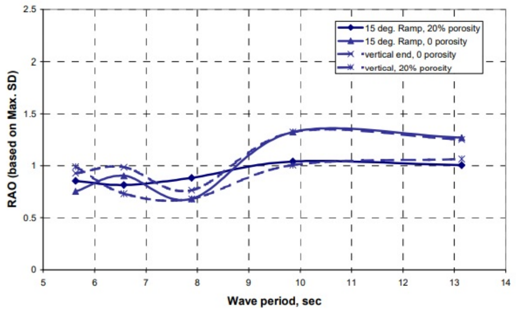

Figure 2.9: Standard deviation of relative motion in well dock, at zero speed in head waves, 9 second period

The last factor was the examination of the well dock dimensions. They examined how the dock size influences the wave height. The depth took two alternate values of 2 and 4m and the length of the well dock was 60 and 120m. The results (figure 2.10) showed that increasing the length and decreasing the water depth of the dock lead to the reduction of the wave elevation within the well dock.[6]

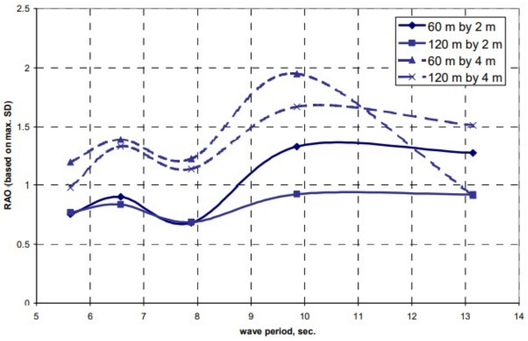

Figure 2.10: Different dock dimensions, high wave amplitude (0.39 m), beach with 15°ramp, zero porosity

2.2. Motions of a landing craft in a flooded well dock - effect of well dock design

In this research paper [3], the authors explore the impact of the well dock design on the movement of landing craft in a seaway. Their investigation involved both experimental and numerical measurements. All simulations were limited to 2D models and focused exclusively on head waves. The ship remained fixed in the fore and aft direction while heave and pitch motions were analyzed based on physical measurements. Heave is defined as the vertical motion of the ship (figure 2.11). Specifically, It is the upward and downward movement of the ship as it rides the waves. Regarding the Pitch motion (figure 2.11) refers to the rotational motion of the ship about its transverse axis. It is the movement of the bow (front) and stern (back) of the ship up and down, causing the angle of the ship's deck to change.

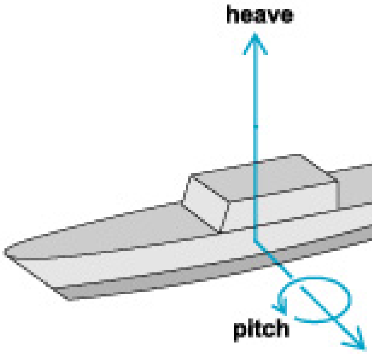

Figure 2.11: Pitch and Heave motions

To set up their numerical model, the researchers placed a beach 6.1 meters behind the ship to reduce any reflected waves produced by the LPD movements as depicted in figure 2.12. Specifically, the researchers employed the SPH technique to simulate the behavior of water and the FE (Finite Element) method to model the ship. The computational time for their simulations was dependent on the number of SPH particles required to represent the volume of water and the size of those particles.

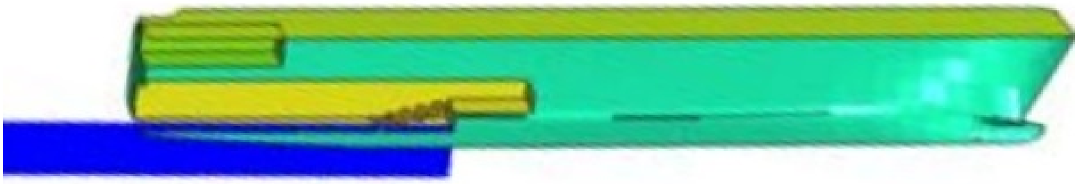

Figure 2.12: Numerical model setup

Simultaneously, the researchers performed a series of hydrodynamic experiments in the Model Test Basin at the Australian Maritime College. Initially, they examined the wave environment at the entrance and inside the well dock, considering both regular and irregular waves. The numerical results were validated by comparing them with experimental tests of the free surface elevation at six different positions as depicted in figure 2.13. All measurements were taken at a water depth of 15 meters as per the experimental setup.

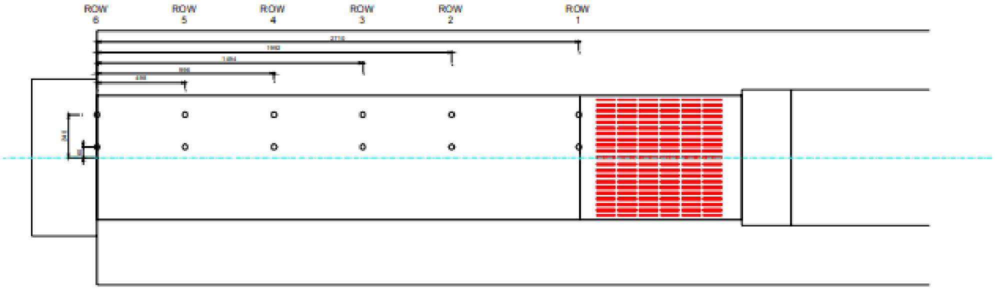

Figure 2.13: Relative wave height lines within the well dock

In figures 2.14 and 2.15, they compared the numerical with the experimental results about the wave height at the well dock entrance and beach respectively. In both figures, the numerical results do not agree with the experimental. The reason for these inaccurate results is the representation of the beach with a coarse mesh.

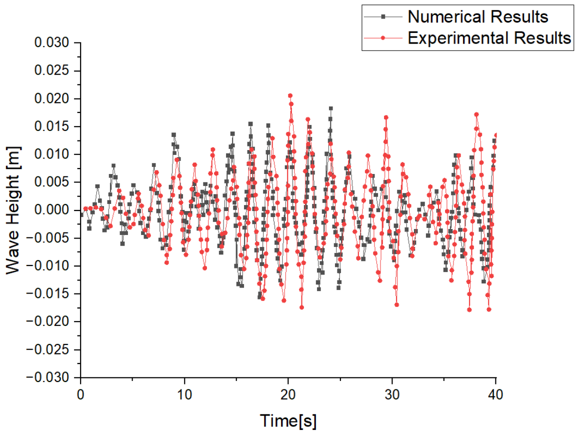

Figure 2.14: Comparison of the relative wave height lines between the numerical and the experimental results at the entrance of the well dock

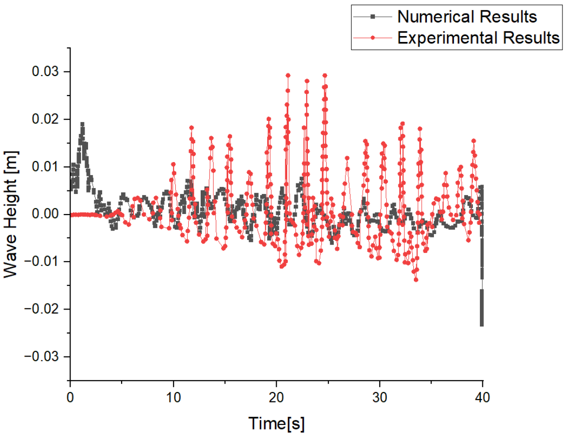

Figure 2.15: Comparison of the relative wave height lines between the numerical and the experimental results at the beach of the well dock

The next step of this project was the study of the well dock design, investigating three geometrical modifications at the dock design which are:

- Well dock depth
- Slope of well dock bottom
- Configuration of well dock door

The first factor was the dock depth. They considered two cases: the shallow case and the base case. The shallow case that was 0.5 meters more shallow than the base case. From figure 2.16 is obvious that the well dock depth does not play an important role for the wave heights at the entrance.

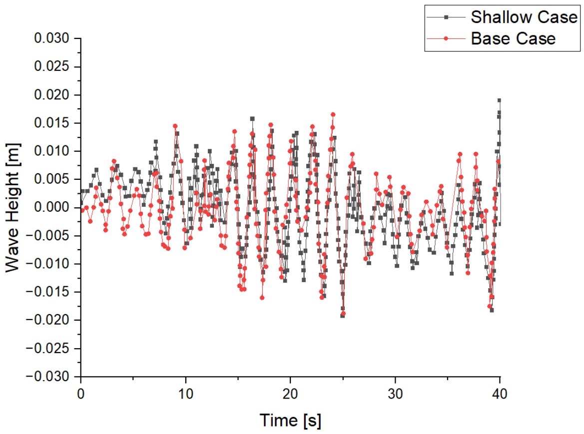

Figure 2.16: Consideration of the dock depth

The second factor was the influence of the slope of the well dock bottom. The bottom of the dock had been inclined by -1.5°, known as "slope down". From figure 2.17 is noticeable that the case of the flat floor reduces the wave heights at the entrance of the well dock compared to the other case.

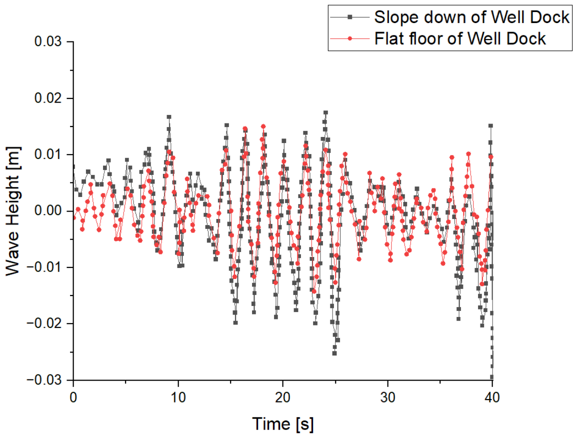

Figure 2.17: Consideration of slope of dock bottom at the entrance of the well dock

The last parameter is the effect of the well dock door. According to the results (figure 2.18), after the presence of the door increases the wave height at the dock entrance compared to the case of the well dock without the door. [3].

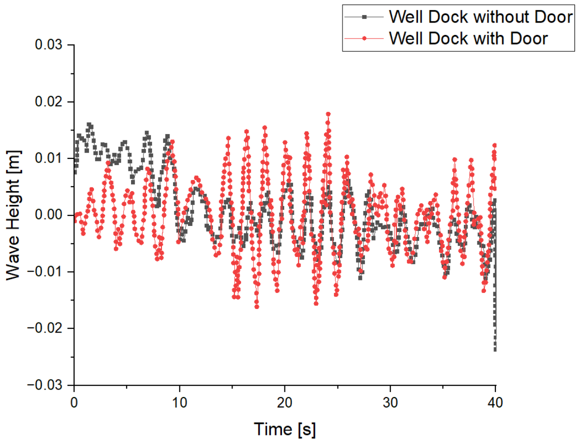

Figure 2.18: Investigation of the influence of dock door

2.3. The Modelling of Landing Craft Motions inside a flooded Well Dock using Smoothed Particle Hydrodynamics

Also, in article [2], the researchers used the SPH method in order to describe the wave behaviour within the well dock of a Land Helicopter Dock Ship (LHD), which is also used for embarking and disembarking of landing crafts [2]. The previous paper of SPH method studied the wave pattern within the well dock for different sea states and speed. This paper studies the numerical behaviour of a landing craft within the well dock.

The numerical model was created using the SPH technique to simulate water and the finite element method to simulate the LHD and landing craft. During the model set-up, they did not take into account the diffraction of the waves around the stern of the well dock. As far as the geometry of the landing craft is concerned, they constructed two models, which are described in detail in table 2.1. In particular, the Length overall (LOA) in a ship is the maximum length of a vessel, measured from the foremost point of the bow to the aftermost point of the stern and the beam of a ship is the width of the vessel at its widest point, usually measured at or near the midpoint of the ship's length. Regarding the model set-up, the first carried a battle tank while the second was empty (shown in figure 2.19). The study examined two scenarios. In the first scenario, the landing craft was stationary, whereas in the second scenario, the landing craft was driven forward within the well dock. As the landing craft moved forward, it was also able to move freely in both heave and pitch.

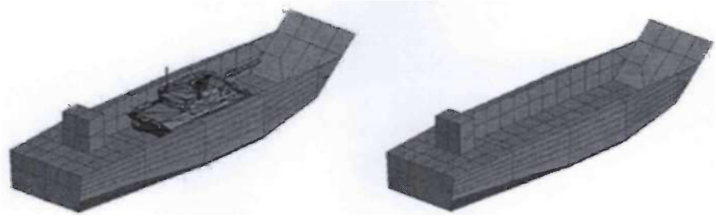

Figure 2.19: Landing Crafts

Length overall (LOA) (m)	24.5	
Beam (m)	6.4	
Models	Light	Heavy
Mass (tonnes)	42.8	90.4

Table 2.1: Landing craft dimensions

To deduce the complete wave conditions within the well dock, it was necessary to identify the motions of the generic LHD when operating in a seaway. Preliminary studies were conducted to determine the LHD's heave and pitch motions. For the simulations, the regular waves had a period of 8.4 seconds and 1 metre height. In figure 2.20, the heave is roughly 0.1 metres and the pitch is roughly 0.18 degrees. A possible cause of the minimal effect of the pitch and heave motions could be due to inadequate wave absorption by the beach at the end of the well dock.

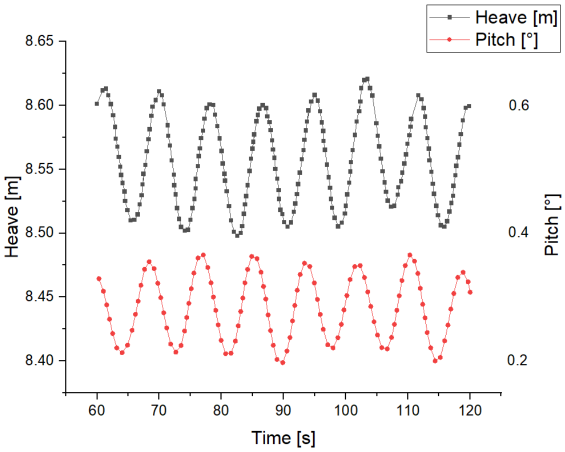

Figure 2.20: Heave and Pitch motions of the LHD

Furthermore, they researched the relative motions between the tethered landing craft within the well dock and the well dock floor. Especially, they investigated two scenarios, one for a light landing craft and the second for a heavy landing craft. In both cases, the only allowed motions of the landing crafts were the heave and the pitch. In graphs 2.21 and 2.22 are depicted the heave and pitch motions of the landing crafts and the vertical displacement of the well dock floor and it is apparent that in both scenarios, the landing craft did not impact the well dock floor.

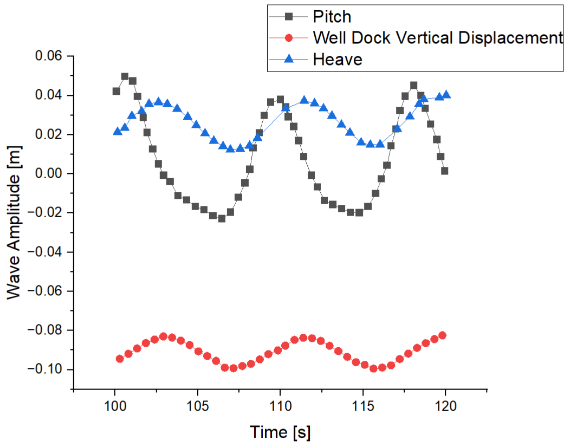

Figure 2.21: Relative motion between the well dock floor and light landing craft

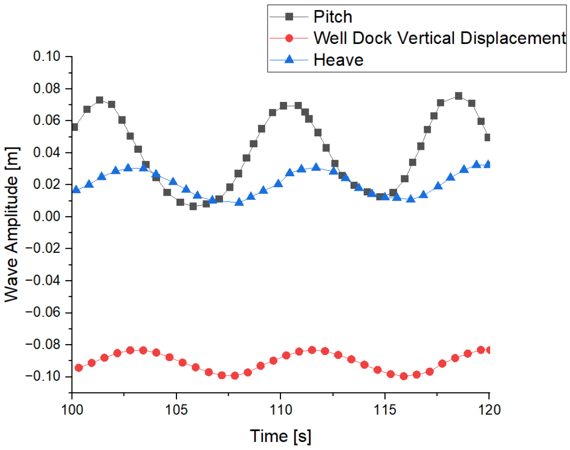

Figure 2.22: Relative motion between the well dock floor and heavy landing craft

2.4. Hydrodynamic Analysis of Ship with Well Deck in the Linear Numerical Wave Tank

In this article [25], they established a linear numerical wave tank for the purpose of examining the hydrodynamic characteristics of the modified version of the original Wigley-III ship model that includes a well dock. This research focuses on analyzing the hydrodynamic effect of the floating structure within the well dock. The ship's data with a well deck are not present in the database, so they created an artificial model of a ship with a well dock. To study the impact of the floating body, they based their model on the original Wigley-III ship model and added a well dock of 0.15 m width and 0.2 m height at the stern. This new model is called the modified Wigley-III ship model and its details are shown in Figure 2.23 and 2.24. To study the effect and interaction of a small floating structure on the modified Wigley-III ship, they placed a rectangular floating object in the well dock.

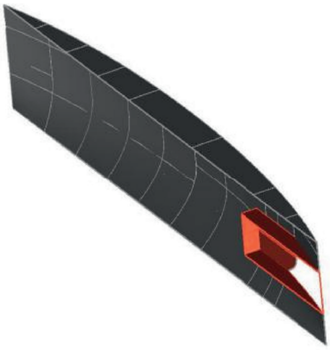

Figure 2.23: The ship model of Wigley-III with integrated the well dock

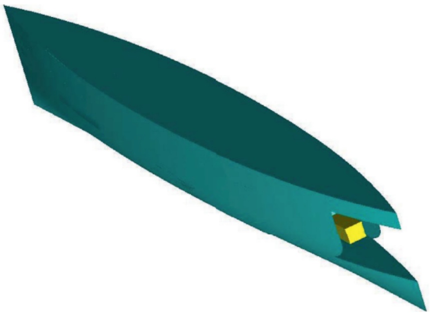

Figure 2.24: The ship model of Wigley-III Wigley-III with the floating body within the well dock

Parameter	Value	Unit
Wave Amplitude	0.013 - 0.022	m
Wavelength	1.5 - 6.0	m
Wavelength/length of the ship)	0.5 - 2.0	-
Wave direction	45, 180	°

Table 2.2: The parameters for numerical simulation

In order to carry out the numerical simulation in this study, two software programs were utilized: ICEM CFD for grid generation, and ANSYS FLUENT for the simulation itself. In this case, they used the Finite Volume Method (FVM) to discretize the governing equations for the simulation. This study employs FLUENT as a fundamental solver, along with User Defined Functions (UDF) which are used for the better modelling of the wave within the Numerical Wave Tank (NWT). The UDF is used to define the wave-generating boundary conditions in the inlet boundary and the wave absorbing zone in the end of the Numerical Wave Tank.

The ICEM CFD of ANSYS was utilized to mesh the model. The grid which is depicted in figure 2.25, is refined near the water surface, in order to capture the position of the free surface and to improve the numerical accuracy. But in the regions further away from the free surface, the grid gradually becomes sparser and specifically in the transverse direction in relation to the free surface.

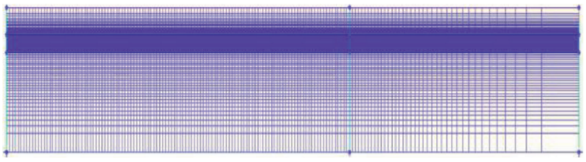

Figure 2.25: Computational Mesh of Numerical Wave Tank

About the pre-processing, they implemented the subsequent configurations:

1. The pressure staggering option for the pressure
2. The 2nd order Upwind Convection scheme
3. The volume of fluid (VOF) method for the modelling of water surface
4. The RNG k-ϵ turbulence model (2-eqn) was chosen to simulate the flow of the incompressible and viscous fluid.

In figures 2.26 and 2.27, they compared the experimental data of the original ship of Wigley-III and the numerical results of the modified Wigley-III with the floating body and without it within the well dock.

During the simulations, the ship was stationary and they explored how the relationship between the wavelength and the length of the ship affects the amplitude of heave and pitch motions in two different wave directions of 45° and 180°.

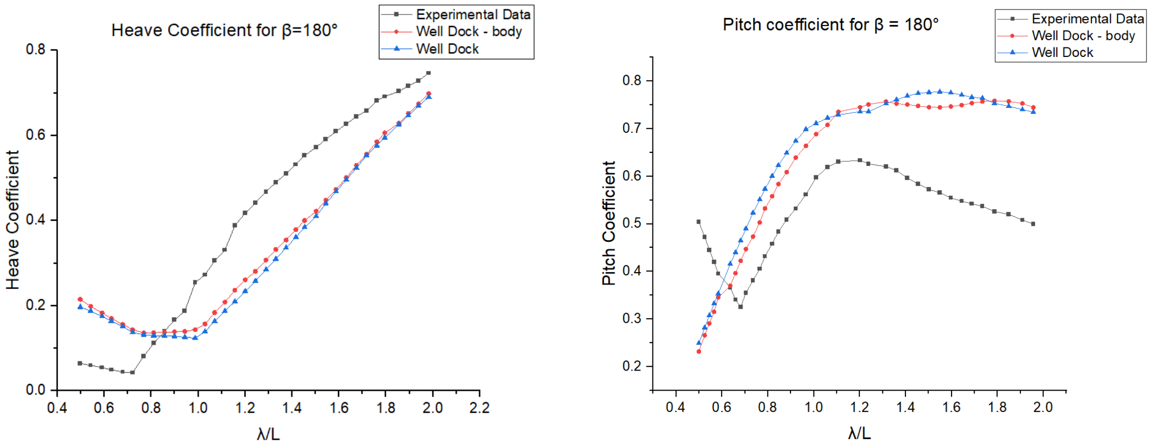

Figure 2.26: Heave and Pitch coefficient for wave direction 180°

Figure 2.26 illustrates that the Wigley-III ship with the well dock has the same behaviour with the experimental results of the original Wigley-III ship. Notably, when the wavelength exceeds the length of the ship, the heave coefficient of the modified Wigley-III ship model is observed to increase. This means that the well dock is effective in increasing heave motion. As far as the pitch coefficient, it is obvious that the ship with the well dock has completely different behaviour than the original ship for the short waves. Furthermore, it is noticed that the floating body in the well dock has a negligible impact on the ship's overall motion.

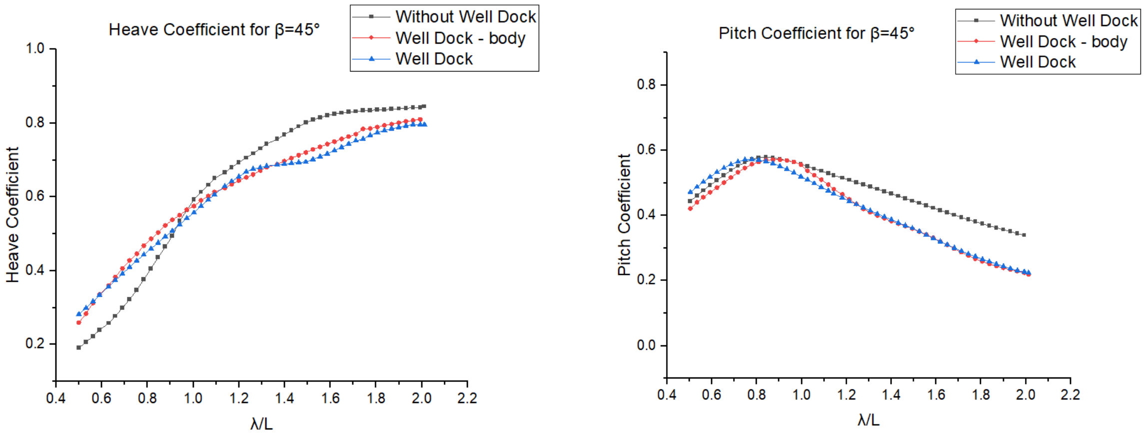

Figure 2.27: Heave and Pitch coefficient for wave direction 45°

According to Figure 2.27, it is evident that the original and the modified ships have similar behaviour and as the wavelength rises the amplitude of the heave motion increases. Meanwhile, in comparison to the original ship, the pitch motion of the modified ship model becomes less important as the wavelength exceeds the ship's length, and the amplitude of the pitch motion diminishes for shorter waves. Also, in this case, the floating body has a negligible impact on the modified Wigley-III ship.

2.5. Predicting the wave climate in the well dock of a Landing Platform Dock ship using Computational Fluid Dynamics

The ComFLOW was used to predict the water motions within the well dock of a Landing Platform Dock (LPD) ship [10]. Initially, they created a model setup to simulate numerically both the LPD1 "Hr. Ms. Rotterdam" and the LPD2 "Hr. Ms. Johan de Witt". The numerical results were validated by comparing them with experimental tests of the free surface elevation at five different positions: Three wave probes were placed inside the well dock, while one wave probe was positioned ahead of the vessel, and another was located at the side of the vessel. In order to execute the simulation using ComFLOW, it is necessary to define multiple parameters that provide details regarding the geometry, computational time step, computational domain, and simulation duration.

As far as the geometry, they created the well dock of the "HR. Ms. Rotterdam" as is depicted in Figure 2.28. The distance from the entrance to the beach is 51.6 m and from the beach to the end of the dock is 11.8 m. The width of the dock is 11 m and the water depth is 2.225 m.

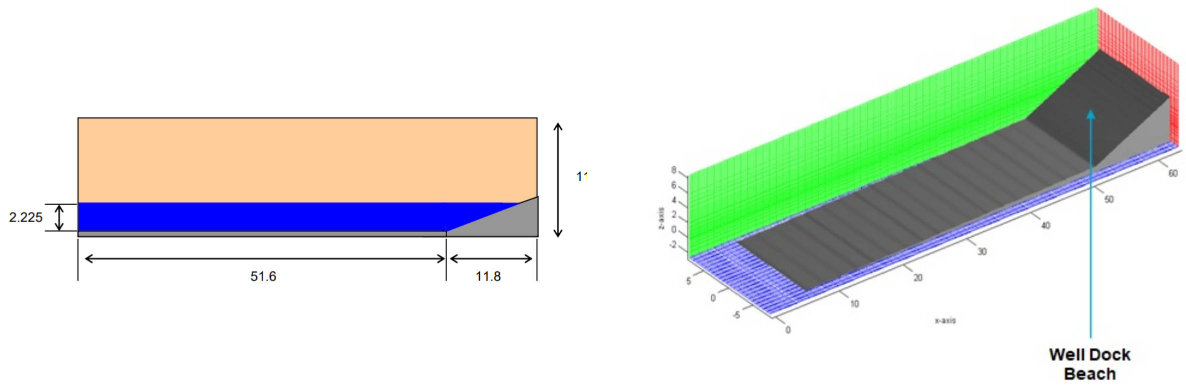

Figure 2.28: 2D and 3D Well Dock Geometry

Additionally, they defined the time step according to the Courant-Friedrichs-Lewis (CFL) number. The computed CFL number is restricted by an upper and a lower limit, chosen to be 0.2 < CFL < 0.5. If the upper limit is crossed, the time step will be halved but if the CFL-number is for ten successive time steps smaller than the lower limit, the time step will be doubled. The CFL number is calculated as in equation 2.3:

$$CFL = \frac{u_x \Delta t}{\Delta x} + \frac{u_y \Delta t}{\Delta y} + \frac{u_z \Delta t}{\Delta z} \tag{2.1}$$

For wave simulations, there is a clear restriction on the time step for reasons of accuracy. This restriction is accounted for by setting the maximum time step for the simulation, dtmax equal to T/250, where T is the wave period in seconds. Every simulation uses a wave height of 2 m, the wave frequency varies from 0.40 rad/s to 1 rad/s and the wave length varies from 61.57 m to 385.337 m. Each simulation is equal to ten wave periods. In appendix B.1, the table includes all the required details of the simulations that were conducted in this thesis.

Regarding the grid with dimensions 240 x 10 x 60 which is shown in figure 2.29, is refined near the water surface, in order to capture the flow phenomena at the free surface. But in the regions further away from the free surface, the grid gradually becomes coarser and specifically in the transverse direction in relation to the free surface.

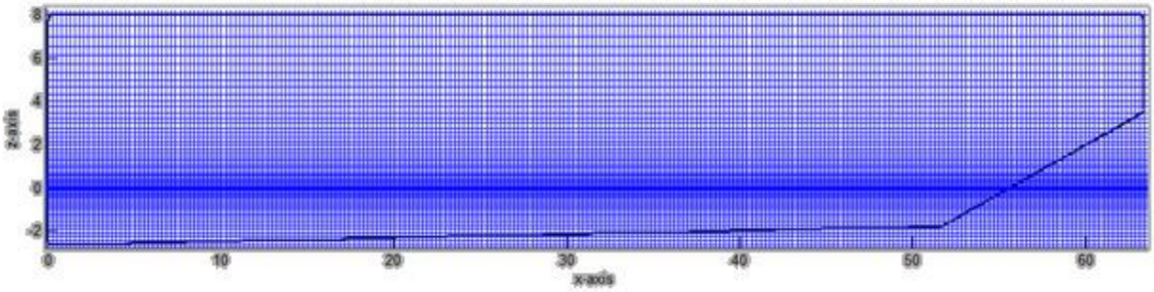

Figure 2.29: grid in two dimensions (240 x 60)

In figure 2.29 is noticed on the right side the well dock beach which absorbs most of the wave energy but also reflects some of this energy. During this thesis, the researcher investigated the influence of the implementation of a numerical beach in ComFLOW. The permeable beach in the well dock is in reality a wooden ramp which starts approximately 12 m before the end of the dock. The empirical reflection coefficient (ε) of the beach (equation 2.2), describes the intensity of the reflected wave relative to the incident wave where ω is the angular frequency.

$$\varepsilon\left(\omega\right) = \frac{1}{2} \cdot \left(1 - tanh\left(\frac{\omega - 0.8}{0.5}\right)\right) \tag{2.2}$$

Based on this empirical formula that was supplied by MARIN, they researched different combinations of length and slope for the beach at three different places within the dock: at the dock entrance (x = 15 m), in the middle of the dock (x = 30 m), and before the well dock beach starts (x = 45 m). According to the results in Figures B.1, B.2 and B.3, it is clear that the numerical beach does not play an important role in any of the locations, and specifically at the first location (at the dock entrance). This is due to the fact that the impact of the reflected waves is less apparent at the entrance of the dock. Also, at the other two locations where the numerical beach slightly influences the wave amplitude and the wave damping is minimal.

The computational domain, which is shown in figure 2.30, is split into a domain focused on the flow in the dock and a far wave field domain. Regarding the modeling, they used a linear diffraction program based on potential theory to compute the far wave field domain and vessel motions and the resulting relative motion and velocity distribution were used as input for the boundaries of the inner ComFLOW domain to calculate the local flow phenomena within the well dock.

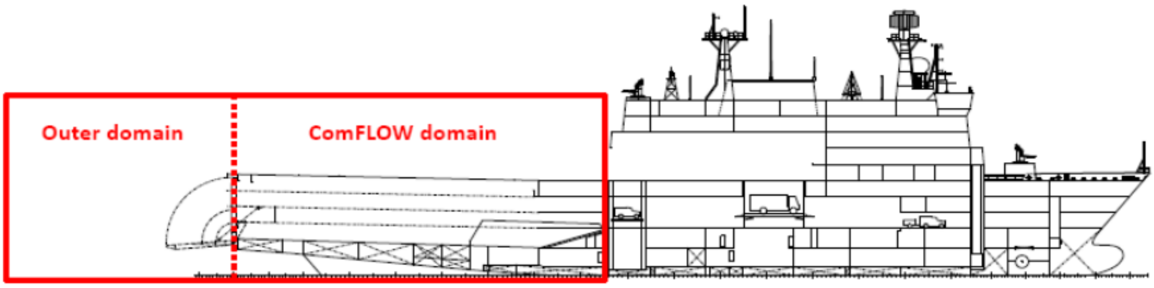

Figure 2.30: Computational Domain of LPD1

For the considered problem, Figure 2.31 gives a schematic description of the boundary conditions. At the two solid walls bounding the flow geometry a no-slip boundary condition, u = 0, is applied (with u the velocity field). This condition ensures that the fluid does not enter or slide along the wall, but it sticks to the wall due to viscous effects. A generating and absorbing boundary condition (GABC) must be utilized at the open boundary on the left, as it serves as both an inflow and outflow boundary. At the outlet boundary, a condition is required to prevent wave reflection within the well dock. This can be achieved through two methods. The first method involves using non-reflecting boundary conditions, where the derivatives of velocity and pressure are set to zero. This allows for extrapolation of the transported quantities in the direction of fluid flow, and is known as the Neumann boundary condition.

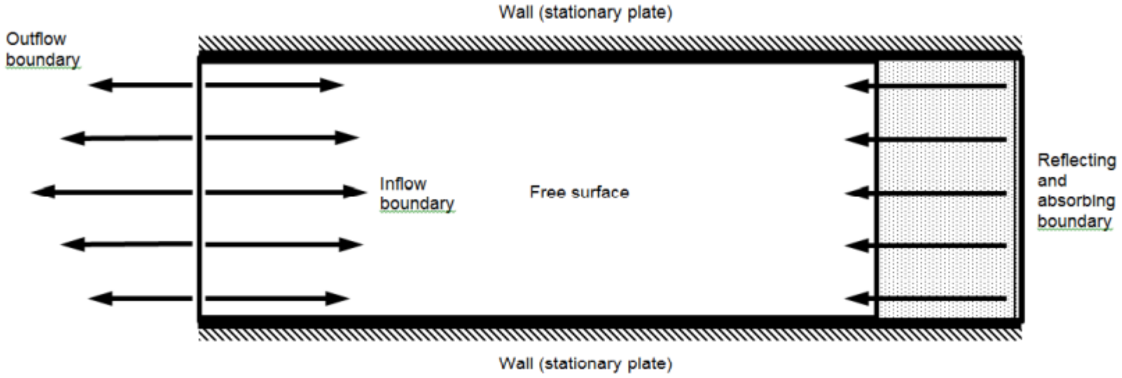

Figure 2.31: Boundary Conditions

The second method involves incorporating a dissipation zone to dampen the waves. In this thesis, both methods were used. Figure 2.32 shows the damping prescription for waves of varying lengths. For short waves, the GABC was utilized, while for long waves, the physical beach was used.

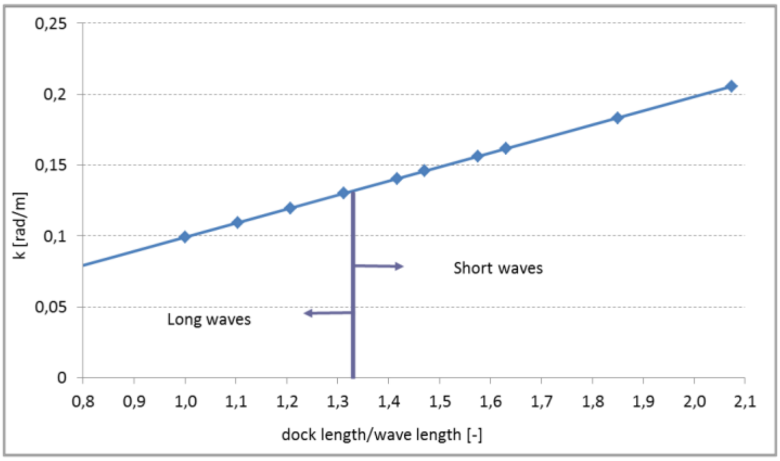

Figure 2.32: Separation in long and short waves, according to the damping prescription

All the measurements were realized with the use of the wave probes for the capturing of the free surface elevation. These wave probes were located at the dock entrance (x=14.8m), in the middle of the dock (x=29.6m) and before the dock beach (x=44.4m). These simulations took place both in 2D and in 3D where their set-up details describe in table B.1.

In appendix B.2.3.1, it is depicted the 2D simulations for the free surface elevation at the dock entrance (x=14.8 m). The estimated wave amplitude for both long and short waves was found to be higher compared to the experimental measurements. However, the results for middle wavelengths were similar to those obtained from the model tests. This discrepancy may be due to inaccurate prediction of the inlet wave amplitude by the linear diffraction program. In appendix B.2.3.2, the free surface elevation at x = 29.6 m is illustrated, and the results obtained from ComFLOW show differences in respect to those obtained from the experimental measurements for waves of all lengths.

The last location is at the end of the well dock (x = 44.4 m) where in Appendix B.2.3.3, the graphs show that there is no similarity between the model tests and the ComFLOW results, particularly for long waves which were damped using the physical beach method.

The simulations in three dimensions were performed for wave frequencies of 0.50 rad/s, 0.70 rad/s, and 0.775 rad/s. The computational effort is higher in three dimensions and for this reason the simulation time endures three periods. The results are depicted in Appendix B.2.3.4, comparing the experimental with the 3D ComFLOW results.

In addition, the researchers attempted to simulate the well dock of the second LPD2 "Hr. Ms. Johan de Witt", whose geometry is depicted in figure 2.33. The red line illustrates the flooded well dock where the water depth at the dock entrance is 2.80 m, whereas towards to the end of the dock the water depth is 1.60 m. They utilized the numerical model of the LPD1 "Hr. Ms. Rotterdam," and validated it using model tests which were carried out in MARIN. The only differences in its well dock design are the shorter length and the different beach shape. Regarding the simulations, the set-up of LPD2 is described in Appendix B.2.4.1 and most of the settings were kept the same, except for the damping prescription on the beach. As a result of the shorter length of the dock, they adjusted the reflection coefficient which was based on the empirical equation of the reflection coefficient (equation 2.2) which was explained earlier in LPD1. Each simulation had a total simulation time of ten wave periods. The wave frequencies ranged from 0.40-0.90 rad/s, and the free surface elevation was measured at four different positions: 0 m, 10.5 m (dock entrance), 21.3 m (dock middle) and 32 m (dock beach).

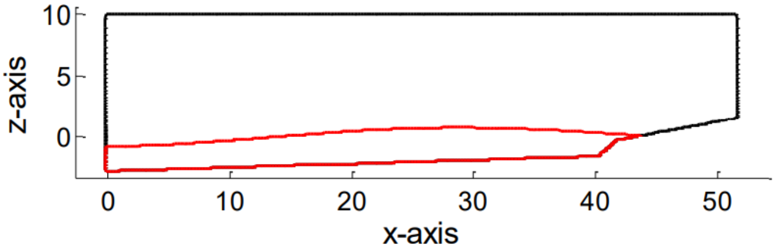

Figure 2.33: Well Dock of LPD2

The results for the free surface elevation of the wave at x = 0 m can be found in Appendix B.2.4.2. Unfortunately, there is no agreement between model test results and the ComFLOW results, for both the long and short waves. One possible explanation for this discrepancy is that the x-coordinate of the first wave probe may not be correctly positioned on the dock door. Appendix B.2.4.3 presents the results for the dock entrance (x = 10.5 m), where the same problem was observed in LPD1. For the long waves, the wave amplitude is overestimated in comparison to the experimental measurements. The wave probe is located at x = 21.3 m, and the results for this position are displayed in Appendix B.2.4.4. The ComFLOW model provides relatively accurate estimates for the free surface elevation of short waves. However, for the long waves (also shown in Appendix B.2.4.4), the ComFLOW model performs poorly. The results obtained at x = 32 m are presented in Appendix B.2.4.5. This location is closest to the beach and the prediction of the wave profile is the most challenging. Unfortunately, the ComFLOW model does not predict the amplitude of the wave very well in both long and short wave scenarios, especially for the free surface elevation of long waves.

2.6. Conclusion

During this chapter, it is evident that physical mechanisms have not been explored in the aforementioned articles and the literature study primarily focuses on the computational domain and the design of the well dock, both of which will significantly impact the future work of this thesis. In terms of the computational domain, most researchers have made various simplifications due to limited computational capacity. They have employed the linear diffraction theory to calculate the amplitude of incoming waves, neglecting viscous forces and non-linearities in the flow. Additionally, they have only modeled the well dock using a CFD code. However, this modeling approach is not accurate since the linear diffraction theory assumes small wave amplitudes, in contrast to CFD codes that can consider nonlinear effects around the structure, resulting in more precise results. Furthermore, in most cases, it has been assumed that sloshing forces within the well dock do not significantly affect the ship's motion, without providing any evidence to support this assumption. Moreover, these studies have relied on 2D simulations, overlooking physical mechanisms in the 3rd dimension, such as reflection and diffraction.

Regarding the design of the well dock, most researchers have investigated four key factors:

1. The slope or flatness of the well dock's bottom floor
2. The configuration of well dock door
3. The depth and length of the well dock
4. Different beach designs at the end of the well dock

These four factors will be thoroughly examined in the final stage of this thesis to propose potential design improvements during the construction of the new LPD.

3

Methodology

This chapter delineates the methodology adopted to address the three primary research questions foundational to this study.

3.1. Research Question 1

The first research question examines the influence of various physical mechanisms combined with wave characteristics on the flow within the well dock. This subsection briefly describes the procedure to explore the physical mechanisms.

The physical mechanisms studied include radiation and diffraction. Diffraction is examined when the LPD is stationary, and incoming waves diffract around the ship's hull before propagating into the well dock. Thus, diffraction captures how these waves interact with the LPD's structure and how they enter and propagate within the well dock. Conversely, during the radiation, when the LPD undergoes surge, heave, and pitch motions, the ship itself generates waves. These radiation waves then propagate into the well dock. Isolating these radiation effects provides insights into how ship motions affect the flow within the well dock.

The model is elaborated comprehensively in Chapter 6. Initially, it investigates the physical mechanisms independently at two distinct wave frequencies. Following this independent analysis, the results derived from each mechanism are added using Equation 6.1. This approach enables a thorough comparison with the experimental results that are documented in Chapter 4[20].This chapter delves into the studies that contributed to the formulation of this specific model. Summarily, these studies cover wave generation, boundary conditions, and all requisite studies for creating a 3D domain (such as wave propagation and domain size) alongside motion integration for the radiation study. Additionally, a grid study (6.1) is conducted for both diffraction and radiation. Section 6.2 delineates the input parameters for the simulations, section 6.3 presents the study results, and section 6.4 discusses these findings.

3.2. Research Question 2

The second research question addresses the development of an accurate and efficient model to capture the physical mechanisms of the flow within the well dock of an LPD. This Section describes the procedure for creating the numerical model, referred to as the "Full Model".

A notable distinction between this model and the one from the first research question is that, in the Full Model, both physical mechanisms are integrated from the onset of the simulation. Whereas the parameters for wave generation, boundary conditions, and the necessary investigations for creating a 3D domain remain unchanged, the grid study is different. Section 7.2 introduces the design modification applied to the original geometry in the ramp region, elucidating the rationale behind such a change. Section 7.3 details the input parameters for the simulation and specifies the exact locations of the wave probes for illustrating the results. Subsequent sections depict the results of the Full Model, juxtaposed against the model of Chapter 6 and the experimental model from Chapter 4[20], followed by a discussion of these findings.

3.3. Research Question 3

The third research question investigates the viability of the model in order to facilitate the design process. This Section briefly delineates the procedure for creating the 2D numerical model, referred to as the "Viable Model".

Utilizing the Full Model from the second research question, a wave probe is used to capture the wave kinematics (wave height, phases) at the door of the well dock. These captured wave kinematics then serve as the input for wave generation in the Viable Model, with vessel motions being integrated into the model. This model is performed in three different wave frequencies: 0.4, 0.7, and 1 rad/s. Its validation is conducted in relation to the model tests elaborated in Chapter 4. More details about the 2D model set-up are provided in chapter 8, with the results being showcased in Section 8.8, and an analysis of these findings is provided in Section 8.9.

4

Experimental Tests

4.1. Introduction

The model tests of the LPD1, carried out at TU Delft [20], were conducted to predict the wave climate in the dock of an LPD. Additionally, these model tests were utilized for validating the results of this thesis. Response Amplitude Operators (RAOs) measuring three degrees of freedom in ship motion were obtained for surge, heave, and pitch. As well as, they measured the wave heights at various locations within the dock using wave probes. A picture of the model of the LPD1 in the basin is given in Figure 4.1 and a picture of the wave probes in the dock is given in Figure 4.2.

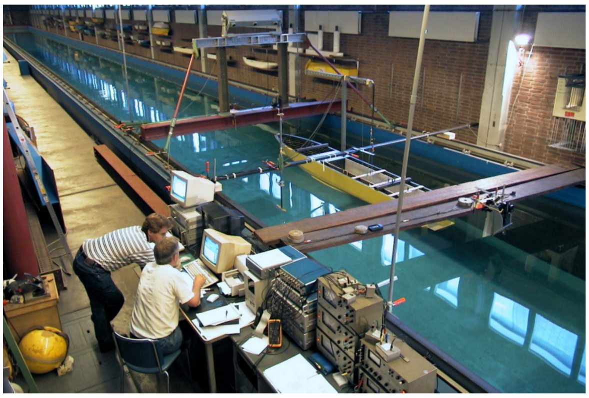

Figure 4.1: LPD in the towing tank

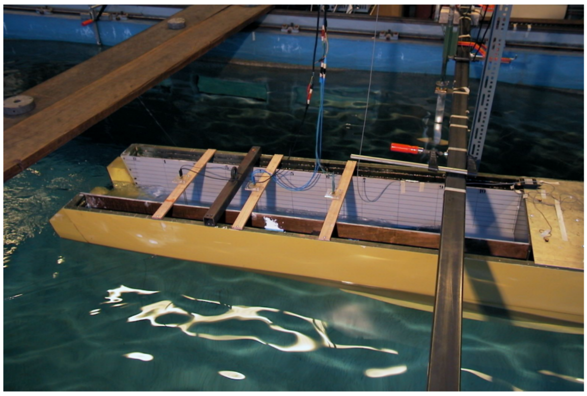

Figure 4.2: Wave probes in the well dock

4.2. Model test set-up

The scale model with the scale factor (1:38) was utilized for the model tests. The vessel was tested in the towing tank at the TU Delft ship Hydromechanics Laboratory. The wave heights were measured at five positions: three wave probes in the well dock, one wave probe before the vessel and one at the side of the vessel. Figure 4.3 depicts a picture of the arrangement for the pre-process of the model test. Figure 4.4 presents in more detail the location of the wave probes within the well dock of the ship, along with illustrating the original geometry of the well dock and the solid ramp where the experiments were conducted. In addition to the information provided in Table 4.1, the following parameters were employed for the experimental tests:

1. Wave headings of 180°
2. Vessel speed of 0 knots
3. Regular waves: ten different wave frequencies between 0.4-1.0 rad/s with the same undisturbed wave heights (Sea State 4)
4. Irregular waves: three spectra of irregular waves.

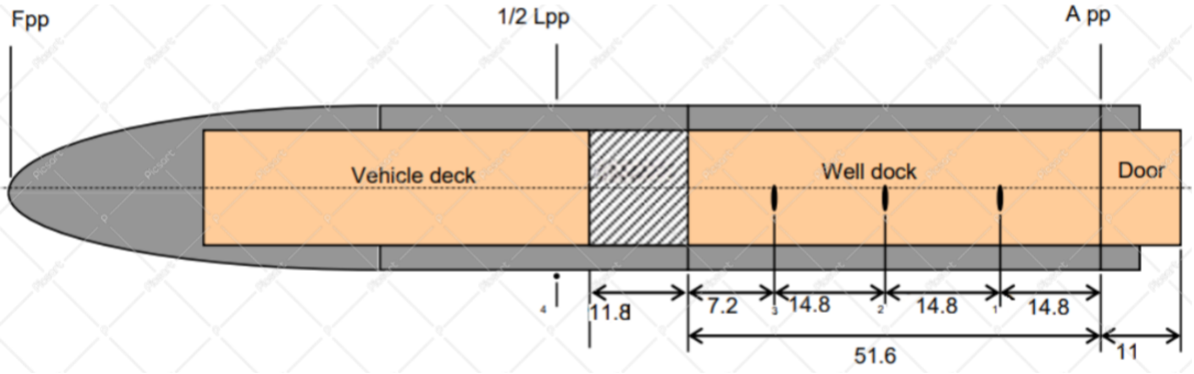

Figure 4.3: Model test set-up LPD

Figure 4.4: Model test set-up LPD-Wave Probes 1-3

Table 4.1 details three model tests, which were conducted at three different wave frequencies. The range of wave frequencies is based on the critical frequencies of the vessel where resonance is expected. During the tests, not only the wave elevation at certain locations in the dock was measured, but also the surge, heave and pitch motions of the vessel were measured.

Model Test	**Parameters on full scale**			
-	**Peak period [s]**	**Frequency [rad/s]**	**Wave height [m]**	**Wave Type**
1	15.71	0.4	2.0	Regular
2	8.98	0.7	2.0	Regular
3	6.28	1.0	2.0	Regular

Table 4.1: Parameters for the model tests

In order to compare the results of ComFLOW with those of the model tests, it is necessary to make scaling analysis between the model and the full scale. The most relevant dimensionless numbers for this problem are the Froude number (Fr) which is the ratio between inertia and gravity forces and the Reynolds number (Re), which represents the ratio between inertia and viscous forces. In this simulation, fluid movement within the dock is significant and is mainly influenced by pressure, inertia, and gravity forces. Since the flow within the dock is predominantly governed by gravity, viscosity is deemed insignificant. Therefore, the Froude scaling law is utilized.

$$Fr = \frac{U}{\sqrt{gL}} \tag{4.1}$$

$$Re = \frac{\rho U L}{\mu} \tag{4.2}$$

5

Numerical model

5.1. Background

The ComFLOW CFD software is utilized to analyze the water motion within the flooded well dock of an LPD. This chapter provides an overview of foundational studies that underping the further studies that conducted in chapters 6, 7 and 8. Specifically, this chapter delves into the flow model, free surface, wave generation, geometry, boundary conditions, wave propagation, domain size in both 2D and 3D dimensions and the method of motion integration. Additionally, it covers the tools used in post-processing and the fundamentals of grid analysis, all of which significantly contribute to the advancement of this thesis. However, it is worth noting that while the wave generation method remains consistent for 3D models (as detailed in chapters 6 and 7), it differs for the 2D domain, which is covered in chapter 8. The grid study approach varies between the 3D domains (chapters 6 and 7) and the 2D domain (chapter 8). and the rack ramp effect is specifically addressed in chapter 7.

5.2. Flow model

For the problem under consideration, a one-phase model has been employed. In this model, water is treated as an incompressible and viscous fluid. Alternatively, a two-phase model treats water as an incompressible, viscous fluid, while air is categorized as a compressible, viscous fluid. The importance of the two-phase model becomes evident particularly near the free surface, where significant interactions between the two phases occur[21]. Such interactions are prevalent in instances of air inclusion. Since in the considered problem, while a free surface is present, there is no strong interaction between air and water. Additionally, the current version of the ComFLOW software is designed solely for the one-phase model. Therefore, the one-phase model is expected to provide results of sufficient precision.

5.3. Free surface

In the current study, the flow domain does not consist entirely of liquid. Instead, it has a free surface, creating a boundary between the liquid and the surrounding air. In the one-phase model, the Navier-Stokes equations are solved exclusively within the liquid cells. Determining the precise position of this free surface is a key aspect of solving the flow problem. If we assume the function $S(x, y, z, t) = 0$ describes the location of the free surface, equation 5.1 can be used to model the temporal evolution of the free surface.

$$\frac{DS}{Dt} = \frac{\partial s}{\partial t} + (\boldsymbol{u}\cdot\triangledown)S = 0 \tag{5.1}$$

In this thesis, the Volume-Of-Fluid (VOF) numerical method was utilized to model the free surface. The VOF method is based on the concept of tracking the fraction of each fluid phase within a given computational cell or element. This fraction is typically integrated into the flow equations. Consequently, the method solves the conservation equations for both the mass and momentum of the fluid phase. By tracking the volume fraction field, the method determines the water properties and behaviors within each cell or element. Generally, the VOF method is capable at managing large deformations and intricate interfaces. Furthermore, it requires minimal storage since each cell is linked with just a single parameter value.

Central to the VOF formulation is the understanding that two (or more) fluids do not interpenetrate. For each additional fluid that is added to a model, a variable F is introduced which indicates the volume fraction of the fluid in the computational cell. This discrete VOF function F has values between zero and one, indicating the fraction of the cell that is filled with fluid. Since F represents the fluid fraction of the cell, its value is unity when the cell is completely filled. Conversely, a value of zero indicates that the cell contains no fluid. Cells with F values between zero and one must then contain a free surface as depicted in figure 5.1.

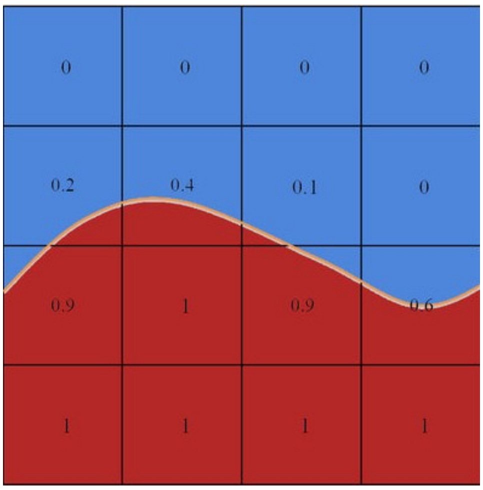

Figure 5.1: Volume-of-Fluid-approach

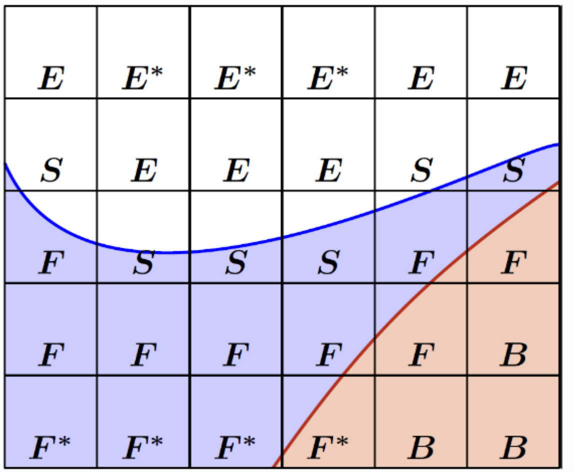

Figure 5.2: Cell labeling in comflow

Equation 5.2 states that F moves with the fluid and indicates which parts of the domain are filled by the fluid, where u is the velocity field (u,v,w):

$$\frac{\partial s}{\partial t} + u\frac{\partial s}{\partial x} + v\frac{\partial s}{\partial y} + w\frac{\partial s}{\partial z} \tag{5.2}$$

In this project, the VOF function is reconstructed using the Piecewise Linear Interface Construction (PLIC) method. PLIC aims to accurately capture the interface between two fluids by approximating it with piecewise linear segments. This approach enhances the VOF method's accuracy by effectively capturing the complex shapes of fluid interfaces. It proves especially beneficial for simulating flows with sharp and intricate interface geometries. To distinguish between cells with varying characteristics in the computational domain, labels are assigned to them. This labeling is essential, as flow equations are not solved throughout the entire domain, as illustrated in Figure 5.2. Cells fully occupied by solid are designated as "B" (Boundary) cells. In contrast, cells that are void of fluid but can potentially facilitate fluid flow are labeled "E" (Empty) cells. Additionally, cells adjacent to the E-cells containing fluid are termed "S" (Surface) cells. The remaining cells are classified as "F" (Fluid) cells. Importantly, F-cells do not necessarily have to be filled with fluid completely.

5.4. Wave Generation

In a simulation tool like ComFLOW, wave generation can be modeled in two primary ways.The first approach involves generating waves at an inflow boundary by setting specific velocity components and water height. In this project, this method is used for the 3D domains and is employed in the studies detailed in chapters 6 and 7. The second approach diverges from the first. It relies on a preliminary simulation to compute the wave field, phase, and wave height, subsequently applying these parameters as input in a new computational 2D domain which is explained in chapter 8. Subsequent paragraphs of this section delve deeper into these two distinct methods of wave generation.

5.4.1. Generation of waves using wave theory

A wave theory is used to generate waves at the inflow boundary of the domain. It should be noted that at this inflow boundary, both positive and negative velocities can occur, allowing fluid to flow in and out. This boundary specifically serves as the point where waves are generated. The wave generation is achieved by prescribing velocities at the inflow boundary. Various wave descriptions can be employed to determine these velocities. The simplest is a linear wave description known as the Airy wave. However, according to Le Mehaute [10], the range of suitability of linear theory in deep water is $H/\lambda < 0.0062$, with H represents the wave height and signifies the wavelength. This implies that only waves with very small amplitudes can be accurately generated using the linear theory. Given the focus of this study on nonlinear waves, the Airy wave method is not the optimal choice.

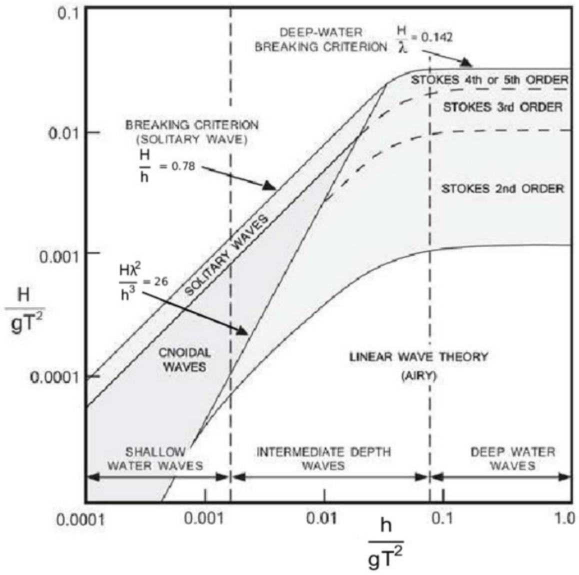

Figure 5.3: Ranges of applicability of various wave theories (source: Le Mehauté 1976 and USACE 2008)

To prescribe nonlinear waves, 5th order Stokes theory are usually implemented as depicted in figure 5.3. However, as stated in the ComFLOW manual, the Rienecker-Fenton wave theory, which is of the 10th order, provides more accurate wave kinematics than the 5th-order Stokes, especially in shallow water and for very steep waves. The theory is based on the shallow water equations, which are simplified equations that describe the motion of fluids in shallow water conditions. These equations are derived by assuming that the water depth is small compared to the wavelength of the waves. The Rienecker-Fenton wave theory takes into account additional factors such as wave dispersion, bottom friction, and wave breaking to provide a more accurate representation of wave behavior in shallow water regions. Its important to highlight that the Rienecker-Fenton wave theory is a specialized model and may demand advanced mathematical and numerical techniques for its implementation and application. The principle underlying Rienecker-Fenton simulation is a Fourier expansion in approximating a potential function which satisfies Laplace equation, and solving a system of non-linear equations by using Newtons method.

5.4.2. Wave Field Calculation by Different Simulation

The second employed approach for wave generation is briefly explained in this section. The process begins with the use of the first approach for wave generation in a 3D simulation. In this stage, waves are generated at an inflow boundary by setting a specific wave height. In this simulation, a wave probe is strategically positioned at the well dock entrance to capture the wave kinematics (such as wave height and phases). Consequently, extracted these wave kinematics, they are then used as input parameters for a 2D simulation. This 2D simulation specifically encompasses the well dock and the region of the solid ramp from the entire ship. The location of the wave probe at the well dock entrance is selected due to its significance as the initial point of interaction between the waves and the well dock. By capturing the wave kinematics at the dock entrance ensures more accurate initial conditions for the simulation. The model simplification to 2D addresses one of the research questions of this project, and this approach is discussed in more detail in chapter 8.

5.5. Geometry

The geometry of the LPD is presented in a side view in Figure 5.4 and in top view in Figure 5.5. The origin of the coordinate system is defined at the ship's center of gravity (CoG), and the coordinates of the ship is:

$$x = [-80.522\ ,\ 75.199],\ y=[-12.5\ ,\ 12.5],\ z= [-6.5\ ,\ 11.7]$$

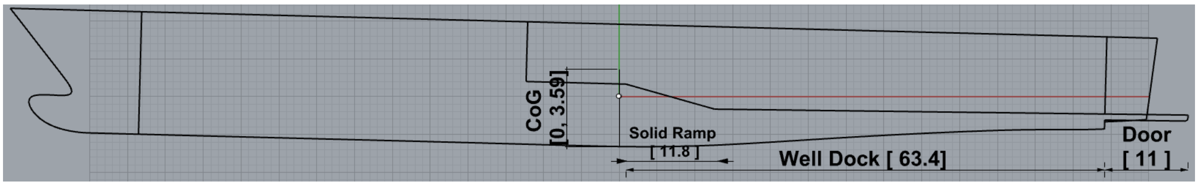

Figure 5.4: Two-dimensional side view of the Lpd ship

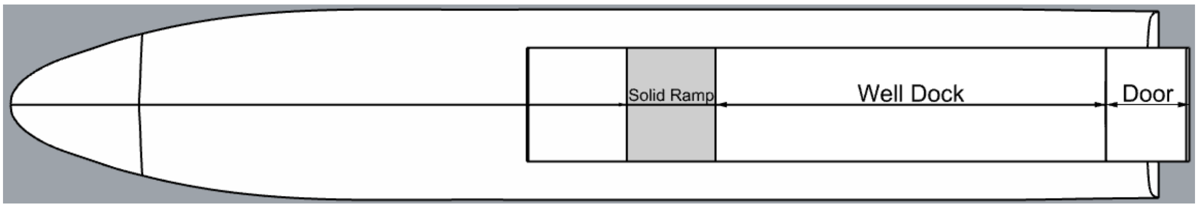

Figure 5.5: Three-dimensional top view of the Lpd ship

The water level within the well dock varies in depth, as illustrated in Figure 5.4. Near the ramp, the depth is approximately 1.80 meters, gradually increasing to 2.65 meters towards the entrance of the dock.

5.6. Physical parameters

The fluid's characteristics are defined by several physical parameters: density, dynamic viscosity, kinematic surface tension, the contact angle between the free surface and the solid boundary. The specific values for these parameters can be found in Table 5.1.

Density	ρ	1.025 x 10^3	[kg/m^3]
Dynamic Viscosity	μ	1.0 x 10^{-3}	[kg/m*s]
Surface tension	σ	0.0	[N/m]
Contact angle	θ	90.0	[°]

Table 5.1: Physical parameters

5.7. Boundary Conditions

Within the ComFLOW 2D domain, there are three distinct types of boundaries. The first is a stationary solid boundary (wall), the second is the GABC (Generated and Absorbing Boundary Condition), and the third is the free surface. Figure 5.6 provides a schematic representation of the boundary conditions relevant to the problem under consideration.

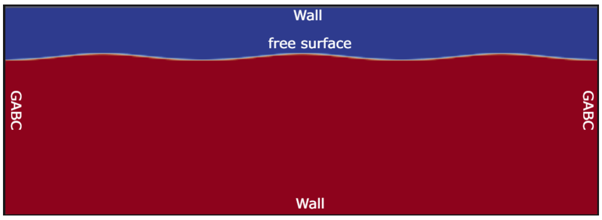

Figure 5.6: 2D Domain - Specified boundary conditions

5.7.1. Wall Boundary Condition

Initially, a no-slip boundary condition is applied to the two solid walls that outline the flow geometry. This condition means that u = 0 set at the fixed boundaries, where u represents the velocity field. The no-slip boundary condition is classified as a homogeneous Dirichlet boundary condition. This indicates that the fluid neither permeates through nor slides along the wall but sticks to it due to viscous effects.

5.7.2. Generating and Absorbing Boundary Condition

The second type of boundary condition is the GABC (Generating and Absorbing Boundary Condition). This condition is used to simulate specific behaviors without the need to explicitly model the entire unbounded domain. The generating boundary condition is responsible for generating waves into the computational domain, ensuring they possess the desired properties, such as the correct flow rate or wave characteristics. This condition is typically implemented at the boundary where the fluid or waves enter the domain. On the other hand, the absorbing boundary condition simulates the behavior of waves or fluid as they exit the domain. Its primary role is to eliminate unwanted reflections from the boundary and absorb outgoing waves or fluid. Typically, this is applied where the fluid or waves exit the domain. To minimize reflection, two common methods are used: dissipation zones like Perfectly Matched Layers (PMLs) and local boundary conditions. The latter is a more computationally efficient alternative to dissipation zones when the aim is to prevent wave reflection.

To minimize reflection and save computational time, the GABC boundary condition is employed. More specifically, it replaces the use of dissipation zones which cover an area much larger than the primary region where wave-structure interactions take place. Also, this boundary condition is designed for irregular free-surface wave simulations.

Finally,this particular boundary condition is uniquely employed in ComFLOW, especially for short waves, to reduce reflections that are more pronounced for short waves than for long waves.

5.7.3. Free Surface Boundary Condition

The third boundary condition belongs to the free surface, where its position must be consistently tracked. Boundary conditions are needed for both velocity and pressure. Both pressure and velocity conditions at the free surface are deduced using the assumption that the stresses are continuous at the free surface. Using continuity of tangential stresses leads to the tangential free-surface condition (equation 5.7), which states that the air impacts no tangential stress upon the fluid.

The free surface boundary conditions for pressure and velocity are calculated using the assumption that the stresses are continuous at the free surface. When the fluid is considered incompressible and the curvature of the free surface is neglected in the viscous stress terms, the continuity of both normal and tangential stress is respectively:

$$\hat{n} \cdot [\underline{T_1}(\mathbf{x}, t) - \underline{T_2}(\mathbf{x}, t)] \cdot \hat{n} = \gamma(\frac{1}{R_1} + \frac{1}{R_2}) \tag{5.3}$$

$$\hat{t} \cdot [\underline{T_1}(\mathbf{x}, t) - \underline{T_2}(\mathbf{x}, t)] \cdot \hat{t} = (- \bigtriangledown \mathbf{s}\gamma) \cdot \hat{t} \tag{5.4}$$

where n denotes the normal and t the tangential direction of the free surface, γ is the surface tension, R is the total curvature of the free surface, $\bigtriangledown \mathbf{s}$ is the surface gradient and the stress tensor $\underline{T}$ is equal to:

$$\underline{T} = -p\underline{I} + 2\mu\underline{E} \tag{5.5}$$

Also, $\underline{\mathrm{I}}$ is the identity tensor, is the pressure, μ is the dynamic viscosity and the rate of strain $\underline{E}$ is equal to:

$$\underline{E} = \begin{bmatrix} \frac{\partial u}{\partial n} & \frac{1}{2}(\frac{\partial u}{\partial t} + \frac{\partial v}{\partial n}) & \frac{1}{2}(\frac{\partial u}{\partial z} + \frac{\partial w}{\partial n}) \\ \frac{1}{2}(\frac{\partial u}{\partial t} + \frac{\partial v}{\partial n}) & \frac{\partial v}{\partial t} & \frac{1}{2}(\frac{\partial v}{\partial z} + \frac{\partial w}{\partial t}) \\ \frac{1}{2}(\frac{\partial u}{\partial z} + \frac{\partial w}{\partial n}) & \frac{1}{2}(\frac{\partial v}{\partial z} + \frac{\partial w}{\partial t}) & \frac{\partial w}{\partial z} \end{bmatrix}$$

The normal and tangential stresses equations lead to:

$$p + 2\mu\frac{\partial u}{\partial n} = p_0 + 2\gamma R \tag{5.6}$$

and

$$\mu(\frac{\partial u}{\partial t} + \frac{\partial v}{\partial n}) = 0 \tag{5.7}$$

Here, u is the normal component of the velocity, v is the tangential component of the velocity, p_0 is the atmospheric pressure,

5.8. wave propagation

After a wave is generated at the inflow boundary of the computational domain, it propagates through the domain. The wave propagation needs to be studied carefully, as dissipation from artificial viscosity can lead to wave damping. The damping of the waves should be small to ensure that the wave height is not underestimated when impacting the LPD. This influence can be explored through simulations. In these simulations, factors such as grid size, convection, and numerical schemes were examined.

Figure 5.7: 2D Domain - Wave Propagation

The computational domain for the wave propagation study is illustrated in Figure 5.7, with the associated simulation parameters presented in Table 5.2. The dimensions of both the inlet and outlet are denoted in terms of wavelengths, indicating their distance from the origin (0,0). Additionally, the X-coordinate of the wave probe is also expressed in terms of wavelength, while the Zmin and Zmax values are specified in meters, also referencing their distance from the origin (0,0). In order to investigate the optimal combination of schemes and grid size, a comparison was conducted using a wave probe to capture the wave height. The location of this probe is illustrated in Figure 5.7 with a red line, and its coordinates can be found in Table 5.2.

Simulation	**Wave Propagation**
Wavelength: L [m]	61.57
Wave frequency [rad/s]	1
Wave Height [m]	2
Inlet In L:Wavelength	1.5L
Outlet In L:Wavelength	1.5L
Zmax [m]	36.98
Zmin [m]	-36.98
Period Time [s]	6.283
Simulation Time in Periods	6
B.C	X: GABC
	Z: Wall
Wave Probe: X, Zmin, Zmax	L, -36.98, 36.98

Table 5.2: Simulation Parameters - Wave Propagation Study

Numerical Scheme	**Euler Forward 1st Order**		
Convection Scheme	**1st order upwind**		
Grid Cell Size	**Cell Size 61.57/60**	**Cell Size 61.57/90**	**Cell Size 61.57/120**
Wave Height	1.9812	1.9852	1.986

Table 5.3: Free surface elevation numerical results for three different grids

The first parameter investigated was the grid cell size. The data for this can be found in Table 5.3, while a visual representation of the wave probe is provided in Figure 5.8. It is observed that the discrepancy between the dimensions of the coarse and the fine grids amounts to a few millimeters. Given the negligible difference and in consideration of computational efficiency, it is determined that the coarse grid is employed for subsequent analyses.

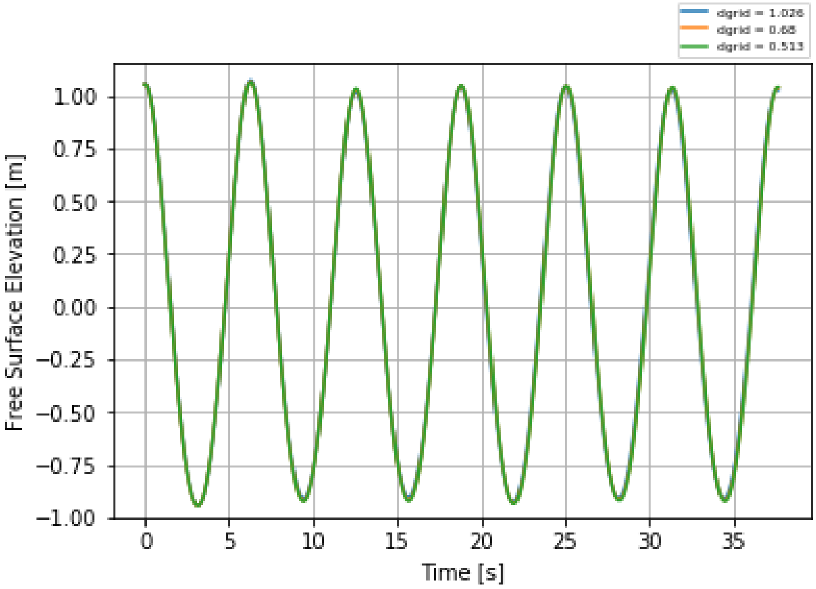

Figure 5.8: Free surface elevation for three different grids

The second parameter investigated is spatial discretization, with further details available in section C.1.1. The compared discretization methods are the central and upwind convection schemes. Results are illustrated by the wave probe in Figure 5.9, but for a comprehensive understanding, the numerical data on wave height is provided in Table 5.4. These findings indicate that the difference in wave height between the two methods is negligible, suggesting minimal numerical diffusion. Moreover, the upwind discretization method exhibits enhanced stability over the central scheme, as elaborated in Appendix C.1.1. Given these results, the upwind discretization method has been chosen for subsequent studies in this project.

Numerical Scheme	**Euler Forward 1st Order**	
Grid Cell Size	61.57/60	
Convection Scheme	Upwind	Central
Wave Height [m]	1.9812	1.9826

Table 5.4: Free surface elevation numerical results for two different spatial discretization methods

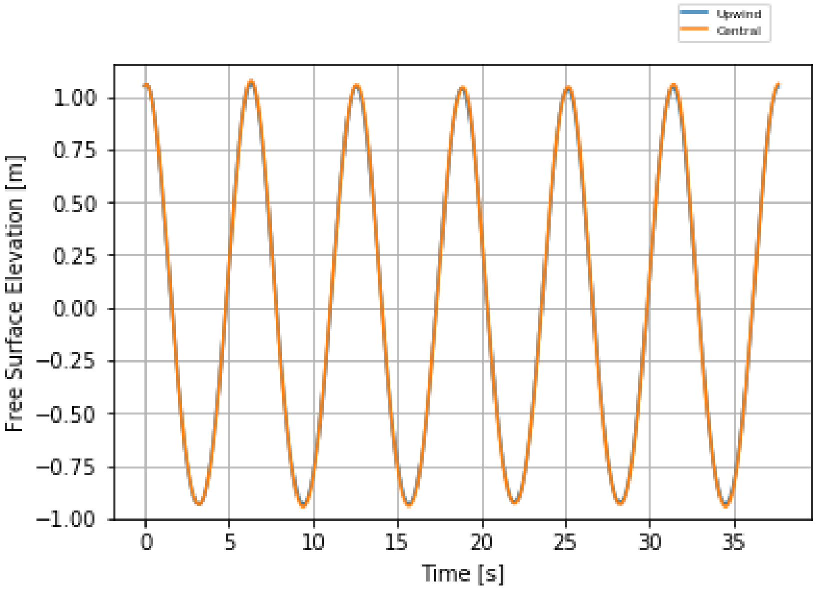

Figure 5.9: Free surface elevation for two different spatial discretization methods

The investigation of time discretization is the third parameter, further detailed in section C.1.2. The compared discretization methods include the Euler Forward 1st order and the Adams-Bashforth 2nd order methods. Results are visually represented by wave height in Figure 5.10, but for a more detailed explanation, they are also presented as numerical data in Table 5.5. The data reveals a slight difference in wave height between the two methods. Furthermore, the Adams method demonstrates superior accuracy compared to the Euler Forward method, as highlighted in Appendix C.1.2. Consequently, the Adams-Bashforth method has been chosen for this thesis.

Convection Scheme	**Upwind**	
Grid Dimension:Cell	61.57/60	
Numerical Scheme	Euler Forward	Adams-Bashforth
Wave Height [m]	1.9812	1.9852

Table 5.5: Free surface elevation numerical results for two different time discretization methods

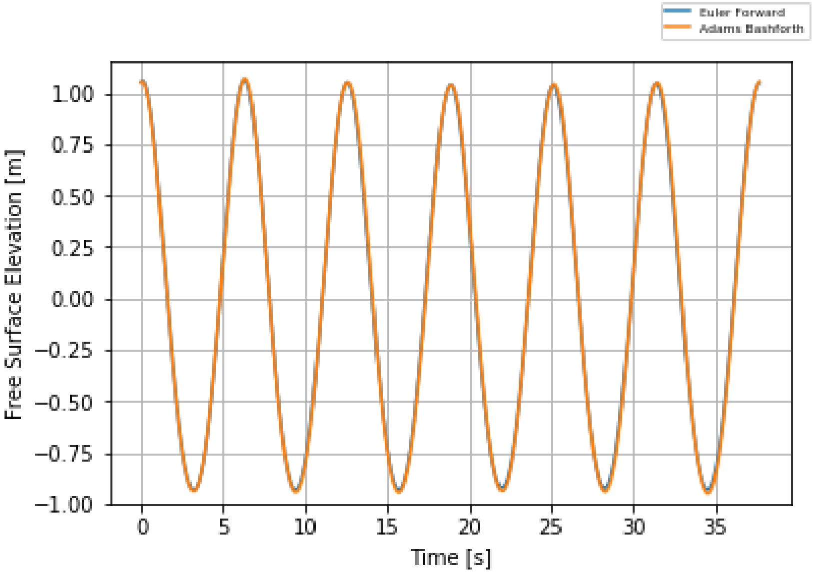

Figure 5.10: Free surface elevation for two different time discretization methods

5.9. Domain Size

An important aspect of creating a domain is ensuring sufficient development of flow dynamics across the length of the computational domain. If the domain is too small, waves might reflect off the boundaries and interfere with the wave dynamics in the primary region of interest. This interference can lead to unphysical results and may not provide accurate predictions for the behavior of the waves. Conversely, unnecessarily large domains can increase computational costs without enhancing the accuracy of the simulation. For this reason, during the Domain Size study, the optimal distance for the inlet, outlet, and width of the computational domain from the LPD ship was investigated to ensure the wave height remains less affected.

Figure 5.11: 2D Domain - Domain Size

To create the computational domain for the domain size study, both the two-dimensional representation of the LPD (as illustrated in Table 5.6) and the dimensions of the entire study domain (as depicted in Table 5.7) are required. All simulation parameters can be found in Table 5.7.

The LPD 'Rotterdam' has the following dimensions:

Ship Dimensions	
Ship Length [m]	155.8
Ship Height [m]	16
Ship Width [m]	25

Table 5.6: LPD Dimensions

Simulation	Domain Size
Wavelength: L [m]	61.57
Wave frequency [rad/s]	1
Wave height [m]	2
Inlet In L:Wavelength	2L - 4L
Outlet In L:Wavelength	2L - 4L
Zmax [m]	36.98
Zmin [m]	-36.98
Period Time [s]	6.283
Simulation Time in Periods	20
B.C	X: GABC
	Z: Wall
Wave Probes: X, Zmin, Zmax	L, -36.98,36.98

Table 5.7: Simulation Parameters- Domain Size Study

In order to determine the appropriate distances for both the inlet and outlet, a comparison is made using a wave probe. Further details regarding the specific location of the wave probe can be found in Table 5.7. In terms of the probe's coordinates, the X-coordinate symbol 'L' denotes a distance of one wavelength from the ship's stern, while Zmin and Zmax represent the distance from Z=0. Its position is clearly illustrated in Figure 5.11.

5.9.1. Inlet length

The inlet length is the first parameter investigated. In this specific research, the inlet ranges between two wavelengths (2L) and four wavelengths (4L), while the outlet remains constant at two wavelengths (2L). Figure 5.12 clearly shows that the wave height remains stable. Thus, to save computational time, the smaller inlet size was chosen for the continuation of this project.

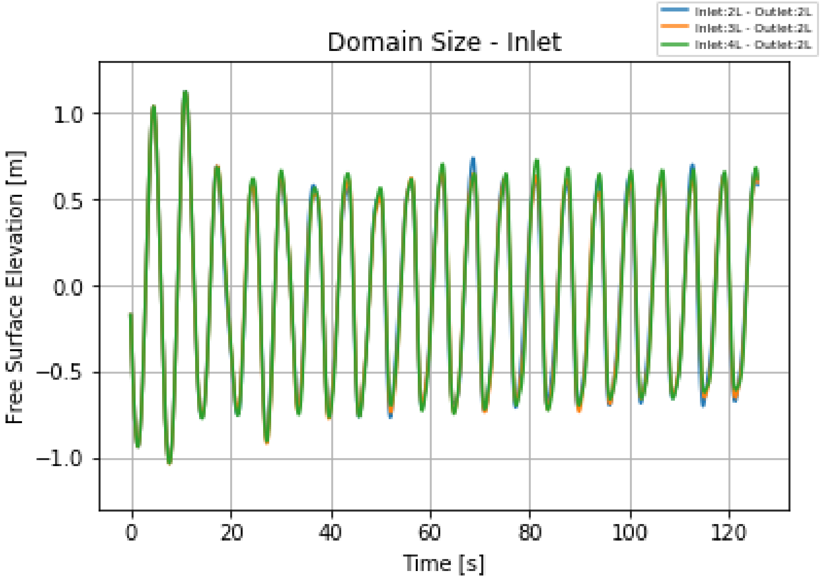

Figure 5.12: Domain Size - Inlet

5.9.2. Outlet length

The outlet length is the second parameter of this study. According to Table 5.7, the outlet varies between two wavelengths (2L) and four wavelengths (4L), whereas the inlet remains constant at two wavelengths (2L). Figure 5.13 shows that the wave height remains unchanged. Therefore, the smaller outlet size is selected for the subsequent studies of this thesis.

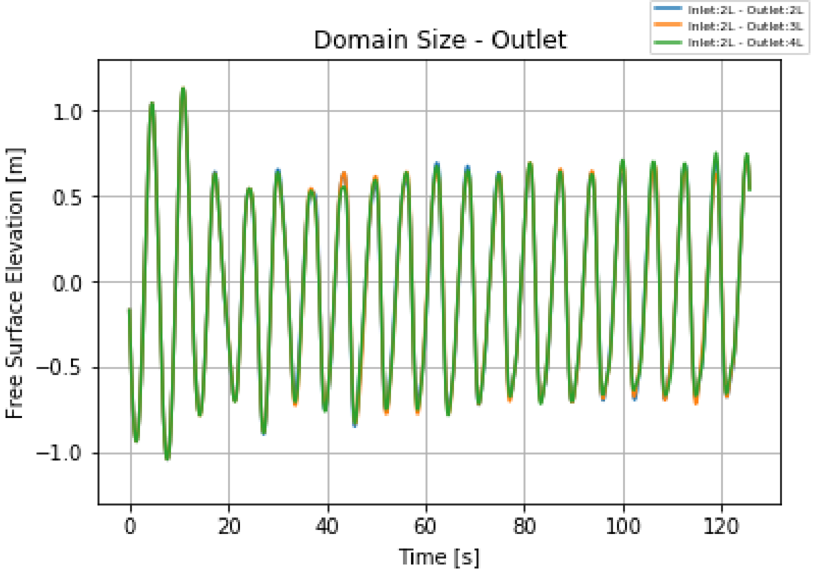

Figure 5.13: Domain Size - Outlet

5.9.3. Width length

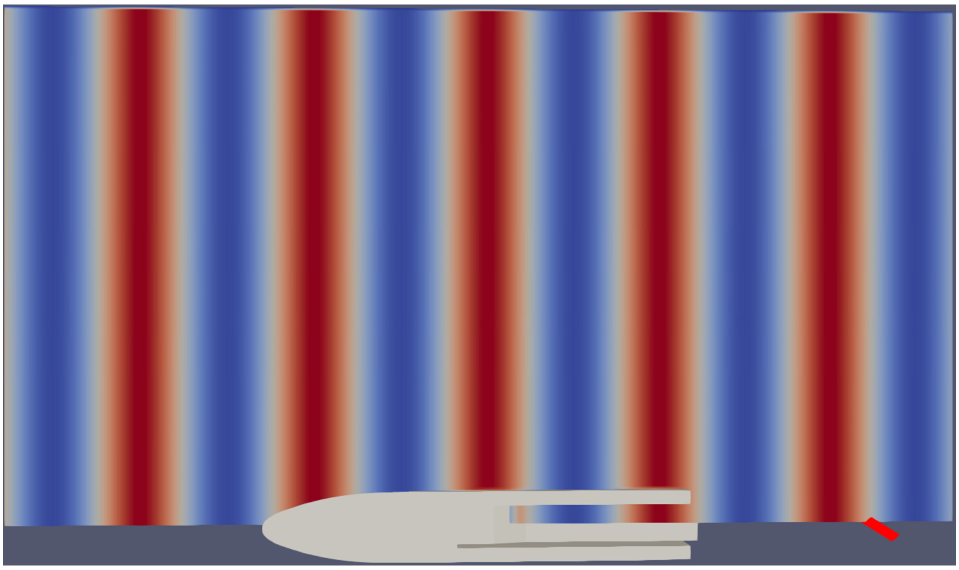

Figure 5.14: Utilizing the red wave probe to determine the optimal width length of the 3D domain

The width length is the third parameter evaluated in the domain size study. The new computational domain incorporates the inlet and outlet sizes discussed in the previous two subsections, aiming to find the optimal size for the y-direction. The 3D computational domain is illustrated in Figure 5.14, with all related simulation parameters are detailed in Table 5.8. As evident from Figure 5.14, the domain represents only half of the ship because both the geometry and flow conditions are symmetrical. The reasoning for this symmetry is: for this project the wave direction is set at 180°, and the model test data includes information only on surge, heave and pitch motions. Subsection 5.2.9 clarifies the conventions for these vessel motions. Taking advantage of this symmetry leads to reduced computational costs. Also, wave probe is utilized to measure the wave height to ensure the accuracy of results. Its placement is specified in Table 5.8 and is also marked by a red line in Figure 5.14. The wave probe's X-coordinate, symbolized by 'L', represents a distance of one wavelength from the ship's stern, while Zmin and Zmax denote the distance from Z=0.

Simulation	**Width Domain**
Wavelength: L [m]	61.57
Wave frequency [rad/s]	1
Wave height [m]	2
Inlet In L:Wavelength	2L
Outlet In L:Wavelength	2L
Width In L:Wavelength	1L - 6L
Zmax [m]	36.98
Zmin [m]	-36.98
Period Time [s]	6.283
Simulation Time in Periods	20
	X: GABC Z: Wall Y: Wall
B.C	
Wave Probes: X, Y, Zmin, Zmax	L, 0, -36.98, 36.98

Table 5.8: Simulation Parameters - Width Domain Size Study

In Figure 5.15, the width varies between one wavelength (1L) and three wavelengths (3L). It is evident that the wave height is not consistent so depends on the width of the domain. This suggests that the domain might not be sufficiently large to prevent side boundary effects. Consequently, the wave might be reflecting off the boundaries, leading to variation in wave heights.

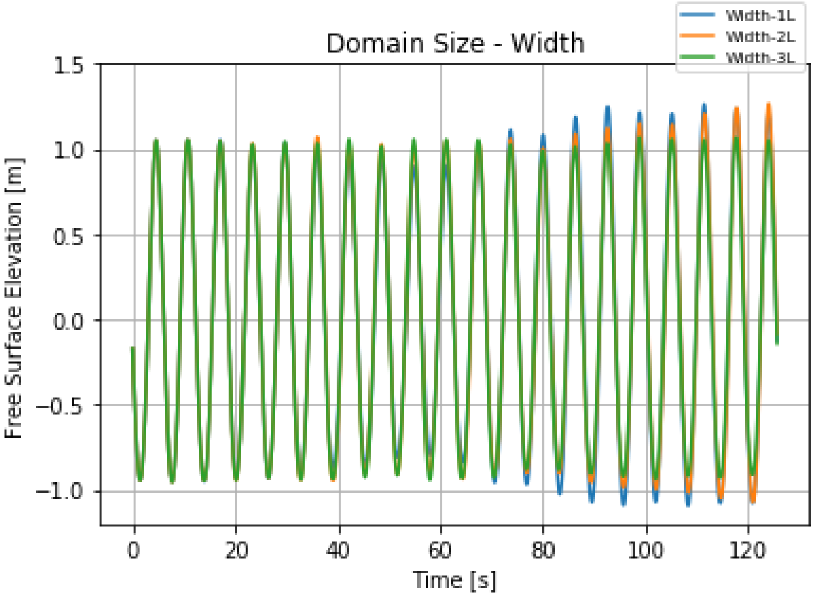

Figure 5.15: Comparison of the time-domain signal of free surface elevation of the wave across three different width lengths (1L -3L)

For this reason, in the next simulation, the width variation is between three wavelengths (3L) and six wavelengths (6L) as depicted in figure 5.16. It is clear that the wave height remains constant, indicating that the domain width of three wavelengths is sufficiently large to prevent the side boundary effects. Thus, for the rest of the project, a width of three wavelengths was chosen.

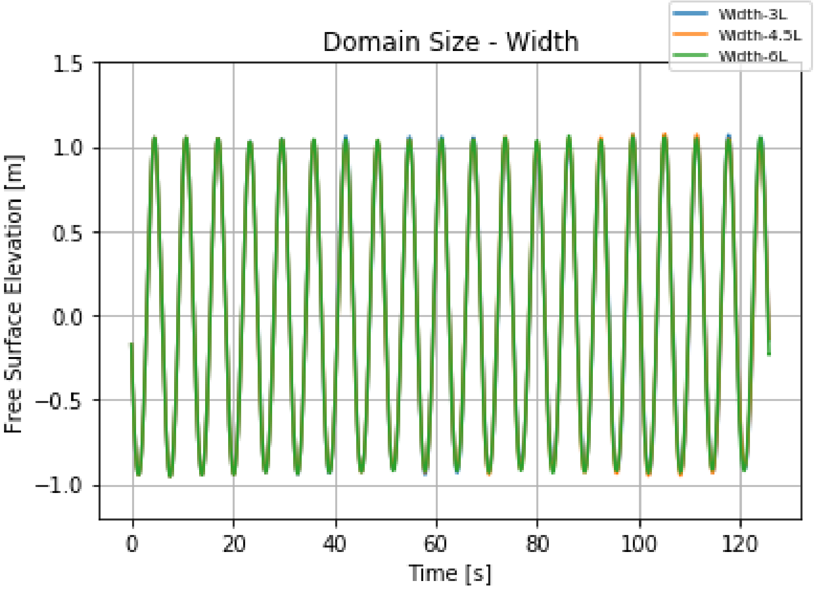

Figure 5.16: Comparison of the time-domain signal of free surface elevation of the wave across three different width lengths (3L -6L)

5.10. Integration of Ship Motions

5.10.1. Coordinate System

The mathematical model used in the ComFLOW software is formulated in a right-handed Cartesian coordinate system, G - xyz. In this ship-fixed coordinate system, the positive z-axis points vertically upwards, the positive x-axis points to the aft of the ship, and the positive y-axis points to the port side (see Figure 5.18). The system's origin is located at the vessel's center of gravity, denoted as G. The G-xyz coordinate system shifts in relation to the ship's movement.
For the ship motion problem, waves are travelling in the positive x-direction. This system is earth-fixed and has its origin in the calm water surface. The angle between the ship-fixed x-axis and the earth-fixed X-axis represents the heading of the vessel as shown by the angle β in Figure 5.17. A wave direction of 180° corresponds to head waves.

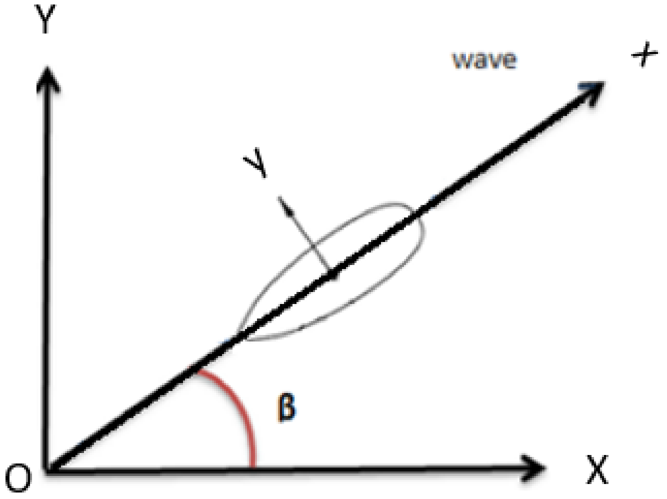

Figure 5.17: Earth-fixed and Ship-fixed coordinate systems

The motions of the vessel are also described in the right-handed Cartesian coordinate system O-xyz. The six positive translations and rotations of the vessel, around the center of gravity (G) of the vessel, are given in Figure 5.18. The body-bound coordinate system is given by respectively the x-, y- and z-axis.

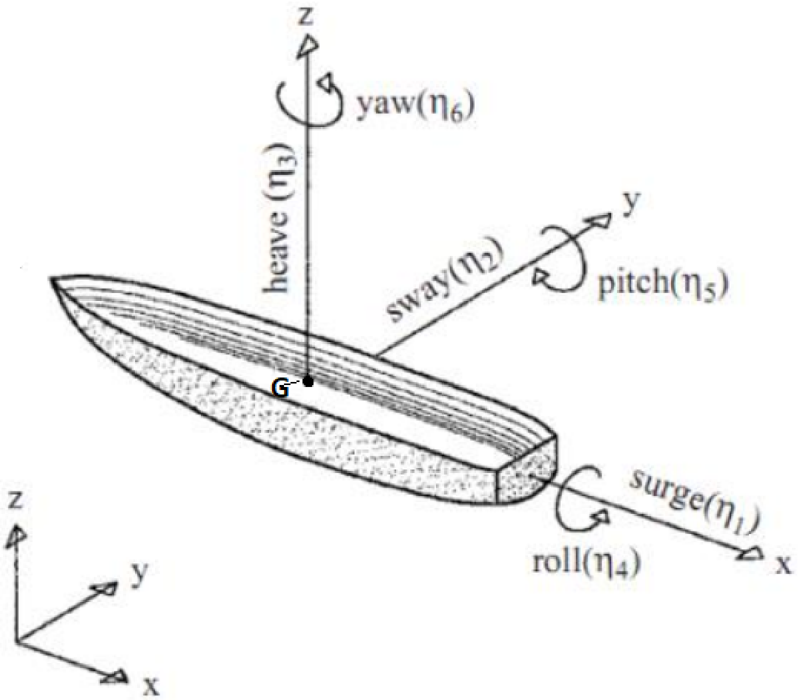

Figure 5.18: Six degrees of freedom of vessel motion

5.10.2. Incorporating Ship Motion into Comflow

To investigate the influence of a vessel's motions on fluid flow within the dock, these motions must be assigned to the domain. The fixed-frame approach is employed in ComFLOW. In this approach, the coordinate frame remains stationary, while the computational domain moves. Within ComFLOW, motions of the computational domain can be prescribed using externally defined time series. External time traces for displacement and velocity of the vessel are provided in an input file. Here, velocity is derived from the displacement series. The files under consideration contain data on time instants and the respective amplitudes and phases for the six degrees of freedom of vessel motion: surge, sway, heave, roll, pitch, and yaw. The amplitudes and phase angles for these six degrees of freedom have been calculated at the vessel's center of gravity based on model tests. Since the model test experiments were conducted in head waves, only the amplitude and phase data for surge (x), heave (z), and pitch (β) motions are sourced from the experimental data. These data contribute in representing the surge, heave, and pitch motions of the ship (equations 5.8 - 5.10) for the first five harmonic frequencies.

$$x = A_0 + \sum_{\mathbf{n=1}}^{\mathbf{5}} A\mathbf{n} * cos(2.0 * \pi * (\mathbf{n} * frequency * t + surgephase\mathbf{n}/360.0)) \tag{5.8}$$

$$z = B_0 + \sum_{\mathbf{n=1}}^{\mathbf{5}} B\mathbf{n} * cos(2.0 * \pi * (\mathbf{n} * frequency * t + heavephase\mathbf{n}/360.0)) \tag{5.9}$$

$$\beta = C_0 + \sum_{\mathbf{n=1}}^{\mathbf{5}} C\mathbf{n} * cos(2.0 * \pi * (\mathbf{n} * frequency * t + pitchphase\mathbf{n}/360.0) \tag{5.10}$$

As far as the following procedure for the correct introduction of the ship motion is:

1. Ship simulation without integrated motion capturing the phase at the wave probe which has distance 1 wave length in front of the ship.
2. Exporting from the experimental results the phase at the same line (1 wave probe in front of the ship).
3. Phases calculation:

$$Surge\,phase = surgephase_{experimental} - experimentalphase_{\textbf{in front of the ship}} + ComFLOWphase_{\textbf{in front of the ship}} \tag{5.11}$$

$$Heave\,phase = heavephase_{experimental} - experimentalphase_{\textbf{in front of the ship}} + ComFLOWphase_{\textbf{in front of the ship}} \tag{5.12}$$

$$Pitch\,phase = pitchphase_{experimental} - experimentalphase_{\textbf{in front of the ship}} + ComFLOWphase_{\textbf{in front of the ship}} \tag{5.13}$$

5.11. Simulation Time

During the computation, the size of the time step can be controlled automatically to numerical stability restrictions without using unnecessarily small time steps. As the simulation progresses, the time step is adjusted based on the Courant-Friedrichs-Lewis (CFL) number. The desired range for the CFL number has been set between 0.5 and 0.9. If the value exceeds the upper limit, the time step is halved. Conversely, if the CFL number remains below the lower limit for ten consecutive time steps, the time step will be doubled. The CFL number is calculated as shown in equation 5.14:

$$CFL = \frac{u_x \Delta t}{\Delta x} + \frac{u_y \Delta t}{\Delta y} + \frac{u_z \Delta t}{\Delta z} \tag{5.14}$$

where Δt is the time step, Δx, Δy, Δz are the local grid spacings in x-direction, y-direction and z-direction, respectively, and u$_x$, u$_y$ and u$_z$ are the local velocity components in x-direction, y-direction and z-direction respectively.

5.12. Post-processing

Post-processing in ComFLOW is conducted using the Python programming language and the software of ParaView for visualization. A lot of data is produced by ComFLOW and put into files that can be visualized using Python. For this specific problem, it is important to visualize the volume of fluid within the computational domain, which can be visualized using ParaView. Additionally, the comparison of the numerical model with the experimental tests is realized measuring the wave height within the well dock using wave proves. The wave probes capture the wave signal which is then plotted in the time domain with wave height on the y-axis and time on the x-axis. Following this, the wave signal is transformed from the time domain to the frequency domain using Fast Fourier Analysis. This transformation is essential, as the data from model tests is presented in this format.

5.13. Grid study

CFD requires the subdivision of the computational domain into subdomains, non-overlapping subdomains to solve the flow physics within the domain geometry. This process results in the generation of a grid covering the entire domain. The accuracy of the solution is generally governed by the size of cells in the grid within the domain. In general, a smaller size of cells yields a more accurate solution but also demands greater computational time and resources. A drawback of a coarse mesh is the increase in numerical dissipation. In ComFLOW, the grid can be specified in the input file. The grid must fully encompass the domain, and the ratio between the sizes of any two neighboring cells should not be excessively large or small.

5.13.1. Procedure of Grid Convergence Study

In any numerical study, grid convergence is paramount. It ensures that the equations are solved correctly and that the solution remains consistent irrespective of grid resolution. Below is a detailed outline of the equations and procedures for the grid convergence study:

1. Use three grids: Coarse, Medium, and Fine. These should have a constant refinement ratio of r=1.5 between each.
2. The parameter for grid convergence is the free surface elevation within the well dock, measured using a wave probe as illustrated in Figures 5.19 and 5.20.
3. Calculate the order of convergence, p, with the equation:

$$p = ln(\frac{f_3 - f_2}{f_2 - f_1})/ln(r) \tag{5.15}$$

4. Conduct a Richardson extrapolation to estimate the value when h = 0.

$$f_{h=0} = f_{fine} + \frac{f_1 - f_2}{rP - 1} \tag{5.16}$$

5. Determine the grid convergence index (GCI) for both medium and fine refinement levels.

$$GCI = \frac{F_s|e|}{r^P - 1} \tag{5.17}$$

6. Confirm that the grids are within the asymptotic range of convergence by checking:

$$\frac{GCI_{2,3}}{r^P CGI_{1,2}} \approxeq 1 \tag{5.18}$$

Figures 5.19 and 5.20 depict the wave probe positioned within the well dock, highlighted in red. This specific location was chosen to conduct the grid convergence study for the models of Chapters 6 and 7.

Figure 5.19: Side View of the Wave Probe within the Well Dock

Figure 5.20: Front view of the Wave Probe within the Well Dock

6

Study on physical mechanisms within the well dock

This model addresses parameters relevant to the first research question, which independently investigates the influence of radiation and diffraction mechanisms within the well dock, in relation to wave characteristics. Following this independent investigation, the next step involves combining these two mechanisms and comparing them with experimental results. Notably, this setup builds on the detailed findings from the numerical model in Chapter 5. This encompasses the generation of waves using wave theory (5.4.1), the 3D geometry of the LPD ship (5.5), physical parameters (5.6), boundary conditions (5.7), studies on wave propagation (5.8), domain size (5.9), and the method of motion integration (5.10). Consequently, section 6.1 delves into the radiation and diffraction grid study. Both of these studies follow the procedure outlined in the Grid Study (5.13). Section 6.2 presents the input parameters for the simulations and the locations within the well dock where comparisons between the physical mechanisms are conducted. In Section 6.3, results from the radiation and diffraction studies are first presented. Subsequently, the figures show comparisons between the model which combines the radiation and diffraction studies with the experimental results. Section 6.4 delves into a discussion regarding the findings presented in Section 6.3.

6.1. Grid Study

A grid study is conducted to determine the grid distribution required for this problem. The following two subsections separate the grid study into the diffraction grid study and the radiation grid study, aiming for a more detailed, accurate, and efficient analysis. This distinction is made because the diffraction grid study examines situations when the LPD is stationary, and incoming waves diffract around the ship's hull before propagating into the well dock. Thus, the diffraction grid study helps capture how these waves interact with the LPD's structure and how they enter and propagate within the well dock. Conversely, during the radiation grid study, where the LPD undergoes surge, heave, and pitch motions, the ship itself generates waves. These radiation waves then propagate into the well dock. Isolating these radiation effects provides insights into how ship motions affect the flow within the well dock.

6.1.1. Diffraction Grid Study

A grid study focused on diffraction was undertaken to analyze the convergence of the free surface elevation at a specific location within the well dock, as illustrated in Figures 5.19 and 5.20. Given that the central emphasis of this research centers on the water height within the dock, the convergence of the free surface elevation emerges as the primary concern. This study delved into the impact of grid cell size on simulation outcomes, with details elaborated in Table 6.2 . Based on the insights derived, the optimal mesh size for the simulations was established. Throughout this grid study, the ship remains stationary. Incoming waves diffract around the vessel's hull. This examination seeks to understand how these waves interact with the ship's structure both prior to and during their propagation within the well dock. Table 6.1 catalogs the input parameters utilized for this study, whereas Table 6.2 elaborates on the specifics of the various grids employed. Visual representations of the three grid resolutions are available in Appendix D.1.

Simulation	**Diffraction Grid Study**
Wavelength: L [m]	61.57
Wave frequency: [rad/s]	1
Wave height: [m]	2
Inlet: [Wavelengths]	2L
Outlet: [Wavelengths]	2L
Ymin: [Wavelengths]	0
Ymax: [Wavelengths]	3L
Zmin: [m]	-36.98
Zmax: [m]	36.98
Period time: [s]	6.28
Simulation time in periods	25
BC	X:GABC
	Ymin: Symmetry
	Ymax: Wall
	Zmin: Free-Slip
	Zmax: Wall
Wave Probe Coordinates (Figures 5.19, 5.20): X, Y, Zmin, Zmax	49.4, 0, -1.1, 36.98

Table 6.1: Simulation Parameters - Diffraction Grid Study

Simulation Diffraction Grid Study									
Diffraction Grid Study 13 - Coarse Grid									
Grid Levels	Extents			Grid Size			Cell Size		
	Coordinates in x-direction	Coordinates in y-direction	Coordinates in z-direction	Cells in x- direction	Cells in y-direction	Cells in z-direction	x	y	z
0	-267.7 , 103.51	0 , 184.71	-36.98 , 36.98	80	40	16	4.64	4.62	4.62
1	-267.7 , 103.51	0 , 184.71	-16.00 , 36.98	160	80	32	2.32	2.31	2.31
4	-45. , 20.	0. , 8.0	-3. , 3.	224	28	21	0.29	0.29	0.28
Diffraction Grid Study 20 - Medium Grid									
Grid Levels	Extents			Grid Size			Cell Size		
	Coordinates in x-direction	Coordinates in y-direction	Coordinates in z-direction	Cells in x- direction	Cells in y-direction	Cells in z-direction	x	y	z
0	-267.7 , 103.51	0 , 184.71	-36.98 , 36.98	120	60	24	3.09	3.08	3.08
1	-267.7 , 103.51	0 , 184.71	-16.00 , 36.98	240	120	48	1.54	1.54	1.54
4	-45. , 20.	0. , 8.0	-3. , 3.	336	42	31	0.19	0.19	0.19
Diffraction Grid Study 30 - Fine Grid									
Grid Levels	Extents			Grid Size			Cell Size		
	Coordinates in x-direction	Coordinates in y-direction	Coordinates in z-direction	Cells in x- direction	Cells in y-direction	Cells in z-direction	x	y	z
0	-267.7 , 103.51	0 , 184.71	-36.98 , 36.98	180	90	36	2.06	2.05	2.05
1	-267.7 , 103.51	0 , 184.71	-16.00 , 36.98	360	180	72	1.03	1.03	1.03
4	-45. , 20.	0. , 8.0	-3. , 3.	508	63	47	0.13	0.13	0.13

Table 6.2: Detail Analysis of Diffraction Grid Study (Grid and Cell Size)

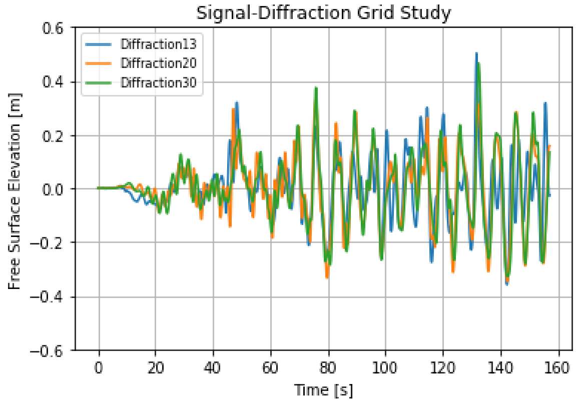

Figure 6.1: Comparison of the Time-Domain signal of Free Surface Elevation of the Wave Across Three Different Grids

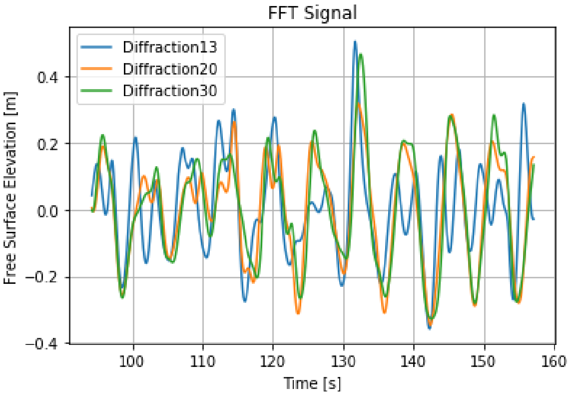

Figure 6.2: Comparison of the Last 10 Periods from the Total Time-Domain Signal for Free Surface Elevation of the Wave Across Three Different Grids

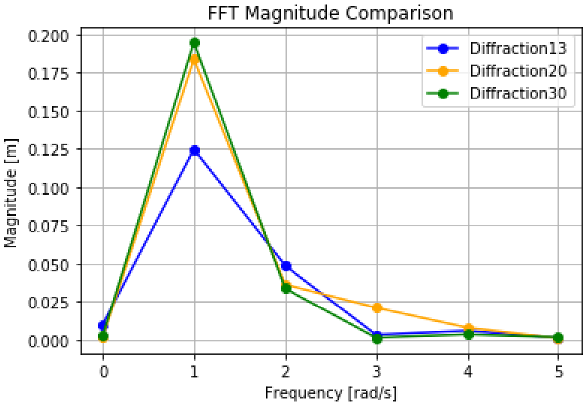

Figure 6.3: Comparison of the Fast Fourier Transformation Analysis for Six Fourier Components Across Three Different Grids

The results are presented in Table 6.3 and are visually represented in Plot 6.4. These outcomes were obtained using the procedure described in the following paragraphs.

Using the wave probe, as referenced in Figures 5.19 and 5.20, the relative wave height over time is charted, as depicted in Figure 6.1. From the last 10 periods of the total time-domain signal (figure 6.2.), it is evident that the wave height within the well dock stabilizes and reaches a quasi-steady state. The signal is not periodic due to complexities of wave interactions within the confines of the well dock and the presence of multiple reflecting waves.

This time-domain signal from the last 10 periods is then transformed into the frequency domain using the Fast Fourier Transformation, as illustrated in Figure 6.3. This transformation shows the first Fourier components (0 to 5). A detailed comparison of the three grid resolutions is focused on the second Fourier component (A1). The A1 Fourier component represents the fundamental wave behavior inside the well dock of the LPD vessel. Given its dominance in the Fourier analysis, it serves as a primary indicator of the underlying wave dynamics and is thus of primary interest. Both Table 6.3 and Plot 6.4 showcase the free surface elevation of this second component derived from the Fast Fourier Transformation.

After carefully examining the results, it is evident that there is a marginal difference between the medium grid and the Richardson extrapolation which amounts to approximately 1 centimeter compared to wave height. This small deviation underscores the accuracy of the medium grid, making it a suitable choice. Choosing a finer grid could increase the computational time significantly without offering a proportionate improvement in accuracy. On the other hand, a coarser grid might not capture the necessary details accurately. Therefore, to strike a balance between computational time, accuracy, and efficiency, the medium grid has been selected for subsequent analyses.

Grid	**Normalized Grid Spacing h**	**Free Surface Elevation [m]**
Richardson Extrapolate	0	0.1952
Fine - Diffraction Grid Study 30	1	0.1946
Medium - Diffraction Grid Study 20	1.5	0.1836
Coarse - Diffraction Grid Study 13	2.25	0.1244

Table 6.3: Diffraction Grid - Convergence Study

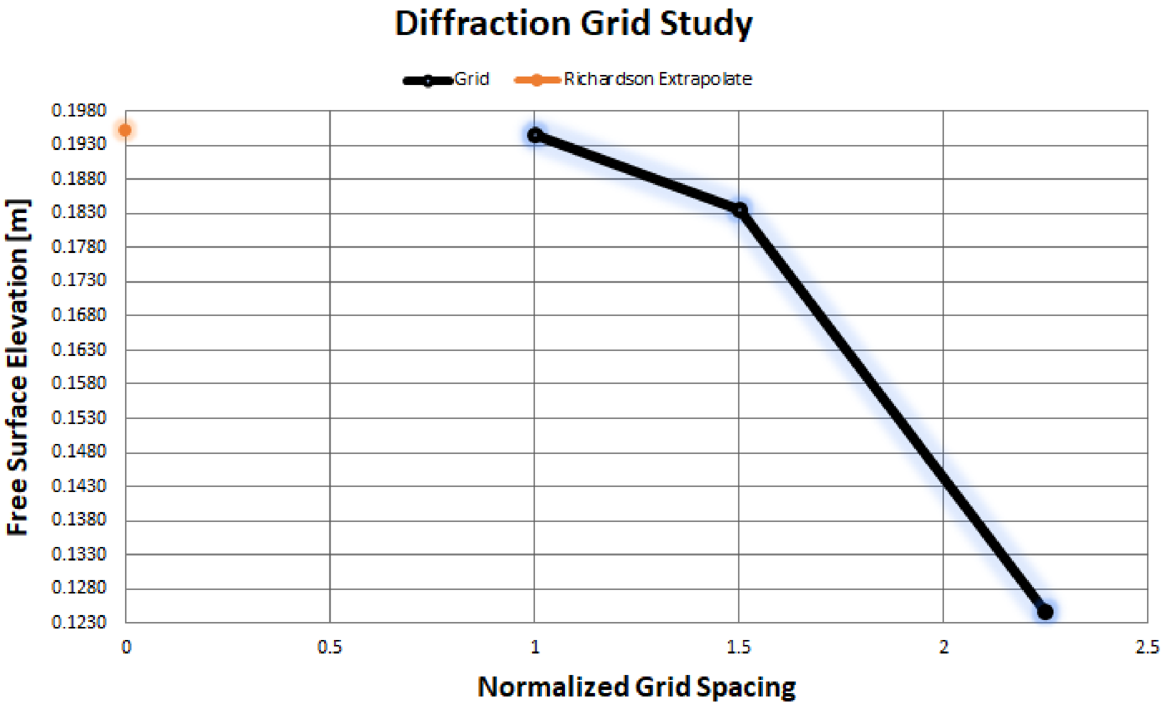

Figure 6.4: Convergence plot for diffraction grid study showcasing the variation of the Fourier component A1 in relation to the grid resolution

6.1.2. Radiation Grid Study

A radiation grid study is conducted to examine the convergence of the free surface elevation at the position indicated by the wave probe in Figures 5.19 and 5.20. In this study, wave generation results solely from the ship's motions, offering an in-depth analysis of how ship motions influence the flow within the well dock. The input parameters for the radiation grid study can be found in Table 6.4, while a detailed analysis of the three different grids is presented in Table 6.5. Additionally, figures depicting the three grids are available in Appendix D.2.

Simulation	**Radiation Grid Study**
Wavelength: L [m]	61.57
Wave frequency: [rad/s]	1
Wave height: [m]	2
Inlet: [Wavelengths]	2L
Outlet: [Wavelengths]	2L
Ymin: [Wavelengths]	0
Ymax: [Wavelengths]	3L
Zmin: [m]	-36.98
Zmax: [m]	36.98
Period time: [s]	6.28
Simulation time in periods	25
BC	X:GABC
	Ymin: Symmetry
	Ymax: Wall
	Zmin: Free-Slip
	Zmax: Wall
Wave Probe Coordinates (Figures 5.19, 5.20): X, Y, Zmin, Zmax	49.4, 0, -1.1, 36.98

Table 6.4: Simulation Parameters - Radiation Grid Study

Simulation Radiation Grid Study									
Radiation Grid Study 13									
Grid Levels	Extents			Grid Size			Cell Size		
	Coordinates in x-direction	Coordinates in y-direction	Coordinates in z-direction	Cells in x- direction	Cells in y-direction	Cells in z-direction	x	y	z
0	-267.7 , 103.51	0 , 184.71	-36.98 , 36.98	80	40	16	4.64	4.62	4.62
1	-267.7 , 103.51	0 , 184.71	-16.00 , 36.98	160	80	32	2.32	2.31	2.31
4	-45. , 20.	0. , 8.0	-3. , 3.	224	28	21	0.29	0.29	0.28
Radiation Grid Study 20									
Grid Levels	Extents			Grid Size			Cell Size		
	Coordinates in x-direction	Coordinates in y-direction	Coordinates in z-direction	Cells in x- direction	Cells in y-direction	Cells in z-direction	x	y	z
0	-267.7 , 103.51	0 , 184.71	-36.98 , 36.98	120	60	24	3.09	3.08	3.08
1	-267.7 , 103.51	0 , 184.71	-16.00 , 36.98	240	120	48	1.54	1.54	1.54
4	-45. , 20.	0. , 8.0	-3. , 3.	336	42	31	0.19	0.19	0.19
Radiation Grid Study 30									
Grid Levels	Extents			Grid Size			Cell Size		
	Coordinates in x-direction	Coordinates in y-direction	Coordinates in z-direction	Cells in x- direction	Cells in y-direction	Cells in z-direction	x	y	z
0	-267.7 , 103.51	0 , 184.71	-36.98 , 36.98	180	90	36	2.06	2.05	2.05
1	-267.7 , 103.51	0 , 184.71	-16.00 , 36.98	360	180	72	1.03	1.03	1.03
4	-45. , 20.	0. , 8.0	-3. , 3.	508	63	47	0.13	0.13	0.13

Table 6.5: Detail Analysis of Radiation Grid Study (Grid and Cell size)

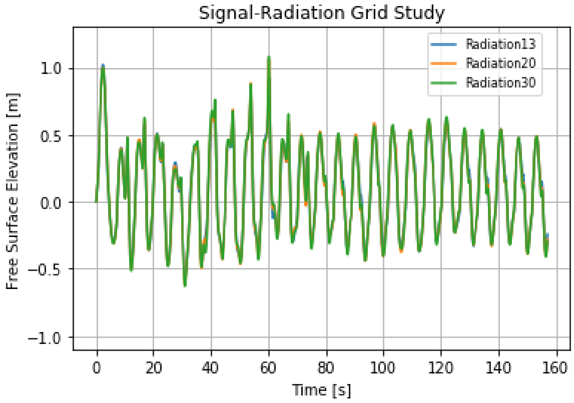

Figure 6.5: Comparison of the Time-Domain signal of Free Surface Elevation of the Wave Across Three Different Grids

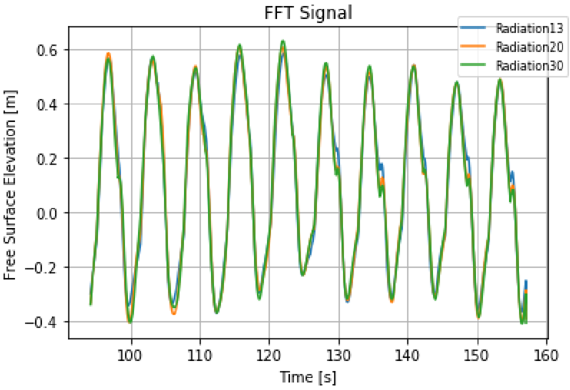

Figure 6.6: Comparison of the Last 10 Periods from the Total Time-Domain Signal for Free Surface Elevation of the Wave Across Three Different Grids

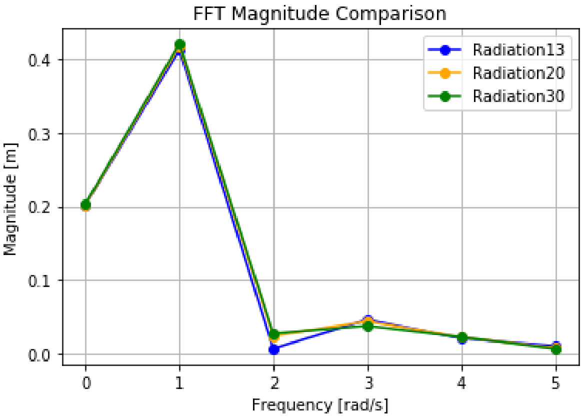

Figure 6.7: Comparison of the Fast Fourier Transformation Analysis for Six Fourier Components Across Three Different Grids

The data results are presented in Table 6.6. For those who prefer a visual interpretation, Plot 6.8 provides a graphical representation. This research leveraged a procedure that aligns with the methodology used in the diffraction grid study. Central to this process was the wave probe, as shown in Figures 5.19 and 5.20. This tool plays a crucial role in capturing and illustrating the time-domain signal of the free surface elevation of the wave. Following the established procedure, the last 10 periods of the total time domain signal were converted into the frequency domain using the Fast Fourier Transformation, as illustrated in Figure 6.7.

Upon examining the results for the first Fourier component of the free surface elevation in Table 6.6 and Plot 6.8, it is evident that the difference between the medium grid and the Richardson extrapolation is less than 0.5 centimeters. To optimize computational time while maintaining accuracy, the medium grid is selected.

Grid	Normalized Grid Spacing h	Free Surface Elevation [m]
Richardson Extrapolate	0	0.4228
Fine - Radiation Grid Study 30	1	0.4214
Medium - Radiation Grid Study 20	1.5	0.4184
Coarse - Radiation Grid Study 13	2.25	0.4129

Table 6.6: Radiation Grid - Convergence Study

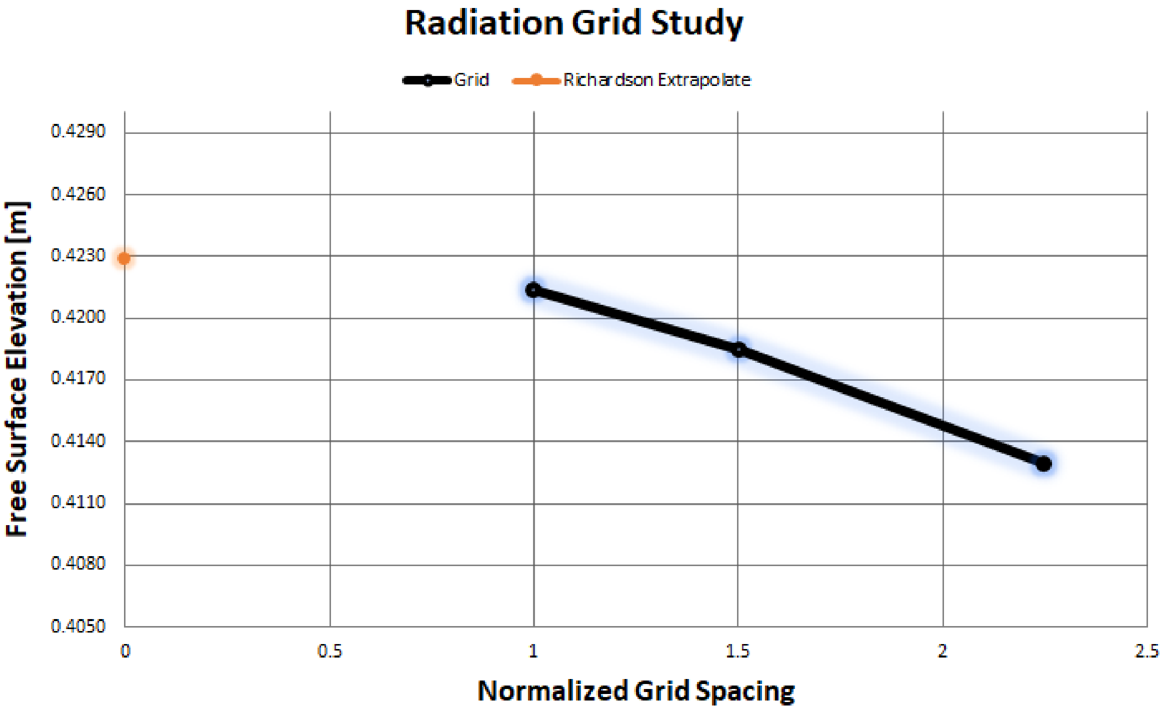

Figure 6.8: Convergence plot for radiation grid study showcasing the variation of the Fourier component A1 in relation to the grid resolution

6.2. Simulation set-up

After the completion of the grid study for both physical mechanisms, the next step is the presentation of the input parameters for the simulations as described in table 6.7 and the post processing is based on the three locations within the well dock, capturing the wave height using the wave probes which are depicted in figure 6.9. The coordinates for these lines are in table 6.7, which also lists the input simulation parameters for the wave frequencies of 0.4 and 1 rad/s.

Simulation: Radiation and Diffraction - Set-up parameters			
Wavelength: L [m]		61.57	385.237
Wave frequency: [rad/s]		1	0.4
Wave height: [m]		2	2
Inlet: [Wavelengths]		2L	2L
Outlet: [Wavelengths]		2L	2L
Ymin: [Wavelengths]		0	0
Ymax: [Wavelengths]		3L	3L
Zmin: [m]		-36.98	-231.57
Zmax: [m]		36.98	36.98
Period time: [s]		6.28	15.70
Simulation time in periods		30	30
BC		X:GABC	X:GABC
		Ymin: Symmetry	Ymin: Symmetry
		Ymax: Wall	Ymax: Wall
		Zmin: Free-Slip	Zmin: Free-Slip
		Zmax: Wall	Zmax: Wall
Wave Probe Coordinates (Figure 6.9): X, Y, Zmin, Zmax	Line 1 (Red Line)	49.4, 0, -1.1, 36.98	49.4, 0, -1.1, 36.98
	Line 2 (Blue Line)	34.6, 0, -1.3, 36.98	34.6, 0, -1.3, 36.98
	Line 3 (Purple Line)	19.8, 0, -1.2, 36.98	19.8, 0, -1.2, 36.98

Table 6.7: Simulation Parameters - Radiation and Diffraction Studies

Figure 6.9: Wave probes located within the well dock for the results exportation and their coordinates are found in table 6.7

After conducting an independent investigation into the physical mechanisms, equation 6.1 was employed to analyze the amplitudes D_0, D_n, R_0, R_n. In this context, 'R' represents the amplitude emanating from Radiation, while 'D' signifies the amplitude associated with Diffraction. Additionally, the phases termed 'radiationphase' and 'diffractionphase' were also considered for the first five harmonic frequencies of both diffraction and radiation processes. The objective of this analysis was to determine whether a separate examination of radiation and diffraction, followed by their integration using Equation 6.1, is feasible. This feasibility of this approach was evaluated by comparing these findings with the experimental results presented in Chapter 4, which integrated both mechanisms from the beginning of the experiment.

$$\begin{aligned} fse = (D_0 + R_0) + \sum_{n=1}^{n=5} [(D_{\boldsymbol{n}} * cos(2\pi(\boldsymbol{n} * frequency * t + diffractionphase_{\boldsymbol{n}}/360))) + \\ (R_{\boldsymbol{n}} * cos(2\pi(\boldsymbol{n} * frequency * t + radiationphase_{\boldsymbol{n}}/360)))] \end{aligned} \tag{6.1}$$

6.3. Results

In this section, a detailed presentation of the results is provided. The analysis begins with the examination of the time-domain signal and its corresponding frequency domain representations for both radiation and diffraction. These results stem from data gathered at three different locations, as visually depicted in Figure 6.9. The focus of the investigation is on two specific wave frequencies: 0.4 and 1 rad/s.

Upon completion of this detailed analysis, the section transitions to a comparative study. This phase entails a juxtaposition of the experimental results with the summation of the diffraction and radiation studies as formulated in equation 6.1. The purpose of this comparison is to assess the agreement between the experimental data and the model that involves summing the independent mechanisms as proposed in equation 6.1.

6.3.1. Line1 - Free Surface Elevation at dock entrance for wave frequency 1 rad/s

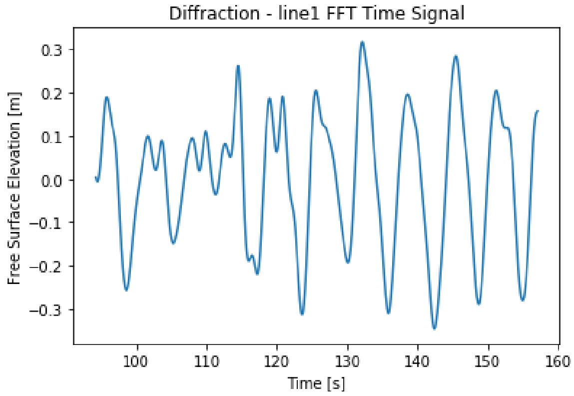

Figure 6.10: Time-domain signal illustrating the free surface elevation of the wave caused by diffraction.

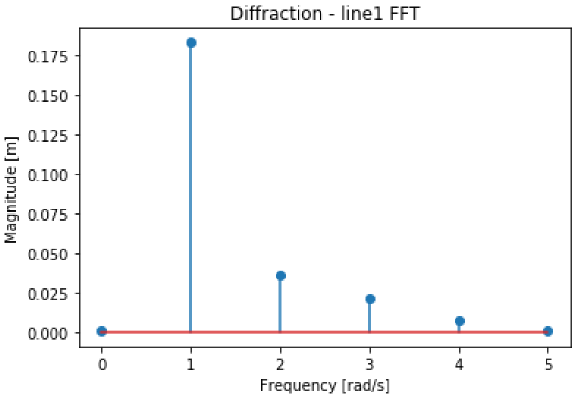

Figure 6.11: Fast Fourier Transformation analysis of the six Fourier components caused by diffraction

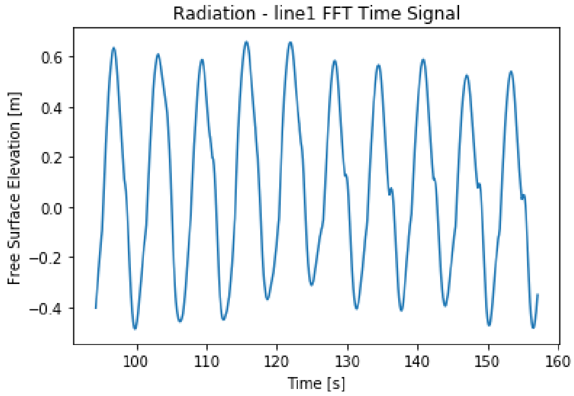

Figure 6.12: Time-domain signal illustrating the free surface elevation of the wave caused by radiation

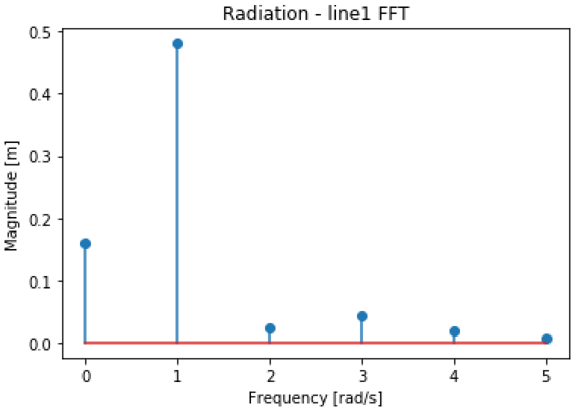

Figure 6.13: Fast Fourier Transformation analysis of the six Fourier components caused by radiation

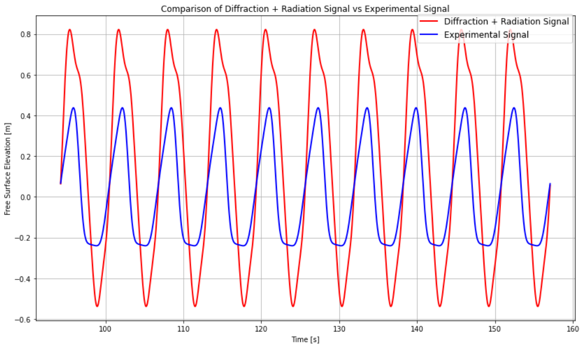

Figure 6.14: Comparison of Time-Domain Signal for Free Surface Elevation between the Experimental Model and the Combined Effects of Diffraction and Radiation Mechanisms

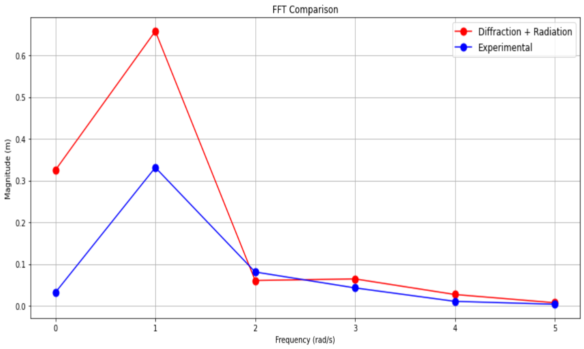

Figure 6.15: Comparison of the Fast Fourier Transformation Analysis for Six Fourier Components between the Experimental Model and the separate Addition of Diffraction and Radiation Mechanisms

6.3.2. Line2 - Free Surface Elevation at middle of ‘the dock for wave frequency 1 rad/s

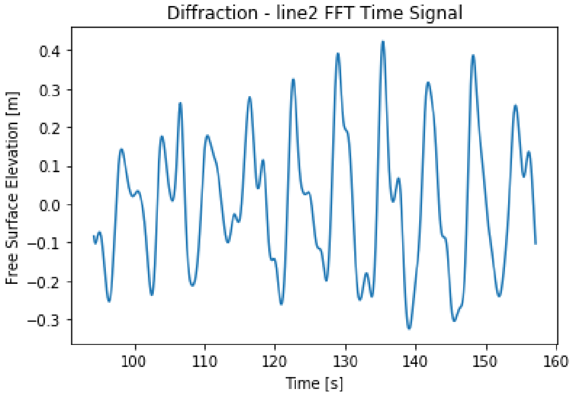

Figure 6.16: Time-domain signal illustrating the free surface elevation of the wave caused by diffraction

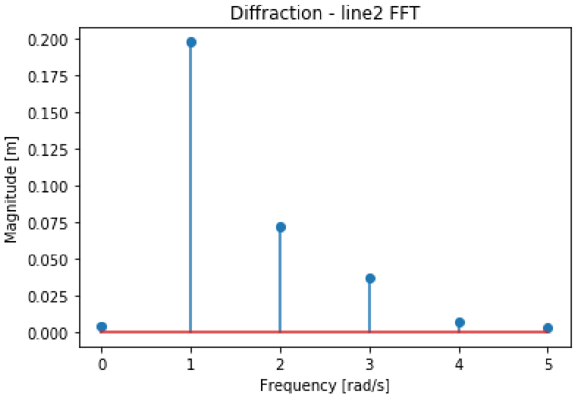

Figure 6.17: Fast Fourier Transformation analysis of the six Fourier components caused by diffraction

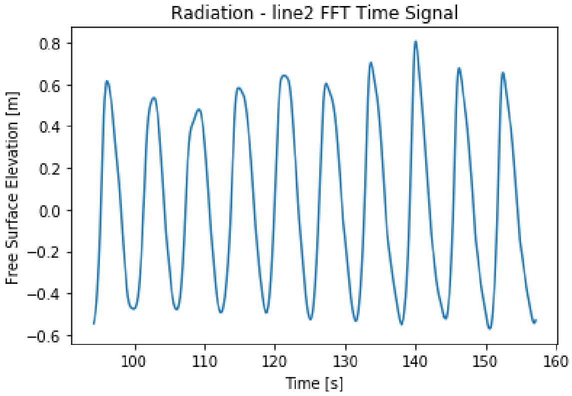

Figure 6.18: Time-domain signal illustrating the free surface elevation of the wave caused by radiation

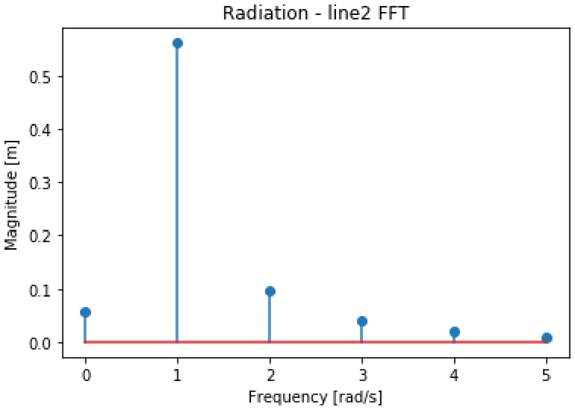

Figure 6.19: Fast Fourier Transformation analysis of the six Fourier components caused by radiation

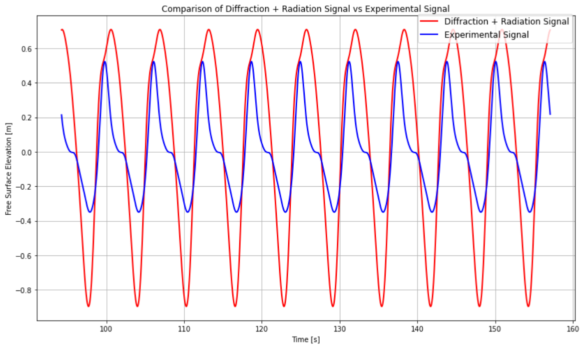

Figure 6.20: Comparison of Time-Domain Signal for Free Surface Elevation between the Numerical Model and the Combined Effects of Diffraction and Radiation Mechanisms

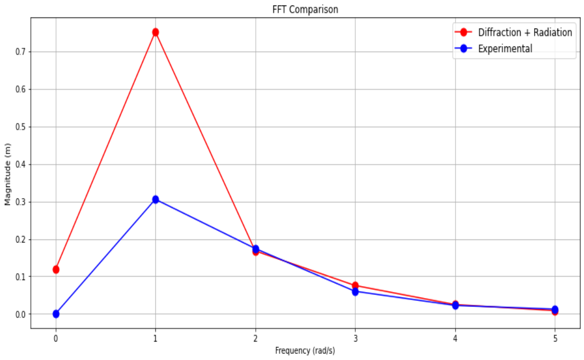

Figure 6.21: Comparison of the Fast Fourier Transformation Analysis for Six Fourier Components between the Experimental Model and the separate Addition of Diffraction and Radiation Mechanisms

6.3.3. Line3 - Free Surface Elevation at end of the dock for wave frequency 1 rad/s

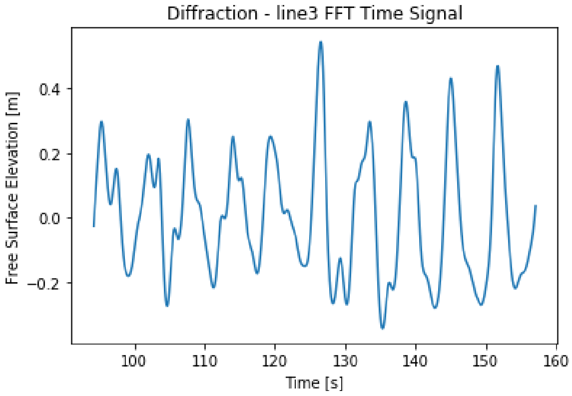

Figure 6.22: Time-domain signal illustrating the free surface elevation of the wave caused by diffraction

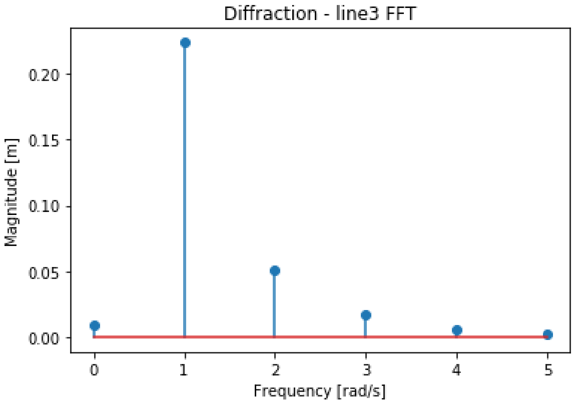

Figure 6.23: Fast Fourier Transformation analysis of the six Fourier components caused by diffraction

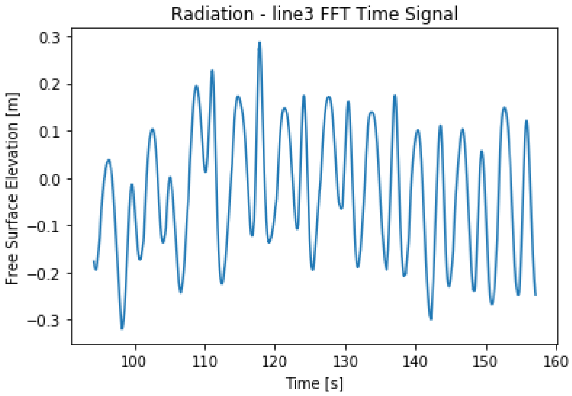

Figure 6.24: Time-domain signal illustrating the free surface elevation of the wave caused by radiation

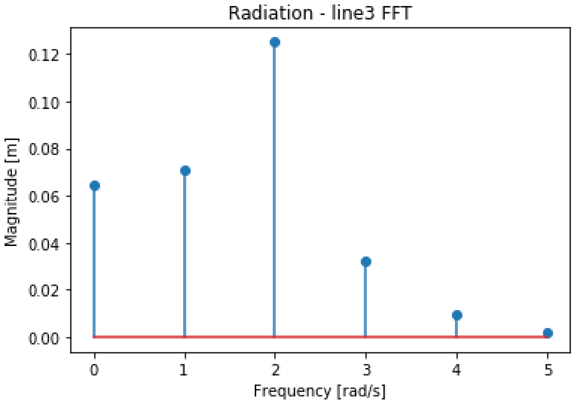

Figure 6.25: Fast Fourier Transformation analysis of the six Fourier components caused by radiation

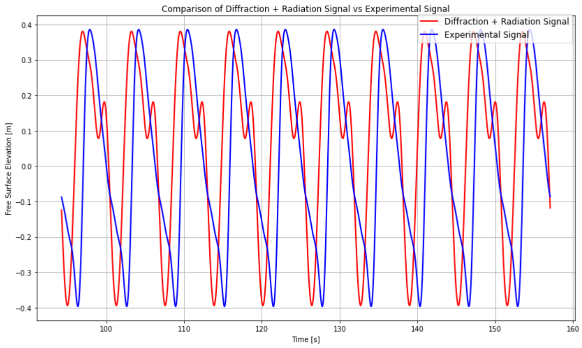

Figure 6.26: Comparison of Time-Domain Signal for Free Surface Elevation between the Numerical Model and the Combined Effects of Diffraction and Radiation Mechanisms

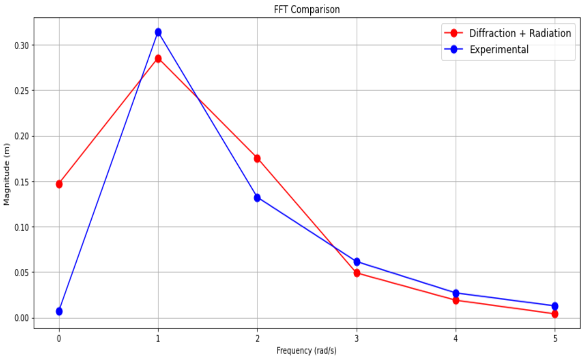

Figure 6.27: Comparison of the Fast Fourier Transformation Analysis for Six Fourier Components between the Experimental Model and the separate Addition of Diffraction and Radiation Mechanisms

6.3.4. Line1 - Free Surface Elevation at dock entrance for wave frequency 0.4 rad/s

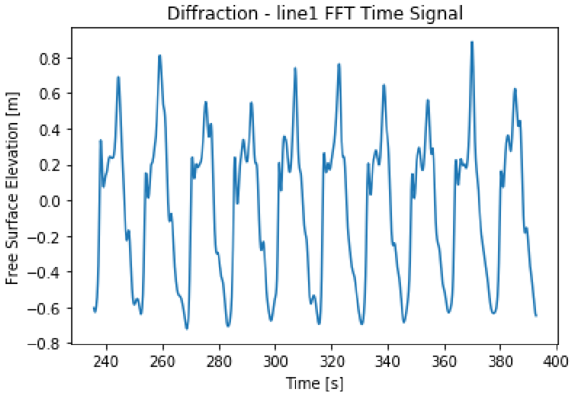

Figure 6.28: Time-domain signal illustrating the free surface elevation of the wave caused by diffraction

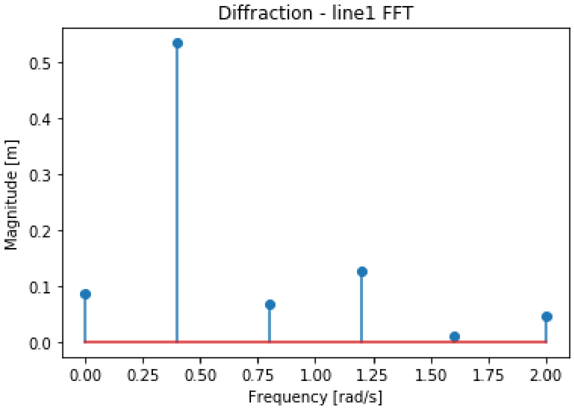

Figure 6.29: Fast Fourier Transformation analysis of the six Fourier components caused by diffraction

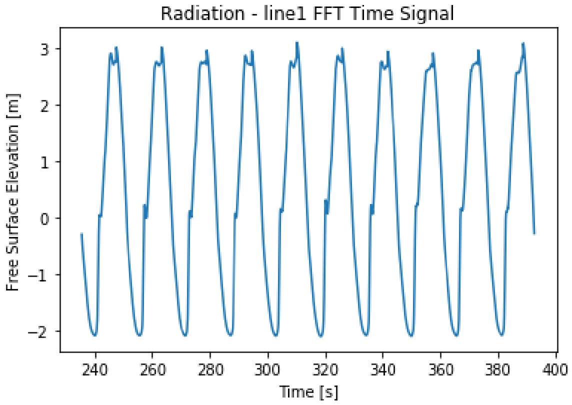

Figure 6.30: Time-domain signal illustrating the free surface elevation of the wave caused by radiation

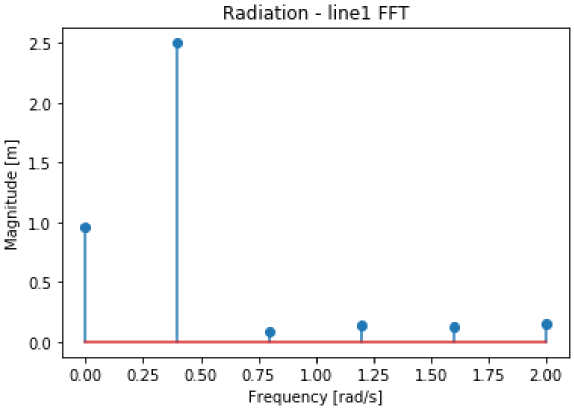

Figure 6.31: Fast Fourier Transformation analysis of the six Fourier components caused by radiation

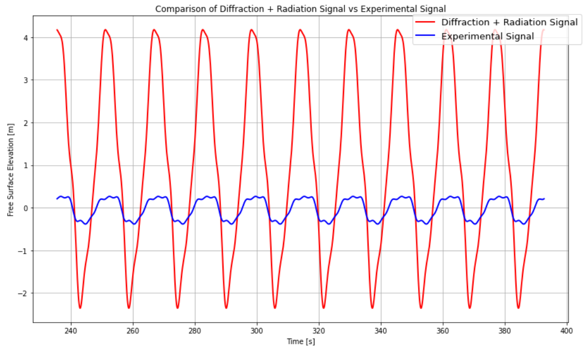

Figure 6.32: Comparison of Time-Domain Signal for Free Surface Elevation between the Numerical Model and the Combined Effects of Diffraction and Radiation Mechanisms

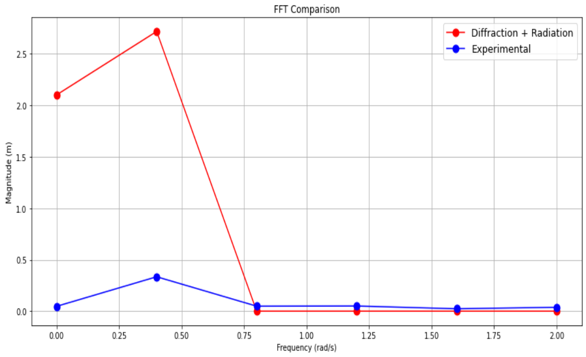

Figure 6.33: Comparison of the Fast Fourier Transformation Analysis for Six Fourier Components between the Experimental Model and the separate Addition of Diffraction and Radiation Mechanisms

6.3.5. Line2 - Free Surface Elevation at middle of the dock for wave frequency 0.4 rad/s

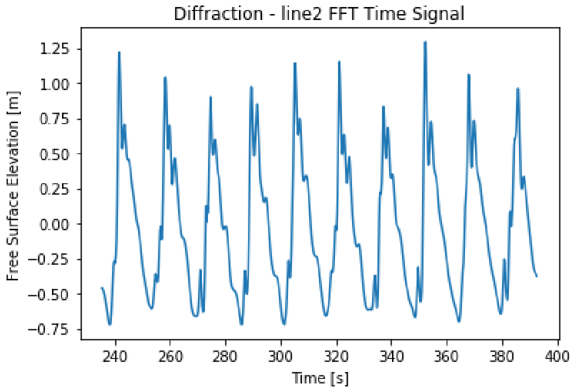

Figure 6.34: Time-domain signal illustrating the free surface elevation of the wave caused by diffraction

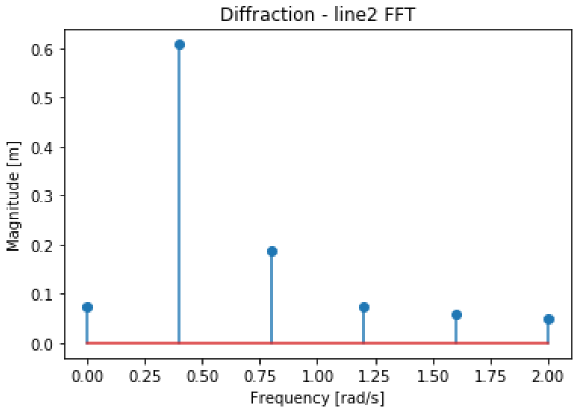

Figure 6.35: Fast Fourier Transformation analysis of the six Fourier components caused by diffraction

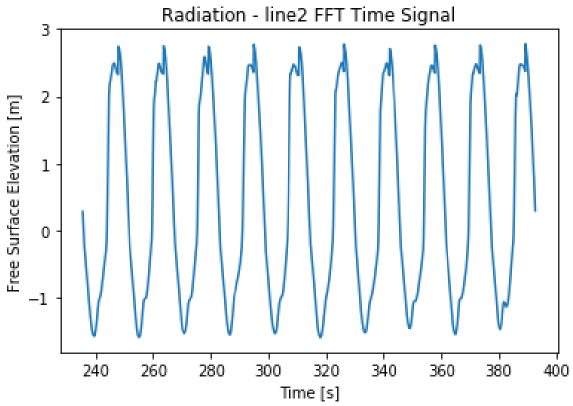

Figure 6.36: Time-domain signal illustrating the free surface elevation of the wave caused by radiation

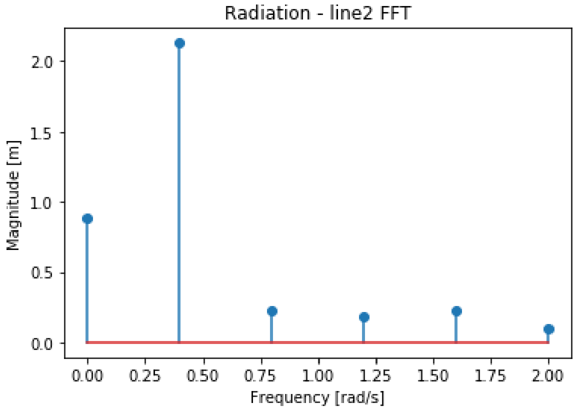

Figure 6.37: Fast Fourier Transformation analysis of the six Fourier components caused by radiation

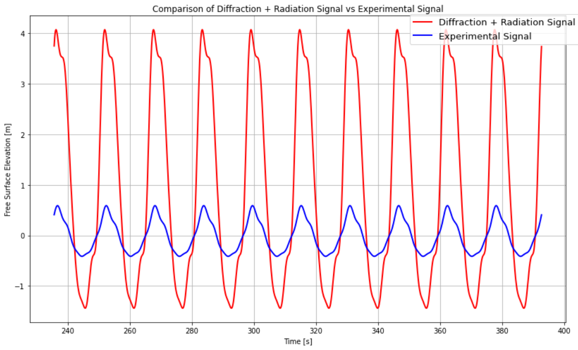

Figure 6.38: Comparison of Time-Domain Signal for Free Surface Elevation between the Numerical Model and the Combined Effects of Diffraction and Radiation Mechanisms

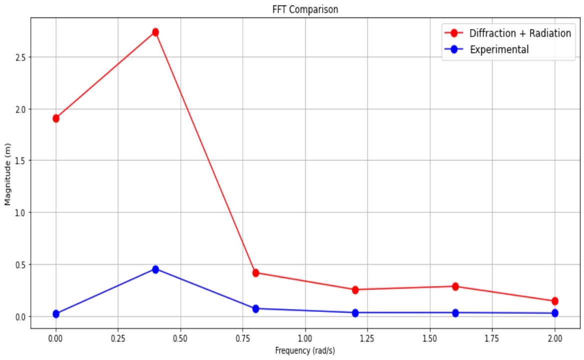

Figure 6.39: Comparison of the Fast Fourier Transformation Analysis for Six Fourier Components between the Experimental Model and the separate Addition of Diffraction and Radiation Mechanisms

6.3.6. Line3 - Free Surface Elevation at the end of the dock for wave frequency 0.4 rad/s

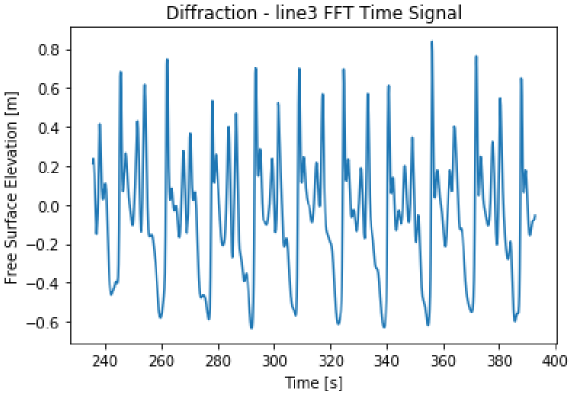

Figure 6.40: Time-domain signal illustrating the free surface elevation of the wave caused by diffraction

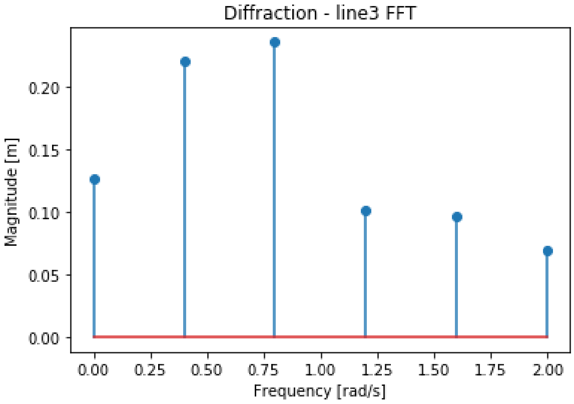

Figure 6.41: Fast Fourier Transformation analysis of the six Fourier components caused by diffraction

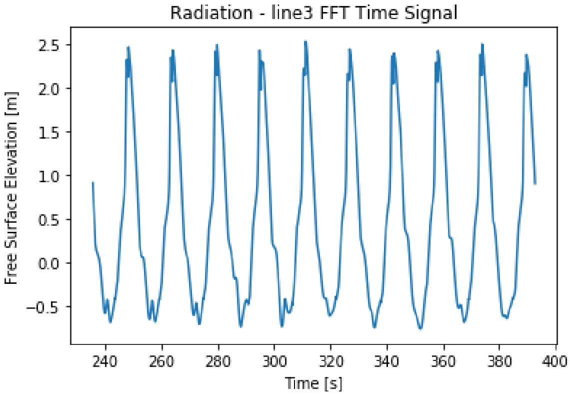

Figure 6.42: Time-domain signal illustrating the free surface elevation of the wave caused by radiation

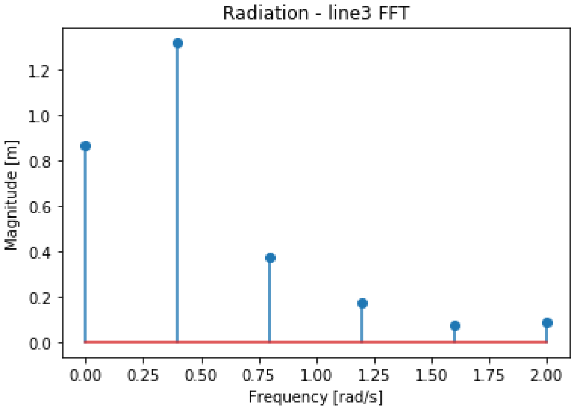

Figure 6.43: Fast Fourier Transformation analysis of the six Fourier components caused by radiation

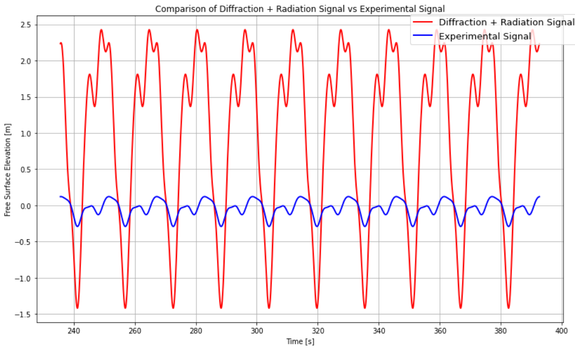

Figure 6.44: Comparison of Time-Domain Signal for Free Surface Elevation between the Numerical Model and the Combined Effects of Diffraction and Radiation Mechanisms

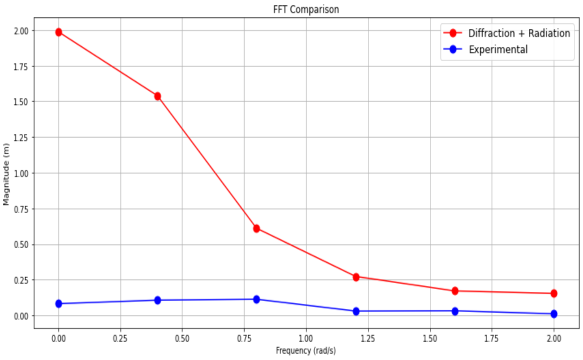

Figure 6.45: Comparison of the Fast Fourier Transformation Analysis for Six Fourier Components between the Experimental Model and the separate Addition of Diffraction and Radiation Mechanisms

6.4. Discussion

This model aims to discern the dominant physical mechanism, either radiation or diffraction, at various locations within the well dock. Additionally, it delves into how two different wave frequencies (0.4, 1 rad/s) affect these mechanisms. A cornerstone of this study is the addition of wave characteristics (phase, amplitude) derived from the independent analysis of physical mechanisms through equation 6.1. This is followed by a comparison with results from experiments where both mechanisms are integrated from the beginning of the experiment. This comparison is crucial for understanding the interplay and relative contributions of radiation and diffraction in the studied context. Additionally, it serves to evaluate the feasibility and effectiveness of independently studying these physical mechanisms.

Section 6.3.1 delineates the findings concerning the free surface elevation at the dock entrance for the short wavelength (1 rad/s). Specifically, Figures 6.10 - 6.13 present a comparative analysis between radiation and diffraction. From the frequency signal domain, it's apparent that radiation holds dominance over diffraction at the dock entrance. Furthermore, this section juxtaposes the combined results from diffraction and radiation with the experimental findings in figures 6.14 and 6.15. Although the behavior aligns with the experiments, a notable deviation is observed for the first two Fourier components (A0 and A1). This deviation stems from the linear summation of outcomes from the diffraction and radiation simulations, which overlooks the interactions between the two mechanisms.

Section 6.3.2 presents the results for the free surface elevation at the middle of the well dock for the short wavelength (1 rad/s), with figures 6.16 - 6.19 illustrating the comparative study between radiation and diffraction mechanisms. Analogous to Section 6.3.1, radiation is found to be more dominant than diffraction at this region. The combined results from diffraction and radiation are compared with the experimental results in Figures 6.20 and 6.21, showcasing similar behavior but with a minor deviation for Fourier component A0 and a significant one for A1. The reason of deviation is the same with the section 6.3.1, as the combined results neglect the interactions between the two mechanisms.

Section 6.3.3 shows the results for the free surface elevation at the end of the well dock for the short wavelength (1 rad/s), with Figures 6.22 - 6.25 elucidating the comparative analysis between radiation and diffraction. Unlike the previous sections, at the dock's end, radiation's influence diminishes, while diffraction remains at the same level with the other two regions of sections 6.3.1 and 6.3.2. The observed attenuation in wave height at the dock's end is attributed to the proximity of the vessel's center of gravity to this location. This suggests that the sections of the ship closest to the center of gravity experience reduced motion compared to the other two regions. The combined results from diffraction and radiation are juxtaposed with the experimental data in figures 6.26 and 6.27. The behavior remains stable, and the time-domain signal reveals that the two signals are almost identical. however, a significant deviation for the first Fourier component (A0) is observed. Similar to earlier sections, this deviation originates from the linear summation of results from diffraction and radiation, which overlooks the interaction between the two mechanisms.

Sections 6.3.4 to 6.3.6 elucidate the findings concerning the free surface elevation at different locations within the dock for the long wavelength (0.4 rad/s). These sections present a comparative analysis between radiation and diffraction, illustrating through Figures 6.28 - 6.45 that radiation is more dominant at all dock regions. However, the radiation results are nonphysically high for the first two Fourier components (A0 and A1), indicating a possible inaccuracy in capturing the radiation mechanism for large wavelengths. A notable deviation is observed when juxtaposing the combined results from diffraction and radiation with the experimental results. This deviation arises from the linear summation of outcomes from the diffraction and radiation simulations, which overlooks the interactions between the two mechanisms and considers the nonphysical wave height of the radiation mechanism. Moreover, figure 6.41 in section 6.3.6, located at the end of the well dock, elucidates that diffraction has less influence in relation to the other two regions in sections 6.3.4 and 6.3.5. Regarding the radiation mechanism at the same location, the behavior is analogous to section 6.3.3 of the short wavelength where the radiation effect decreases due to its location near the vessel's center of gravity and the reflections near the solid ramp.

Generally, the results offer a plethora of insights into the behavior and impact of radiation and diffraction within the well dock. Radiation stands out as the paramount mechanism. Particularly in areas near to the dock entrance (line 1), the radiation has the major influence and approaching the end of the dock (line 3) the radiation decreases. When considering diffraction, short waves (1 rad/s) exert a consistent effect throughout the well dock. For long waves (0.4 rad/s), however, diffraction's impact is more pronounced in the regions of the middle and dock entrance than at the end of the dock (line 3) and this is obvious because diffraction effects are most noticeable and significant near the dock's entrance.

When examining the importance of wavelength in this context, a clear trend emerges. As the wavelength increases from 61.57 meters (1 rad/s) to 385.237 meters (0.4 rad/s), both physical mechanisms - radiation and diffraction - become more pronounced in their effects. Among them, radiation sees a particularly heightened influence, which is unrealistically indicative of a possible inaccuracy in capturing the radiation mechanism in large wavelengths.

Lastly, the study explores the feasibility of treating the diffraction and radiation mechanisms independently, and then adding their individual outcomes for comparison with experiments where both mechanisms are integrated from the beginning. Upon reviewing the results, it becomes clear that this method of adding the physical mechanisms presents a behaviour similar with the experimental findings, albeit with a notable deviation observed for the first two Fourier components (A0 and A1). This deviation arises from the linear summation of outcomes from the diffraction and radiation simulations, which overlooks the interactions between the two mechanisms.

7

Full Model

This model, termed the "Full Model", was developed to address the second research question aimed at establishing a setup to capture the physical flow mechanisms within the vessel's well dock. Unlike the model discussed in Chapter 6, this model integrates both physical mechanisms from the onset of the simulation. The setup is grounded on the studies from the numerical model presented in Chapter 5. This encompasses wave generation using wave theory (5.4.1), the 3D geometry of the LPD ship (5.5), physical parameters (5.6), boundary conditions (5.7), studies on wave propagation (5.8), domain size (5.9), and the method of motion integration (5.10). The completion of the full model setup requires a grid study, which is elucidated in Section 7.1. Section 7.2 introduces the design modification made to the original geometry in the ramp region and explains the reason for such change. Section 7.3 outlines the input parameters for the simulation and specifies the exact locations of the wave probes for the results illustration. In Section 7.4, the depicted results of the full model with the solid ramp are compared with the model from Chapter 6, which incorporates the physical mechanisms using equation 6.1, with a discussion of the outcomes in Section 7.5. Section 7.6 compares the results of the Full Model with a solid ramp to the experimental results, with a subsequent discussion in Section 7.7. Additionally, Section 7.8 juxtaposes the Full Model with a solid ramp against the modified Full Model with a rack ramp, alongside the experimental tests. Lastly, Section 7.9 delves into a detailed discussion on the implications of the latest findings.

7.1. Grid study

The simulation parameters for the grid study can be found in table 7.1. These parameters remain the same with those used in the model of chapter 6.

Simulation	**Full Model Grid Study**
Wavelength: L [m]	61.57
Wave frequency: [rad/s]	1
Wave height: [m]	2
Inlet: [Wavelengths]	2L
Outlet: [Wavelengths]	2L
Ymin: [Wavelengths]	0
Ymax: [Wavelengths]	3L
Zmin: [m]	-36.98
Zmax: [m]	36.98
Period time: [s]	6.28
Simulation time in periods	25
BC	X:GABC
	Ymin: Symmetry
	Ymax: Wall
	Zmin: Free-Slip
	Zmax: Wall
Wave Probe Coordinates (Figures 5.19, 5.20): X, Y, Zmin, Zmax	49.4, 0, -1.1, 36.98

Table 7.1: Simulation Parameters - Grid Study of Full model

The grid study follows an approach similar to the model in Chapter 6. However, in contrast to the model of the previous chapter, this study combines both the diffraction and radiation analyses, aiming to develop a model which corresponds to the Model Tests presented in chapter 4. In this model configuration, stretching at the grid cells is applied both vertically and horizontally. The objective is to ensure smaller cells at the free surface relative to other cells. Table 7.2 displays a stretching ratio of 1.02, which means that adjacent cells are 2% larger than the central cell that is the cell in the middle of the whole geometry (1.02 times the size of the central cell). This approach achieves a finer grid near the free surface while still keeping the total number of computational cells to a manageable count.

Simulation Grid Study									
Grid Study 13									
Grid Levels	Extents			Grid Size			Cell Size		
	Coordinates in x-direction	Coordinates in y-direction	Coordinates in z-direction	Cells in x-direction	Cells in y-direction Stretching Ratio = 1.02	Cells in z-direction Stretching Ratio = 1.02	x	y larger cell smaller cell	z larger cell smaller cell
0	-203.70 198.4	0.00 184.71	-61.57 36.98	85	29	19	4.73	7.79 4.73	7.03 4.73
1	-203.70 198.4	0.00 184.71	-16.00 36.98	170	58	22	2.36	3.89 2.36	3.51 2.36
2	-80.522 75.199	0.00 12.5	-6.6 11.68	132	11	15	1.18	1.94 1.18	1.75 1.18
3	10. 110.0	0. 40.	-3.0 3.0	170	68	10	0.59	0.97 0.59	0.87 0.59
Grid Study 20									
Grid Levels	Extents			Grid Size			Cell Size		
	Coordinates in x-direction	Coordinates in y-direction	Coordinates in z-direction	Cells in x-direction	Cells in y-direction Stretching Ratio = 1.02	Cells in z-direction Stretching Ratio = 1.02	x	y larger cell smaller cell	z larger cell smaller cell
0	-203.70 198.4	0.00 184.71	-61.57 36.98	131	40	28	3.06	6.27 3.07	4.24 3.07
1	-203.70 198.4	0.00 184.71	-16.00 36.98	262	80	35	1.53	3.13 1.53	2.12 1.53
2	-80.522 75.199	0.00 12.5	-6.6 11.68	205	16	24	0.76	1.56 0.76	1.06 0.76
3	10. 110.0	0. 40.	-3.0 3.0	263	105	16	0.38	0.78 0.38	0.53 0.38

Simulation Grid Study									
Grid Study 30									
Grid Levels	Extents			Grid Size			Cell Size		
	Coordinates in x- direction	Coordinates in y- direction	Coordinates in z- direction	Cells in x- direction	Cells in y- direction Stretching Ratio = 1.02	Cells in z- direction Stretching Ratio = 1.02	x	y larger cell smaller cell	z larger cell smaller cell
0	-203.70 198.4	0.00 184.71	-61.57 36.98	196	52	39	2.05	5.52 2.05	3.20 2.05
1	-203.70 198.4	0.00 184.71	-16.00 36.98	392	104	52	1.02	2.76 1.02	1.60 1.02
2	-80.522 75.199	0.00 12.5	-6.6 11.68	305	24	36	0.51	1.38 0.51	0.80 0.51
3	10. 110.0	0. 40.	-3.0 3.0	400	160	24	0.25	0.69 0.25	0.40 0.25

Table 7.2: Detail Analysis of Grid Study (Grid and Cell Size)

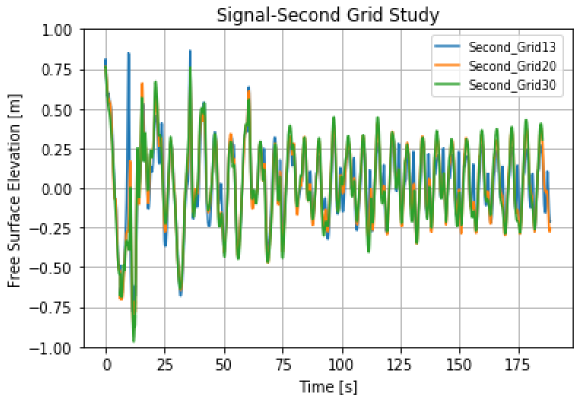

Figure 7.1: Comparison of the Time-Domain signal of Free Surface Elevation of the Wave Across Three Different Grids

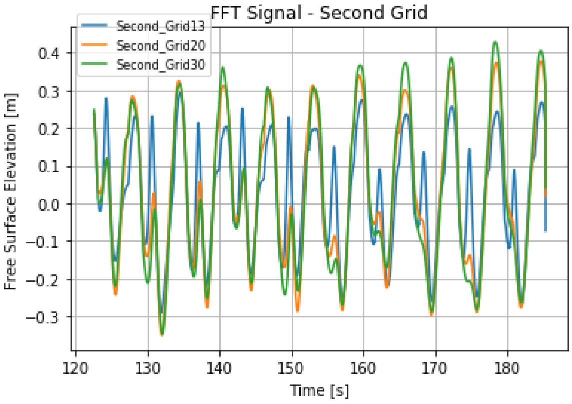

Figure 7.2: Comparison of the Last 10 Periods from the Total Time-Domain Signal for Free Surface Elevation of the Wave Across Three Different Grids

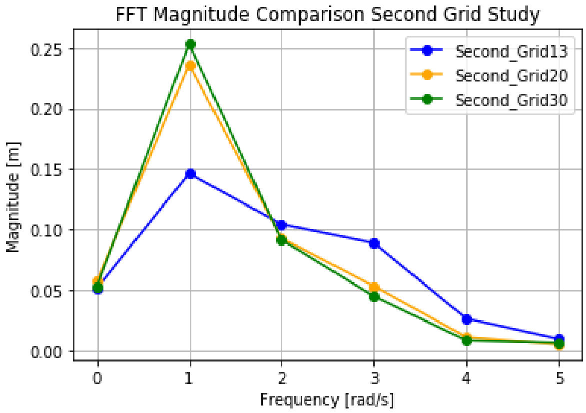

Figure 7.3: Comparison of the Fast Fourier Transformation Analysis for Six Fourier Components Across Three Different Grids

The results are presented in table 7.3 and illustrated in plot 7.4. The methodology employed is the same as that used in the model described in Chapter 6. Using the wave probe, as referenced in figures 5.19 and 5.20, the relative wave height over time is charted, as can be seen in Figure 7.1. From the total time-domain signal, the last 10 periods were selected, during which the signal attains a quasi-steady state. The wave signal is depicted in Figure 7.2. This time-domain data undergoes a transformation into the frequency domain using the Fast Fourier Transformation, as demonstrated in Figure 7.3. This transformation highlights the first six Fourier components (0 to 5). Emphasis is given to a detailed comparison of the three grid resolutions, particularly focusing on the second Fourier component (1). Both table 7.3 and plot 7.4 exhibit the free surface elevation of this second component, derived from the Fast Fourier Transformation. Upon close examination of the results, a minor difference is noticeable between the medium grid and the Richardson extrapolation, approximately equating to 1 centimeter. This small difference underscores the accuracy of the medium grid, endorsing it as an appropriate selection. Thus, to optimize the balance between computational time, accuracy, and efficiency, the medium grid was chosen for further analyses.

Grid	Normalized Grid Spacing h	Free Surface Elevation [m]
Richardson Extrapolate	0	**0.2520**
Fine - Second Grid Study 30	1	0.2513
Medium - Second Grid Study 20	1.5	0.2416
Coarse - Second Grid Study 13	2.25	0.1490

Table 7.3: Convergence Grid Study

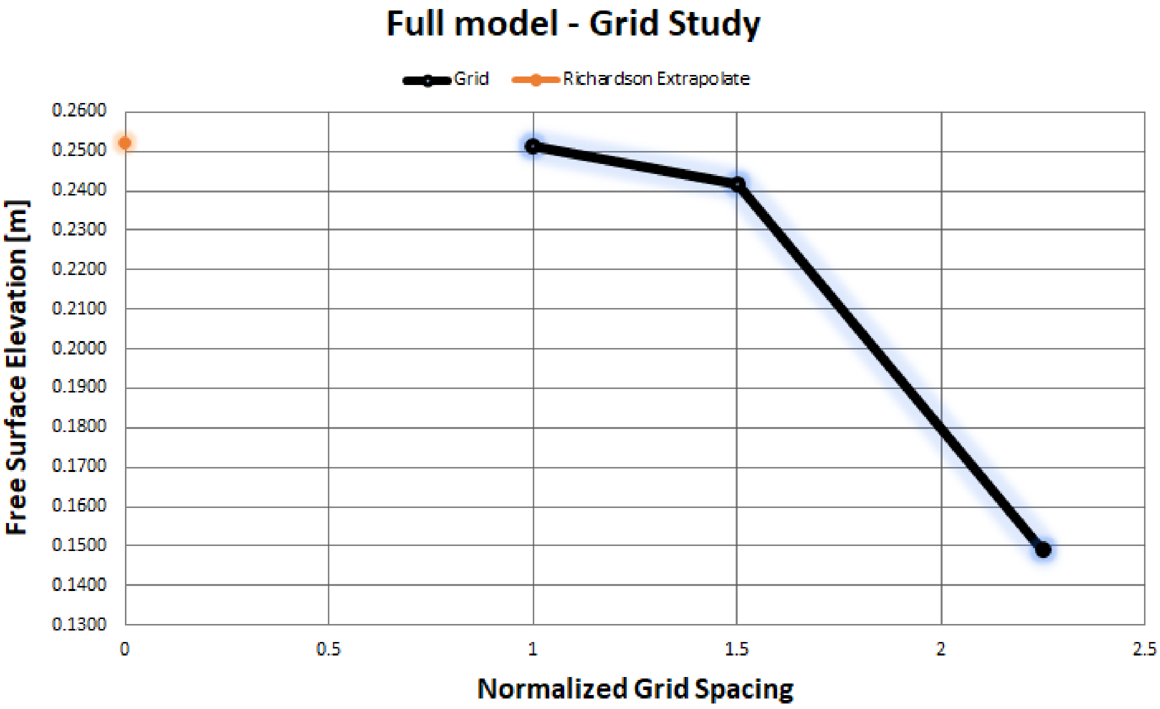

Figure 7.4: Plot of Convergence Grid Study

7.2. Design Modification at the ramp region

Utilizing a rack ramp in place of a solid ramp is aimed at mitigating the reflection of waves caused by incoming waves in an LPD vessel. The presence of reflective waves in the well dock of an LPD can pose challenges. When a solid ramp is present, incoming waves can reflect, potentially making it difficult for smaller vessels to safely enter or exit the well dock. In contrast, a rack ramp, characterized by its perforated design, seeks to curtail this problem, by allowing part of the wave energy to pass through and dissipate rather than reflect back. The following paragraph elaborates on the two options.

A solid Ramp acts as a barrier. When a wave hits the solid structure, the energy has two main paths: reflection and absorption. In most cases, a significant portion of the energy is reflected back into the well dock, leading to possible operational challenges. Rack Ramp is designed with perforations as illustrated in figures 7.6 and 7.7 and its dimensions are provided in table 7.4. Instead of entirely reflecting or absorbing the wave's energy, a rack ramp allows some of it to pass through. This can effectively dissipate the wave energy and reduce the magnitude of reflections.

Rack Ramp - Bar Dimensions	
Length [m]	0.25
Width [m]	14.96
Height [m]	0.1
Number of Bars [-]	24
Distance between Bars [m]	0.25

Table 7.4: Rack Ramp Dimensions

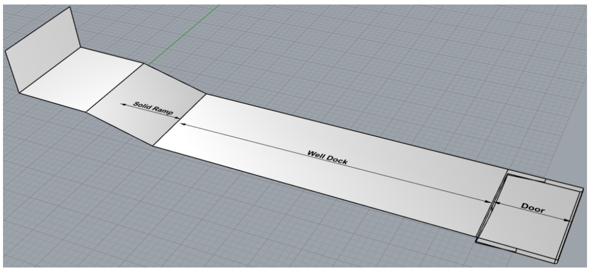

Figure 7.5: Original well dock arrangement with solid ramp

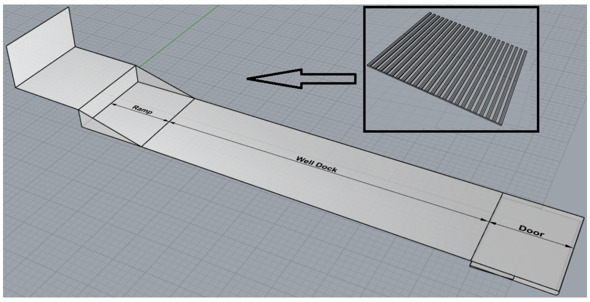

Figure 7.6: Modification of the ramp region to integrate the rack ramp

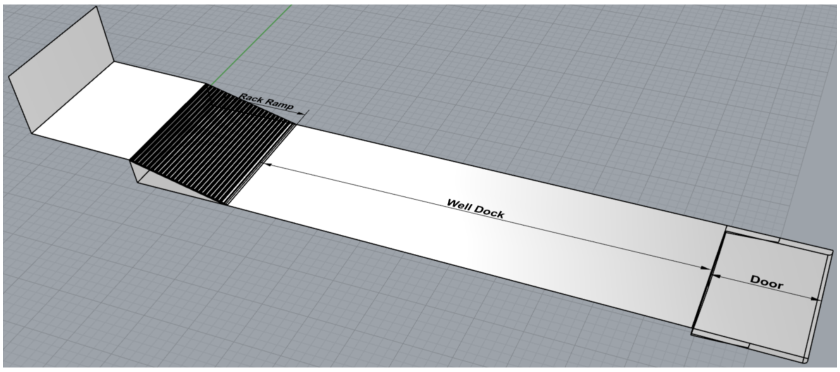

Figure 7.7: Well dock with rack ramp

7.3. Simulation method

Upon completing the grid study of the full model, the subsequent step entailed presenting the design modification at the ramp region, along with the rationale of this change. This section outlines the input parameters for the simulations of the full model, showcasing both the original LPD geometry with the solid ramp and the modified geometry with the rack ramp. These models share the same input parameters, and their post-processing is based on three specified locations within the well dock, as illustrated in figure 7.8. Table 7.5 provides the coordinates of these locations and also lists the simulation parameters for different wave frequencies. Furthermore, table 7.5 addresses the concept of Zmin, the water depth, important in ensuring the assumption of deep water conditions in the model. In scenarios where the water depth, h, is more than half the wavelength, λ, so: $h/\lambda > 1/2$ or $\lambda/h < 2$, the wave behavior is not influenced by the bottom topography [11]. For this model, the ratio $h/\lambda = 0.6$ was chosen for computational efficiency and to stay within the deep water regime. The following section depicts the results of the two full models (solid ramp and rack ramp) in comparison with the experiments and the model discussed in chapter 6, which incorporates the original LPD geometry with the solid ramp.

Figure 7.8: Wave probes located within the well dock for the results exportation and their coordinates are found in table 7.5

Simulation		**Full Model - Set-up parameters**		
Wavelength: L [m]		61.57	125.79	385.237
Wave frequency: [rad/s]		1	0.7	0.4
Wave height: [m]		2	2	2
Inlet: [Wavelengths]		2L	2L	2L
Outlet: [Wavelengths]		2L	2L	2L
Ymin: [Wavelengths]		0	0	0
Ymax: [Wavelengths]		3L	3L	3L
Zmin: [m]		-36.98	-75.9	-231.57
Zmax: [m]		36.98	36.98	36.98
Period time: [s]		6.28	8.98	15.70
Simulation time in periods		35	35	35
BC		X:GABC	X:GABC	X:GABC
		Ymin: Symmetry	Ymin: Symmetry	Ymin: Symmetry
		Ymax: Wall	Ymax: Wall	Ymax: Wall
		Zmin: Free-Slip	Zmin: Free-Slip	Zmin: Free-Slip
		Zmax: Wall	Zmax: Wall	Zmax: Wall
Wave Probe Coordinates: X, Y, Zmin, Zmax (Figure 7.8)	Line 1 (Red Line)	49.4, 0, -1.1, 36.98	49.4, 0, -1.1, 36.98	49.4, 0, -1.1, 36.98
	Line 2 (Blue Line)	34.6, 0, -1.3, 36.98	34.6, 0, -1.3, 36.98	34.6, 0, -1.3, 36.98
	Line 3 (Purple Line)	19.8, 0, -1.2, 36.98	19.8, 0, -1.2, 36.98	19.8, 0, -1.2, 36.98

Table 7.5: Simulation parameters for original Full model (solid ramp) and modified Full model (rack ramp)

7.4. Results - Full Model with Solid Ramp vs. Diffraction + Radiation

Within this section, a detailed presentation of the results of the full model with solid ramp against the combined results of radiation and diffraction as presented in chapter 6 is provided. Specifically, the time-domain signal and its corresponding frequency domain for both models are illustrated. These results are coming from three different locations all of which are visually represented in Figure 7.8, and are examined across two distinct wave frequencies: 0.4 and 1 rad/s.

7.4.1. Line1 - Free Surface Elevation at dock entrance : Full Model with Solid Ramp vs. Diffraction + Radiation at 1 rad/s

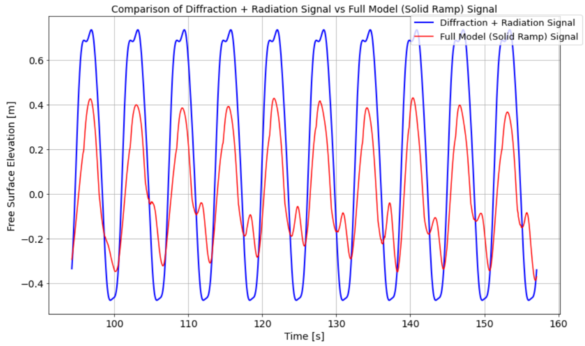

Figure 7.9: Comparison of Time-Domain Signal for Free Surface Elevation between the Full Model with Solid Ramp and the separate Addition of Diffraction and Radiation Mechanisms

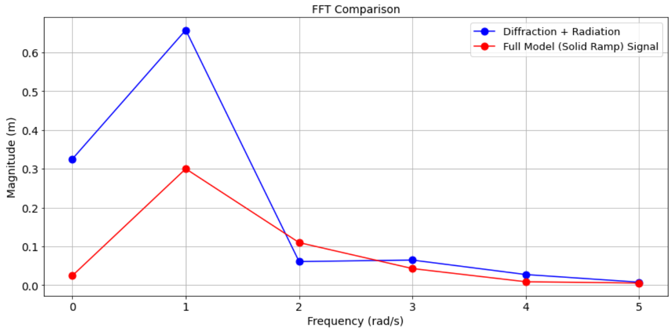

Figure 7.10: Comparison of the Fast Fourier Transformation Analysis for Six Fourier Components between Full Model with Solid Ramp and the separate Addition of Diffraction and Radiation Mechanisms

7.4.2. Line2 - Free Surface Elevation at middle of the dock : Full Model with Solid Ramp vs. Diffraction + Radiation at 1 rad/s

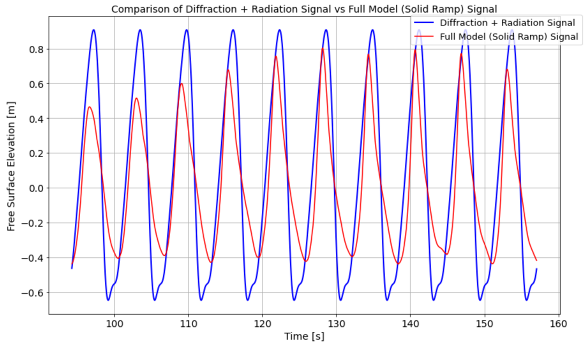

Figure 7.11: Comparison of Time-Domain Signal for Free Surface Elevation between the Full Model with Solid Ramp and the separate Addition of Diffraction and Radiation Mechanisms

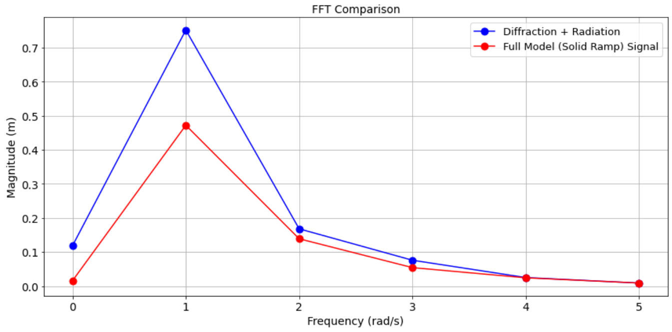

Figure 7.12: Comparison of the Fast Fourier Transformation Analysis for Six Fourier components between Full Model with Solid Ramp and the separate Addition of Diffraction and Radiation Mechanisms

7.4.3. Line3 - Free Surface Elevation at end of the dock: Full Model with Solid Ramp vs. Diffraction + Radiation at 1 rad/s

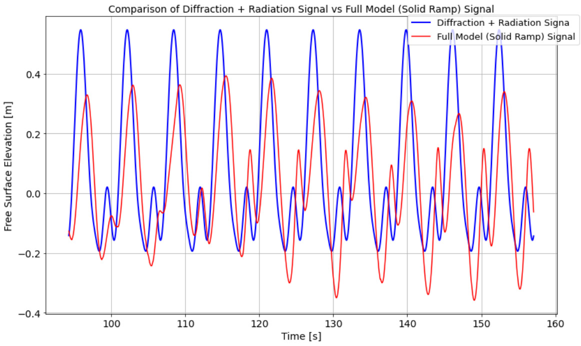

Figure 7.13: Comparison of Time-Domain Signal for Free Surface Elevation between the Full Model with Solid Ramp and the separate Addition of Diffraction and Radiation Mechanisms

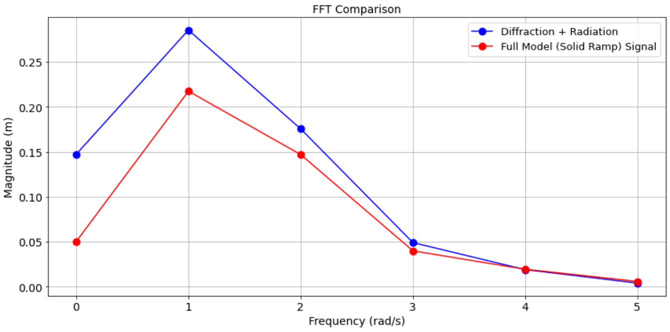

Figure 7.14: Comparison of the Fast Fourier Transformation Analysis for Six Fourier components between Full Model with Solid Ramp and the separate Addition of Diffraction and Radiation Mechanisms

7.4.4. Line1 - Free Surface Elevation at dock entrance: Full Model with Solid Ramp vs. Diffraction + Radiation at 0.4 rad/s

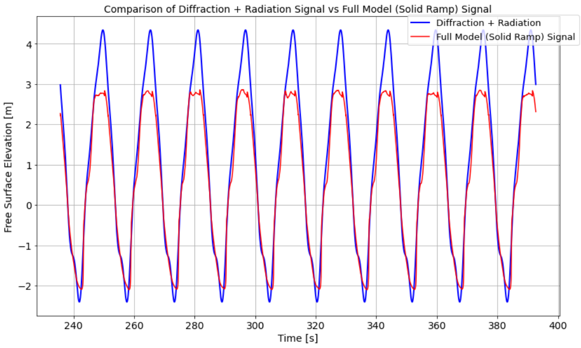

Figure 7.15: Comparison of Time-Domain Signal for Free Surface Elevation between the Full Model with Solid Ramp and the separate Addition of Diffraction and Radiation Mechanisms

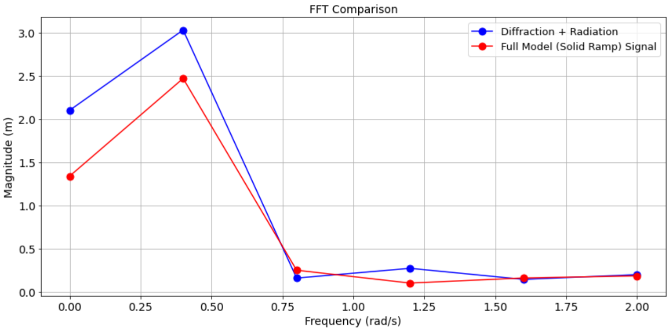

Figure 7.16: Comparison of the Fast Fourier Transformation Analysis for Six Fourier Components between Full Model with Solid Ramp and the separate Addition of Diffraction and Radiation Mechanisms

7.4.5. Line2 - Free Surface Elevation at middle of the dock: Full Model with Solid Ramp vs. Diffraction + Radiation at 0.4 rad/s

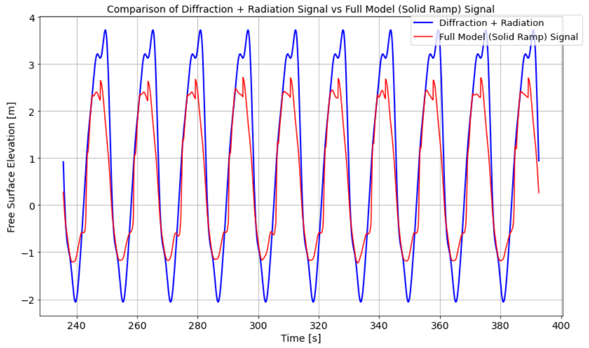

Figure 7.17: Comparison of Time-Domain Signal for Free Surface Elevation between the Full Model with Solid Ramp and the separate Addition of Diffraction and Radiation Mechanisms

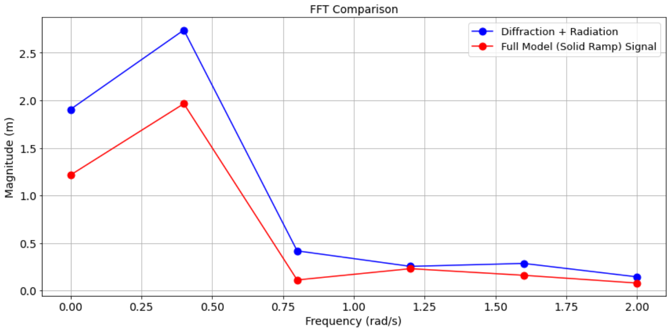

Figure 7.18: Comparison of the Fast Fourier Transformation Analysis for Six Fourier Components between Full Model with Solid Ramp and the separate Addition of Diffraction and Radiation Mechanisms

7.4.6. Line3 - Free Surface Elevation at end of the dock: Full Model with Solid Ramp vs. Diffraction + Radiation at 0.4 rad/s

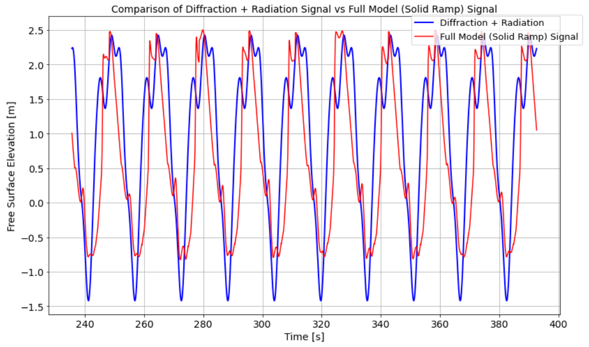

Figure 7.19: Comparison of Time-Domain Signal for Free Surface Elevation between the Full Model with Solid Ramp and the separate adding of Diffraction and Radiation Mechanisms

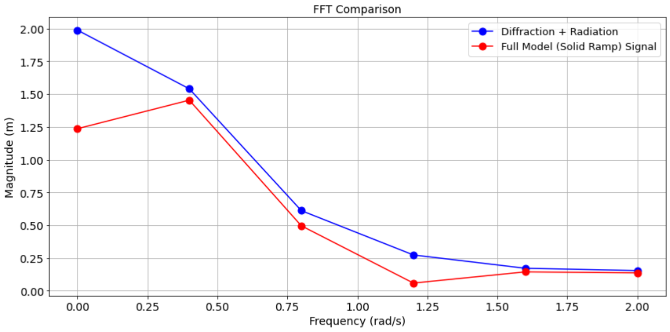

Figure 7.20: Comparison of the Fast Fourier Transformation Analysis for Six Fourier components between Full Model with Solid Ramp and the separate Addition of Diffraction and Radiation Mechanisms

7.5. Discussion - Full Model with Solid Ramp vs. Diffraction + Radiation

The full model captures both physical mechanisms - radiation and diffraction - from the outset of the simulation, contrasting it with the model from Chapter 6, which calculates the results for radiation and diffraction separately and then adds them together using Equation 6.1. The primary objective is to assess the feasibility of simplifying the problem by tackling the mechanisms independently. This examination is conducted at two different wave frequencies (0.4, 1 rad/s).

Section 7.4.1 delves into the results concerning the free surface elevation at the dock entrance for the short wavelength (1 rad/s), as depicted in Figures 7.9 and 7.10. It becomes evident that the behavior of the separate adding of the mechanisms is the same with the full model, albeit with a higher free surface elevation. The deviation, particularly more pronounced in the frequency signal domain, is observed for Fourier components A0 and A1. This deviation is attributed to the linear summation of the diffraction and radiation simulations, which overlooks their interactions. According to equation 6.1, constructive interference is implied at the dock entrance. however, the full model suggests a destructive interference scenario due to the phase difference between reflected and incoming waves.

Section 7.4.2 presents the analysis for the free surface elevation at the middle of the dock, as depicted in Figures 7.11 and 7.12. Similar to Section 7.4.1, the separate addition of mechanisms fits with the behavior of the full model. The deviation is primarily for Fourier component A1 and less for the component A0.

Section 7.4.3 explores the free surface elevation at the end of the dock, as showcased in Figures 7.13 and 7.14. The models present a similar behavior with the deviation being more pronounced for Fourier components A0 and A1.

Sections 7.4.4 to 7.4.6 show the findings concerning the free surface elevation at different locations within the dock for the long wavelength (0.4 rad/s), contrasting the full model with a solid ramp against the separate addition of diffraction and radiation mechanisms through Figures 7.15 - 7.20. From the figures, it is clear that the results exhibit similar trend, except at the location at the end of the dock which is noticeable from the frequency domain signal for Fourier component A0 in figure 7.20. The deviation, more pronounced in the frequency signal domain, is observed for Fourier components A0 and A1. The deviation follows a similar pattern as discussed in earlier sections, underscoring the significance of capturing the interactions between mechanisms for precise modeling.

In all sections, the deviation for Fourier components (A0 and A1) emanates from the linear summation approach, which fails to account for the interactions between the diffraction and radiation mechanisms. This trend underlines the importance of considering these interactions for a more accurate representation of the physical phenomena occurring within the dock.

7.6. Results - Full Model with Solid Ramp vs. Experimental Results

In this section, a comprehensive presentation of the results from the full model with a solid ramp is provided, juxtaposed against the experimental results as detailed in Chapter 4. Specifically, both the time-domain signals and their corresponding frequency domain representations for both models are illustrated. These results are coming from three different locations all of which are visually represented in Figure 7.8, and are examined across three distinct wave frequencies: 0.4, 0.7 and 1 rad/s.

7.6.1. Line1 - Free Surface Elevation at dock entrance: Full Model with Solid Ramp vs. Experimental Results at 1 rad/s

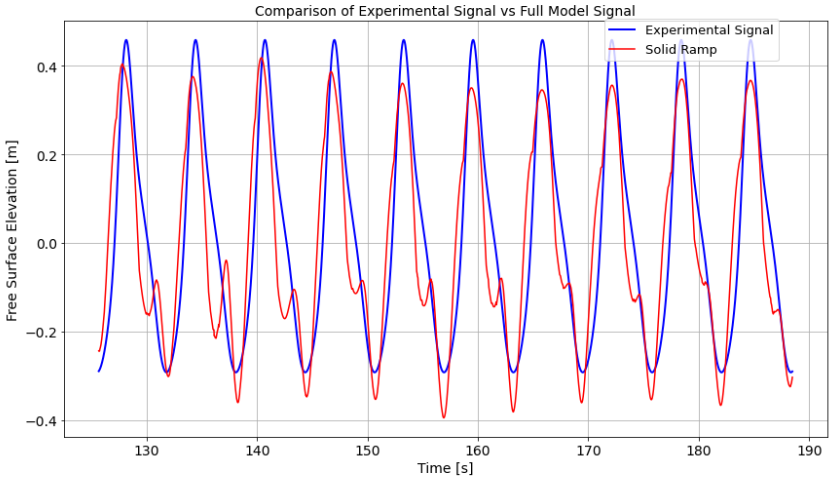

Figure 7.21: Comparison of Time-Domain Signal for Free Surface Elevation between the Full Model with Solid Ramp and Experimental Model

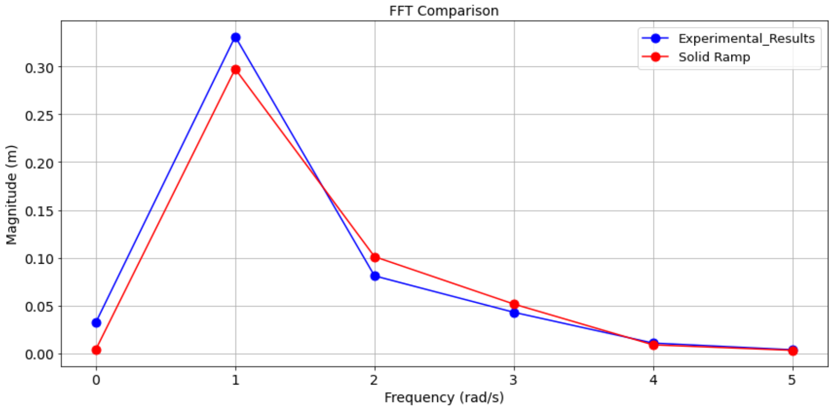

Figure 7.22: Comparison of the Fast Fourier Transformation Analysis for Six Fourier Components between the Full Model with Solid Ramp and Experimental Model

7.6.2. Line2 - Free Surface Elevation at middle of the dock for wave frequency 1 rad/s

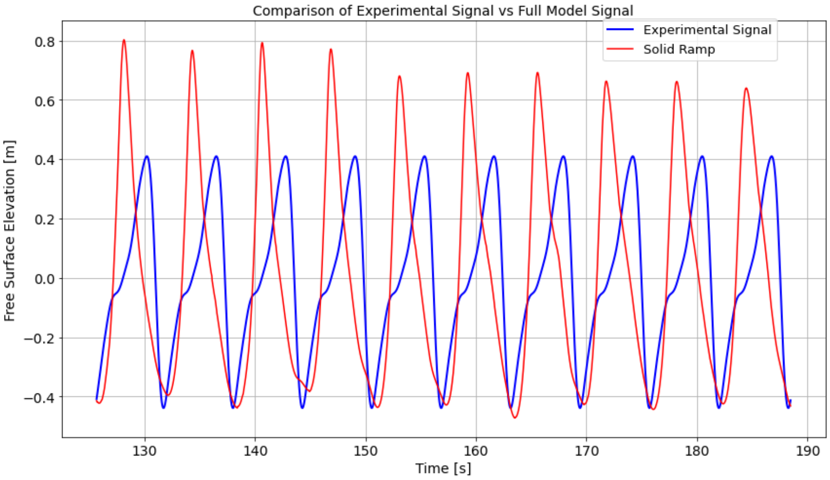

Figure 7.23: Comparison of Time-Domain Signal for Free Surface Elevation between the Full Model with Solid Ramp and Experimental Model

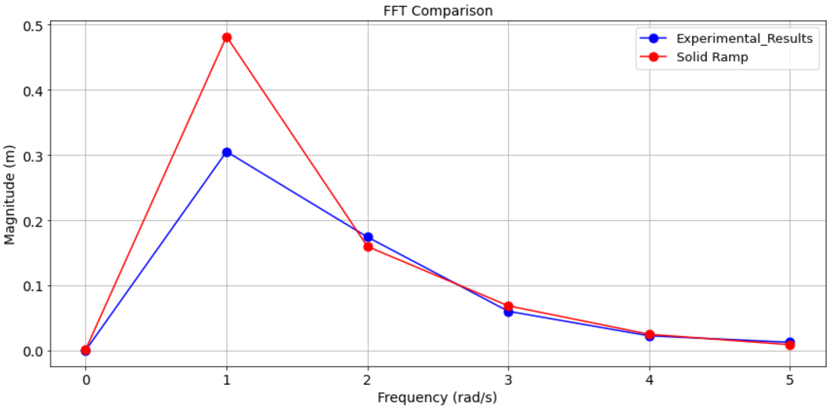

Figure 7.24: Comparison of the Fast Fourier Transformation Analysis for Six Fourier Components between the Full Model with Solid Ramp and Experimental Model

7.6.3. Line3 - Free Surface Elevation at end of the well dock for wave frequency 1 rad/s

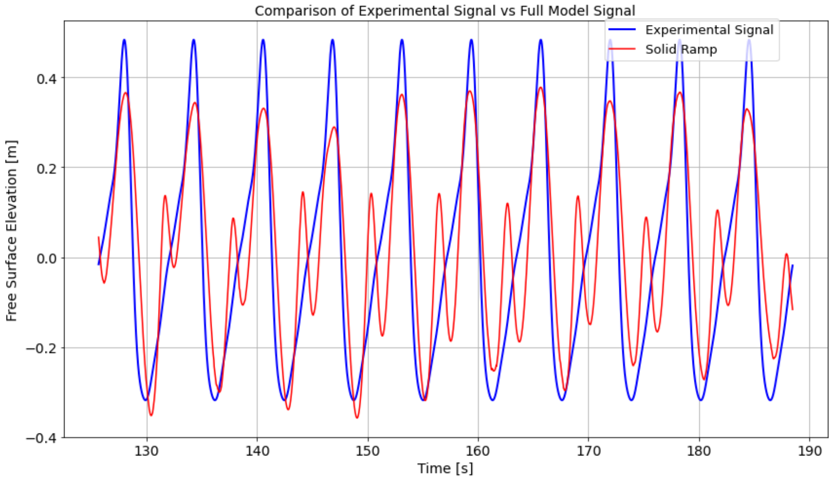

Figure 7.25: Comparison of Time-Domain Signal for Free Surface Elevation between the Full Model with Solid Ramp and Experimental Model

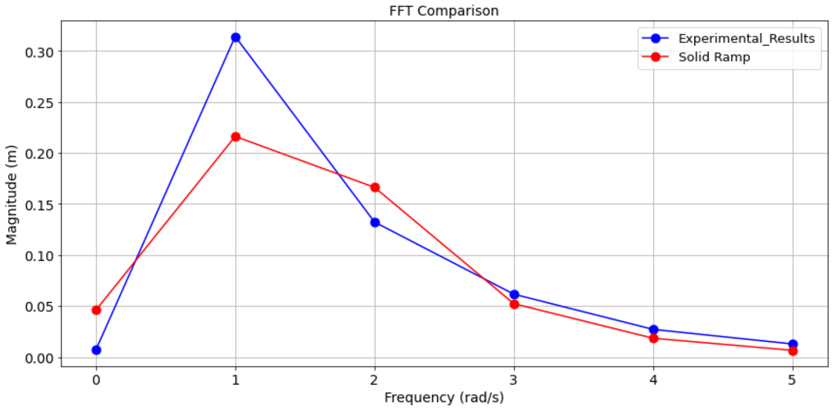

Figure 7.26: Comparison of the Fast Fourier Transformation Analysis for Six Fourier Components between the Full Model with Solid Ramp and Experimental Model

7.6.4. Line1 - Free Surface Elevation at dock entrance for wave frequency 0.7 rad/s

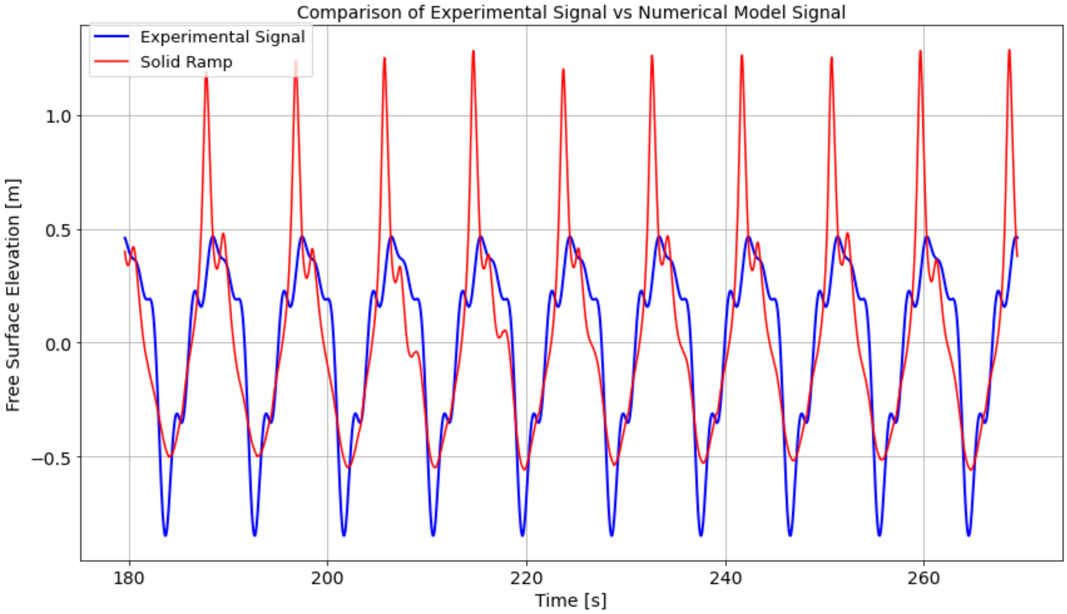

Figure 7.27: Comparison of Time-Domain Signal for Free Surface Elevation between the Full Model with Solid Ramp and Experimental Model

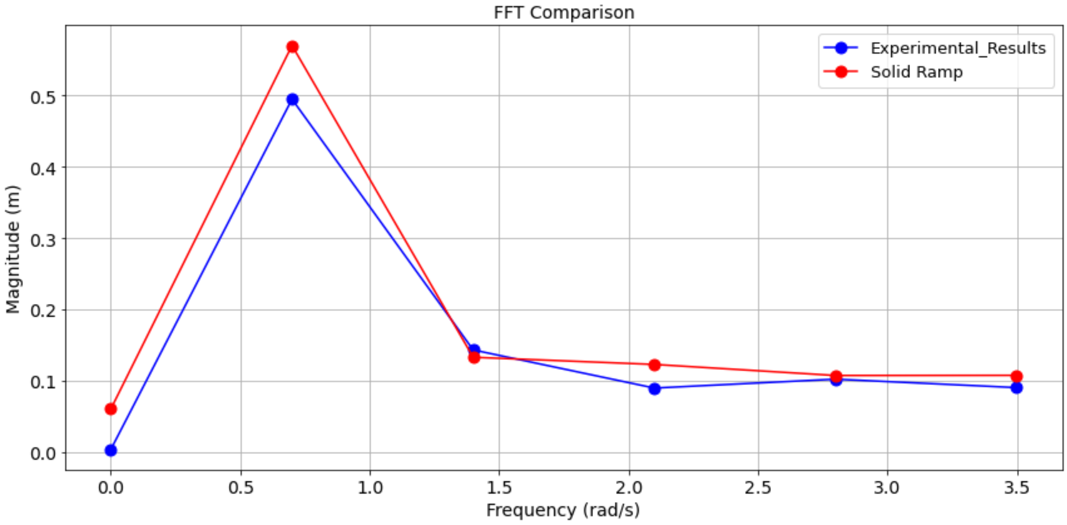

Figure 7.28: Comparison of the Fast Fourier Transformation Analysis for Six Fourier Components between the Full Model with Solid Ramp and Experimental Model

7.6.5. Line2 - Free Surface Elevation at middle of the well dock for wave frequency 0.7 rad/s

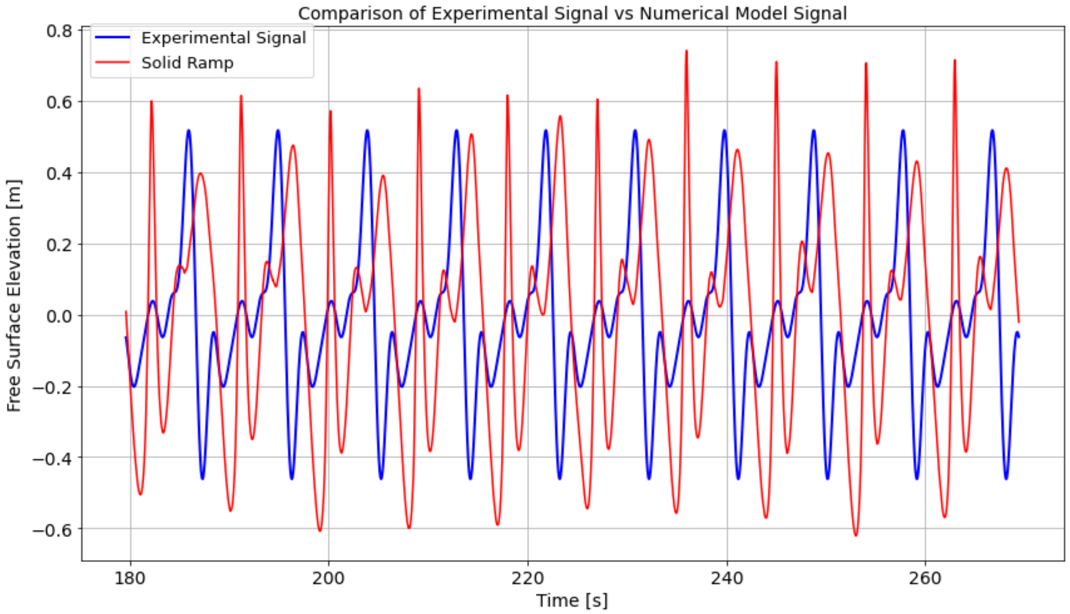

Figure 7.29: Comparison of Time-Domain Signal for Free Surface Elevation between the Full Model with Solid Ramp and Experimental Model

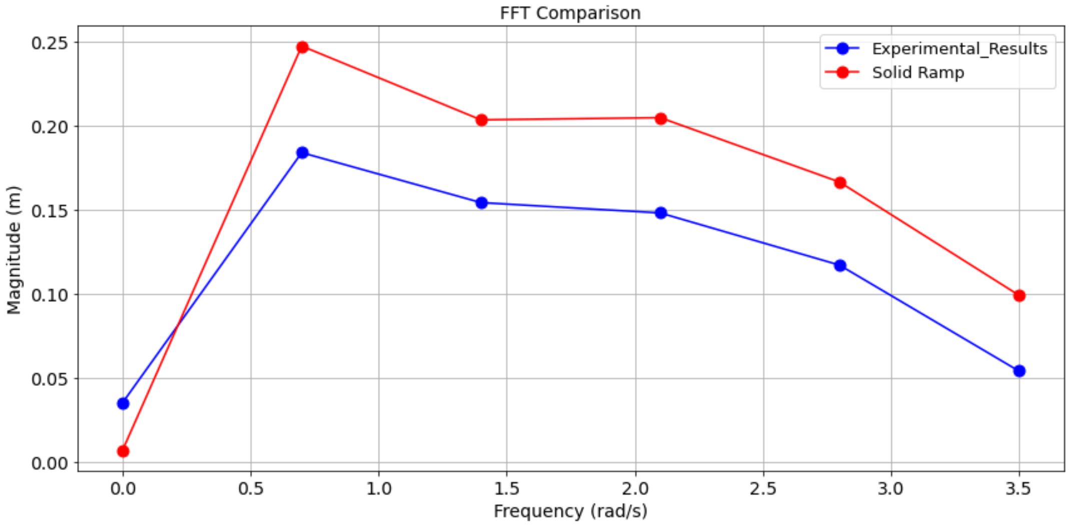

Figure 7.30: Comparison of the Fast Fourier Transformation Analysis for Six Fourier Components between the Full Model with Solid Ramp and Experimental Model

7.6.6. Line3 - Free Surface Elevation at end of the well dock for wave frequency 0.7 rad/s

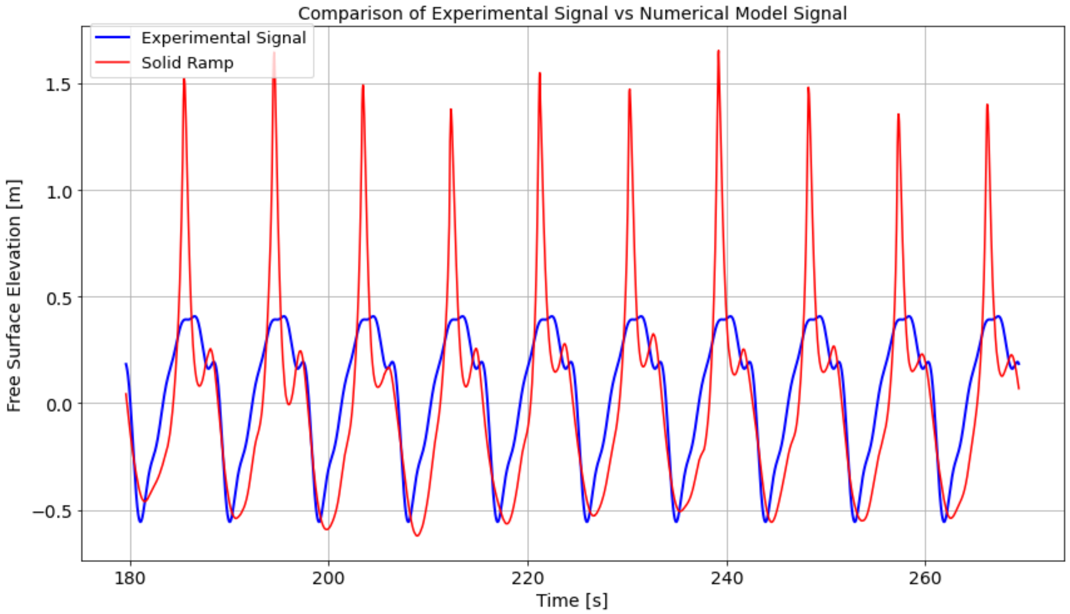

Figure 7.31: Comparison of Time-Domain Signal for Free Surface Elevation between the Full Model with Solid Ramp and Experimental Model

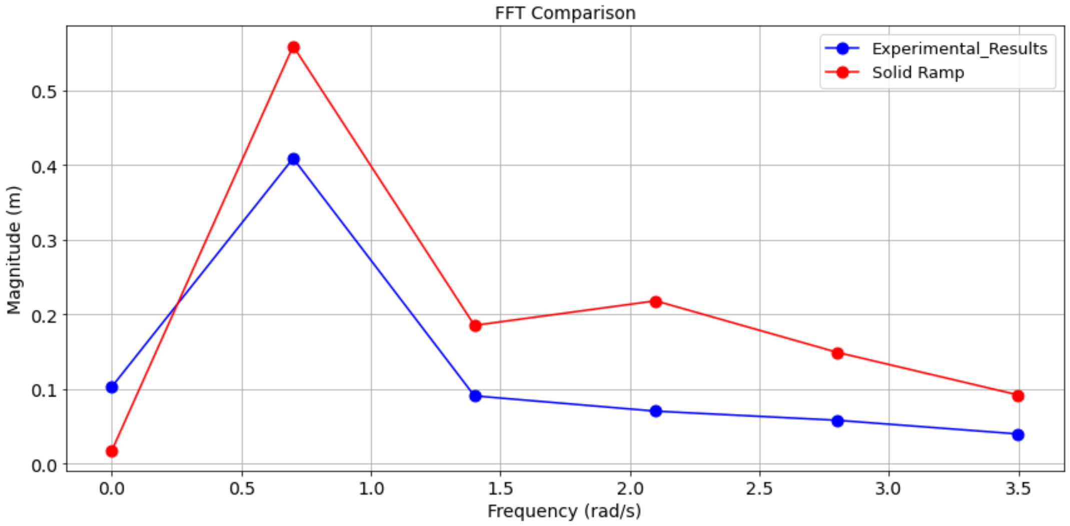

Figure 7.32: Comparison of the Fast Fourier Transformation Analysis for Six Fourier Components between the Full Model with Solid Ramp and Experimental Model

7.6.7. Line1 - Free Surface Elevation at dock entrance for wave frequency 0.4 rad/s

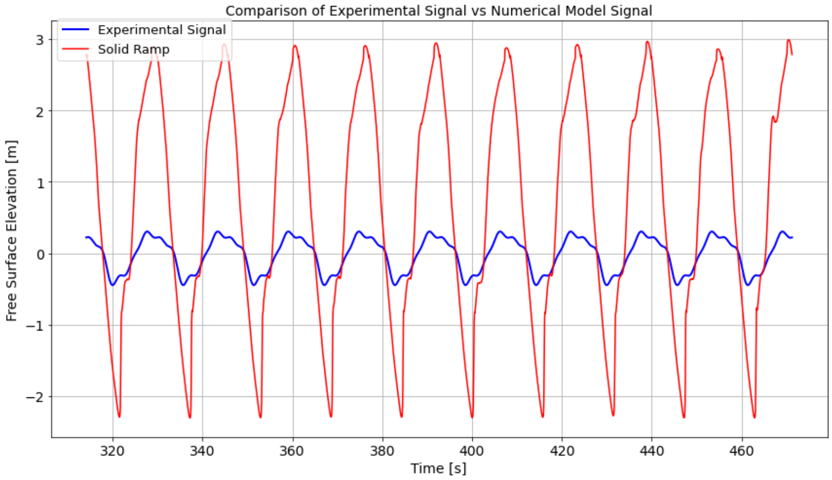

Figure 7.33: Comparison of Time-Domain Signal for Free Surface Elevation between the Full Model with Solid Ramp and Experimental Model

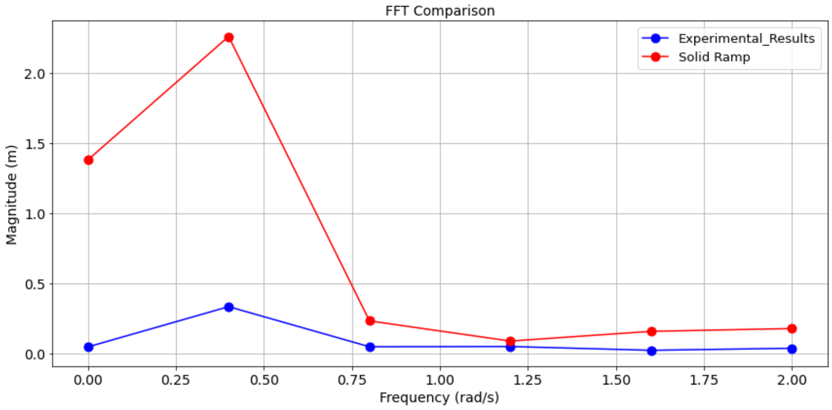

Figure 7.34: Comparison of the Fast Fourier Transformation Analysis for Six Fourier Components between the Full Model with Solid Ramp and Experimental Model

7.6.8. Line2 - Free Surface Elevation at middle of the well dock for wave frequency 0.4 rad/s

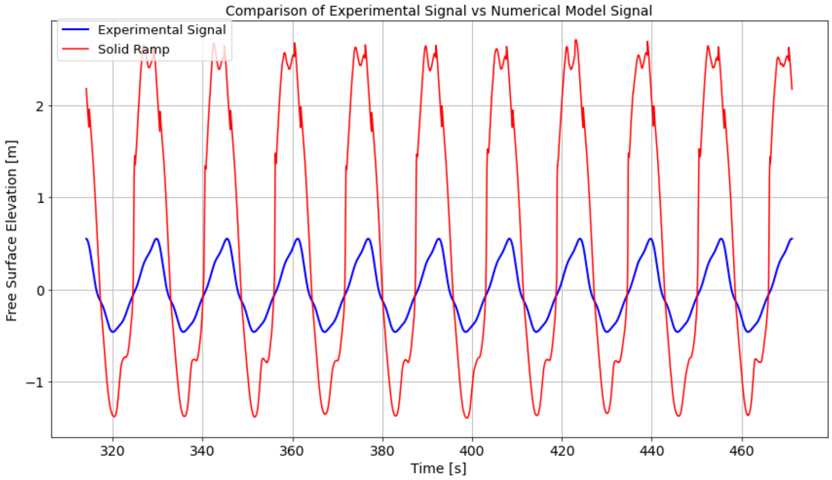

Figure 7.35: Comparison of Time-Domain Signal for Free Surface Elevation between the Full Model with Solid Ramp and Experimental Model

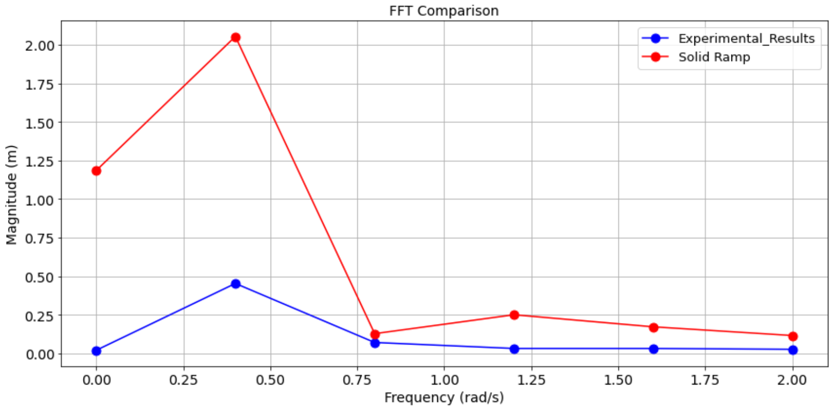

Figure 7.36: Comparison of the Fast Fourier Transformation Analysis for Six Fourier Components between the Full Model with Solid Ramp and Experimental Model

7.6.9. Line3 - Free Surface Elevation at end of the well dock for wave frequency 0.4 rad/s

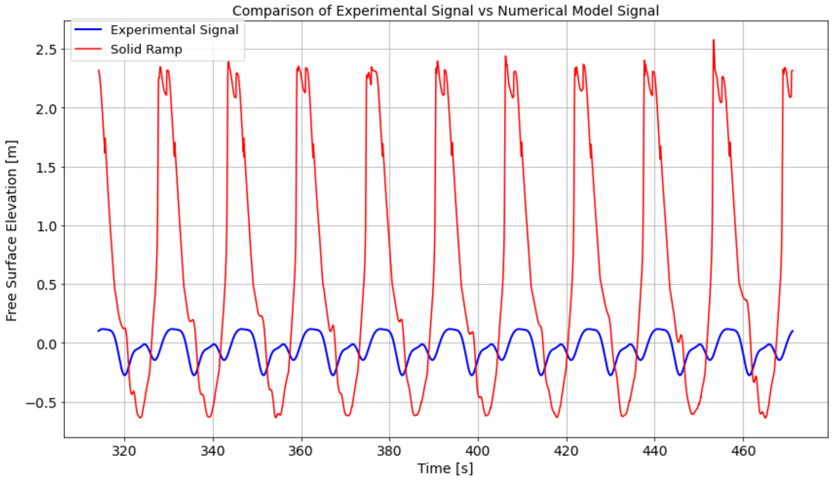

Figure 7.37: Comparison of Time-Domain Signal for Free Surface Elevation between the Full Model with Solid Ramp and Experimental Model

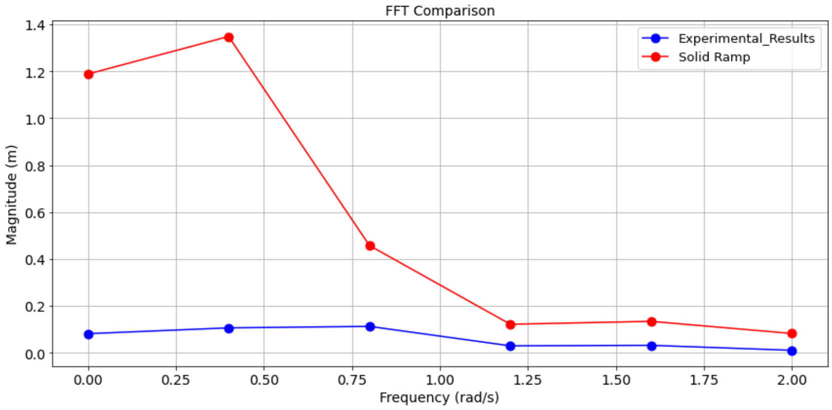

Figure 7.38: Comparison of the Fast Fourier Transformation Analysis for Six Fourier Components between the Full Model with Solid Ramp and Experimental Model

7.7. Discussion - Full Model with Solid Ramp vs. Experimental Results

The full model captures both physical mechanisms - radiation and diffraction - from the outset of the simulation, contrasting it with the experimental model from Chapter 4. This examination is conducted at three different wave frequencies: 0.4, 0.7, 1 rad/s, according to table 4.1 where depicted the parameters for the experimental tests.

Sections 7.6.1, 7.6.2, and 7.6.3 delve into the wave frequency of 1 rad/s. A close examination of the results shows a clear alignment between the full model and the experimental model. Yet, when delving into the fast Fourier transformation analysis, a variance is noticeable in the first Fourier component of the wave probe, especially within the dock's central region, as illustrated in Figure 7.24. In contrast, Figures 7.22 and 7.26 depict the first Fourier component (A1) as being slightly below the experimental data.

Sections 7.6.4, 7.6.5, and 7.6.6 provide a detailed graphical representation of the data for a wave frequency of 0.7 rad/s. The results evidently showcase that the numerical model closely mirrors the findings of the model test. These plots present the results from the model test at the specific frequency, and it is noteworthy that the numerical model accurately represent these outcomes across all three wave probes, ensuring the data have similar behaviour with the experimental findings. However, a deeper inspection through the fast Fourier transformation analysis reveals certain discrepancies. Specifically, the first Fourier component of the wave probe which is located at the end of the dock is higher compared to the model tests, as highlighted in Figure 7.32.

In sections 7.6.7, 7.6.8, and 7.6.9, the analysis focuses on the free surface elevation of the longer wave with a frequency of 0.4 rad/s. The presented results highlight that the full model's predictions do not align closely with the observed behavior from the experimental model. The main problem is found in the first two Fourier components (A0 and A1), where a significant deviation is observed in comparison with the experimental data. This deviation was initially noted in Chapter 6, where the physical mechanisms were explored independently, and the model's inability to accurately capture the radiation mechanism for large wavelengths was observed.

Another critical aspect pertains to wave damping in ComFLOW, especially concerning the differential behavior between short and long waves. As Westhuis (2001) noted in his study [22], short waves exhibit stronger damping compared to long waves.

Section 2.5 of the report, citing Marlinde de Jonge (2011) [10], details the simulation approach for long waves ($\omega = 0.4$ rad/s). It describes the use of a numerical beach with a 5% reflection coefficient (as calculated by equation 2.2) to emulate the physical beach used in model tests. Conversely, for short waves, the Generalized Absorbing Boundary Condition (GABC) was implemented, effectively absorbing all wave energy. De Jonge's findings also indicate that ComFLOW's prediction of reflections for long waves lacks accuracy. This analysis leads to the insight that while the GABC proves effective for absorbing short, steep waves prone to breaking (thus minimizing back reflection), its effectiveness in absorbing long waves with minimal reflection is less certain. For long waves, the implementation of more sophisticated techniques may be necessary to adequately minimize reflections. This could entail employing relaxation zones, or other specialized absorbing boundary conditions tailored to the unique characteristics of long waves.

In conclusion, the comparison across three different wave frequencies demonstrates that a shorter wavelength (61.57m) leads to a better representation of flow within the well dock. As the wavelength increases, the accuracy of the results diminishes.

7.8. Results - Full Model with Solid Ramp and Rack Ramp and Experimental Results

In this section, a thorough presentation of the results from the full model with a solid ramp is provided, and compared against both the modified full model with the rack ramp, and the experimental tests as detailed in Chapter 4. Specifically illustrated are both the time-domain signals and their corresponding frequency domain representations for all three models. These results are coming from three different locations all of which are visually represented in Figure 7.8, and are examined across three different wave frequencies: 0.4, 0.7 and 1 rad/s.

7.8.1. Line1 - Free Surface Elevation at dock entrance for wave frequency 1 rad/s

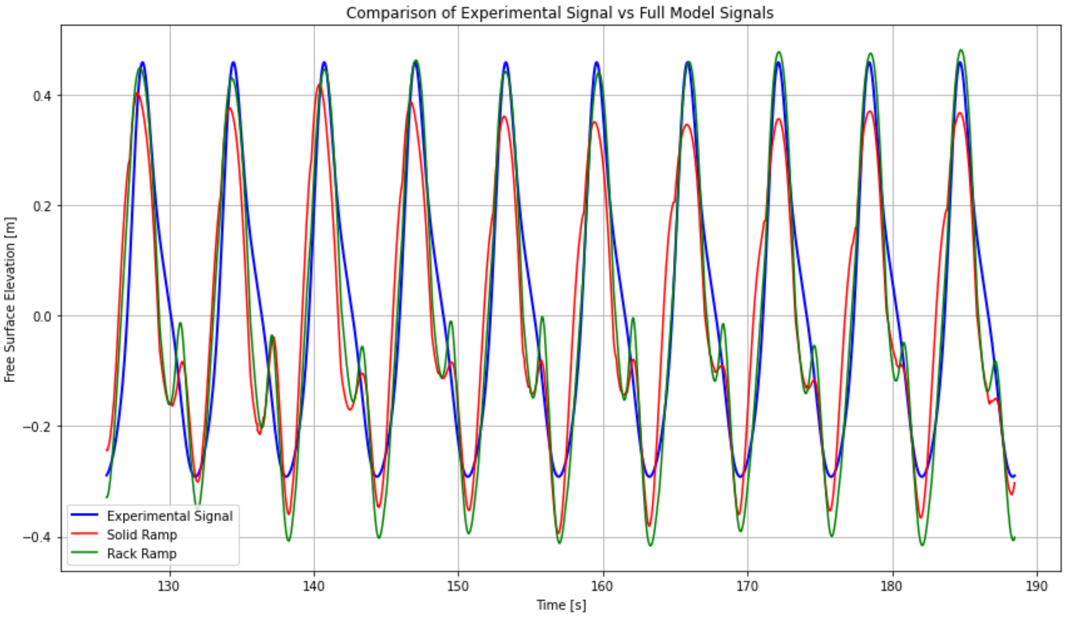

Figure 7.39: Comparison of Time-Domain Signals of Free Surface Elevation between the Numerical Models with Solid Ramp vs. Rack Ramp and the Experimental Model

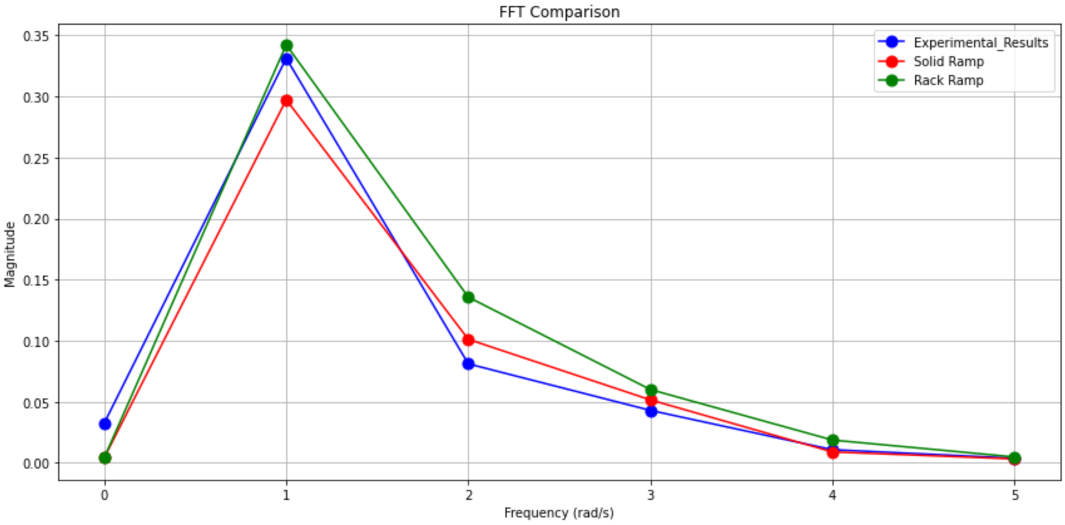

Figure 7.40: Comparison of the Fast Fourier Transformation Analysis for Six Fourier Components between the Numerical Models with Solid Ramp vs. Rack Ramp and the Experimental Model

7.8.2. Line2 - Free Surface Elevation at middle of the dock for wave frequency 1 rad/s

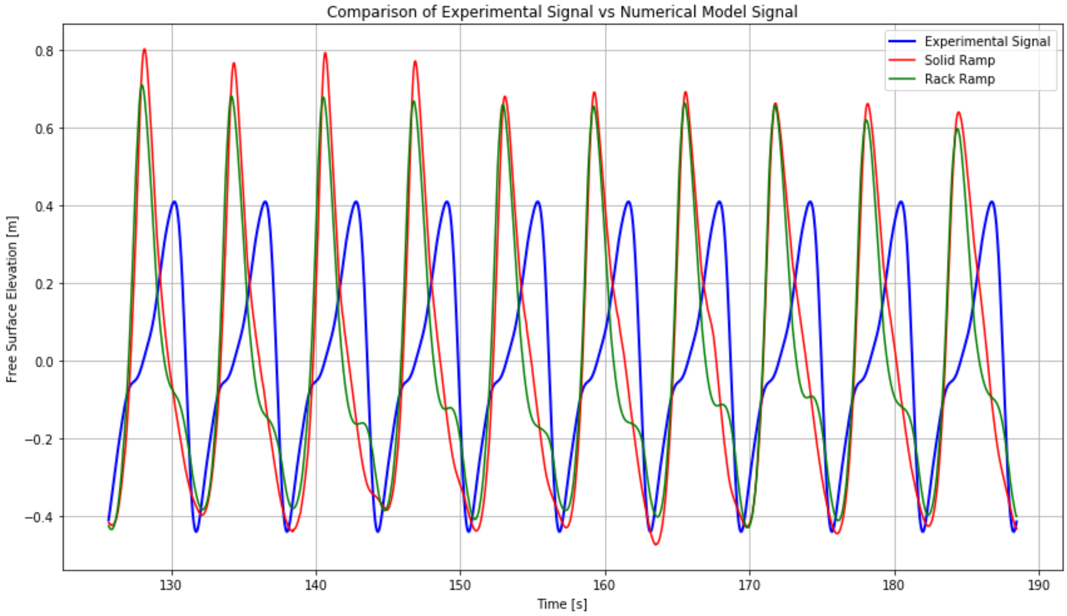

Figure 7.41: Comparison of Time-Domain Signals of Free Surface Elevation between the Numerical Models with Solid Ramp vs. Rack Ramp and the Experimental Model

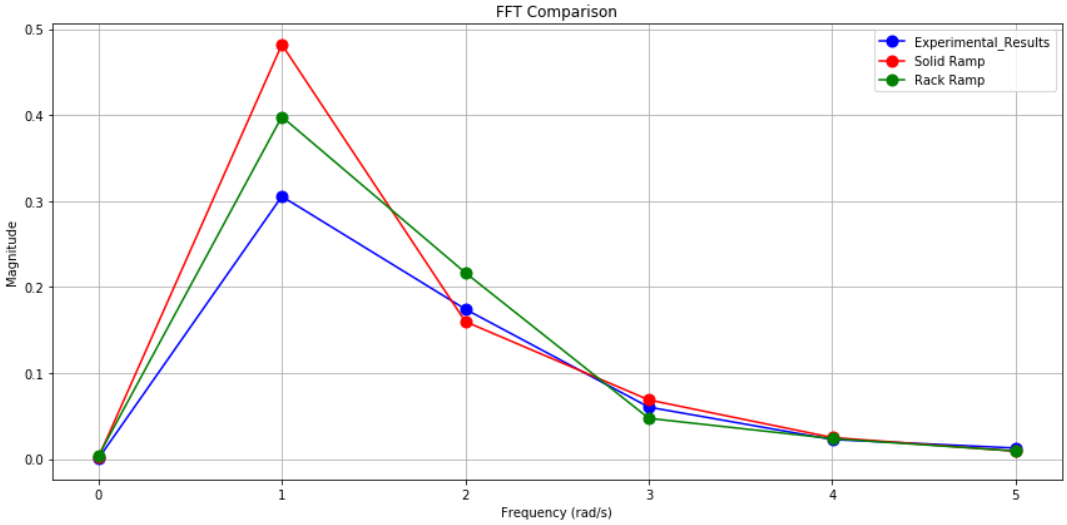

Figure 7.42: Comparison of the Fast Fourier Transformation Analysis for Six Fourier Components between the Numerical Models with Solid Ramp vs. Rack Ramp and the Experimental Model

7.8.3. Line3 - Free Surface Elevation at end of the well dock for wave frequency 1 rad/s

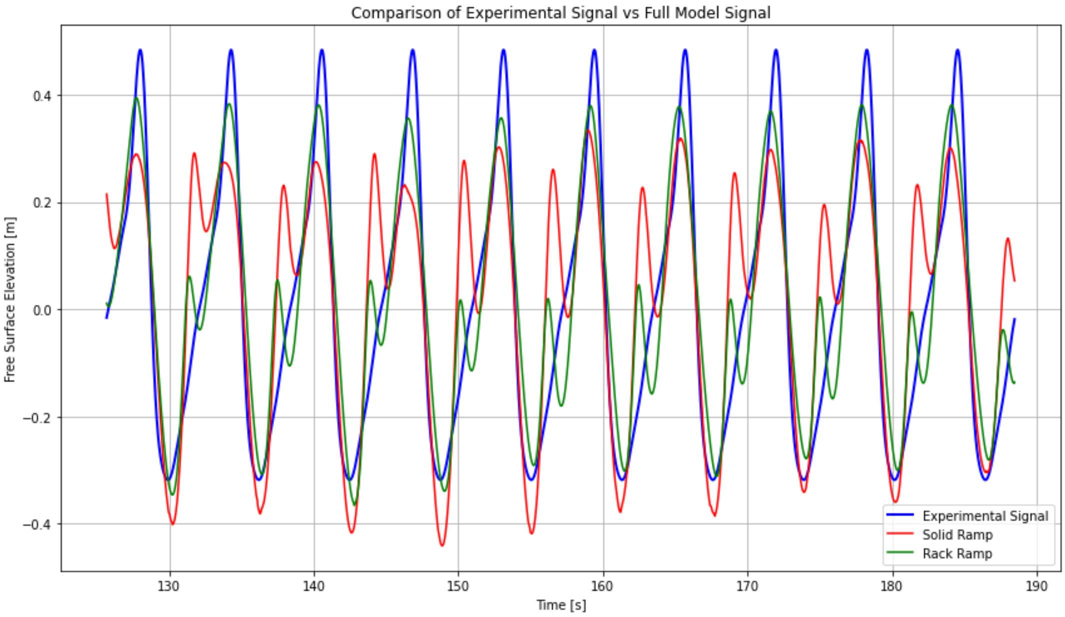

Figure 7.43: Comparison of Time-Domain Signals of Free Surface Elevation between the Numerical Models with Solid Ramp vs. Rack Ramp and the Experimental Model

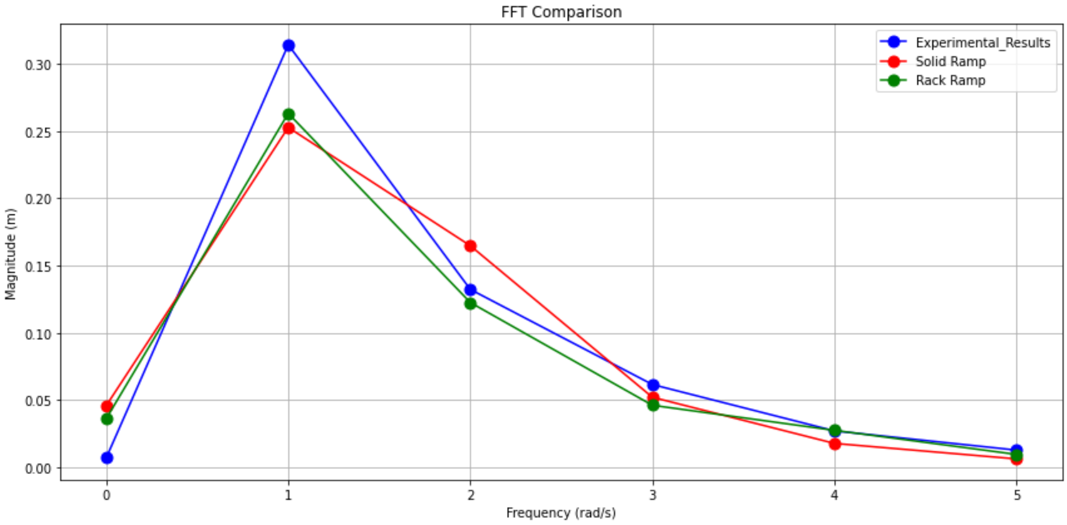

Figure 7.44: Comparison of the Fast Fourier Transformation Analysis for Six Fourier Components between the Numerical Models with Solid Ramp vs. Rack Ramp and the Experimental Model

7.8.4. Line1 - Free Surface Elevation at dock entrance for wave frequency 0.7 rad/s

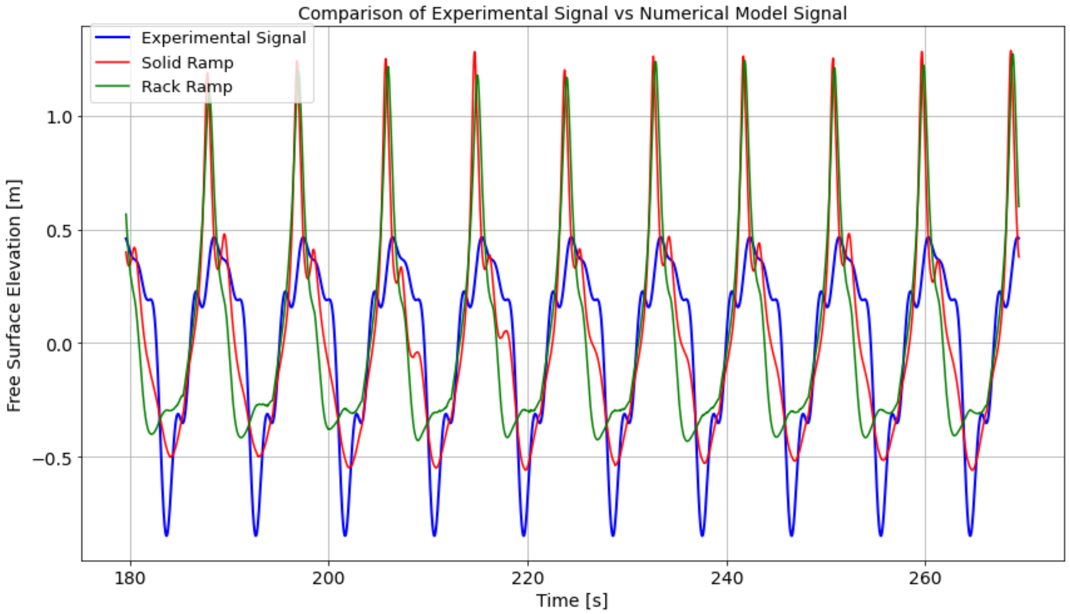

Figure 7.45: Comparison of Time-Domain Signals of Free Surface Elevation between the Numerical Models with Solid Ramp vs. Rack Ramp and the Experimental Model

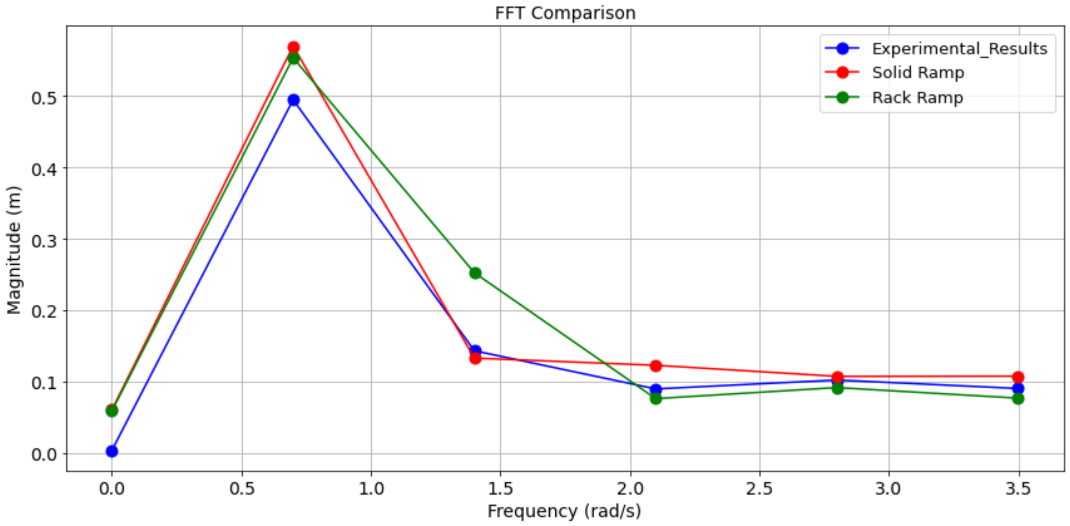

Figure 7.46: Comparison of the Fast Fourier Transformation Analysis for Six Fourier Components between the Numerical Models with Solid Ramp vs. Rack Ramp and the Experimental Model

7.8.5. Line2 - Free Surface Elevation at middle of the dock for wave frequency 0.7 rad/s

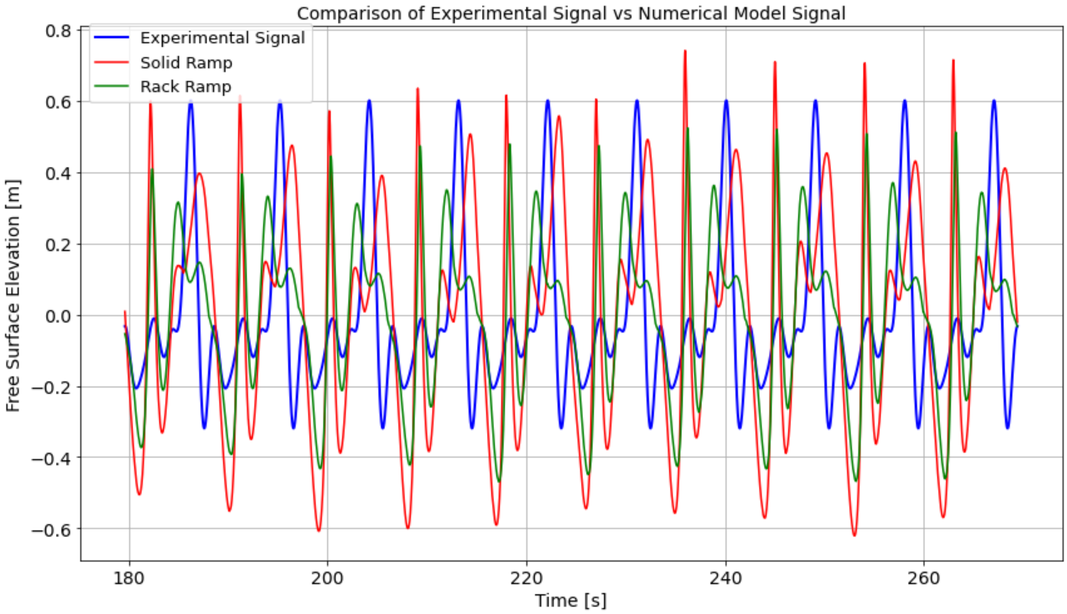

Figure 7.47: Comparison of Time-Domain Signals of Free Surface Elevation between the Numerical Models with Solid Ramp vs. Rack Ramp and the Experimental Model

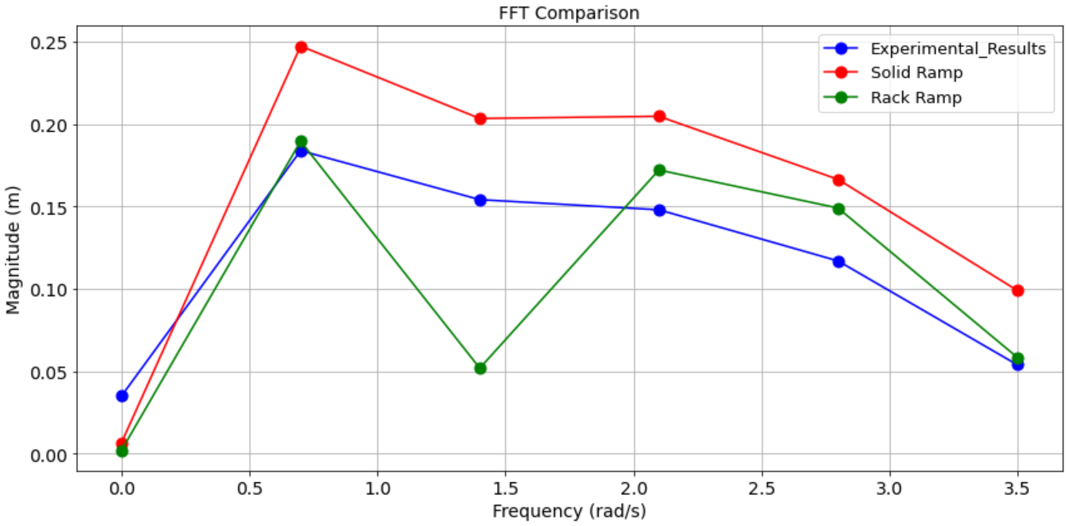

Figure 7.48: Comparison of the Fast Fourier Transformation Analysis for Six Fourier Components between the Numerical Models with Solid Ramp vs. Rack Ramp and the Experimental Model

7.8.6. Line3 - Free Surface Elevation at end of the well dock for wave frequency 0.7 rad/s

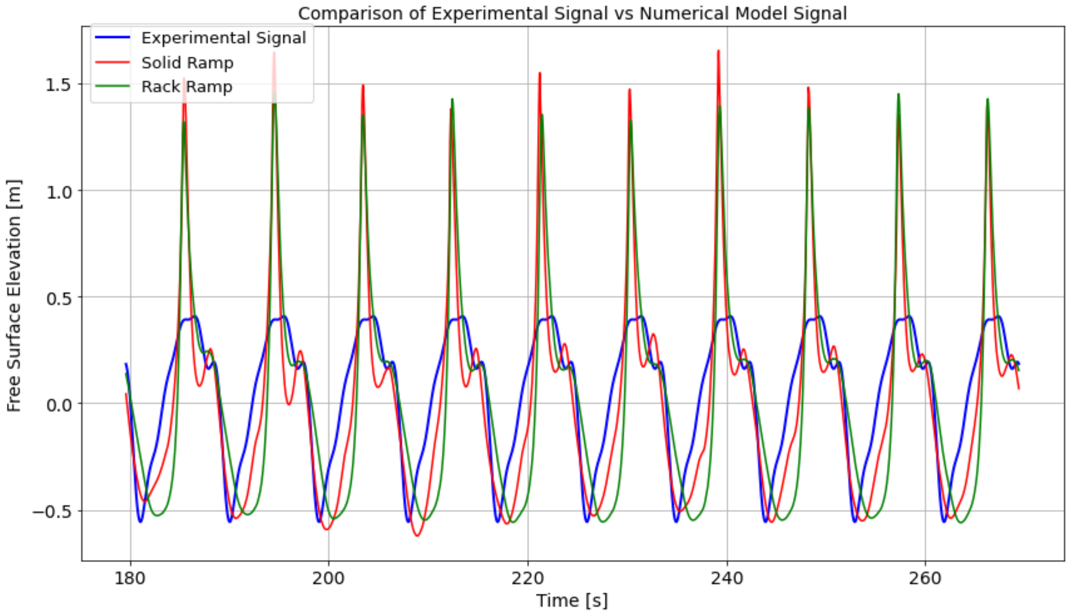

Figure 7.49: Comparison of Time-Domain Signals of Free Surface Elevation between the Numerical Models with Solid Ramp vs. Rack Ramp and the Experimental Model

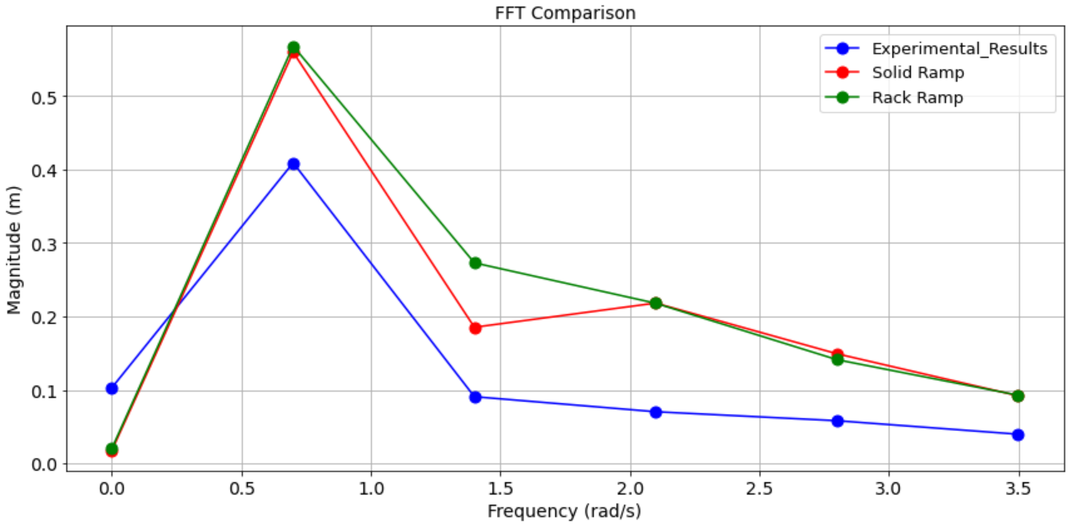

Figure 7.50: Comparison of the Fast Fourier Transformation Analysis for Six Fourier Components between the Numerical Models with Solid Ramp vs. Rack Ramp and the Experimental Model

7.8.7. Line1 - Free Surface Elevation at dock entrance for wave frequency 0.4 rad/s

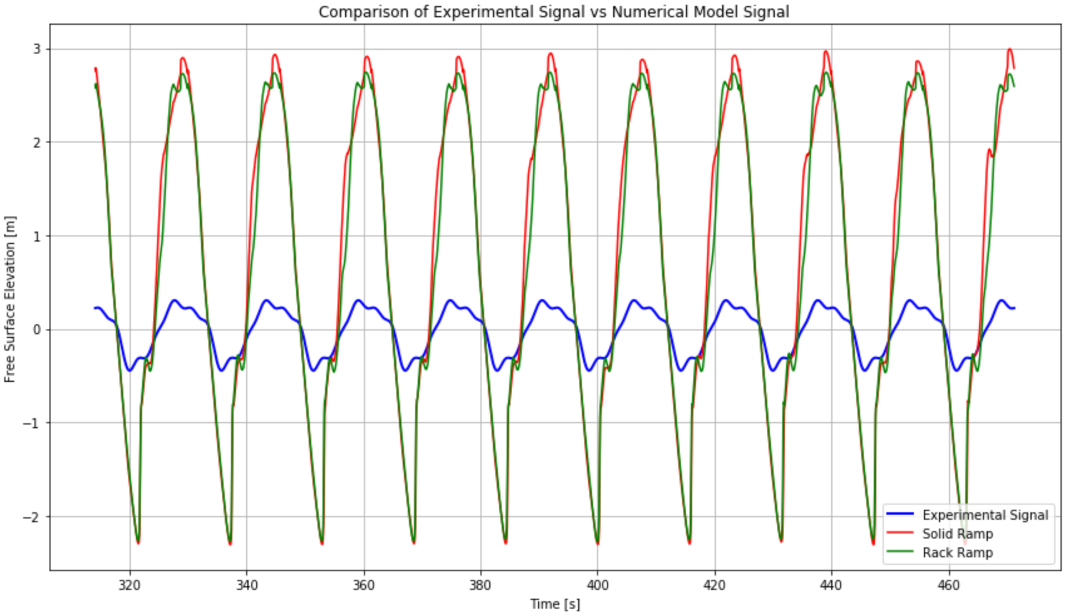

Figure 7.51: Comparison of Time-Domain Signals of Free Surface Elevation between the Numerical Models with Solid Ramp vs. Rack Ramp and the Experimental Model

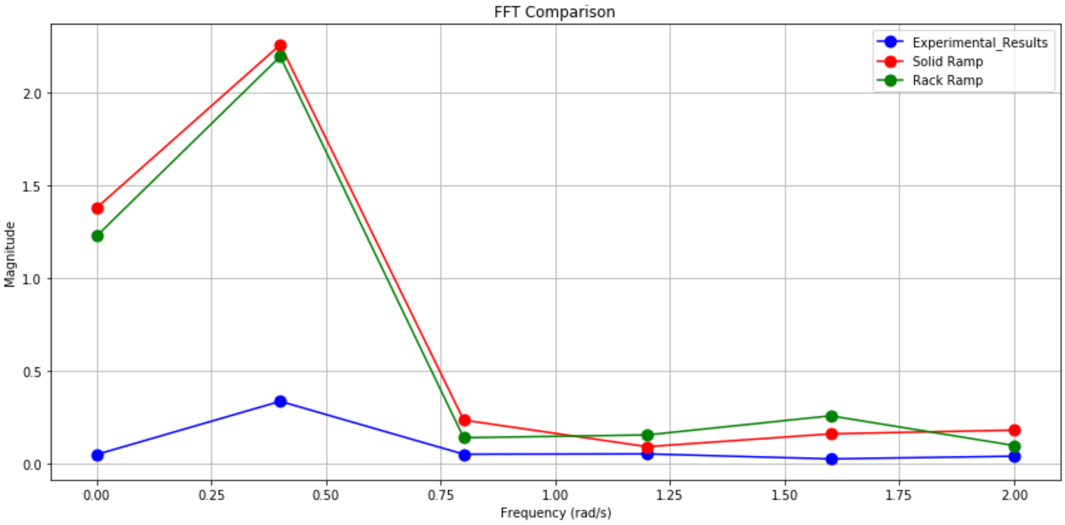

Figure 7.52: Comparison of the Fast Fourier Transformation Analysis for Six Fourier Components between the Numerical Models with Solid Ramp vs. Rack Ramp and the Experimental Model

7.8.8. Line2 - Free Surface Elevation at middle of the dock for wave frequency 0.4 rad/s

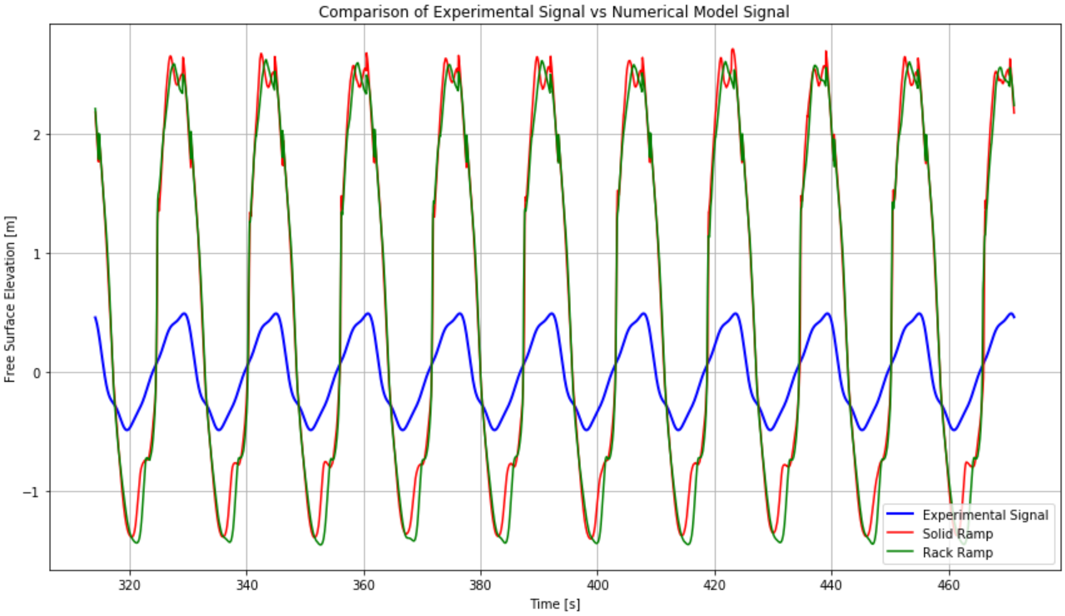

Figure 7.53: Comparison of Time-Domain Signals of Free Surface Elevation between the Numerical Models with Solid Ramp vs. Rack Ramp and the Experimental Model

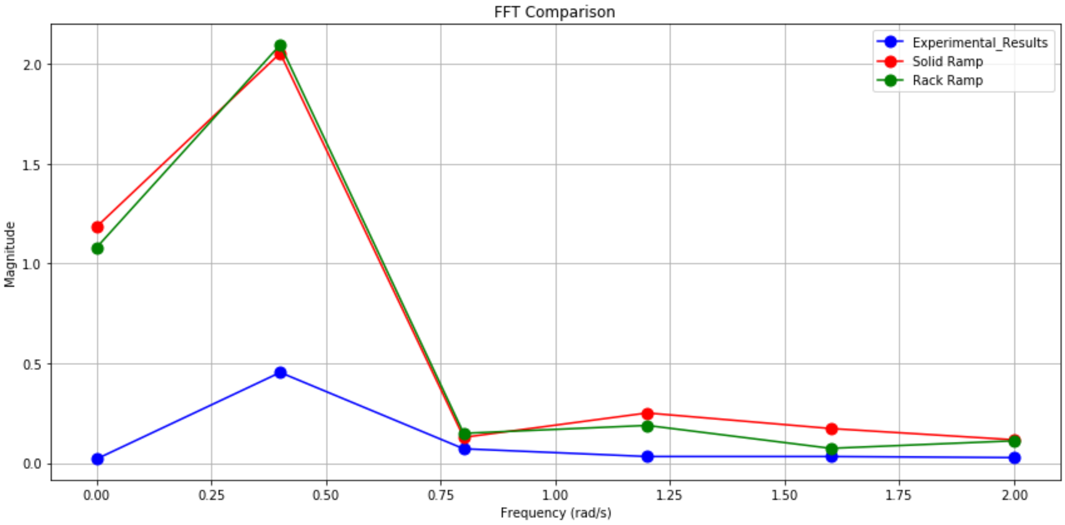

Figure 7.54: Comparison of the Fast Fourier Transformation Analysis for Six Fourier Components between the Numerical Models with Solid Ramp vs. Rack Ramp and the Experimental Model

7.8.9. Line3 - Free Surface Elevation at end of the well dock for wave frequency 0.4 rad/s

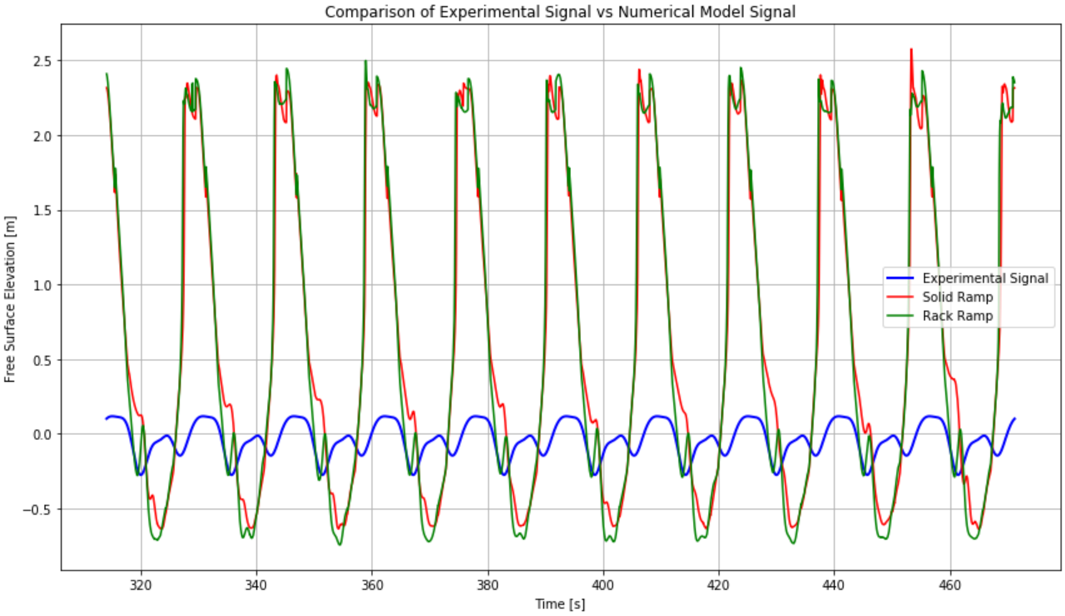

Figure 7.55: Comparison of Time-Domain Signals of Free Surface Elevation between the Numerical Models with Solid Ramp vs. Rack Ramp and the Experimental Model

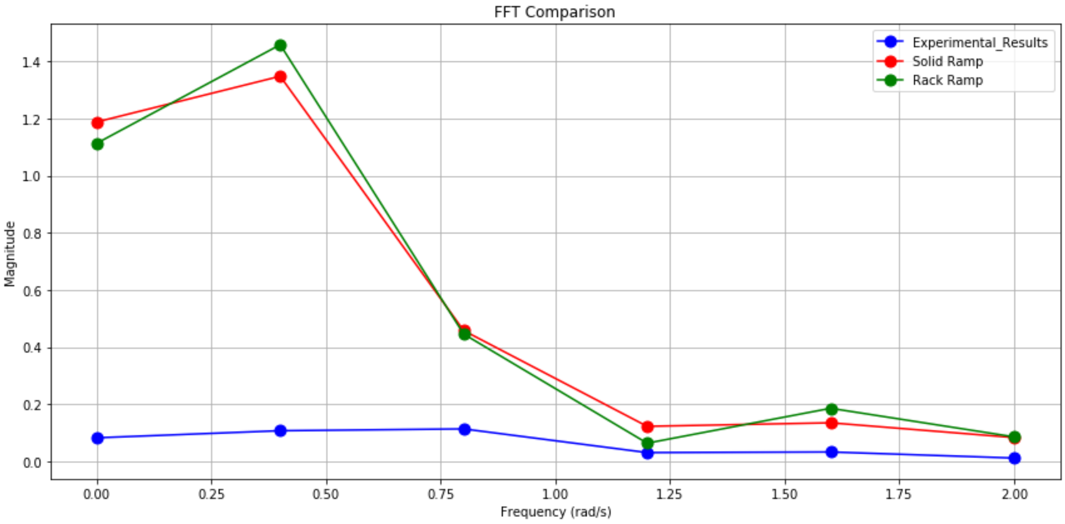

Figure 7.56: Comparison of the Fast Fourier Transformation Analysis for Six Fourier Components between the Numerical Models with Solid Ramp vs. Rack Ramp and the Experimental Model

7.9. Discussion - Full Model with Solid Ramp and Rack Ramp and Experimental Results

The full model with the solid ramp is compared with the experimental model from Chapter 4 and the full model with the rack ramp. This examination is conducted at three different wave frequencies: 0.4, 0.7, and 1 rad/s. A main goal of this study is to explore the potential geometric modification of the ramp region to mitigate the effects of reflected waves within the well dock.

In subsections 7.8.1 through 7.8.3, the free surface elevation at a wave frequency of 1 rad/s is analyzed. The findings indicate an improvement in the results compared to those obtained from the solid ramp, aligning more accurately with the model test outcomes. Notably, the wave height, as measured by the middle wave probe within the dock, is significantly diminished. Conversely, in the other two regions, the wave height increases, more closely mirroring the experimental findings.

In subsections 7.8.4, 7.8.5 and 7.8.6, the free surface elevation at a wave frequency of 0.7 rad/s is presented. The plots indicate that the numerical model predicts well the behaviour of the model test. A similar trend, as observed with the shorter wave of 1 rad/s, emerges. Upon the integration of the rack ramp, there is a marked reduction in wave height at the middle of the dock. However, closer to both the entrance and the end of the dock, there is an increase in wave height.

In subsections 7.8.7 through 7.8.9, the free surface elevation for a wave with a frequency of 0.4 rad/s is discussed. The data shows that the full model with the rack ramp does not align with the model test outcomes, nor does it show any notable improvement over the results using a solid ramp. The primary reason behind this misalignment, as referenced in the previous Section 7.7, is observed in the first two Fourier components (A0 and A1) where a significant deviation from the experimental data is observed. This deviation was initially noted in Chapter 6, where the physical mechanisms were explored independently, and the inaccuracy in capturing the radiation mechanism for large wavelengths was observed. This scenario results in a non-physically high wave height.

In conclusion, this study demonstrates that the full model with the rack ramp provides better results than the full model with the solid ramp for the short (61.57 meters) and medium (125.79 meters) wavelengths and align well with the model tests, especially for the shorter wavelength. Conversely, the long wavelength (385.237 meters) does not present any improvement in respect to the full model with the solid ramp, and the results for the first two Fourier components (A0 and A1) from the frequency domain signal do not agree with the experimental tests. The meticulous research carried out in Chapter 6 indicates that the main problem lies in the radiation mechanism, which is not accurately captured. Additionally, the deviation between solid ramp and rack ramp is smallest at the line nearest the end of the dock (closest to the ramp). This could be attributed to the different wave characteristics, like wave reflection and transmission, associated with each ramp type. However, these differences become more pronounced as the waves propagate further away from the ramp. This is because the effects of reflection, transmission, and diffraction related to the ramp's structure become more pronounced with distance, allowing the waves more space and time to develop and exhibit the variations induced by the ramp's structure. This phenomenon leads to larger deviations in Fast Fourier Transformation analysis at lines further from the ramp, a fact that is clearly demonstrated by the results from the other two wave probes. Another critical aspect, as discussed in Section 7.7, pertains to wave damping in ComFLOW. This section highlights the contrasting behaviors between short and long waves and the ineffectiveness of the Generalized Absorbing Boundary Condition (GABC) in minimizing reflections for long waves.

8

Viable Model

8.1. Background

This model was developed to address the third research question, which examines the viability of the model to facilitate the design process. The starting point is the Full Model with solid ramp from Chapter 7, from which wave kinematics, especially wave height and phase, are extracted at the dock entrance using a wave probe. This extracted data serves as the input for a subsequent 2D simulation that encompasses only the well dock and the ramp from the 3D geometry of the LPD vessel. Specifically, this study elaborates how wave kinematics are extracted from the Full Model with the solid ramp (8.2), and how these kinematics subsequently serve as the input parameters for the creation of a 2D domain (8.3). In section 8.4, there is a visual representation of the boundary conditions, followed by the approach for the creation of the moving domain (8.5), the explanation of the grid study (8.6) and in section 8.7, the simulation parameters for the comparison with the experimental tests of Chapter 4 are presented to ascertain the feasibility of this viable model. In Section 8.8, the results of the viable model are compared with the experimental results. Finally, Section 8.9 delves into a detailed discussion explaining the implications of these findings.

8.2. Wave probe location for capturing the wave kinematics at the well dock entrance

The initial step utilizes the Full Model with solid ramp from Section 7.4, specifically using the input parameters detailed in table 7.5. The only modification is in the location of the wave probe to capture specific wave kinematics: wave height and phase. Figures 8.1 and 8.2 showcase the red wave probe at the dock entrance. The location of the wave probe at the well dock entrance is strategically selected, due to its significance as the initial point of interaction between the incoming waves and the well dock. The probe's coordinates are x = 64.2m , y = 0m, zmin = -1.1m, zmax = 36.98m.

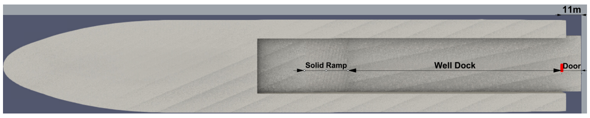

Figure 8.1: Top view of the wave probe at the dock entrance

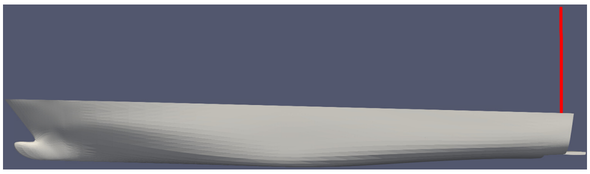

Figure 8.2: Side view of the wave probe at the dock entrance

8.3. 2D-domain

The next step is to construct the 2D domain. Figure 8.3, which is delineated by a red rectangle, demonstrates that only the well dock and the solid ramp region from the entire ship are incorporated into the 2D domain. In this 2D representation, as depicted in figure 8.4, neither the well dock nor the solid ramp have their geometries explicitly displayed. Excluding the well dock's geometry and its replacement from the region in figure 8.4 is justified due to its nearly flat characteristic, which simplifies its representation. In contrast, the solid ramp in the 3D domain, or the ramp region in the 2D domain, features an incline. This incline has been substituted with a boundary condition that acts as a damping region, similar to the approach used by Marlinde de Jonge in her thesis [10]. Further details on this aspect of the model, particularly concerning the boundary conditions, are discussed in Section 8.4. Another significant adjustment involves the domain's reversed orientation along the x-axis in comparison to the 3D domain. This means the positive x-axis now points towards the ship's bow. This reorientation adheres to ComFLOW's convention, as waves are consistently generated from left to right. The coordinate intervals defining the well dock and the ramp region are:

$$x = [12.474\ ,\ 75.86],\ z = [-2.225\ ,\ 6.00]$$

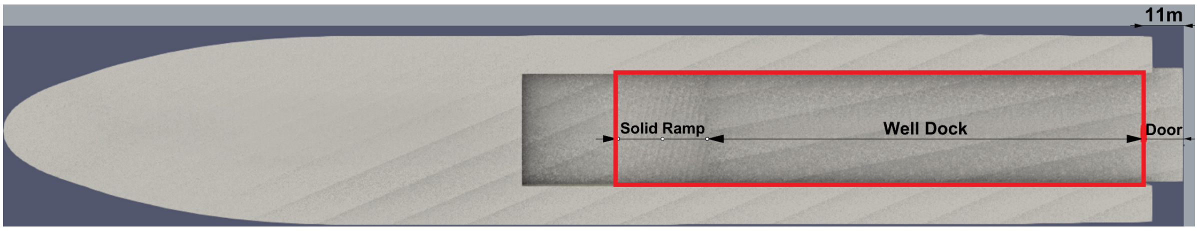

Figure 8.3: Parts of the Ship Included in the 2D Domain

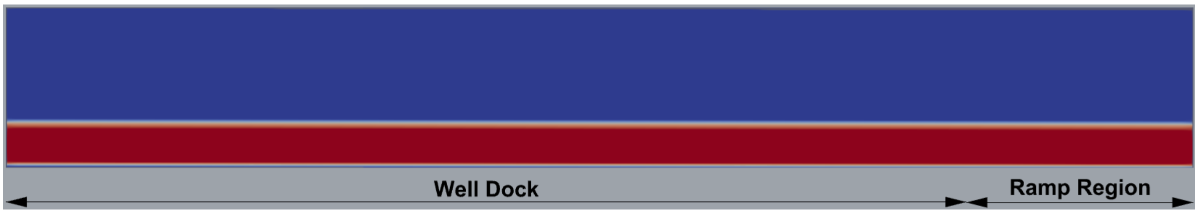

Figure 8.4: Two-dimensional side view of the closed well dock

8.4. Boundary conditions

Another critical aspect to consider is the boundary conditions. Figure 8.5 offers a schematic representation of the boundary conditions associated with the problem under consideration. A detailed discussion of these conditions and their specific applications can be found in Section 5.7. In this set-up, the GABC on the right side substitutes the function previously served by the solid ramp. Its primary purpose is to absorb the wave energy, thereby minimizing reflections. This approach contrasts with the wave damping method discussed in Section 2.5 of the literature study, where equation 2.2 is used to calculate the reflection coefficient. This thesis was focused on adjusting the absorption coefficients of the GABC boundary condition, specifically employing the 1st order GABC, as the 2nd order GABC did not function as expected.

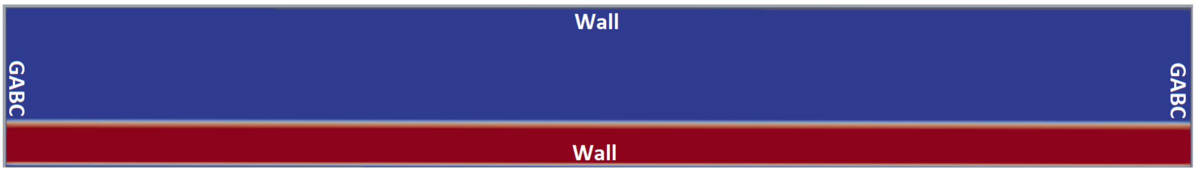

Figure 8.5: 2D Domain - Specified boundary conditions

8.5. Moving frame

The approach of the moving frame is adopted in this particular model, as it encompasses the entirety of the well dock along with the region of the solid ramp. The procedure is similar to the one outlined in subsection 5.10.2. However, a notable distinction in this model is that the computational domain remains stationary, while the coordinate frame is what moves. Within ComFLOW, the movement of this coordinate frame can be dictated by externally predefined time series.

Data related to displacement, velocity, and acceleration of the vessel are input into a file, where both velocity and acceleration are derived from the displacement series. The considered files provide time instants, and associated with these are the amplitudes and phases for the six degrees of freedom of vessel motion: surge, sway, heave, roll, pitch and yaw. The amplitudes and phase angles corresponding to each degree of freedom are grounded in model tests. Since these experimental tests were conducted in head waves, only the amplitude and phase data pertinent to surge (x), heave (z), and pitch (β) motions are extracted from the experimental data. These data contribute in representing the surge, heave, and pitch motions of the ship (equations 5.8 - 5.10 in subsection 5.10.2) for the first five harmonic frequencies.

8.6. Grid Study

The methodology employed in the 2D grid study is analogous that used in the models discussed in Chapters 6 and 7. However, the specific approach to implementing the 2D grid study methodology adheres to the procedure outlined in Section 8.2, which is essential for accurately capturing wave kinematics notably wave height and phase. These variables are crucial as they serve as input parameters for the 2D grid study. Table 8.1 enumerates the input parameters utilized in the 2D grid study. Notably, the wave height data is derived from the results of the Full Model with solid ramp from section 7.4. Figure 8.6 displays the wave probe, which is the main tool for the grid convergence study as previously discussed in subsection 5.13.1. The details of the different grids used are expounded upon in Table 8.2. Visual depictions of the three grid resolutions can be found in Appendix F.

Simulation	**Viable Model - Grid Study**
Wavelength: L [m]	29.35
Wave frequency [rad/s]	1
Wave Height [m]	0.8
Inlet [m]	12.474
Outlet [m]	75.86
Zmax [m]	6.00
Zmin [m]	2.225
Period Time [s]	6.28
Simulation Time in Periods	30
BC	X: GABC
	Z: Wall
Wave Probe Coordinates (Figure: 5.41): X, Zmin, Zmax	27.3, -1.1, 4.00

Table 8.1: Simulation Parameters - Viable Model Grid Study

Figure 8.6: Wave Probe within the Well Dock for the 2D Grid Study

Simulation Grid Study						
Grid Study - Coarse						
Grid Levels	Extents		Grid Size		Cell Size	
	Coordinates in x-direction	Coordinates in z-direction	Cells in x-direction	Cells in z-direction	x	z
0	12.47 75.86	-2.225 6.00	80	11	0.79	0.75
1	12.47 75.86	-2.225 6.00	160	22	0.39	0.37
Grid Study - Medium						
Grid Levels	Extents		Grid Size		Cell Size	
	Coordinates in x-direction	Coordinates in z-direction	Cells in x-direction	Cells in z-direction	x	z
0	12.47 75.86	-2.225 6.00	120	16	0.52	0.52
1	12.47 75.86	-2.225 6.00	240	32	0.26	0.26
Grid Study - Fine						
Grid Levels	Extents		Grid Size		Cell Size	
	Coordinates in x-direction	Coordinates in z-direction	Cells in x-direction	Cells in z-direction	x	z
0	12.47 75.86	-2.225 6.00	180	24	0.34	0.34
1	12.47 75.86	-2.225 6.00	360	48	0.17	0.17

Table 8.2: Detail Analysis of Grid Study (Grid and Cell Size)

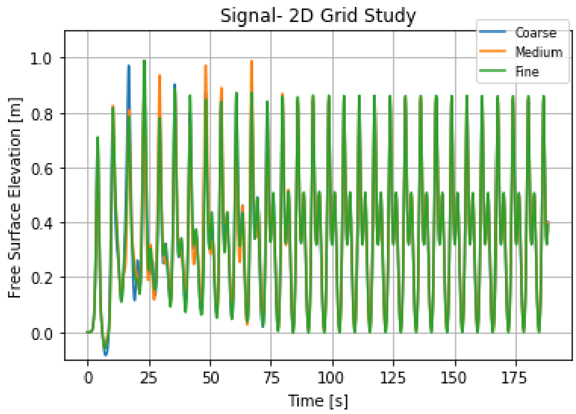

Figure 8.7: Comparison of the Time-Domain signal of Free Surface Elevation of the Wave Across Three Different Grids

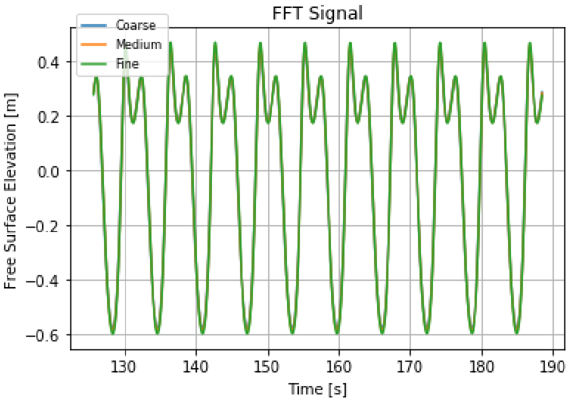

Figure 8.8: Comparison of the Last 10 Periods from the Total Time-Domain Signal for Free Surface Elevation of the Wave Across Three Different Grids

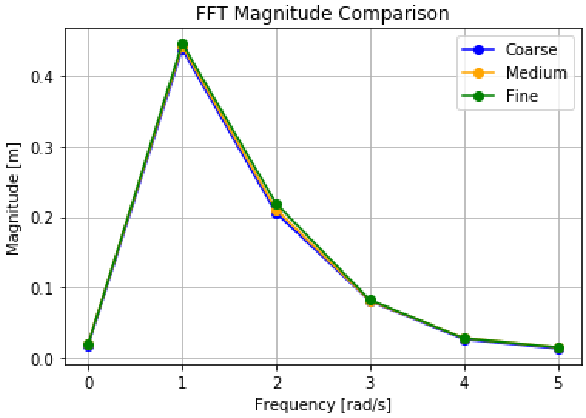

Figure 8.9: Comparison of the Fast Fourier Transformation Analysis for Six Fourier Components Across Three Different Grids

The data results are presented in Table 8.3, with Plot 8.10 providing a graphical interpretation for visual clarity.

Using the wave probe, as shown in Figure 8.6, the relative wave height over time is plotted, as shown in figure 8.7. Once the signal becomes periodic - particularly over the last 10 periods - the periodic wave signal is illustrated in Figure 8.8.

Subsequently, this time-domain data is converted to the frequency domain using the Fast Fourier Transformation as demonstrated in figure 8.9. A detailed examination of these results, particularly focusing on the second Fourier component of the free surface elevation is showcased in both Table 8.3 and Plot 8.10, and they indicate an exact difference of 0.5 centimeters between the medium grid and the Richardson extrapolation. In order to achieve a balance between computational efficiency and precision, the medium grid has been chosen for subsequent analyses.

Grid	**Normalized Grid Spacing h**	**Free Surface Elevation [m]**
Richardson Extrapolate	0	0.447
Grid Study - Fine	1	0.446
Grid Study - Medium	1.5	0.442
Grid Study - Coarse	2.25	0.433

Table 8.3: Viable Model Grid - Convergence Study

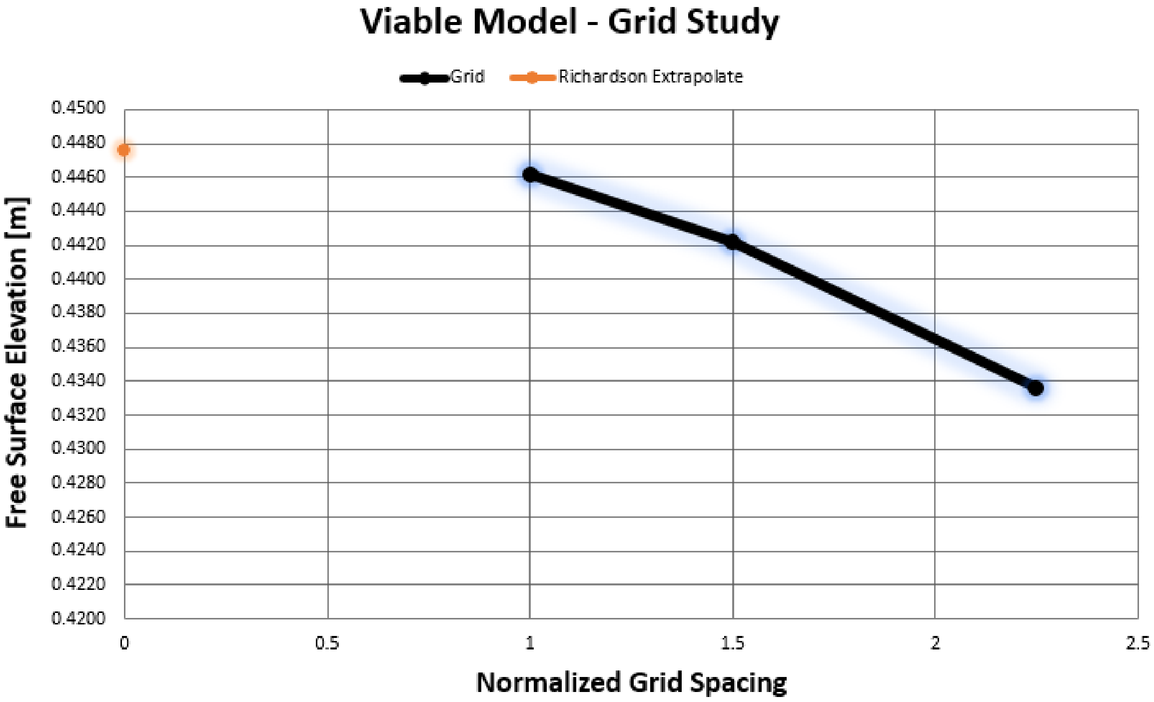

Figure 8.10: Convergence plot for viable model grid study showcasing the variation of the Fourier component A1 in relation to the grid resolution

8.7. Simulation method

Following the completion of the grid study for the model, the subsequent step involves presenting the input parameters for the simulation, as detailed in Table 8.4. Also, the post processing is conducted at three locations within the well dock to capture wave height, utilizing wave probes depicted in Figure 8.11. The coordinates for these locations are provided in Table 8.4, alongside the input simulation parameters for wave frequencies of 0.4, 0.7, and 1 rad/s.

Upon a closer examination of Table 8.4, a notable difference in the values of wavelengths is observed when compared to their counterparts in Chapters 6 and 7. This discrepancy arises because the models developed in Chapters 6 and 7 were designed for deep waves, whereas this model is based on shallow water conditions. Therefore, the dispersion relationship for shallow water is applied, with specific wavelengths determined by equations 8.1 and 8.2.

$$\omega = k\sqrt{gh} \tag{8.1}$$

The wave length can be derived from:

$$\lambda = \frac{2\pi}{k} \tag{8.2}$$

Simulation		**Viable Model - Set-up parameters**		
Wavelength: L [m]		29.35	41.93	73.38
Wave frequency [rad/s]		1	0.7	0.4
Wave Height [m]		0.8	1.15051	1.64046
Inlet [m]		12.474	12.474	12.474
Outlet [Wavelengths]		2L	2L	2L
Zmax [m]		6.00	6.00	6.00
Zmin [m]		2.225	2.225	2.225
Period Time [s]		6.28	8.98	15.70
Simulation Time in Periods		30	30	30
BC		X: GABC	X: GABC	X: GABC
		Z: Wall	Z: Wall	Z: Wall
Wave Probe Coordinates: X, Zmin, Zmax	Line1	27.3, -1.1, 4.00	27.3, -1.1, 4.00	27.3, -1.1, 4.00
	Line2	42.134, -1.3, 4.00	42.134, -1.3, 4.00	42.134, -1.3, 4.00
	Line3	56.934, -1.2, 4.00	56.934, -1.2, 4.00	56.934, -1.2, 4.00

Table 8.4: Simulation parameters for Viable Model

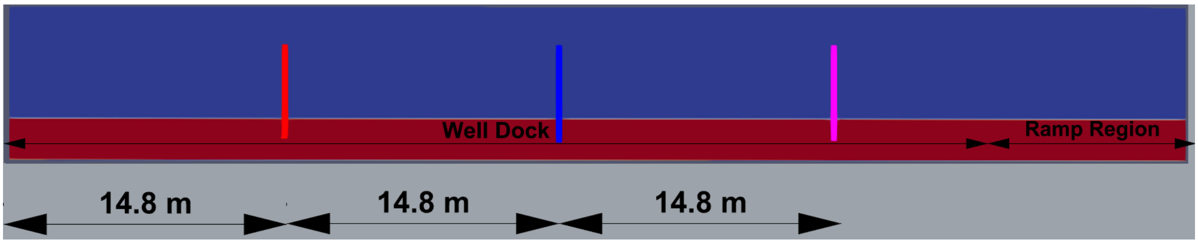

Figure 8.11: Wave probes located within the well dock for the results exportation

The following section presents the results of the viable model, comparing its performance and accuracy with the experimental tests.

8.8. Results - Viable Model vs. Experimental Results

In this section, a comprehensive presentation of the results from the viable model is provided, juxtaposed against the experimental results as detailed in Chapter 4. Specifically, both the time-domain signals and their corresponding frequency domain representations for both models are illustrated. These results are coming from three different locations all of which are visually represented in Figure 8.11, and are examined across three distinct wave frequencies: 0.4, 0.7 and 1 rad/s.

8.8.1. Line1 - Free Surface Elevation at dock entrance for wave frequency 1 rad/s

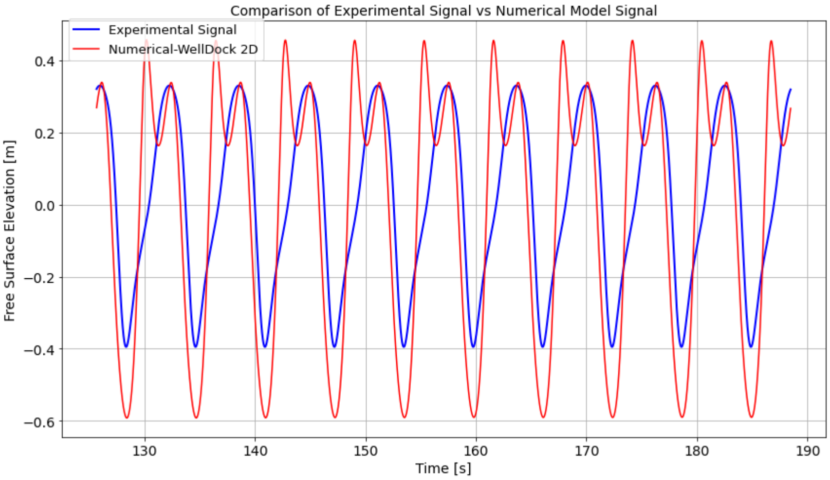

Figure 8.12: Comparison of Time-Domain Signal for Free Surface Elevation between the Viable Model and the Experimental Model

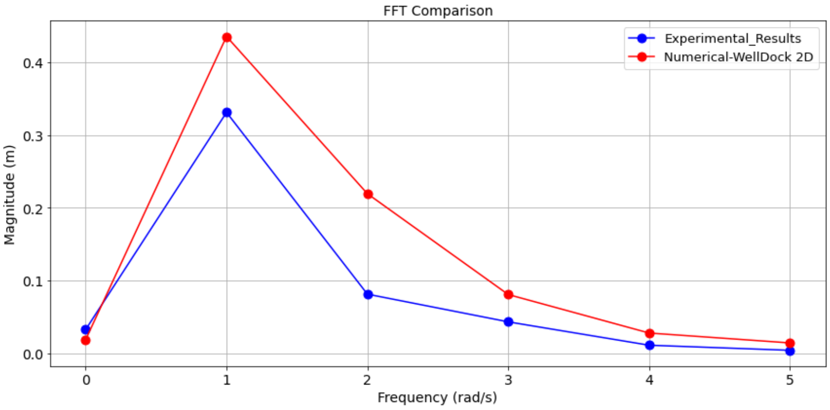

Figure 8.13: Comparison of the Fast Fourier Transformation Analysis for Six Fourier Components between the Viable Model and the Experimental Model

8.8.2. Line2 - Free Surface Elevation at middle of the well dock for wave frequency 1 rad/s

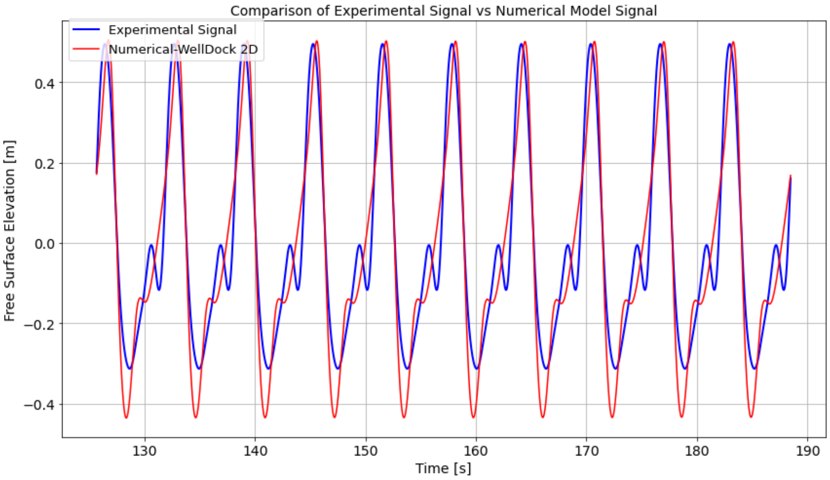

Figure 8.14: Comparison of Time-Domain Signal for Free Surface Elevation between the Viable Model and the Experimental Model

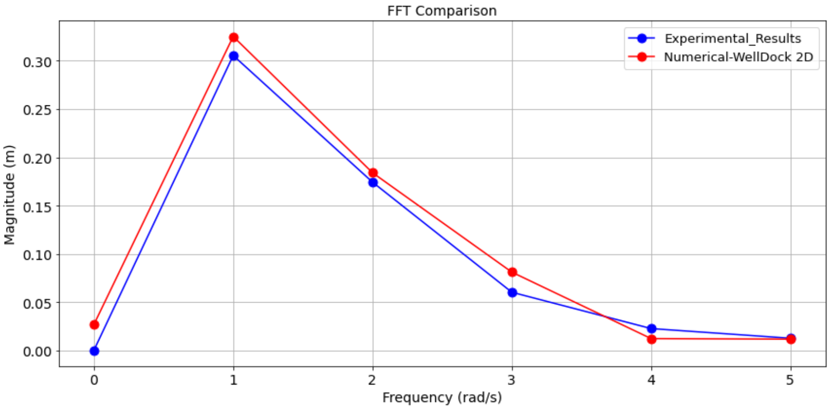

Figure 8.15: Comparison of the Fast Fourier Transformation Analysis for Six Fourier Components between the Viable Model and the Experimental Model

8.8.3. Line3 - Free Surface Elevation at end of the well dock for wave frequency 1 rad/s

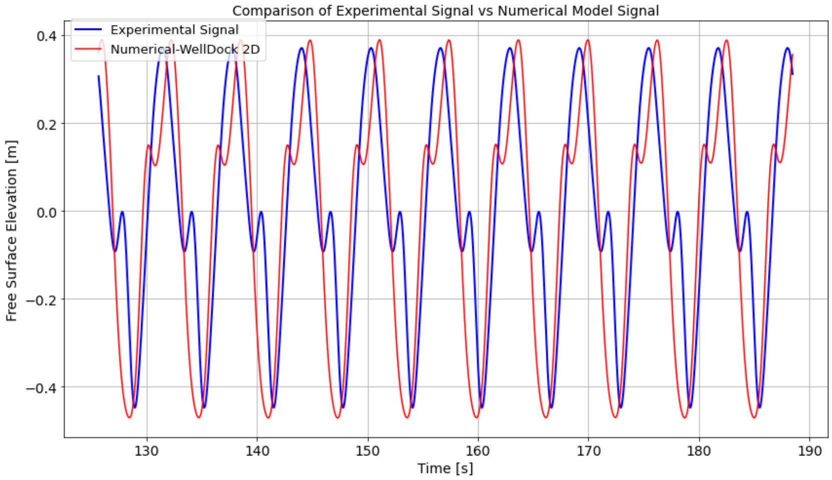

Figure 8.16: Comparison of Time-Domain Signal for Free Surface Elevation between the Viable Model and the Experimental Model

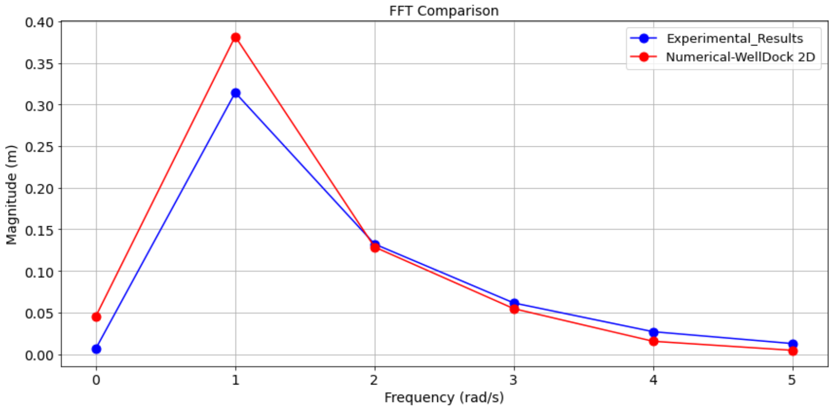

Figure 8.17: Comparison of the Fast Fourier Transformation Analysis for Six Fourier Components between the Viable Model and the Experimental Model

8.8.4. Line1 - Free Surface Elevation at dock entrance for wave frequency 0.7 rad/s

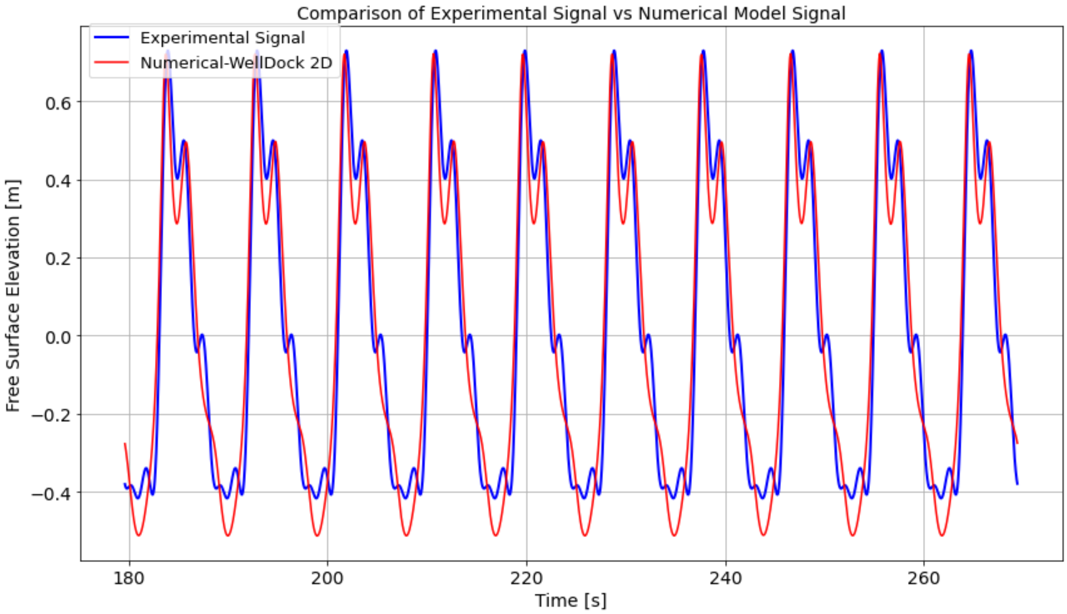

Figure 8.18: Comparison of Time-Domain Signal for Free Surface Elevation between the Viable Model and the Experimental Models

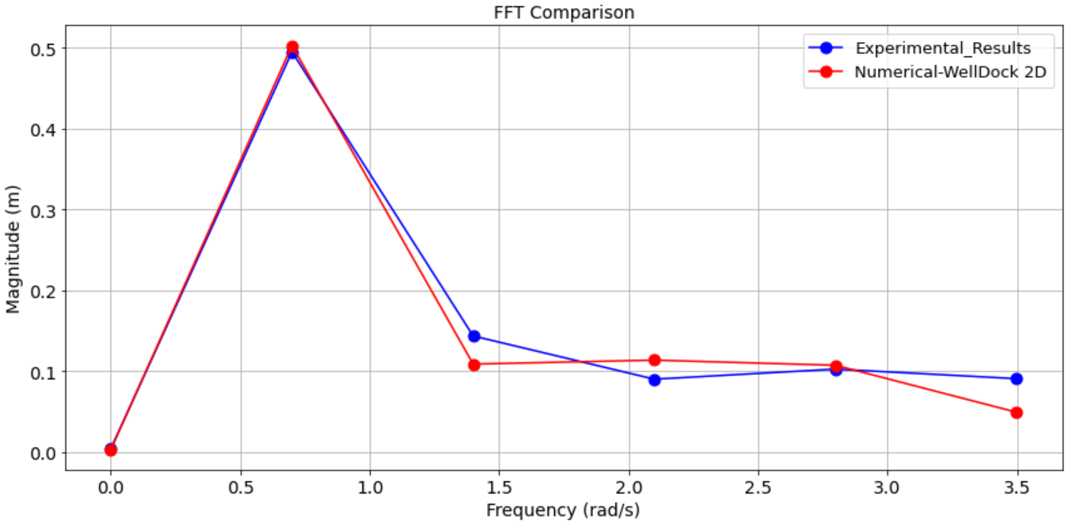

Figure 8.19: Comparison of the Fast Fourier Transformation Analysis for Six Fourier Components between the Viable Model and the Experimental Models

8.8.5. Line2 - Free Surface Elevation at middle of the dock for wave frequency 0.7 rad/s

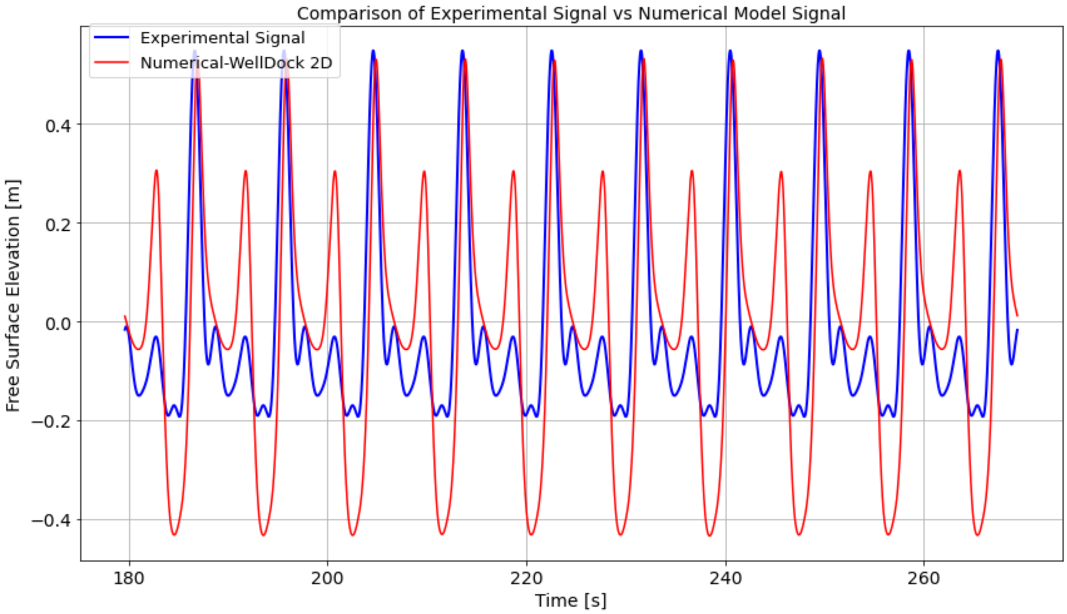

Figure 8.20: Comparison of Time-Domain Signal for Free Surface Elevation between the Viable Model and the Experimental Models

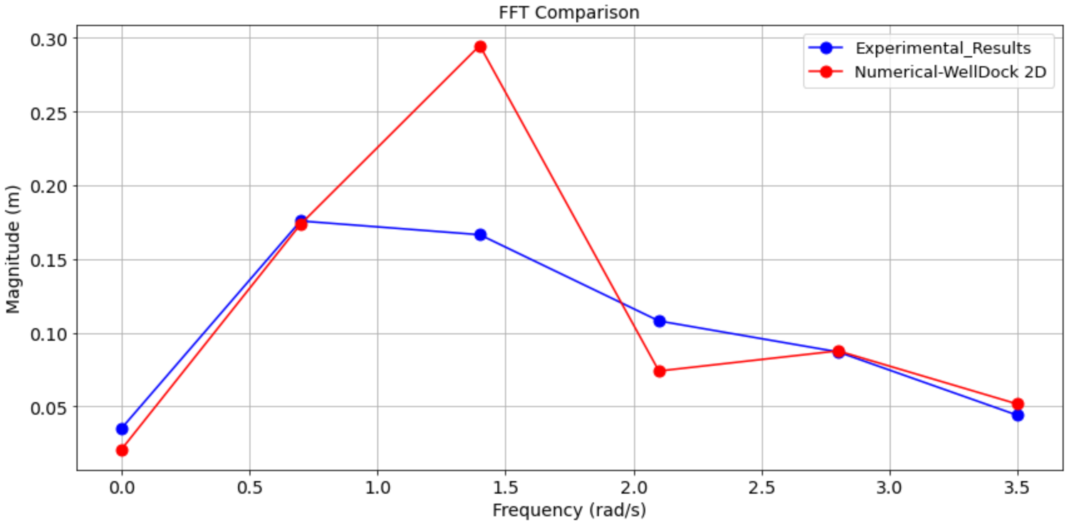

Figure 8.21: Comparison of the Fast Fourier Transformation Analysis for Six Fourier Components between the Viable Model and the Experimental Models

8.8.6. Line3 - Free Surface Elevation at end of the dock for wave frequency 0.7 rad/s

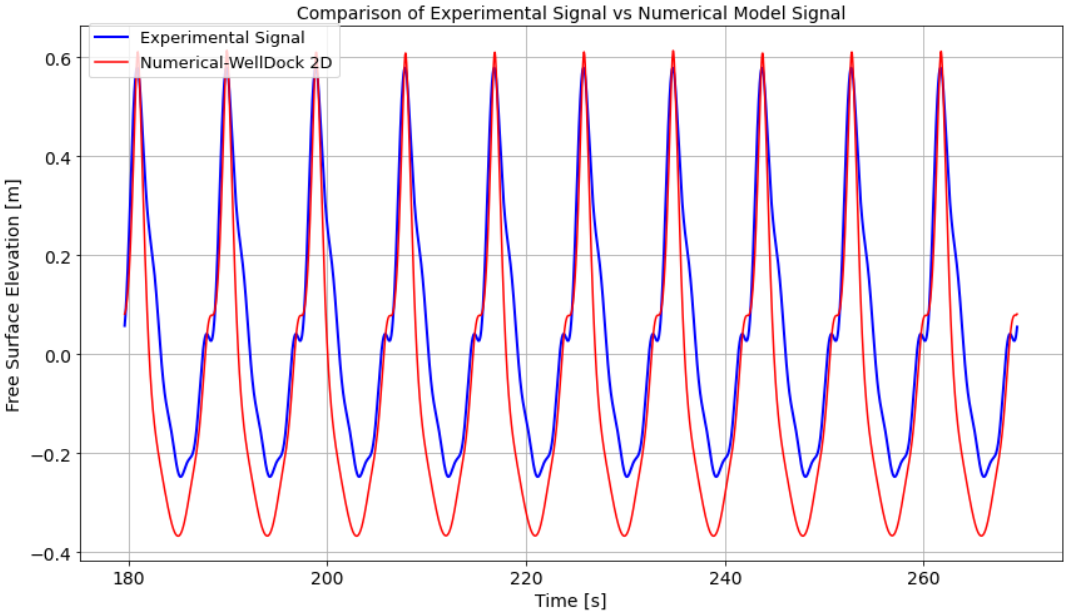

Figure 8.22: Comparison of Time-Domain Signal for Free Surface Elevation between the Viable Model and the Experimental Models

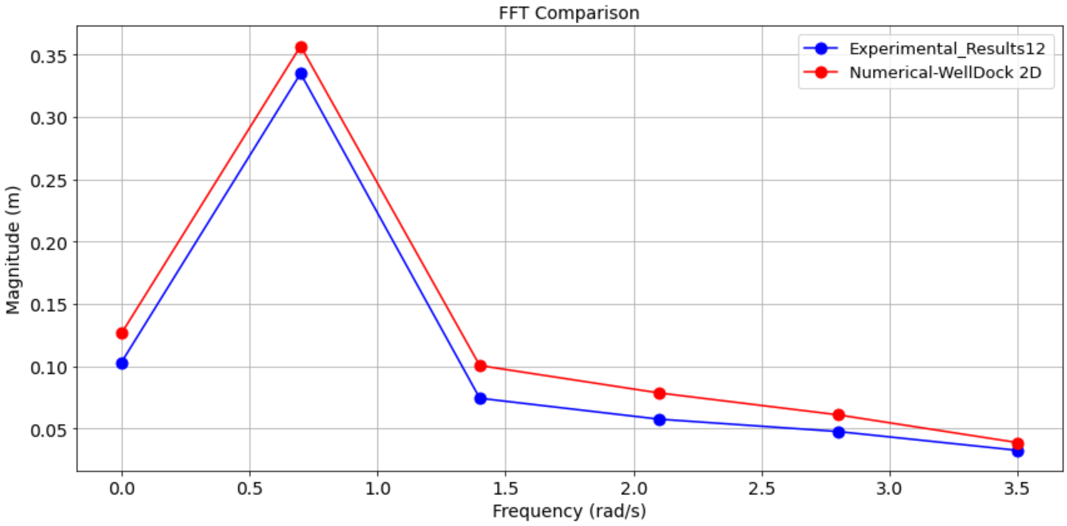

Figure 8.23: Comparison of the Fast Fourier Transformation Analysis for Six Fourier Components between the Viable Model and the Experimental Models

8.8.7. Line1 - Free Surface Elevation at dock entrance for wave frequency 0.4 rad/s

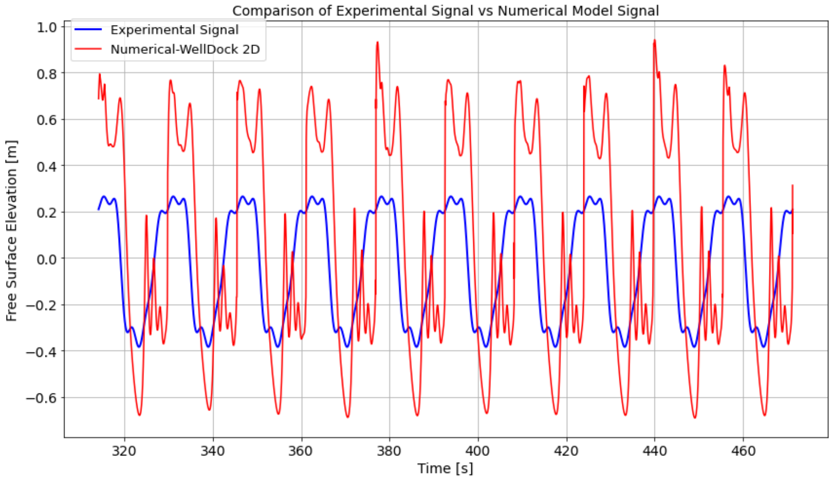

Figure 8.24: Comparison of Time-Domain Signal for Free Surface Elevation between the Viable Model and the Experimental Model

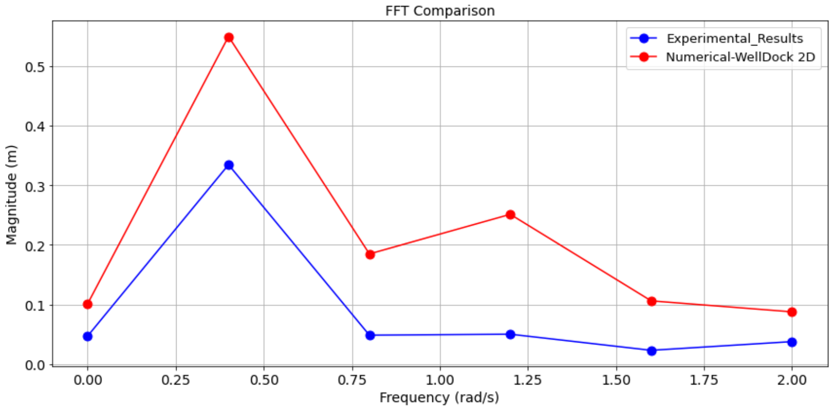

Figure 8.25: Comparison of the Fast Fourier Transformation Analysis for Six Fourier Components between the Viable Model and the Experimental Model

8.8.8. Line2 - Free Surface Elevation at middle of the dock for wave frequency 0.4 rad/s

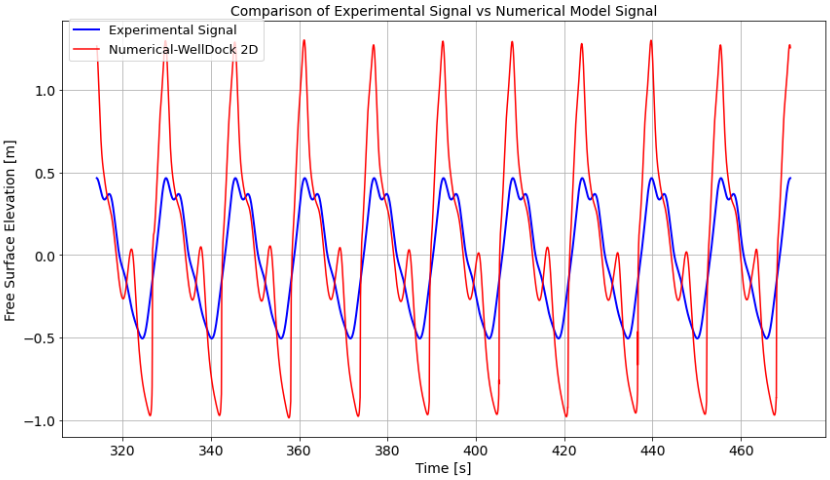

Figure 8.26: Comparison of Time-Domain Signal for Free Surface Elevation between the Viable Model and the Experimental Model

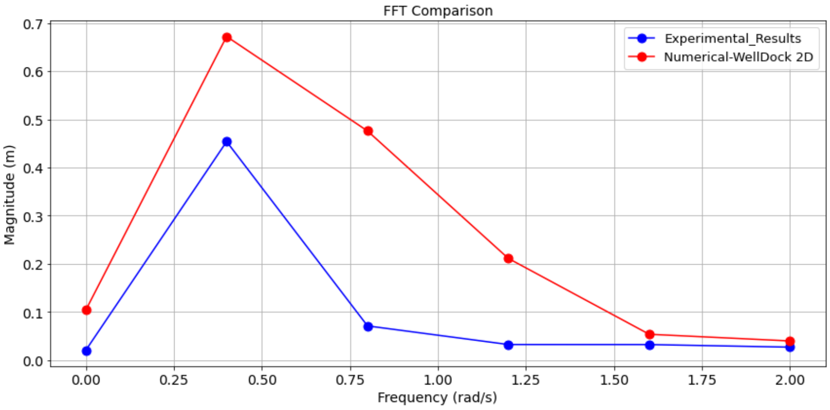

Figure 8.27: Comparison of the Fast Fourier Transformation Analysis for Six Fourier Components between the Viable Model and the Experimental Model

8.8.9. Line3 - Free Surface Elevation at end of the dock for wave frequency 0.4 rad/s

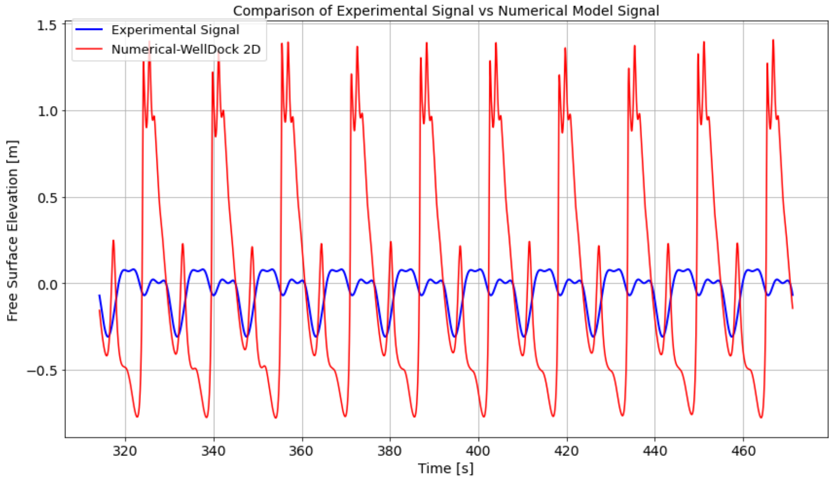

Figure 8.28: Comparison of Time-Domain Signal for Free Surface Elevation between the Viable Model and the Experimental Model

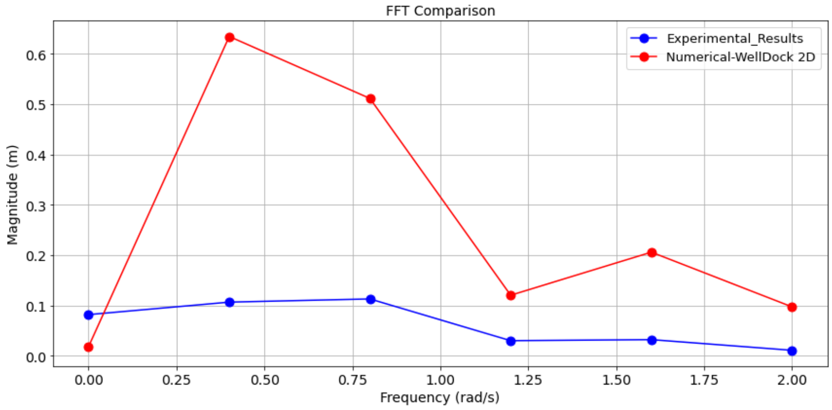

Figure 8.29: Comparison of the Fast Fourier Transformation Analysis for Six Fourier Components between the Viable Model and the Experimental Model

8.9. Discussion - Viable Model vs. Experimental Results

This section discusses the graphs presented in Section 8.8, which compare the viable model-developed to enhance the efficiency of the design process-with the experimental model from Chapter 4. This examination is conducted across three different wave frequencies: 0.4, 0.7, and 1 rad/s, comparing the experimental and the viable model. The cornerstone of this section is to explore the possibility of utilizing the viable model as a tool for the flow analysis within the well dock, aiming to reduce computational costs and time.

Sections 8.8.1, 8.8.2, and 8.8.3 focus on the wave frequency of 1 rad/s. A close examination of the results shows a clear alignment between the viable model and the model tests. Yet, when delving into the fast Fourier transformation analysis, a difference is noticeable in the wave probe at the dock entrance as illustrated in Figure 8.13, where the first (A1) and second (A2) Fourier components are a bit higher than the experimental. However, the wave probes in the other two regions predict almost perfectly the model tests.

Sections 8.8.4, 8.8.5, and 8.8.6 offer a detailed graphical analysis of data for a wave frequency of 0.7 rad/s. The results consistently demonstrate that, in most instances, the numerical model aligns closely with the experimental findings from the model test. Nevertheless, upon a closer examination through the fast Fourier transformation analysis reveals some notable discrepancies. Notably, the amplitude of the second Fourier component, recorded by the wave probe located in the middle of the dock, is higher compared to the model test, a discrepancy that is clearly illustrated in Figure 8.21. In contrast, the trends of the Fourier components at the dock's entrance and end align well with the experimental results, as depicted in Figures 8.19 and 8.23.

In Sections 8.8.7, 8.8.8, and 8.8.9, the analysis delves into the free surface elevation of a longer wave with a frequency of 0.4 rad/s. The findings show a discrepancy between the predictions from the viable model and the observed behavior in the model tests. A primary factor contributing to this discrepancy is the difference in the length of the well dock compared to the wavelength of the wave. In this scenario, the discrepancy between these two measurements plays a crucial role because the entire domain is the well dock, and there is no space for the development of the wavelength as occurs in the models of Chapter 6 (Physical Mechanisms Model) and Chapter 7 (Full Models). To elaborate further, the well dock has a length of approximately 65 meters, whereas the wavelength measures 73.38 meters. Consequently, the ratio of the dock's length to the wavelength, denoted as Ldock/λ, is roughly 0.88. Due to this size disparity with the wavelength being larger than the well dock (73.38 meters in contrast to 65 meters) the well dock cannot accommodate a complete wave cycle. This means that the wave does not fully develop within the confines of the dock, leading to a wave height that is not physically high. Additionally, a significant issue is identified in the first two Fourier components (A0 and A1), where there is a notable deviation when compared to the experimental data. This deviation was initially highlighted in Chapter 6, where the physical mechanisms were analyzed independently, revealing an inaccuracy in capturing the radiation mechanism for large wavelengths. Additionally, Chapter 7 identifies an inaccuracy in capturing the radiation mechanism in the Full Model with a solid ramp, which provides the input parameters for the 2D model. Another factor contributing to these discrepancies is the inefficiency of the Generalized Absorbing Boundary Condition (GABC) in minimizing reflections for long waves, as established in Chapter 7.

In conclusion, this model closely mirrors experimental behaviors across all wave frequencies, with the notable exception of the longer wave, where significant deviations were observed. Following the analysis of the results, it was realized that the initial target of this model-utilizing the viable model as a tool for the flow analysis within the well dock, aiming to reduce computational costs and time-is achievable. Nevertheless, the use of the model for longer waves requires further investigation. In more detail, the constrained computational domain in the 2D simulation, the challenges in capturing the radiation mechanism and the inadequacy of GABC in effectively minimizing long wave reflections in the 3D simulation, are identified as key factors contributing to the non-physical wave amplitudes and the discrepancies between the simulation and experimental outcomes.

9

Conclusions and Recommendations

In September 1991, the Royal Netherlands Navy commenced the development of its first LPD vessel. For operating landing crafts, the LPD vessel was commissioned with a well dock at the stern, designed to station several landing crafts. Its primary task is to support amphibious operations, thus the vessel needs to have flexibility in (un)loading operations, not only in well-equipped ports but also in areas where limited or even no port facilities exist. Ensuring the safety of these operations is crucial, which necessitates a thorough investigation of water motions within the well dock.

9.1. Conclusions

During this thesis, the research questions were investigated in detail. The first research question explored the influence of the physical mechanisms (radiation and diffraction) and the effect of wavelength on these mechanisms. Furthermore, the interaction of these mechanisms was found to play an important role, contrasting with the cumulative effects of simply adding the physical mechanisms together. The second research question delved into the comparison between the Full Model and the Experimental findings, focusing on the deviations observed at longer wavelengths and the geometric modification of the ramp region, followed by an exploration of its integration in the Full Model. The third research question explored the Viable Model, aiming to enhance the efficiency of the design process. The following paragraphs elucidate the outcomes of these three research questions in greater detail.

Firstly, this thesis explored the physical mechanisms within the well dock independently, utilizing the ComFLOW software. The study prominently highlighted the dominance of radiation over diffraction at the dock entrance and the middle of the well dock for a short wavelength of 1 rad/s. The comprehensive analysis has showcased that the radiation mechanism significantly impacts the flow behavior, especially near the dock entrance, where its influence is pronounced. Additionally, the effect of varying wavelengths on radiation and diffraction was explored. In detail, a distinct trend was observed: both radiation and diffraction effects amplify as the wavelength increases from 61.57 meters to 385.237 meters. This finding emphasizes the importance of wavelength in influencing the physical mechanisms governing the flow within the well dock.

Furthermore, the cumulative effects of simply adding the physical mechanisms together was compared with both their experimental and the Full Model outcomes, which account for both radiation and diffraction from the outset. Notable deviations were observed, particularly for the first two Fourier components (A0 and A1), underscoring the importance of considering the interactions between radiation and diffraction for more accurate modeling. Regarding interactions, this refers to the interplay between incoming and reflected waves, noting destructive and constructive interference that significantly impact the wave height within the dock. A simplistic summation of the physical mechanisms neglects the interactions and non-linearities in these processes, as well as their significant implications on flow dynamics, which are crucial for a more accurate representation of the physical phenomena within the dock.

During the investigation of the second research question, the Full Model demonstrated a closer alignment with the experimental data, especially at shorter wavelengths. This alignment accentuates the potential accuracy of the full model in representing the flow dynamics within the well dock. On the flip side, deviations were observed at longer wavelengths, hinting at possible inaccuracies in capturing the radiation mechanism for these wavelengths. The deviations are most pronounced in the first two Fourier components (A0 and A1), indicating potential areas for model refinement. Moreover, the study investigated geometric modifications, particularly in the ramp region, to mitigate the effects of reflected waves within the well dock. The findings indicate a potential pathway for improving the model by considering geometric modifications that align more accurately with experimental outcomes. In addition, assessments conducted on the Full Model incorporating a rack ramp demonstrated improved outcomes for short wavelengths; however, these improvements were not observed for medium wavelengths when compared to the Full Model with a solid ramp. Interestingly, no substantial enhancements were noted for long wavelengths, indicating areas for further investigation and model refinement.

Regarding the inaccuracy in long wave simulations, a key aspect noted was the differential behavior in wave damping in ComFLOW, particularly between short and long waves. As Westhuis (2001) [22] indicated, short waves experience stronger damping than long waves. Section 2.5, citing Marlinde de Jonge (2011) [10], describes the simulation approach for long waves ($\omega = 0.4$ rad/s). A numerical beach with a 5% reflection coefficient (calculated by equation 2.2) was used, contrasting with the use of the GABC for short waves, which effectively absorbed all wave energy. De Jonge's findings suggest that ComFLOW may not accurately predict reflections for long waves.

During the exploration of the third research question, the focus was directed towards the Viable Model to ascertain its capability in reducing computational costs while still retaining accuracy. The insights derived from comparing the Viable Model against the Experimental Model yielded a notable finding: the Viable model can be used as a viable tool for the design process for flow analysis within the well dock. However, when it comes to its application for longer waves, there appears to be a necessity for additional research. The aim of this further investigation would be to enhance computational efficiency without compromising the level of accuracy.

9.2. Recommendations

Recommendations are made for further research on the flow analysis within the well dock for the improvement in Simulation Models, Modification of Well Dock Geometry, and in Experimental Set-up:

Improvement in Simulation Models

In scenarios involving longer wavelengths, inaccuracies were observed in capturing the radiation mechanism, resulting in non-physical wave heights. Addressing these inaccuracies could enhance the model's reliability and its applicability to real-world scenarios. One potential solution could be to separate the radiation mechanism into the vessel's different motions: surge, heave, and pitch, and to study them independently in order to find the inaccuracy. Another possible study is the investigation of different wave angles between the ship's bow and the wave direction in the model (thus including also the wave directions of 45° and 60° in the dock) to simulate more realistic scenarios. Furthermore, investigate the effects of a broader range of wave frequencies on the flow dynamics within the well dock. This study focused on wave frequencies of 0.4, 0.7, and 1 rad/s. Expanding the range of wave frequencies analyzed could provide a more comprehensive understanding of flow dynamics within the well dock.

Reflection Minimization for Long Waves

This study highlights that while the GABC is effective in absorbing short, steep waves (thus minimizing back reflection), its performance in absorbing long waves with minimal reflection is uncertain. For long waves, more advanced techniques might be necessary for effective reflection minimization. Potential strategies include employing sponge layers, relaxation zones, or specialized absorbing boundary conditions that are tailored to the unique characteristics of long waves.

Modification of Well Dock Geometry

Modifying the geometry in the ramp region showed the potential this has in reducing the effects of reflected waves. Exploring other geometric modifications, like altering the shape of the ramp or the dock door, could further improve the model.

Experimental Setup

Conducting more experimental studies with different well dock geometries and wave conditions could provide a broader understanding of the flow dynamics and validate the numerical models further.

These recommendations reflect a rich, nuanced understanding of the flow dynamics within the well dock of an LPD vessel. They highlight areas of success, potential model refinements, and pathways for future investigations. The aim is to foster a deeper understanding and more accurate modeling of the complex interactions occurring within such maritime structures, which will, in turn, contribute to enhancing operational effectiveness and safety.

References

[1] *Ansys Fluent Theory Guide*. USA, July 2021.

[2] Bruce Cartwright, Damian McGuckin, T. Turner, and S. Cannon. “The modeling of landing craft motions inside a flooded well dock using smoothed particle hydrodynamics”. In: (Apr. 2006).

[3] Bruce Cartwright, G. Renilson, Gregor Macfarlane, Damian McGuckin, and S. Cannon. “Motions of a landing craft in a flooded well dock - effect of well dock design”. In: (Jan. 2007).

[4] Paul H.L. Groenenboom Bruce K. Cartwright. “Hydrodynamics and fluid-structure interaction by coupled SPH-FE method”. In: *Journal of Hydraulic Research* (Dec. 2010).

[5] Damen. URL: `https://career.damen.com/about-damen/`.

[6] David Molyneux Kevin McTaggart Don Bass. “Simulating Wave Action In The Well Deck Of Landing Platform Dock Ships Using Computational Fluid Dynamics”. In: *Naval Engineers Journal* (June 2004).

[7] G. Fekken, Arthur Veldman, and Bas Buchner. “Simulation Of Green Water Loading Using The Navier-Stokes Equations”. In: (June 2001).

[8] Geert K. Kapsenberg Egbert Marnix Krikke Hans Hopman. “Design and Hydromechanic Aspects of the Amphibious Transport Vessel for the Royal Netherlands Navy”. In: *Naval Engineers Journal* (May 1994), pp. 163–174. DOI: `10.1111/j.1559-3584.1994.tb02849.x`.

[9] C. W. Hirt and B. D. Nichols. “Volume of fluid (VOF) method for the dynamics of free boundaries”. In: *Journal of Computational Physics* (1981).

[10] Marlinde de Jonge. “Predicting the wave climate in the well dock of a Landing Platform Dock ship using Computational Fluid Dynamics”. In: (July 2011).

[11] J.M.J. Journée, W.W. Massie, Faculty of Civil Engineering Delft University of Technology, Geosciences, R.H.M. Huijsmans, et al. *Offshore Hydromechanics*. TU Delft, 2000. URL: `https://books.google.gr/books?id=eN66jwEACAAJ`.

[12] C. W. Hirt M. R. Barkhudarov. “Casting simulation: Mold filling and solidification – Benchmark calculations using FLOW-3D”. In: (Dec. 1995). URL: `https://www.osti.gov/biblio/227825`.

[13] Philip Mocz. “Smoothed Particle Hydrodynamics: Theory, Implementation, and Application to Toy Star”. In: (Sept. 2011).

[14] Damen Naval. URL: `https://media.damen.com/image/upload/v1632689459/catalogue/defence-and-security/custom-built-lpds/product-seet-rotterdam-lpd1-800.pdf`.

[15] Damen Naval. URL: `https://media.damen.com/image/upload/v1632689461/catalogue/defence-and-security/custom-built-lpds/product-sheet-johan-de-witt.pdf`.

[16] Damen Naval. URL: `https://www.damen.com/companies/naval`.

[17] P. van der Plas. 2018. URL: `https://poseidon.housing.rug.nl/sphinx/index.html`.

[18] Marine Schepen. URL: `https://marineschepen.nl/schepen/rotterdam.html`.

[19] Marine Schepen. URL: `https://marineschepen.nl/schepen/johandewitt.html`.

[20] OFA van Straten. “Onderzoek naar het bewegingsgedrag van de Enforcer serie”. In: (Oct. 1999).

[21] Rik Wemmenhove, Erwin Loots, and Arthur Veldman. “Hydrodynamic Wave Loading on Offshore Structures Simulated by a Two-Phase Flow Model”. In: Jan. 2006. DOI: `10.1115/OMAE2006-92253`.

[22] Jaap-Harm Westhuis. "The numerical simulation of nonlinear waves in a hydrodynamic model test basin". English. In: (May 2001).

[23] Frank M. White. *Viscous Fluid Flow*. 3rd ed. New York, USA: McGraw-Hill, 2006.

[24] Lynyrd de Wit. "A Study of the possibilities of SPH in hydraulic engineering". In: (Apr. 2006).

[25] Gang Xu, Tian-Rui Mei, Ming-Liang Hu, Zhen Chen, and Jun-Ming Hu. "Hydrodynamic Analysis of Ship with Well Deck in the Linear Numerical Wave Tank". In: *Mathematical Problems in Engineering* 2020 (2020), pp. 1–15. URL: `https://EconPapers.repec.org/RePEc:hin:jnlmpe:3804748`.

A

Landing Platform Dock Ship

A.1. Introduction

In September 1991, it was decided that the Netherlands would build an Amphibious Transport Ship (ATS), designed as a Landing Platform Dock (LPD), to support the Dutch armed forces in general and the Royal Netherlands Navy (RLNL) specifically. The ship is to be deployed in both national and international scenarios, e.g. in conjunction with the Royal Navy (RN) in the United Kingdom/Netherlands Amphibious Force (UK/NL AF). Therefore commonalities in design and operation with British amphibious ships have been a leading principle as far as operationally relevant.

A.2. Operations and Tasks

The ATS was deployed to operate as part of the UK/NL AF(Amphibious Force), but the ship may also participates in another NATO or multinational (amphibious) task group or force. Also there are occasions where the ATS operates independently and/or within non-military scenarios. The main tasks of the ATS are:

1. **Support of Amphibious Operations**

   The vessel requires versatility of its embarkation and disembarkation methods, not just in well-equipped ports, but also in locations where there are limited or no port facilities available.

2. **Non-Amphibious Tasks**

   In conditions where the ship is not required for redeploying the landing force, it can be utilized for the transfer of reserves or the evacuation of casualties.

3. **Peacetime Tasks**

   The ship can serve as a platform for conducting counter-terrorism operations. In addition, it is utilized for fleet replenishment, disaster relief, humanitarian aid operations such as providing assistance to refugees and medical treatment for casualties, as well as for environmental purposes.

A.3. Well Dock Procedure

The primary responsibility of the LPD is to provide support for amphibious operations. However, landing craft operations also play a vital role in this support and therefore have a significant impact on the design of the well dock in order to meet the necessary requirements. When the ship is in transit, the dock gate is closed, and the dock floor, which carries the landing craft, remains above water level. Once the ship reaches its location, the ballast tanks in the aft of the ship are filled to the required water level. The stern gate is lowered and held in place with hydraulically operated rams. The sloping stern gate creates a suitable environment for embarking and disembarking landing craft. The inboard end of the dock is typically a ramp, which is useful for driving equipment from the parent ship into the landing craft. To load the landing craft into the flooded well dock, the craft approaches the parent ship from behind. Once it reaches a short distance from the gate, the landing craft turns into the wake and enters the flooded dock.[8]

A.4. Landing Platform Dock ship Hr. Ms. Rotterdam

Damen constructed the first LPD vessel in 1998, which was named "Hr. Ms. Rotterdam." This ship is designed to provide support for amphibious operations around the world. The Rotterdam has the ability to conduct helicopter operations in high sea states of up to Sea State 6, and it can also operate with landing craft in up to Sea State 4. As an amphibious support ship, it is capable of transporting and disembarking a Marine Corps battalion, including all associated combat and logistical support vehicles and equipment. The ship's key dimensions are listed in Table 1.[18]

Overall Length (m)	166.2
Moulded Beam (m)	25
Draught (m)	5.8
Displacement full load (ton)	12750
Speed (max power) (knots)	20

Table A.1: Dimensions LPD1

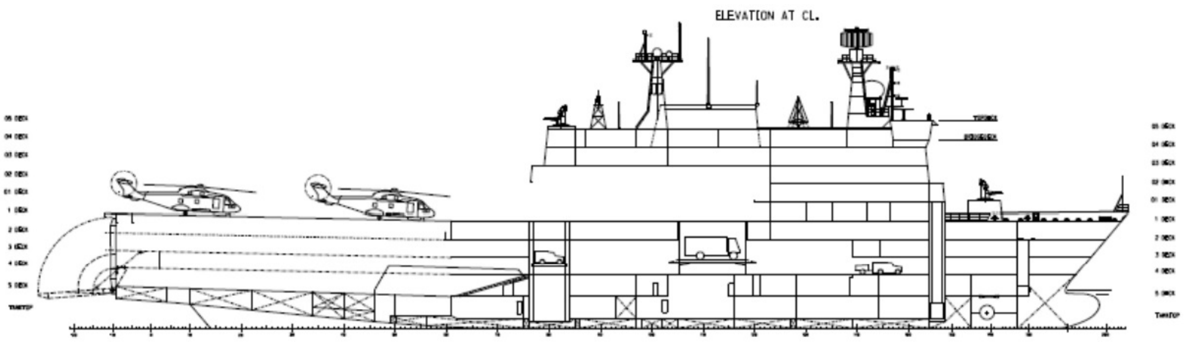

Figure A.1: Side view "HR. MS. Rotterdam"[14]

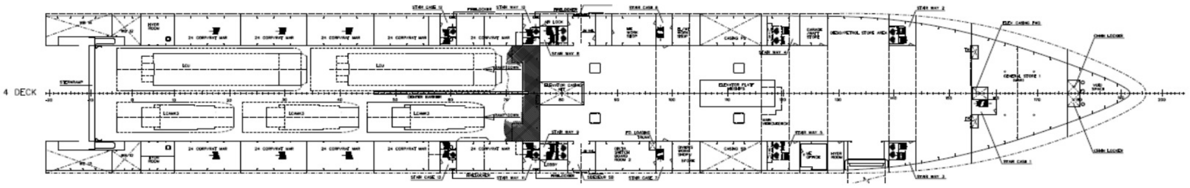

Figure A.2: Top view at fourth deck "HR. MS. Rotterdam"[14]

A.5. Landing Platform Dock ship Hr. Ms. Johan de Witt

In 2007, the Dutch Navy commissioned the second ship in this category. This new ship is an upgraded version of the Rotterdam, with additional capabilities for amphibious command and control, as well as a larger flight deck. The ship is also 10 meters longer and one meter wider than its predecessor. One of the ship's unique features is its ability to accommodate a Combined Joint Task Force headquarters, which can include up to 400 personnel. The ship is versatile and can be used for a variety of missions, including military transportation or disaster relief efforts. The Johan de Witt can transport more vehicles than the Rotterdam and has proven to be effective in dock and helicopter operations in various weather conditions. The design of the Johan de Witt includes spacious operational areas, deck areas, and access routes, making it adaptable to a variety of tasks. The ship also has advanced medical and surgical facilities.[19]

Overall Length (m)	176.35
Moulded Beam (m)	27.2
Draught full load (m)	6.15
Displacement full load (ton)	16680
Speed (max power) (knots)	18

Table A.2: Dimensions LPD2

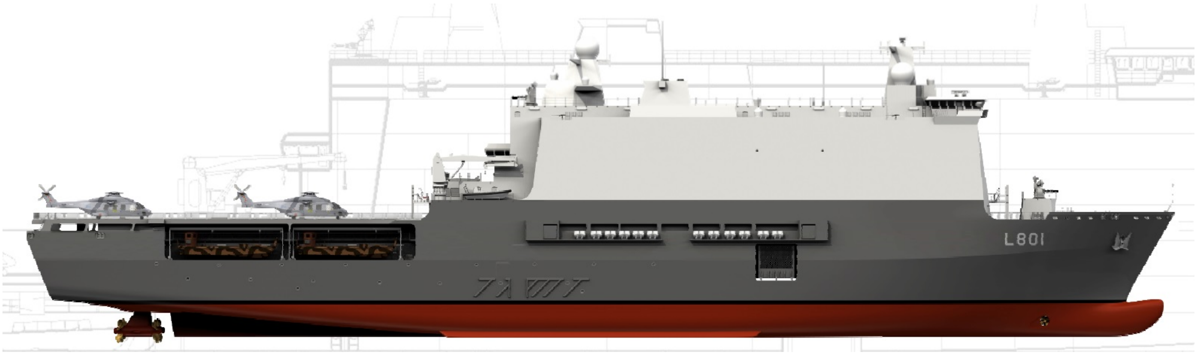

Figure A.3: Side view "HR. MS. Johan De Witt"[15]

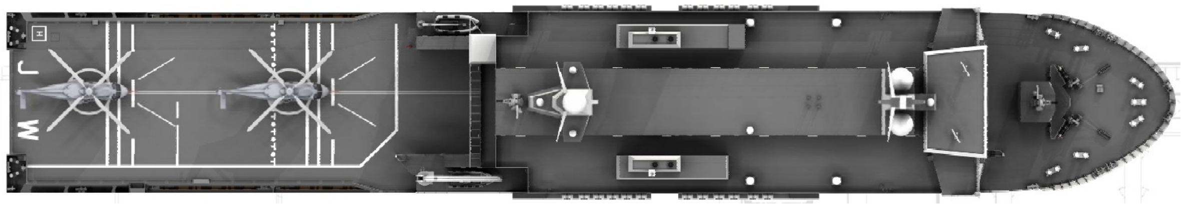

Figure A.4: Top view at fourth deck "HR. MS. Johan De Witt"[15]

A.6. Damen Shipyards Group

Damen Shipyards was founded in 1927 by Jan and Marinus Damen in Hardinxveld. In 1969, Kommer Damen, the son of Jan Damen, took over the company. Damen is renowned for its innovative approach to building standardized ships, series production, and the ability to deliver ships off the shelf. The Damen Shipyards Group consists of 55 companies worldwide, with 24 located in the Netherlands and 31 in other countries. Overall, Damen Shipyards employs more than 12,000 people worldwide. Since 1969, it has designed and built over 6,000 vessels and delivers more than 150 vessels annually. Damen is actively engaged in ship construction, as well as maintenance and repair activities. It offers a diverse product range, including tugs, workboats, patrol craft, cargo vessels, dredgers, superyachts, and fast ferries. In 2020, Arnout Damen, the son of Kommer, became CEO, a decision that reflects a forward-looking focus on sustainability, digitalization, and operational excellence.[5]

A.7. Damen Naval

Royal Schelde was founded in the year 1875 and became a member of the Damen Shipyards Group in 2000. Today Royal Schelde's main activity is Naval Shipbuilding. In fact Royal Schelde has been involved in most projects for the Royal Netherlands Navy's new surface combatants and support ships such as the Enforcer.Having delivered more than 400 vessels to customers all around the world, Damen Schelde Naval Shipbuilding is a naval shipyard that makes optimal use of its know-how and experience from both the military and commercial sectors and is specialised in the design and construction of naval vessels and complex commercial vessels.[16]

B

Literature Study

B.1. Computational Fluid Dynamics

Computational Fluid Dynamics is a branch of engineering and applied mathematics that involves the use of numerical methods and algorithms to analyze and solve problems related to fluid dynamics, such as the motion and behavior of liquids and gases. CFD simulations are used to predict how fluids will behave in various situations, such as how air will flow around an aircraft wing or how water will flow through a pump. CFD simulations involve creating a virtual model of the fluid system being studied, and applying mathematical equations that describe the behavior of the fluid under different conditions. These equations may include the Navier-Stokes equations, which describe the motion of fluids, as well as equations for heat transfer and other physical phenomena. The equations used in Computational Fluid Dynamics (CFD) depend on the specific problem being studied and the assumptions made about the fluid flow. However, in general, CFD equations can be categorized into two main types: governing equations and closure models. Governing equations are the fundamental equations of fluid dynamics that describe the behavior of the fluid being studied. These equations include:[23]

1. Continuity equation: This equation expresses the conservation of mass in a fluid system, stating that the rate of change of mass within a control volume is equal to the net mass flow into or out of the volume.

$$\frac{\partial \rho}{\partial t} + \nabla\left(\rho \boldsymbol{u}\right) = 0 \tag{B.1}$$

   where ρ is the fluid density, t is time, $\boldsymbol{u}$ is the velocity vector, and ∇ is the divergence operator.
2. Momentum equations: These equations describe the motion of fluid particles in terms of their velocity, pressure, and density, and include terms for the viscous forces that result from friction between fluid particles.

$$\rho\left[\frac{\partial \boldsymbol{u}}{\partial t} + \boldsymbol{u}\left(\boldsymbol{\nabla}\cdot\boldsymbol{u}\right)\right] = -\boldsymbol{\nabla} p + \rho \boldsymbol{g} + \mu \boldsymbol{\nabla}^2 \boldsymbol{u} \tag{B.2}$$

   where $\frac{\partial \boldsymbol{u}}{\partial t}$ is the change of velocity with time, $\boldsymbol{\nabla} p$ is the pressure gradient, $\rho\boldsymbol{g}$ is the body force term with represents all the external forces that act on the fluid and the last term which is $\mu\boldsymbol{\nabla}^2\boldsymbol{u}$ and represents the diffusion term.

Closure models are additional equations that are used to model the effects of turbulence, heat transfer, and other phenomena that are not explicitly described by the governing equations. These models are based on empirical data and are used to provide closure to the governing equations.
CFD equations are typically solved numerically using techniques such as finite volume, finite element, or finite difference methods, and the resulting solutions provide detailed information about the fluid flow variables, such as velocity, pressure, and temperature, over a given domain and time period.

B.1.1. Fractional Volume-of-Fluid (FVOF)

The FVOF method enhances the accuracy of the basic VOF method by employing a more precise advection scheme for the volume fraction function. FVOF considers the movement of the volume fraction in a more detailed manner, capturing the dynamics of the interface with higher fidelity. By preserving sharpness in the interface, the FVOF method can better represent phenomena such as breaking waves, droplet formation, and splashing[9]. This method is used from FLOW-3D software that developed by Flow Science and was initially designed to model fluid sloshing within liquid fuel tanks for rockets. Furthermore, FLOW-3D has the capability to simulate nonlinear, time-dependent flows in the time domain and utilizes the finite volume method for solving the Navier-Stokes equations. [12]

B.1.2. Smooth Particle Hydrodynamics

The smooth particle hydrodynamics (SPH) technique is a method that uses particles to simulate physical systems. Initially, its purpose was to model polytropic stellar structures when subjected to non-axisymmetric conditions, as proposed by Gingold and Monaghan (1977) and Lucy (1977)[13].

The SPH method is computationally expensive and represents fluids as a collection of individual particles, each characterized by its mass, position, velocity, and other relevant properties. The dynamics of the fluid are simulated by solving equations of motion for every particle while considering interactions with neighboring particles. However, the method has the advantage of being able to handle complex geometries and free surfaces, and can be used to model fluids with high viscosity.[24].

Unlike finite-difference approaches, SPH is a non-grid-based method. This method is fairly different from the previous one, which makes use of the VOF method to discretize the Navier-Stokes equations. Traditional calculation methods have a pure Eulerian approach, describing the fluid flow at a fixed point as a function of time. It is Langrangian in nature, which means that it calculates interactions and derivatives relative to a moving fluid element's coordinate system. SPH operates on two main principles: (1) updating particle positions and velocities by computing forces acting on each particle at each time step, and (2) using a smoothing/interpolating kernel to calculate forces and spatial derivatives.SPH is designed for strong nonlinear phenomena and has been used to calculate the wave climate in the dock of an LPD and even model the motions of the landing craft in the dock. Being a Lagrangian technique, SPH is well-suited for fluid-structure interaction problems [4]. Disadvantages of SPH are the complex determination of the correct boundary conditions and the accurate distribution of the particles. Regarding the boundary conditions, the SPH method can have difficulties in accurately simulating boundary conditions, such as solid walls and free surface. This could lead to inaccuracies in the simulation results near boundaries. As far as the particle distribution, if it is not uniform, it causes non-accurate results. Thus, SPH is a meshless method, with the body of the fluid represented by particles of fluid that are subjected to the second law of Newton, which says that a body of mass m, subject to a force F, undergoes an acceleration a that has the same direction as the force and a magnitude that is directly proportional to the force and inversely proportional to the mass.

B.1.3. Volume-of-Fluid (VOF)

At the heart of the VOF method is the concept of the volume fraction. This is a scalar value assigned to each computational cell which indicates the volume fraction of a particular phase (e.g., liquid) within that cell. A volume fraction of "1" means the cell is fully occupied by the fluid of interest (e.g., water). A value of "0" indicates the cell is devoid of that fluid (e.g., all air). A fraction between 0 and 1 indicates the cell is partially filled with the fluid, and there's an interface within that cell.The VOF method can handle topological changes, meaning it can simulate phenomena like merging or breaking apart of fluid bodies, making it versatile for a wide range of free surface problems. This method is used to capture and track the free surface in Ansys Fluent which is a computational fluid dynamics (CFD) software package. Ansys Fluent uses a set of partial differential equations (PDEs) to model fluid flow and heat transfer. These equations are derived from the fundamental principles of fluid mechanics and thermodynamics, including conservation of mass, momentum, and energy. The specific set of equations solved by Fluent depends on the type of fluid flow being simulated and the features of the geometry being analyzed. Fluent solves these equations numerically using finite volume method. The resulting solutions provide detailed information on the fluid flow behavior, temperature distribution, and other relevant parameters of the system being analyzed [1].

B.1.4. Piecewise Linear Interface Construction (PLIC) method

The VOF function is reconstructed using the Piecewise Linear Interface Construction (PLIC) method. PLIC aims to accurately capture the interface between two fluids by approximating it with piecewise linear segments. This approach enhances the VOF methods accuracy by effectively capturing the complex shapes of fluid interfaces. It proves especially beneficial for simulating flows with sharp and intricate interface geometries. To distinguish between cells with varying characteristics in the computational domain, labels are assigned to them. More details about this method are detailed in section 4.3. The PLIC method is used in ComFLOW software. The first CFD code to consider is ComFLOW, developed in 1995 at the University of Groningen to research the sloshing of liquid fuel in a spacecraft. ComFLOW is a program for the numerical simulation of fluid flow, based on the Navier-Stokes equations. Initially, it studied fluid flow problems concerning with free surface flows. Later, it was extended to study the impacting waves on moving objects, for example the analysis of green water loading. This makes ComFLOW a method that simulates flow problems with both free surfaces and the motions of offshore structures [7]. ComFLOW is based on the solution of the incompressible Navier-Stokes equations. It solves the Navier-Stokes equations in both water and (in)compressible air.The interface between fluid and gas is considered as a moving boundary. Since the finite volume approach is adopted in the discretization of the flow equations, the equations are given in conservative integral form. A stationary Cartesian grid is used to cover the computational domain and the variables are staggered, which means that the velocities are defined on the cell faces and the pressure is defined in the cell centers [17].

B.2. ComFLOW Literature Results

B.2.1. LPD1 set-up

SIMULATION MATRIX											
Run	ω [rad/s]	**T** [sec]	[m]	**d/λ** [-] **d: depth**	**Tmax** [sec]	**dtmax** [sec] **max timestep**	**Length domain** [-]	**Cell size** **x** [-]	**y** [-]	**z** [-]	Nr. of cells [*10^5]
2D Simulations											
1	0.40	15.71	80	0.028	157	0.063	0.8*	0.3	-	0.2	0.144
2	0.50	12.57	63	0.035	126	0.050	1.0*	0.3	-	0.2	0.144
3	0.55	11.42	57	0.039	114	0.046	1.1*	0.3	-	0.2	0.144
4	0.60	10.47	53	0.042	105	0.042	1.2*	0.3	-	0.2	0.144
5	0.65	9.67	48	0.046	97	0.039	1.3*	0.3	-	0.2	0.144
6	0.70	8.98	45	0.050	90	0.036	1.4*	0.3	-	0.2	0.144
7	0.725	8.67	43	0.052	87	0.035	1.5*	0.3	-	0.2	0.144
8	0.775	8.10	40	0.055	81	0.032	1.6*	0.3	-	0.2	0.144
9	0.80	7.85	39	0.057	79	0.031	1.6*	0.2	-	0.1	0.256
10	0.90	6.98	34	0.065	70	0.028	1.9*	0.2	-	0.1	0.256
11	1.00	6.28	31	0.073	63	0.025	2.1*	0.2	-	0.1	0.256
3D Simulations											
12	0.50	12.57	63	0.04	38	0.050	1.0*	0.3	0.8	0.2	2.88
13	0.70	8.98	45	0.05	27	0.036	1.4*	0.3	0.8	0.2	2.88
14	0.775	8.11	40	0.06	24	0.032	1.6*	0.3	0.8	0.2	2.88

Table B.1: Simulation matrix for 2D and 3D simulations of LPD1

B.2.2. Influence Numerical Beach

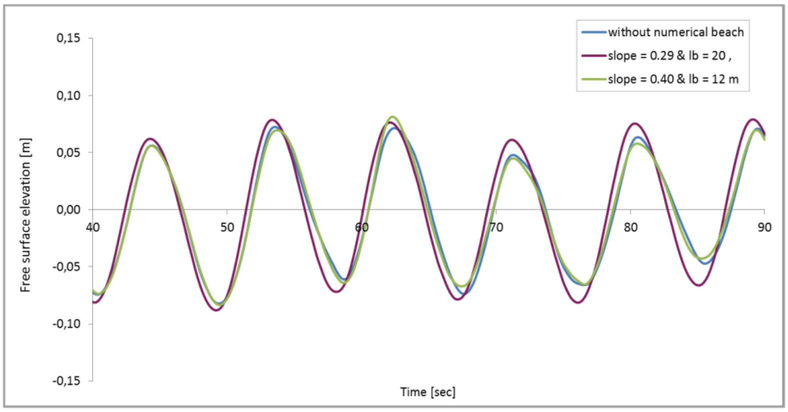

Figure B.1: Free surface elevation at the dock entrance

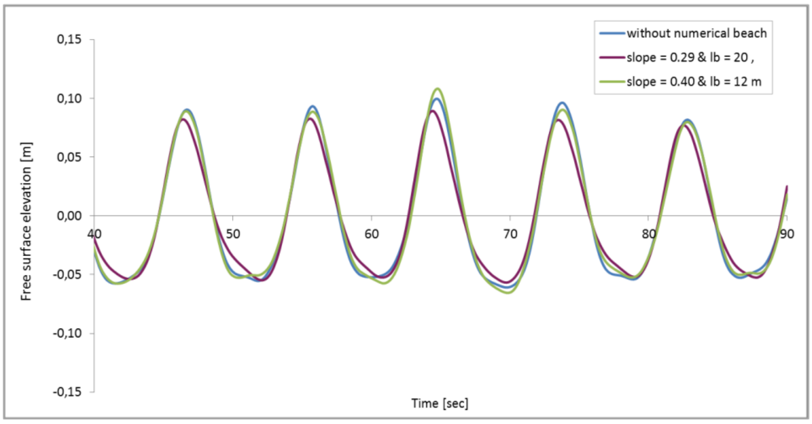

Figure B.2: Free surface elevation in the middle of the dock entrance

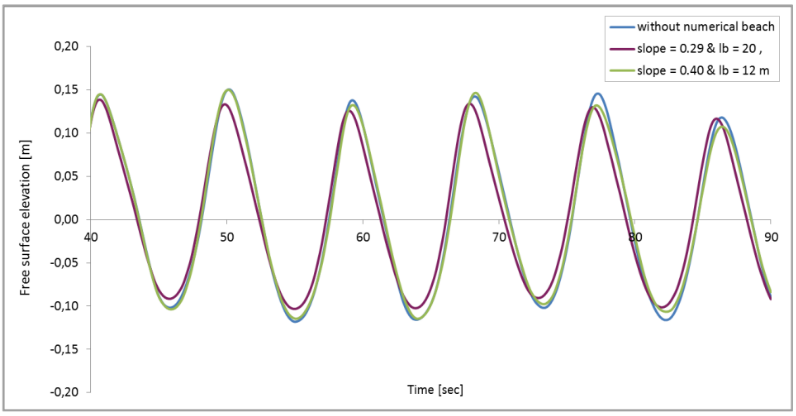

Figure B.3: Free surface elevation in the end of the dock

B.2.3. Results LPD1

B.2.3.1 Time traces free surface elevation at dock entrance

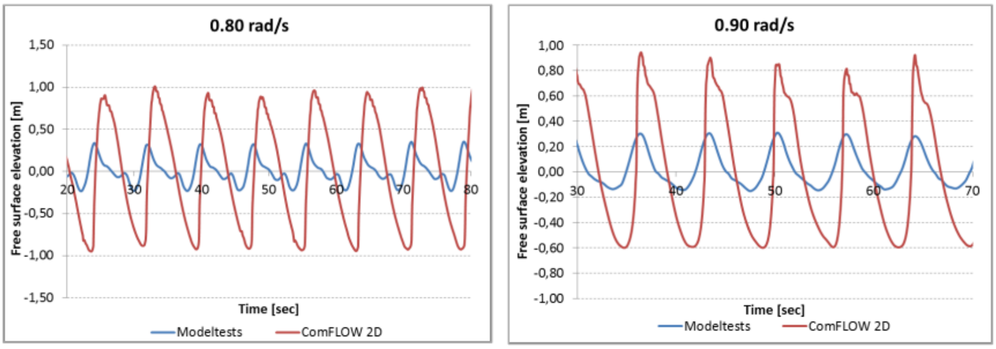

Figure B.4: Short waves for 2D simulations at x = 14.8m

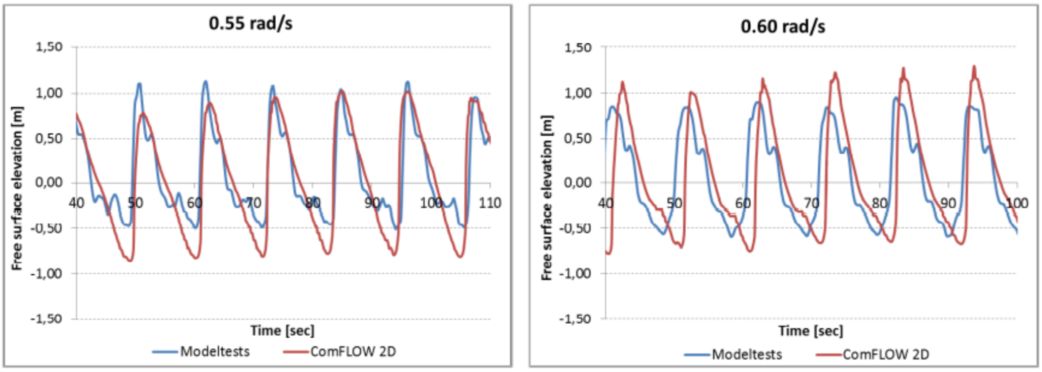

Figure B.5: Middle length of waves for 2D simulations at x = 14.8m

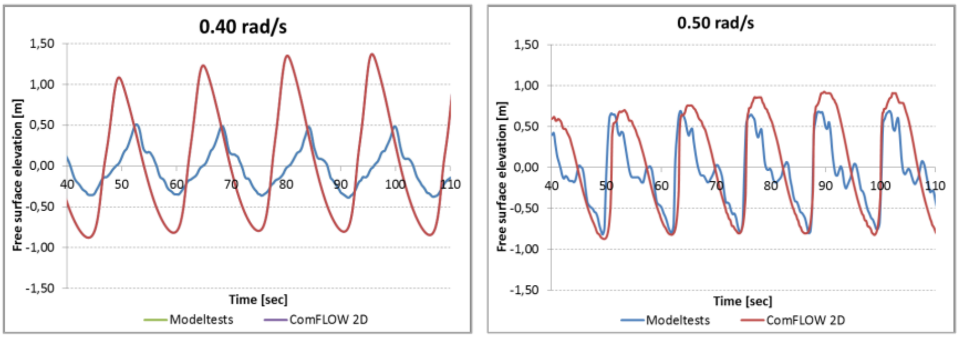

Figure B.6: Long waves for 2D simulations at x = 14.8m

B.2.3.2 Time traces free surface elevation at middle dock

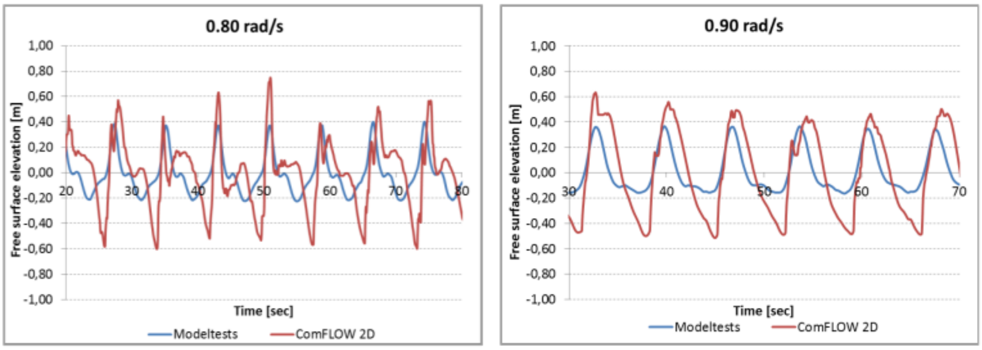

Figure B.7: Short waves for 2D simulations at x = 29.6m

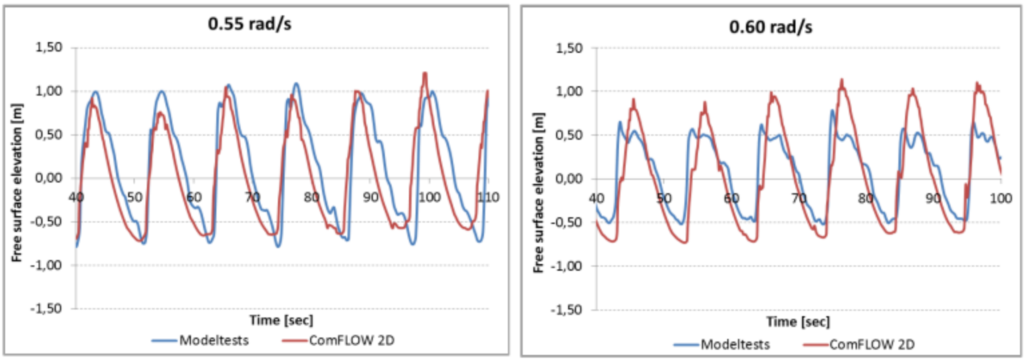

Figure B.8: Middle length of waves for 2D simulations at x = 29.6m

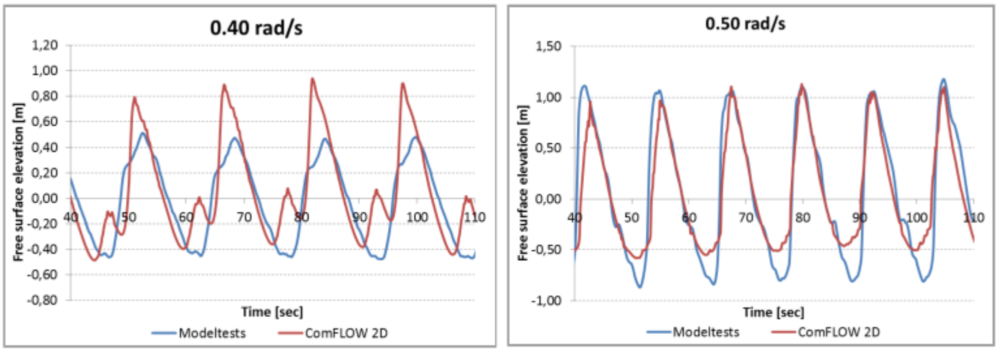

Figure B.9: Long waves for 2D simulations at x = 29.6m

B.2.3.3 Time traces free surface elevation at well dock end

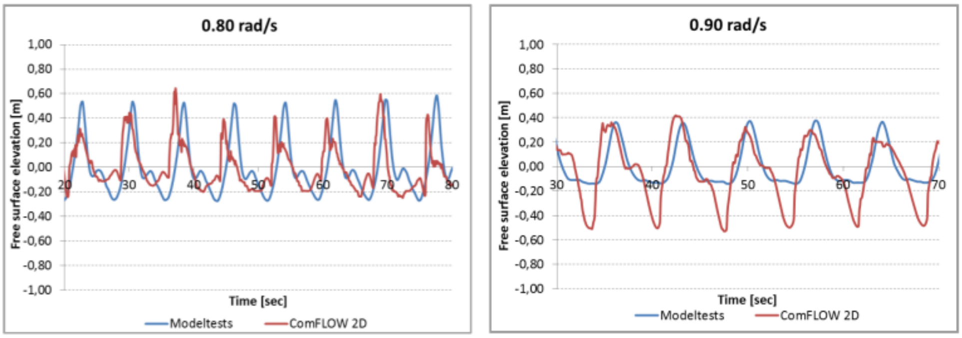

Figure B.10: Short waves for 2D simulations at x = 44.4m

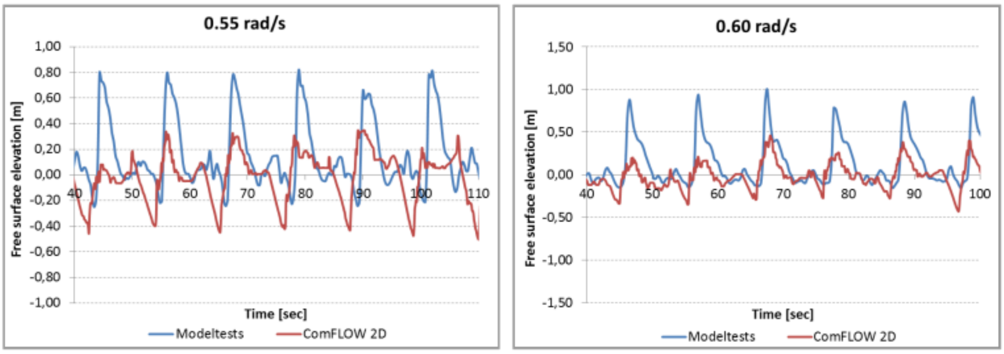

Figure B.11: Middle length of waves for 2D simulations at x = 44.4m

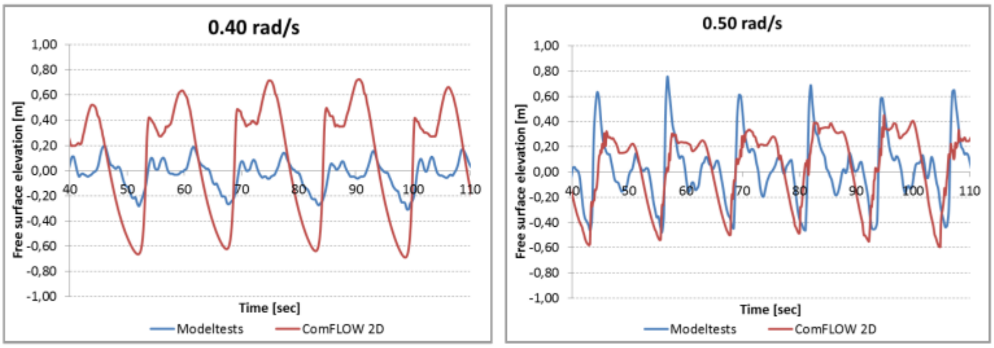

Figure B.12: Long waves for 2D simulations at x = 44.4m

B.2.3.4 Time traces three-dimensional simulations-model test

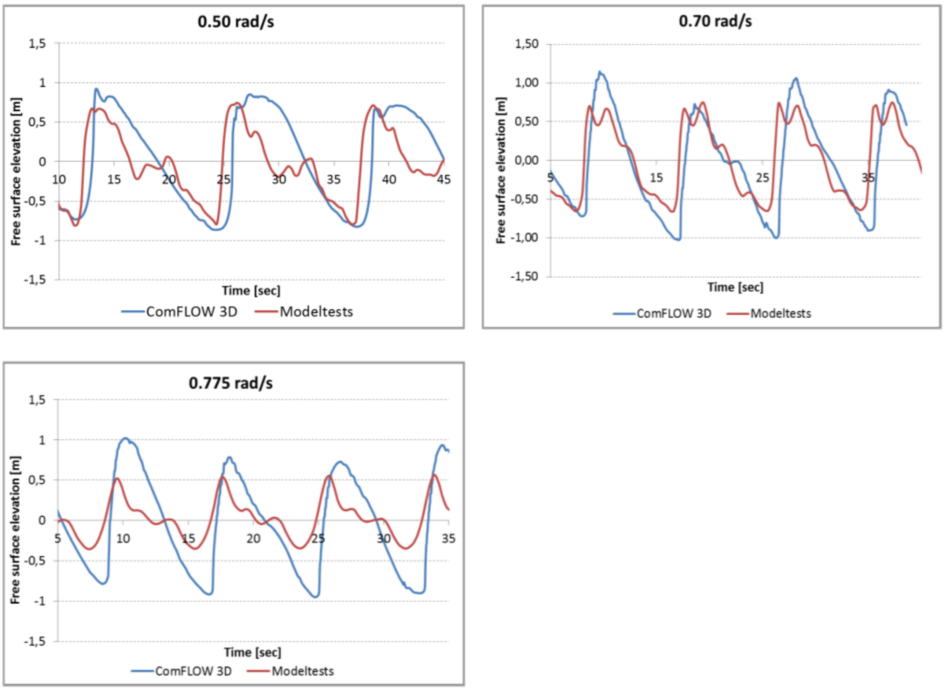

Figure B.13: Short waves for 3D simulations at x = 14.4m

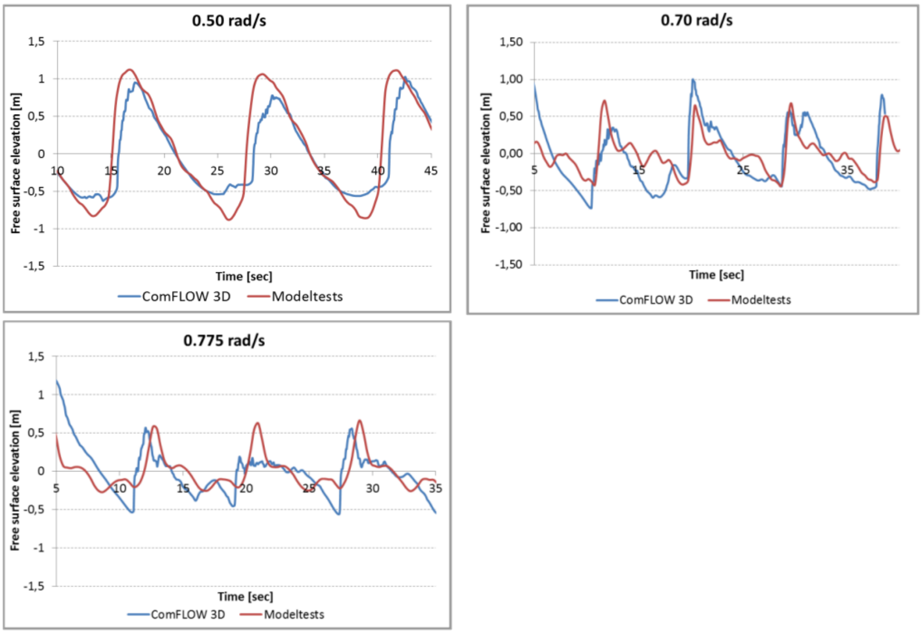

Figure B.14: Middle length of waves for 3D simulations at x = 29.6m

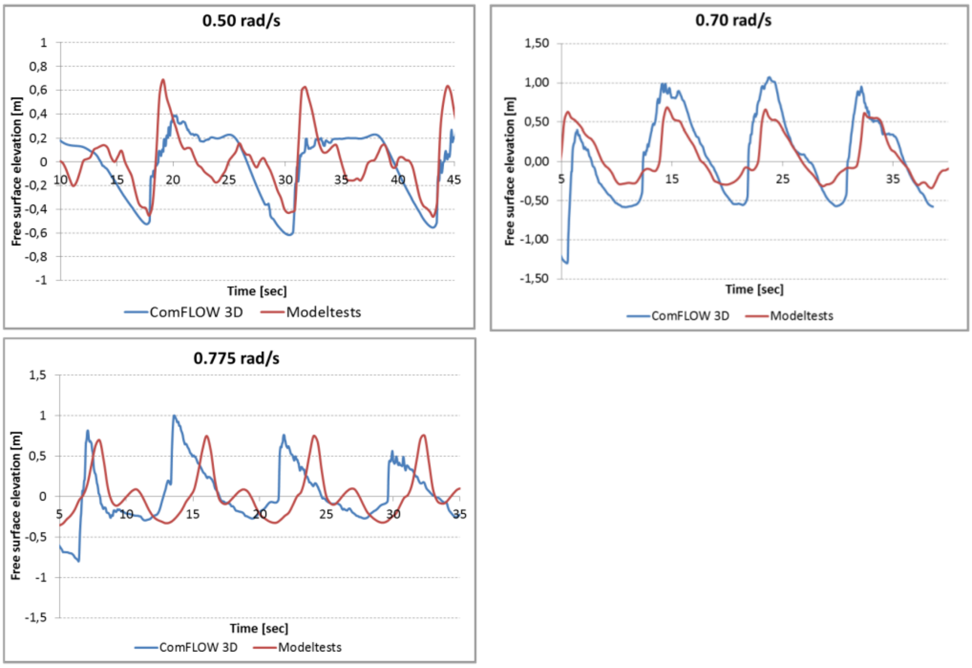

Figure B.15: Long waves for 3D simulations at x = 44.4m

B.2.4. LPD2

B.2.4.1 LPD2 set-up

SIMULATION MATRIX											
Run	ω [rad/s]	**T** [sec]	λ [m]	**d/λ** [-] **d: depth**	**Tmax** [sec]	**dtmax** [sec] **max timestep**	**Length domain** [-]	**Cell size x y z** [-] [-] [-]			Nr. of cells [*10ˆ5]
2D Simulations											
1	0.40	15.71	80	0.028	157	0.063	0.7*	0.22	-	0.17	0.14
2	0.50	12.57	63	0.035	126	0.050	0.8*	0.22	-	0.17	0.14
4	0.60	10.47	53	0.042	105	0.042	1.0*	0.22	-	0.17	0.14
6	0.70	8.98	45	0.049	90	0.036	1.2*	0.22	-	0.17	0.14
9	0.80	7.85	39	0.056	79	0.031	1.3*	0.16	-	0.13	0.26
10	0.90	6.98	34	0.065	70	0.028	1.5*	0.16	-	0.13	0.26

Table B.2: Simulation matrix for 2D simulations of LPD2

B.2.4.2 Free Surface Elevation at x = 0 m

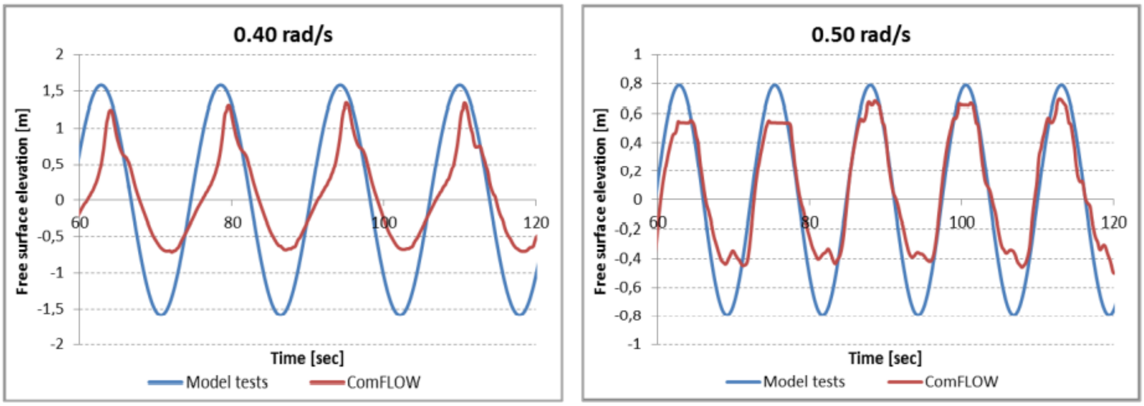

Figure B.16: Long waves free surface elevation at x=0 m

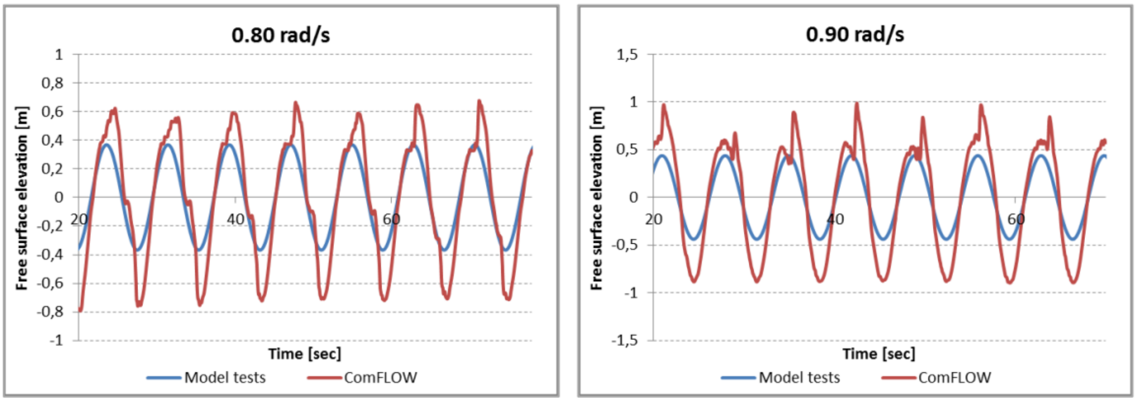

Figure B.17: Short waves free surface elevation at x=0 m

B.2.4.3 Free Surface Elevation at x = 10.5 m

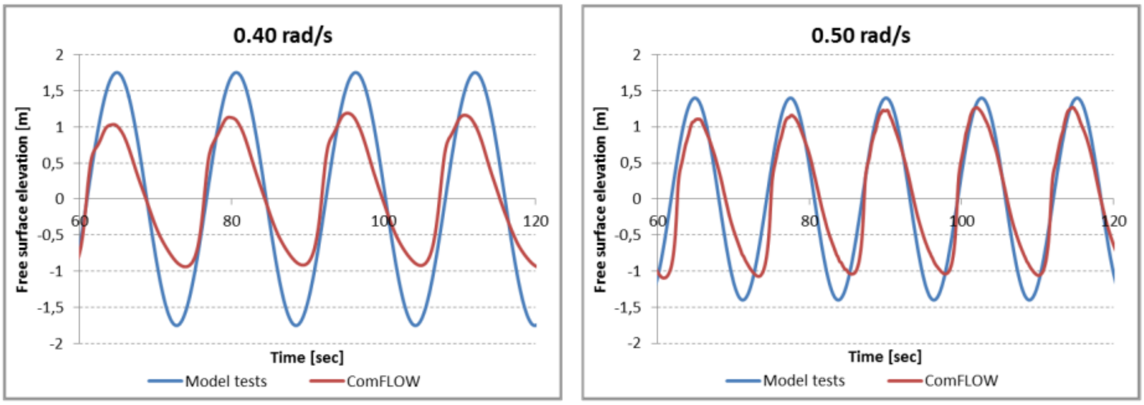

Figure B.18: Long waves free surface elevation at x=10.5 m

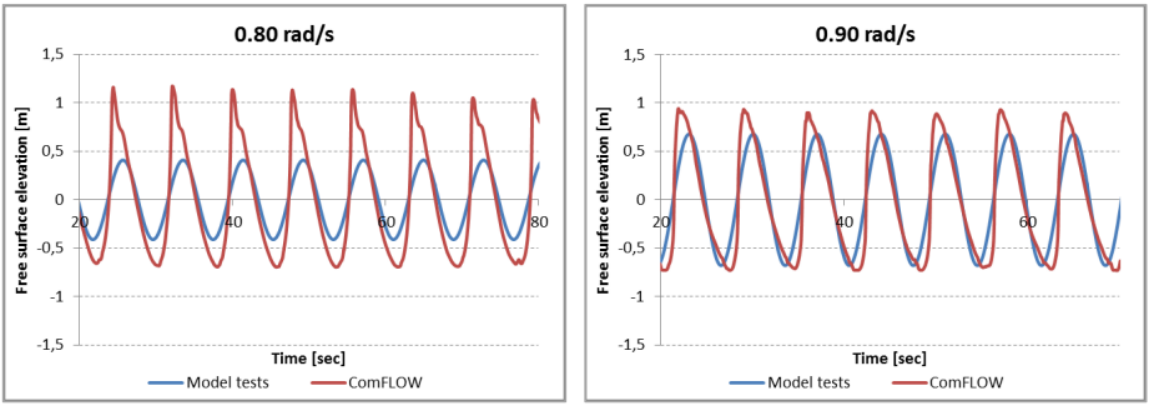

Figure B.19: Short waves free surface elevation at x=10.5 m

B.2.4.4 Free Surface Elevation at x = 21.3 m

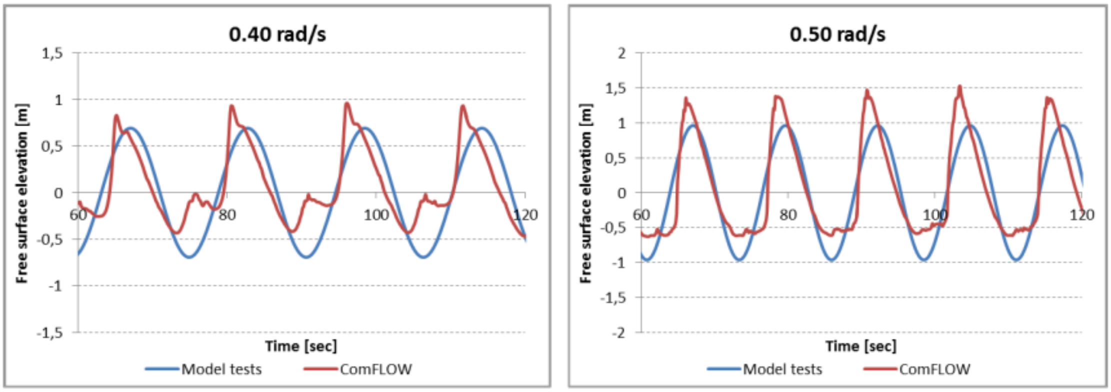

Figure B.20: Long waves free surface elevation at x=21.3 m

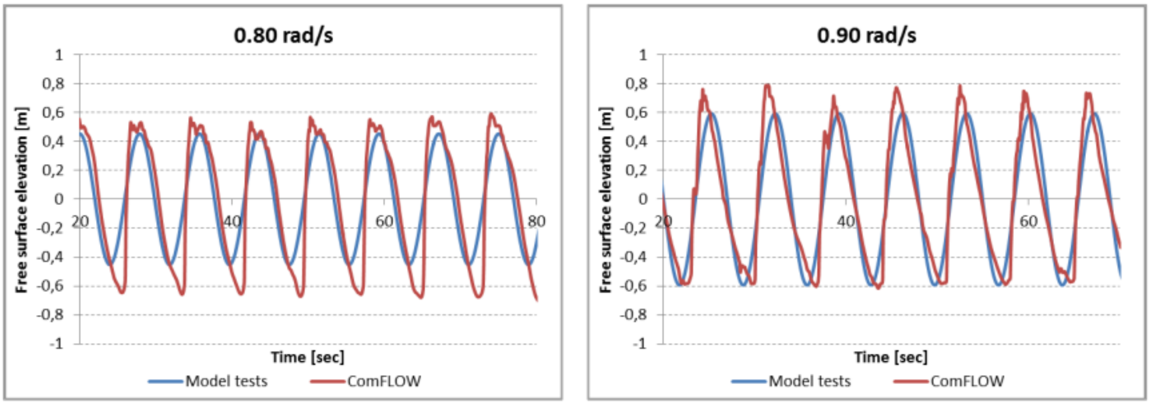

Figure B.21: Short waves free surface elevation at x=21.3 m

B.2.4.5 Free Surface Elevation at x = 32 m

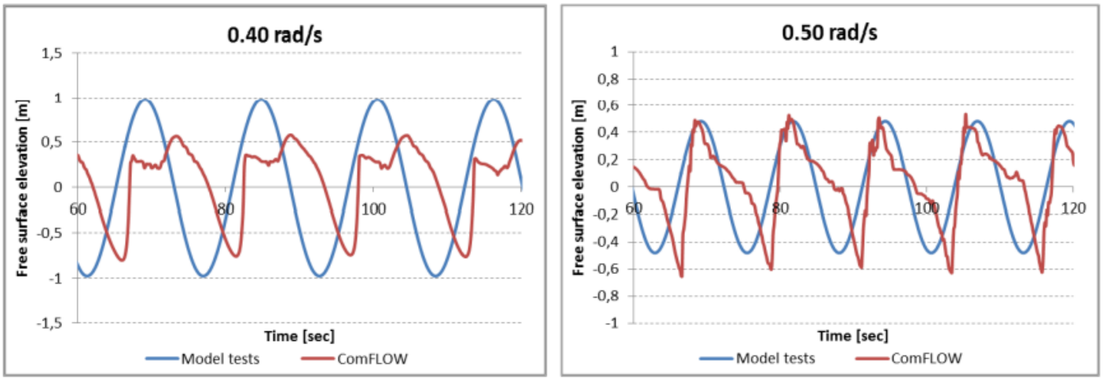

Figure B.22: Long waves free surface elevation at x=32 m

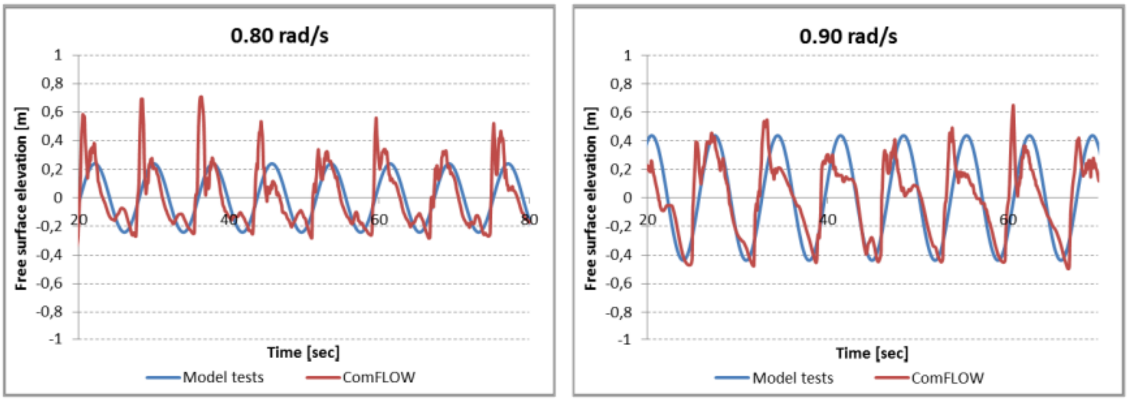

Figure B.23: Short waves free surface elevation at x=32 m

C

ComFLOW Modeling

C.1. Discretization

Discretization in space and time is a fundamental aspect of Computational Fluid Dynamics (CFD) simulations. It involves dividing the continuous domain and time into discrete elements to solve the governing equations (Navier-Stokes equations) numerically.

C.1.1. Spatial Discretization

In space discretization, the computational domain is divided into smaller regions or cells. This process is typically done using techniques such as structured grids (e.g., Cartesian, cylindrical, or spherical grids) or unstructured grids (e.g., triangular or tetrahedral meshes). Various numerical methods can be used for spatial discretization, including finite difference, finite volume, and finite element methods. In this thesis, the Finite Volume discretization method in space was used to solve the Navier-Stokes equations.

The two main issues in the discretization of the incompressible Navier-Stokes equations are the relation between convection and diffusion.The Reynolds number expresses the balance between convection and diffusion: for low Reynolds numbers (laminar flow) the diffusion term dominates the equations, but for high Reynolds numbers (turbulent flow) the convection terms dominates.

During the study of wave propagation, two methods were investigated, the central and upwind convection schemes for approximating the convective fluxes in the Finite Volume Method (FVM) of Computational Fluid Dynamics (CFD). In the next subsections, there is a detailed explanation of the differences between these schemes.

Central Convection Scheme

The central convection scheme approximates the flux across the control volume face by taking the average of the neighboring cell values as illustated in figure A.23. The central scheme provides second-order accuracy in smooth regions and can accurately capture gradients with minimal numerical diffusion. However, it is prone to numerical oscillations and smearing of sharp gradients or discontinuities.The discretization according to figure A.23 is:

$$\frac{u^n(i-\frac{1}{2},j)-u^n(i+\frac{1}{2},j)}{2dx} \tag{C.1}$$

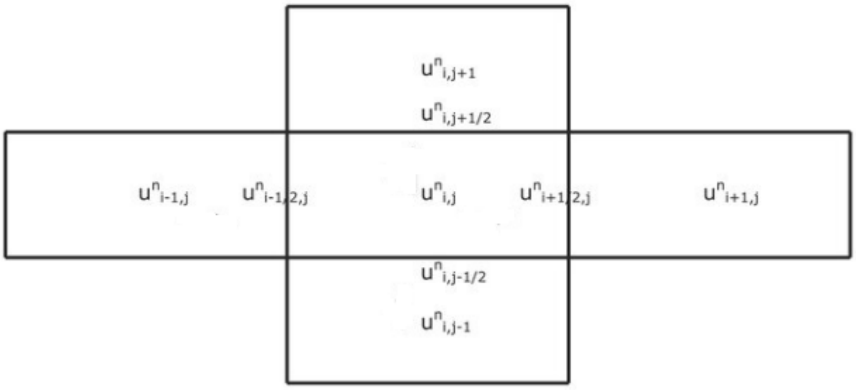

Figure C.1: Grid for Central Difference and Upwind Schemes for Discretization

Upwind Convection Scheme

On the other hand, the upwind convection scheme is designed to handle the transport of information in a preferred direction based on the local flow direction. It considers the values from the upwind neighboring cell to approximate the flux across the control volume face. Additionally, this scheme is particularly suitable for capturing sharp gradients and discontinuities, such as shock waves. Also, it provides a monotonic solution and reduces numerical oscillations. However, it introduces significant numerical diffusion and may result in a loss of accuracy in smooth regions.

The discretization according to figure A.23 is:

$$\frac{u^n(i-\frac{1}{2},j)-u^n(i,j)}{dx} \tag{C.2}$$

C.1.2. Time Discretization

In the finite volume method, time discretization is a crucial component used to solve time-dependent partial differential equations (PDEs). It involves dividing the time interval into discrete time steps and approximating the solution at each time step based on the conservation principles applied to control volumes. During this thesis, the Euler's Forward and Adams-Bashforth methods were used.

The key difference between the Euler forward method and the Adams-Bashforth 2nd order method lies in their accuracy and the number of previous time steps used for approximating the solution. The Euler forward method is a first-order method, meaning that its local truncation error is proportional to the size of the time step, resulting in lower accuracy. On the other hand, the Adams-Bashforth 2nd order method is a higher-order method, specifically second-order. This means that the Adams-Bashforth 2nd order method generally provides better accuracy compared to the Euler forward method for the same time step size. Furthermore, the Euler forward method only uses information from the previous time step to approximate the solution at the current time step, making it a one-step method. In contrast, the Adams-Bashforth 2nd order method uses information from the current and the previous time step. It is a two-step method, which enables it to incorporate additional information and improve the accuracy of the approximation.

D

Study on physical mechanisms within the well dock - Grid Study

D.1. Diffraction Grid Study

D.1.1. Diffraction Grid 13

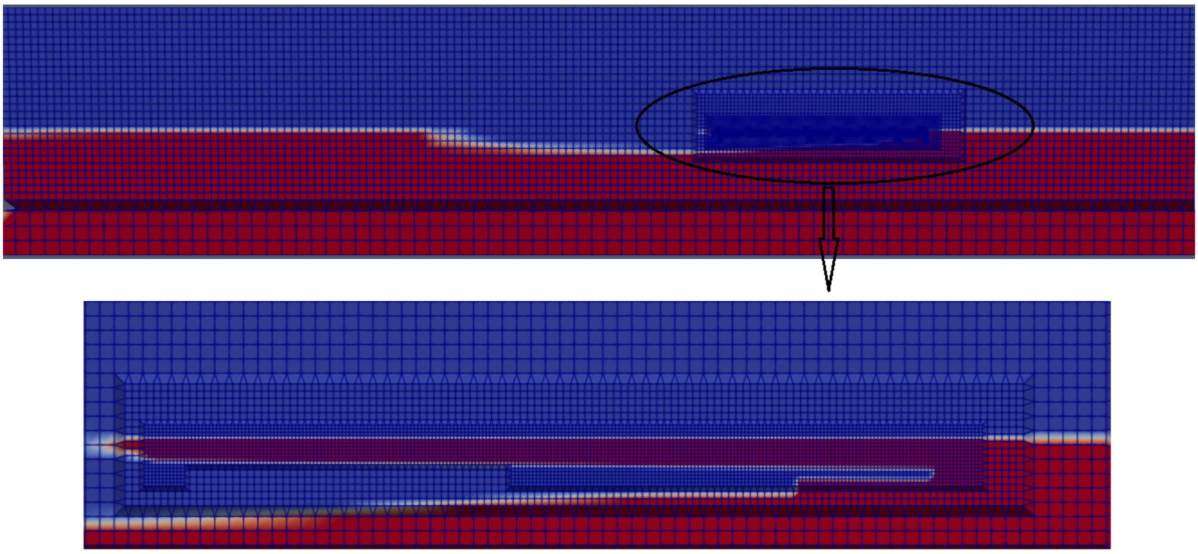

Figure D.1: Front View of the Diffraction Grid Study 13 and the Sub-grids within the well dock

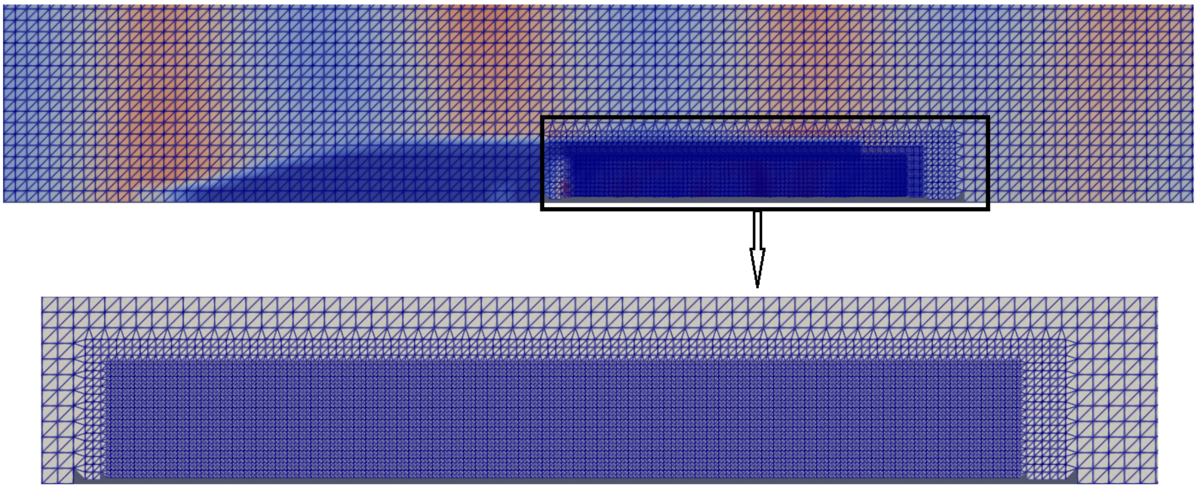

Figure D.2: Side View of the Diffraction Grid Study 13 and the Sub-grids within the well dock

D.1.2. Diffraction Grid 20

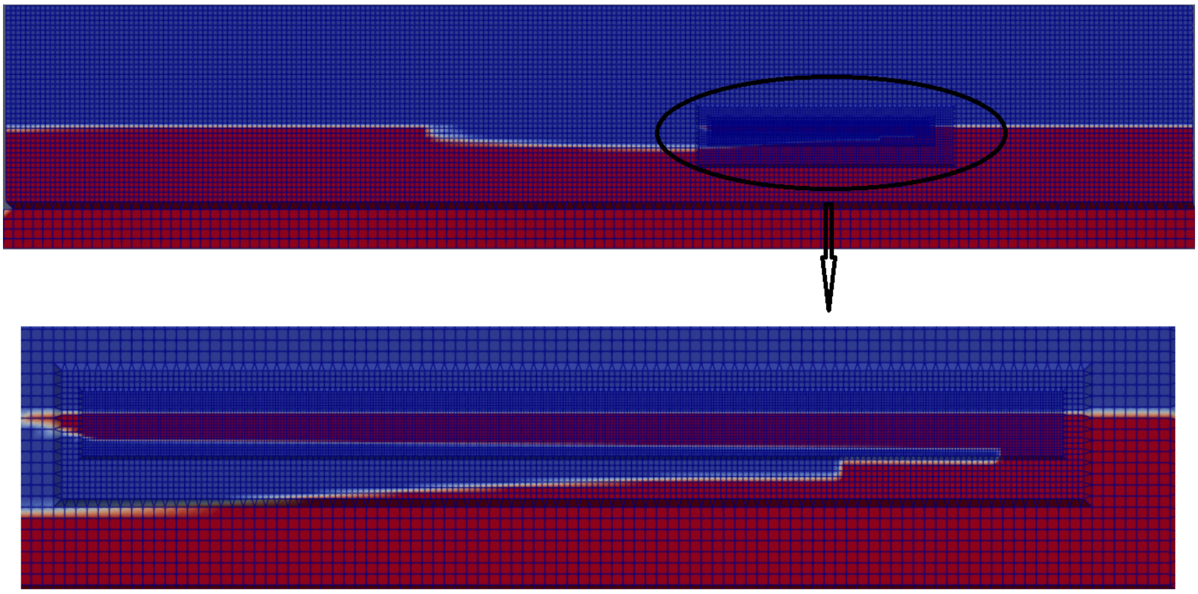

Figure D.3: Front View of the Diffraction Grid Study 20 and the Sub-grids within the well dock

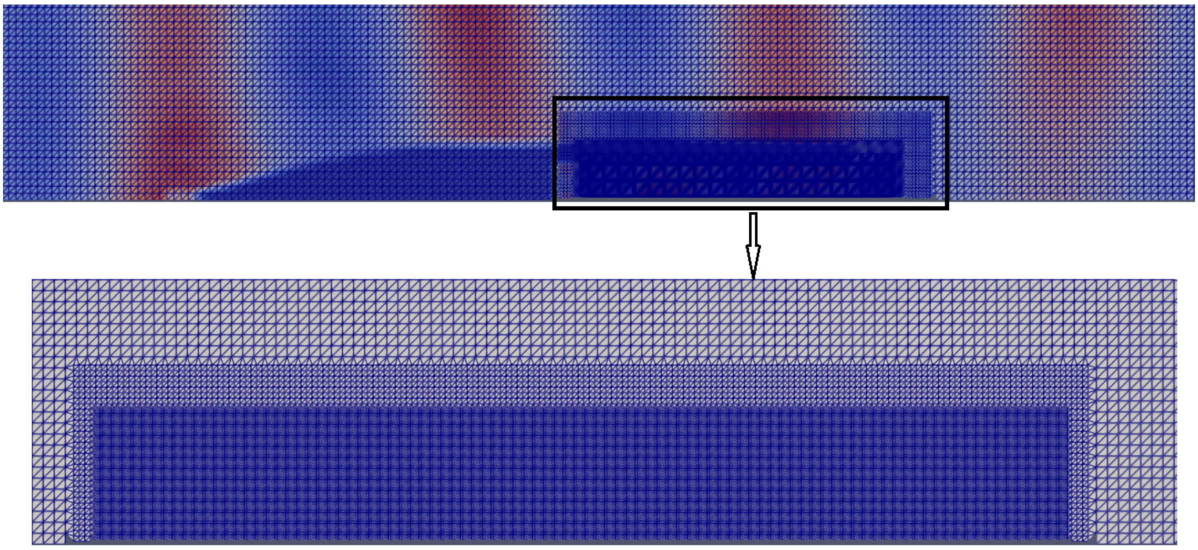

Figure D.4: Side View of the Diffraction Grid Study 20 and the Sub-grids within the well dock

D.1.3. Diffraction Grid 30

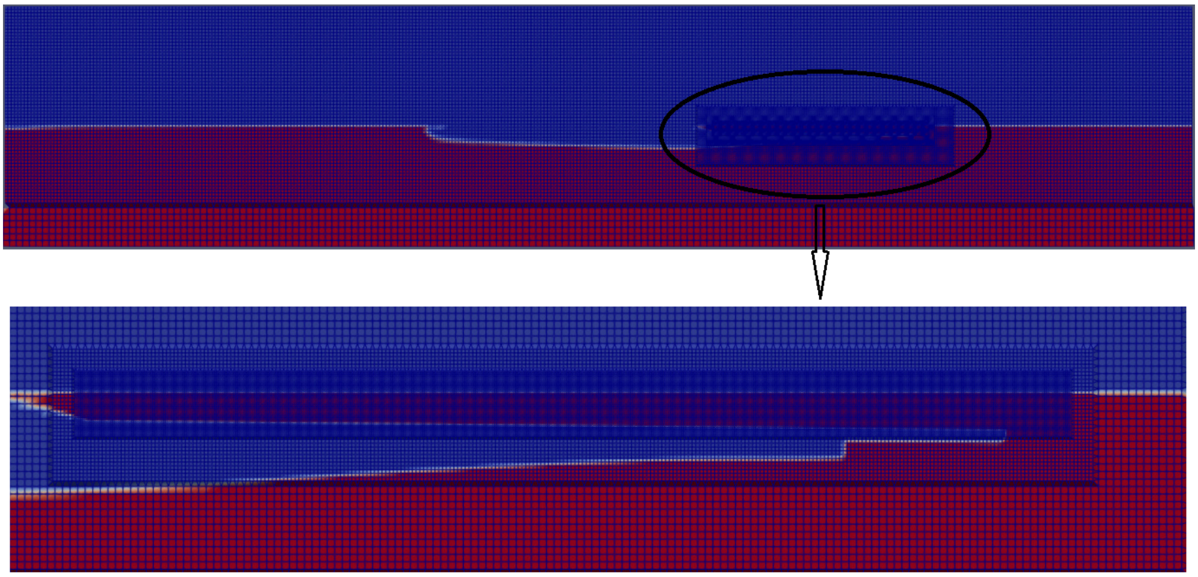

Figure D.5: Front View of the Diffraction Grid Study 30 and the Sub-grids within the well dock

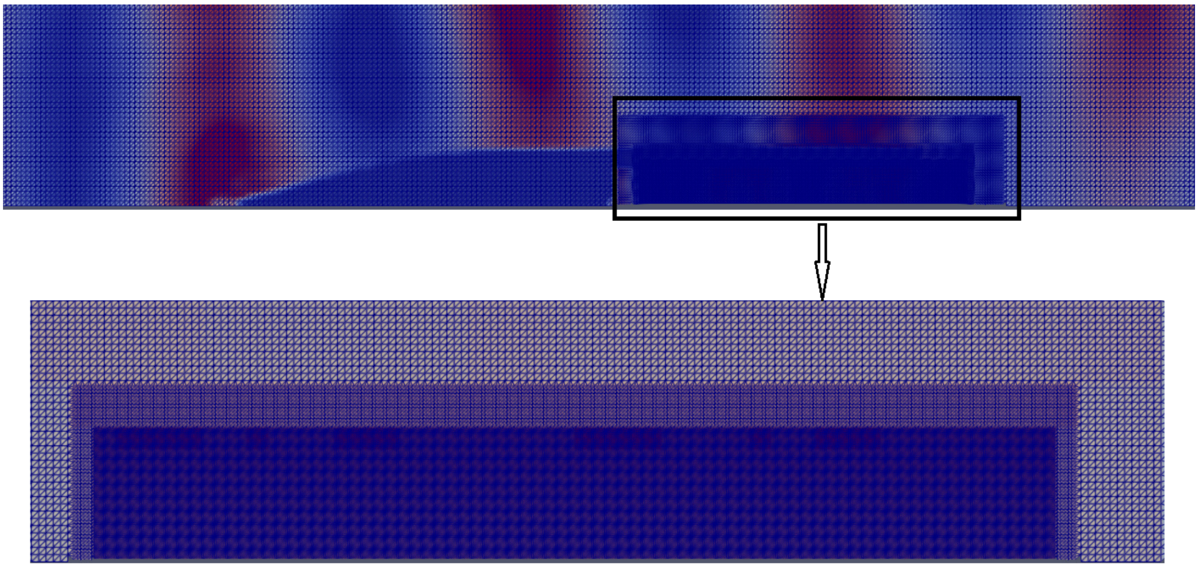

Figure D.6: Side View of the Diffraction Grid Study 30 and the Sub-grids within the well dock

D.2. Radiation Grid Study

D.2.1. Radiation Grid 13

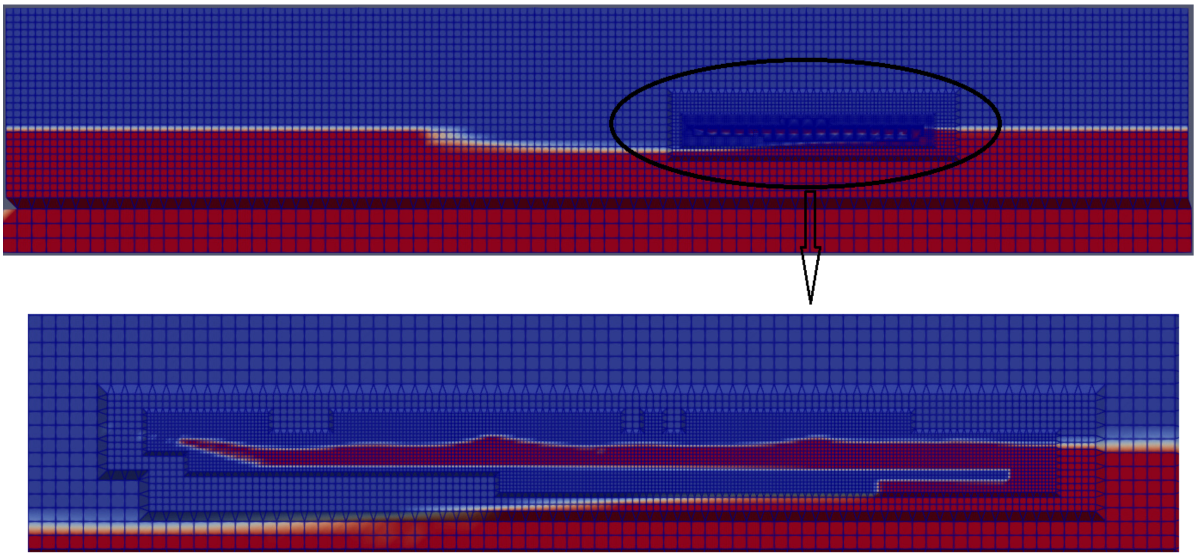

Figure D.7: Front View of the Radiation Grid Study 13 and the Sub-grids within the well dock

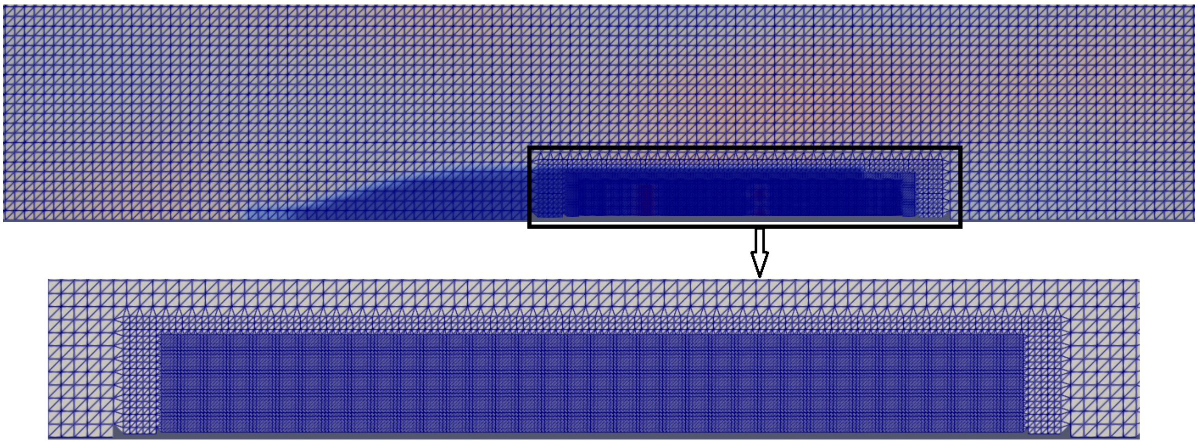

Figure D.8: Side View of the Radiation Grid Study 13 and the Sub-grids within the well dock

D.2.2. Radiation Grid 20

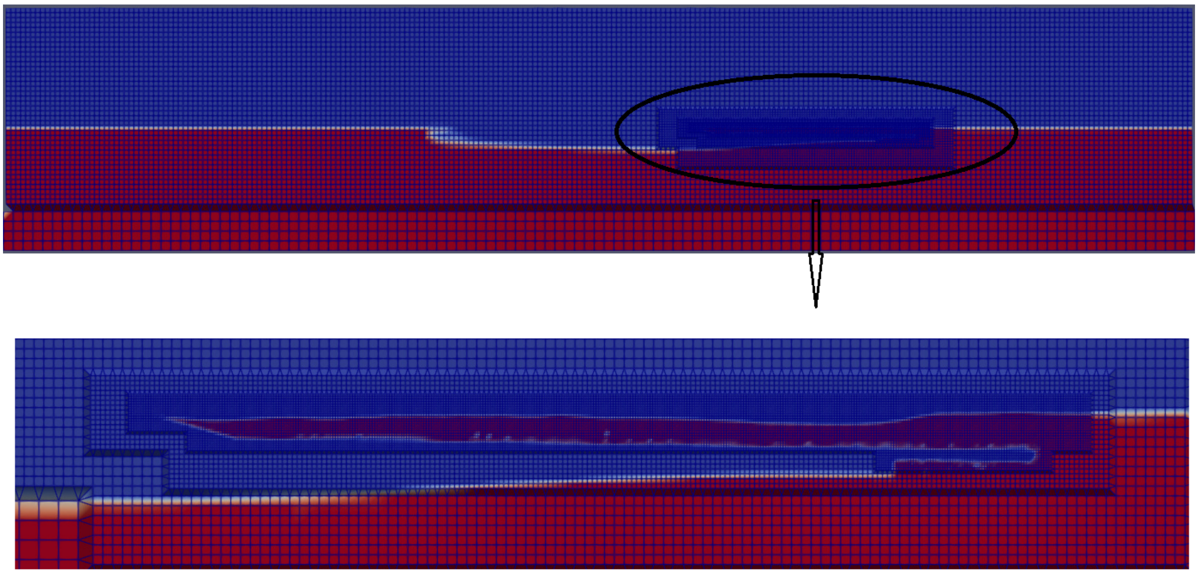

Figure D.9: Front View of the Radiation Grid Study 20 and the Sub-grids within the well dock

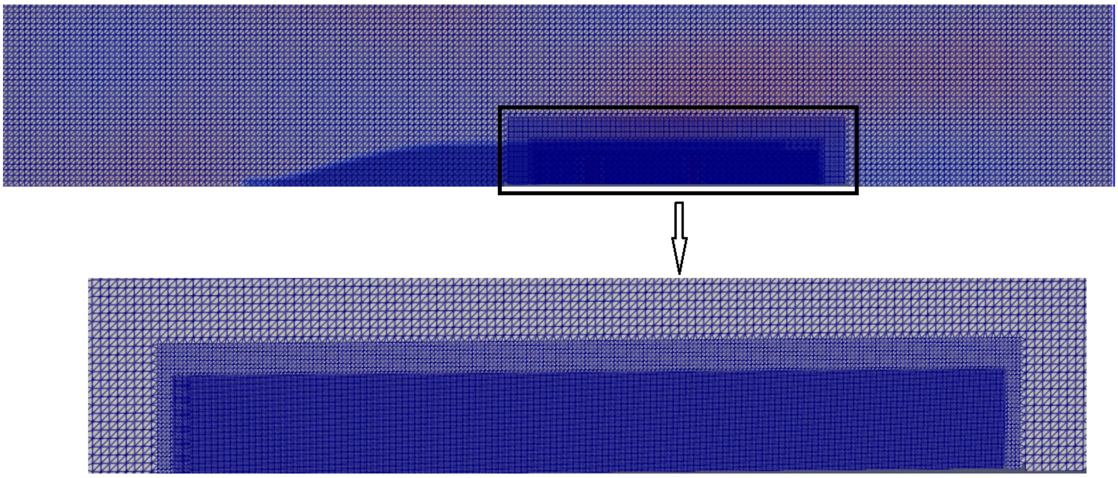

Figure D.10: Side View of the Radiation Grid Study 20 and the Sub-grids within the well dock

D.2.3. Radiation Grid 30

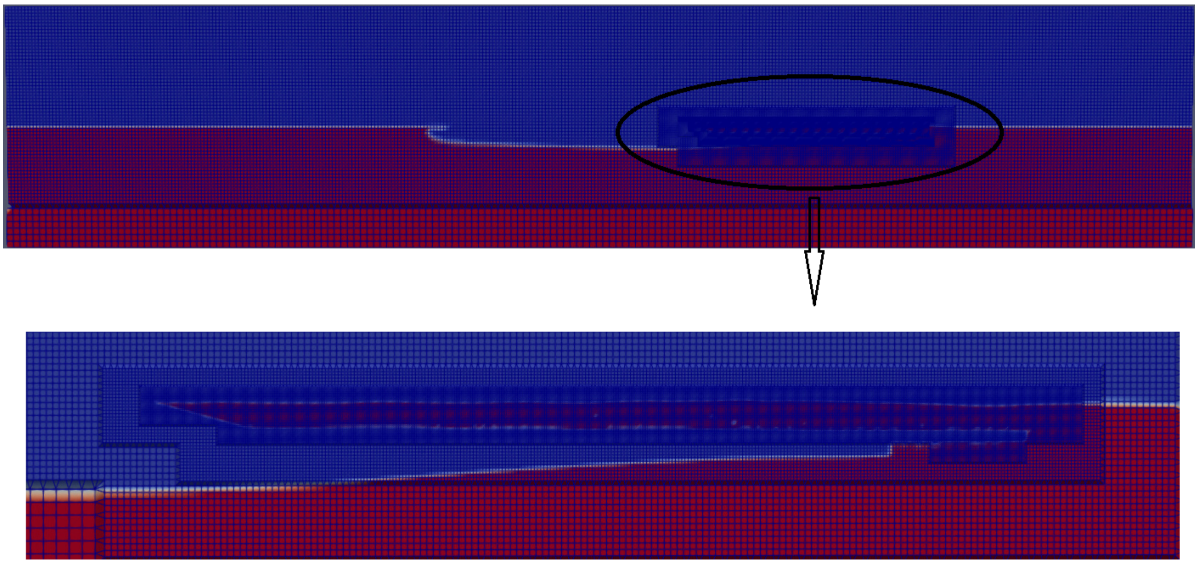

Figure D.11: Front View of the Radiation Grid Study 30 and the Sub-grids within the well dock

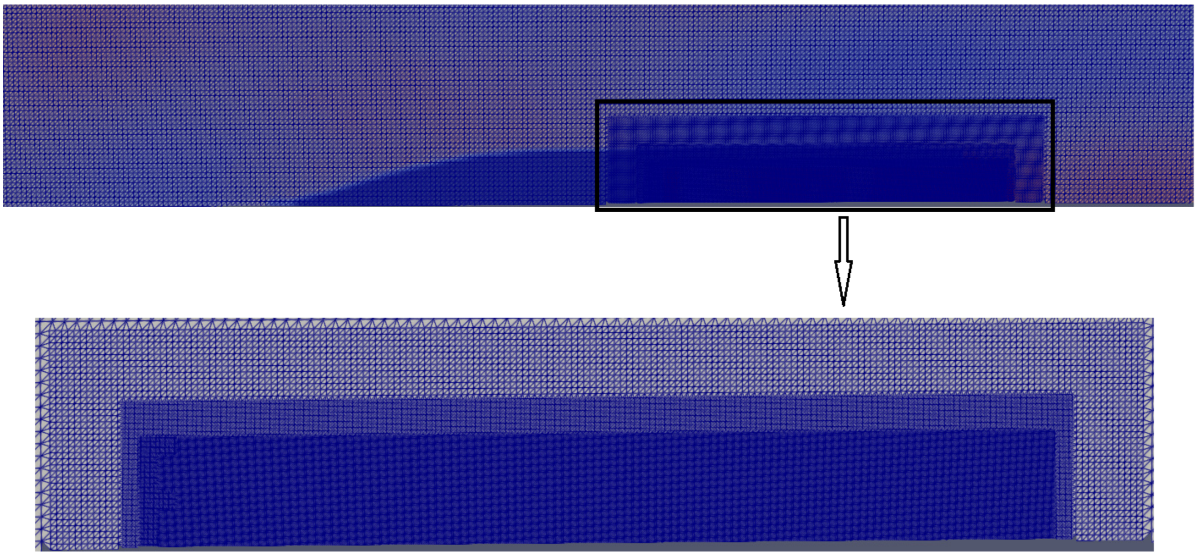

Figure D.12: Side View of the Radiation Grid Study 30 and the Sub-grids within the well dock

E

Full Model - Grid Study

E.1. Grid 13

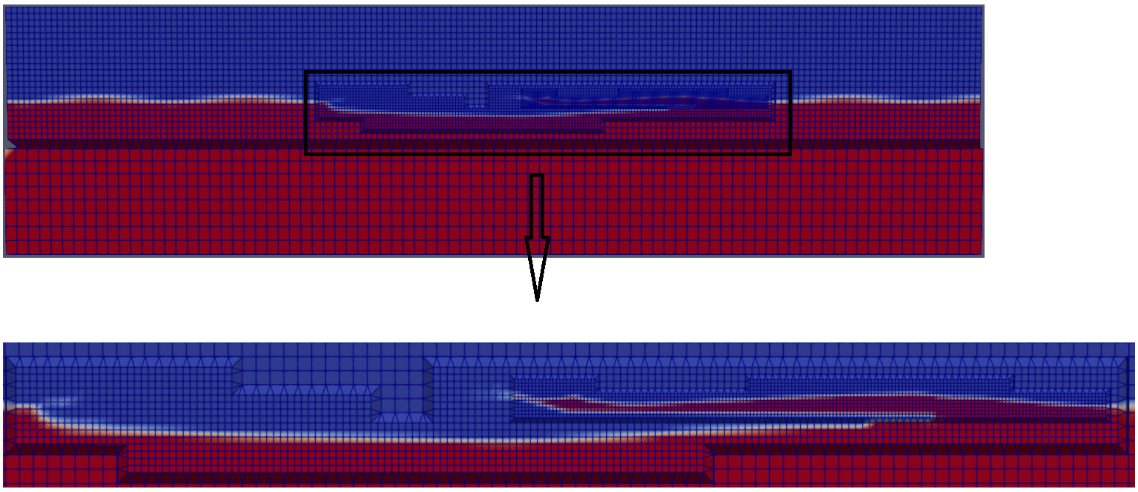

Figure E.1: Front View of the Second Grid Study 13 and the Sub-grids within the well dock

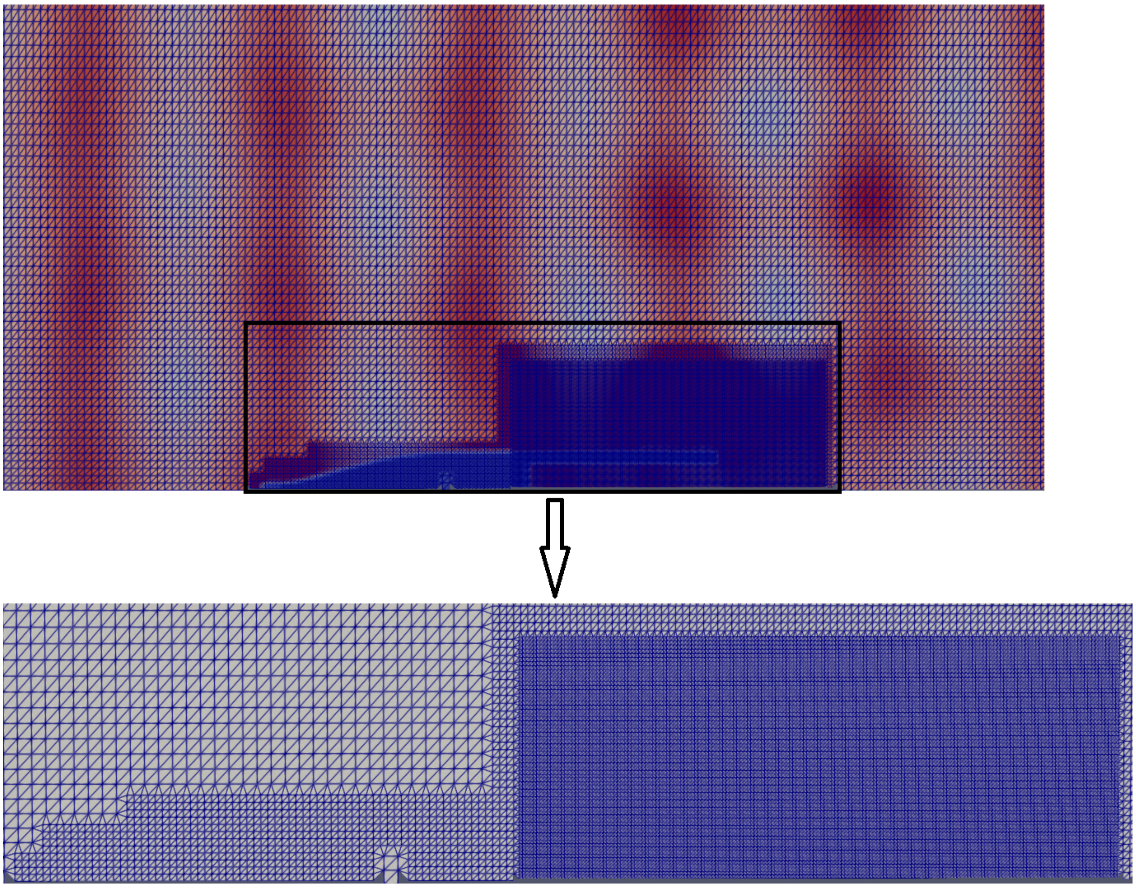

Figure E.2: Side View of the Second Grid Study 13 and the Sub-grids within the well dock

E.2. Grid 20

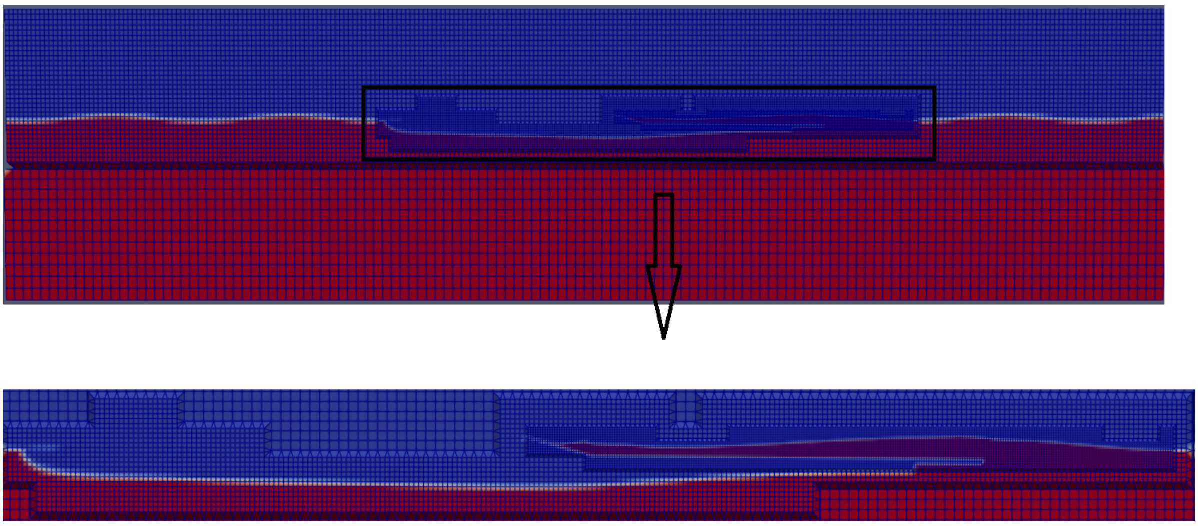

Figure E.3: Front View of the Second Grid Study 20 and the Sub-grids within the well dock

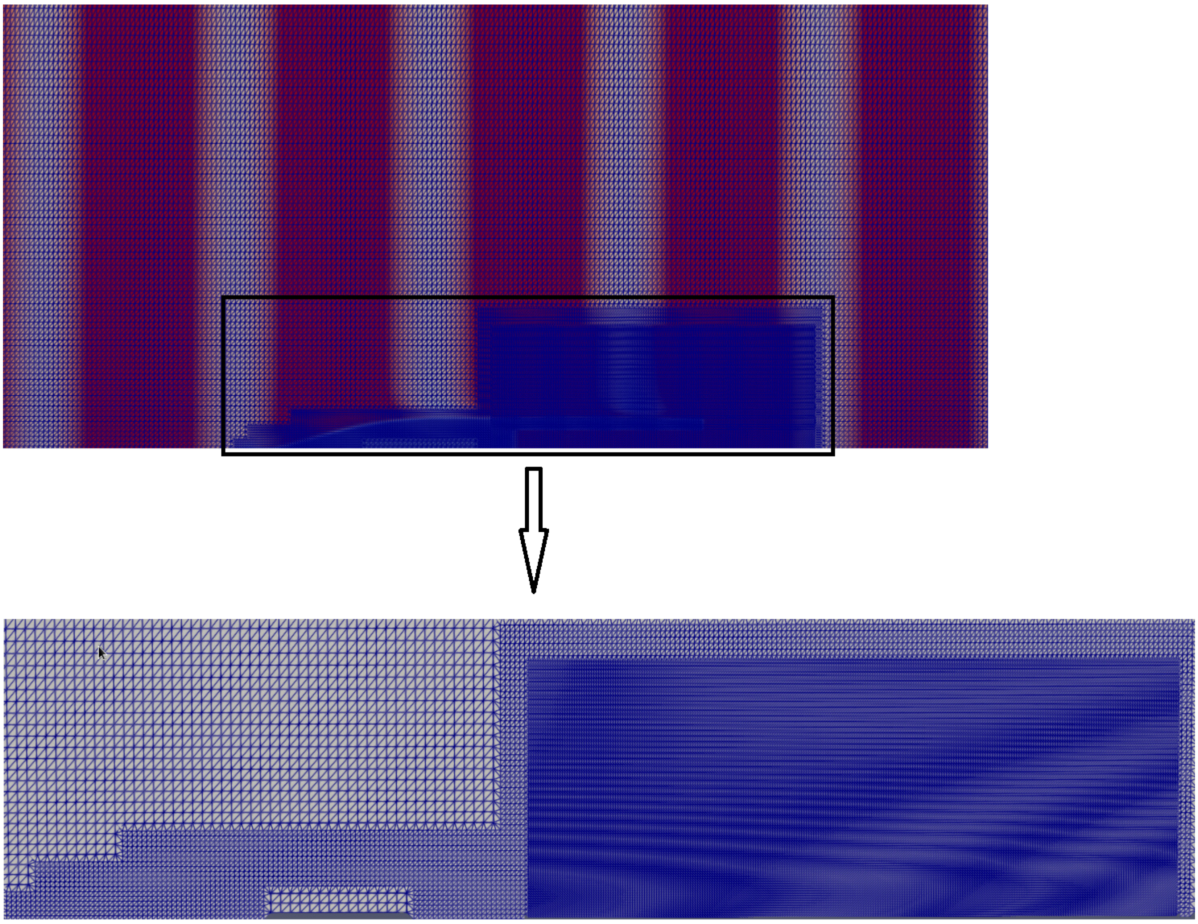

Figure E.4: Side View of the Second Grid Study 20 and the Sub-grids within the well dock

E.3. Grid 30

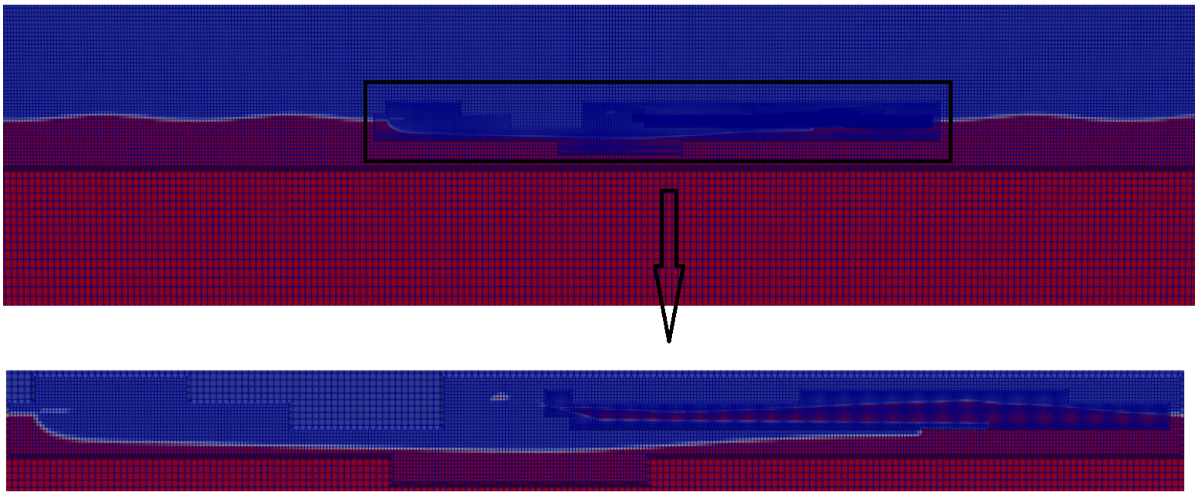

Figure E.5: Front View of the Second Grid Study 30 and the Sub-grids within the well dock

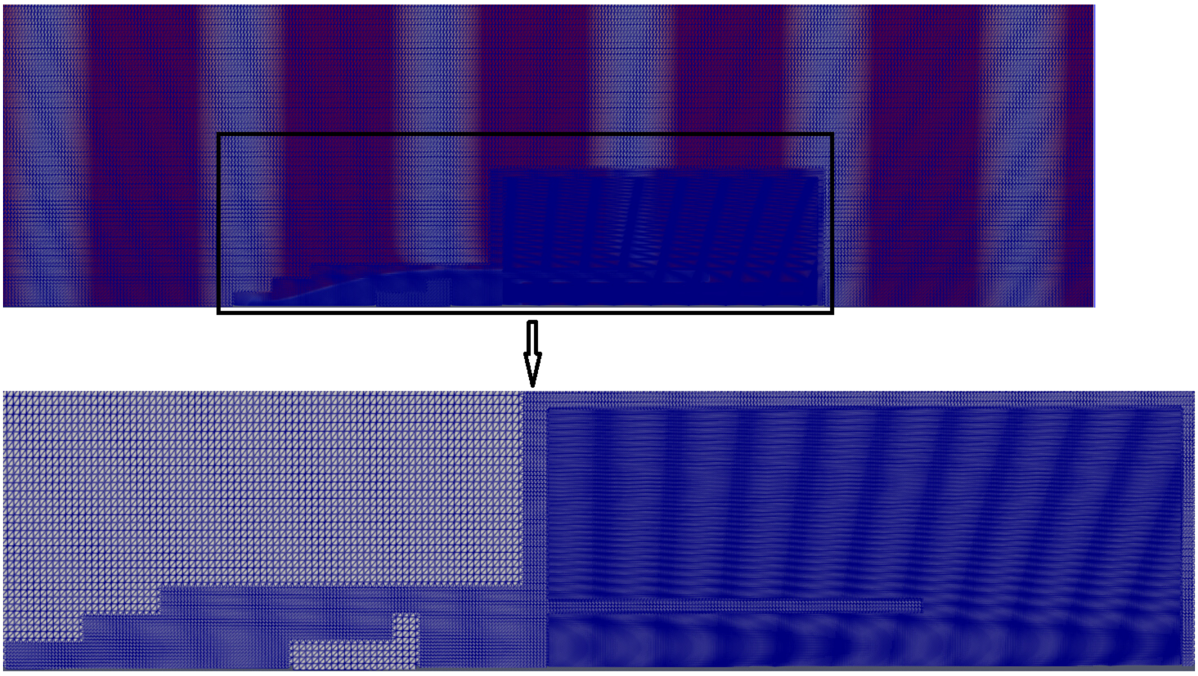

Figure E.6: Side View of the Second Grid Study 30 and the Sub-grids within the well dock

F

Viable Model - Grid Study

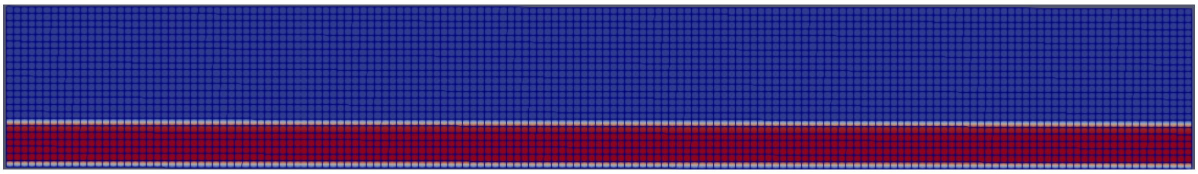

Figure F.1: Front View of the Coarse Grid and the Sub-grids within the well dock

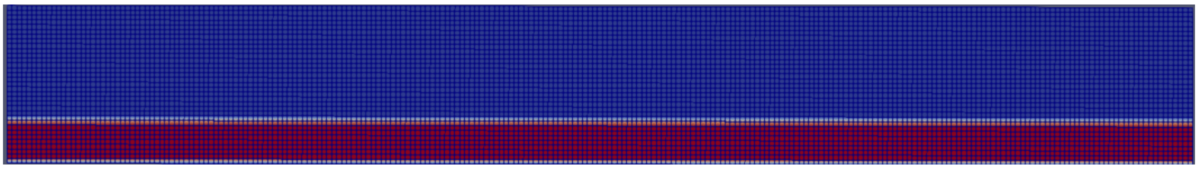

Figure F.2: Front View of the Medium Grid and the Sub-grids within the well dock

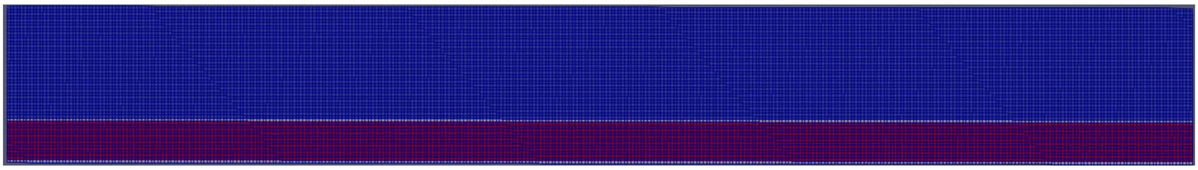

Figure F.3: Front View of the Fine Grid and the Sub-grids within the well dock